Porosity in Aluminum Alloys: Visualization, Characterization, and Modeling

THÈSE N^{O} 4639 (2010)

PRÉSENTÉE LE 12 MARS 2010

À LA FACULTÉ SCIENCES ET TECHNIQUES DE L'INGÉNIEUR
LABORATOIRE DE SIMULATION DES MATÉRIAUX
PROGRAMME DOCTORAL EN SCIENCE ET GÉNIE DES MATÉRIAUX

ÉCOLE POLYTECHNIQUE FÉDÉRALE DE LAUSANNE

POUR L'OBTENTION DU GRADE DE DOCTEUR ÈS SCIENCES

PAR

Milan FELBERBAUM

acceptée sur proposition du jury:

Prof. L. Zuppiroli, président du jury
Prof. M. Rappaz, directeur de thèse
Dr Ph. Gilgien, rapporteur
Dr L. Salvo, rapporteur
Prof. P. Uggowitzer, rapporteur

ÉCOLE POLYTECHNIQUE
FÉDÉRALE DE LAUSANNE
Suisse
2010

“Le hasard, c’est Dieu qui se promène incognito.”
Albert Einstein

Remerciements

Pour faire une thèse, on doit ouvrir ses yeux et ses oreilles. A la fin, en silence et dans le noir, on fait une synthèse de ce qu'on a appris. Mais pour ce faire, j'ai eu besoin d'un peu d'aide, et je voudrais maintenant remercier les personnes qui m'ont aidé tout au long de ce travail.

Tout d'abord, je voudrais remercier le professeur Michel Rappaz, directeur de thèse et "premier de cordée", pour m'avoir accueilli dans son labo et pris sous son aile. Sa motivation, sa rigueur, sa perspicacité et sa bonne humeur ont été autant de facteurs déterminants pour la bonne démarche de cette thèse. Outre ses fantastiques qualités scientifiques, ce sont ses qualités humaines ainsi que sa capacité à bien s'entourer qui m'ont marqué. Elles ont fait de son laboratoire un endroit non seulement renommé mais aussi plaisant, où chaque matin on se réjouit d'aller travailler.

Je voudrais aussi remercier les membres de mon jury pour avoir pris le temps d'évaluer cette thèse: le Prof. L. Zuppirolli, président du jury, qui a su diriger les débats d'une main experte; le Prof. P. Uggowitzer de Zürich, le Dr. Ph. Gilgien de Novelis, et le Dr. L. Salvo de Grenoble qui se sont tous déplacés jusqu'à Lausanne pour venir discuter de mon travail. Leurs questions, remarques et suggestions ont encore enrichi cette thèse.

Je voudrais ensuite remercier les différents "Sherpas" du laboratoire, en commençant par Jean-Daniel Wagnière; qu'aurais-je fait sans son aide pour la partie expérimentale! J'ai beaucoup appris de lui, autant sur les choses à faire que (peut-être encore plus important?) sur les choses à ne pas faire quand on veut mener à bien des expériences. Nous avons passé beaucoup de temps ensemble pour obtenir des résultats exploitables, et ces moments étaient vraiment chouettes!

Un grand merci aussi au Dr. Alain Jacot: c'est principalement grâce à lui qu'un nouveau modèle de champ de phase pour la porosité a été développé. De nouveau, je relève autant son esprit scientifique que sa bonne humeur et sa disponibilité. Et que serait-ce un café sans une de ses fameuses blagues!

Au début de ce travail, j'avais pas mal de lacunes dans le domaine de la programmation. Combien de fois suis-je venu toquer à la porte de Jean-Luc Desbiolles pour lui poser des questions! A chaque fois, il s'interrompait dans son travail et me répondait aussi gentiment que clairement. J'ai vraiment pu apprendre beaucoup de choses grâce à lui, et je l'en remercie énormément.

Le début d'année 2008 fut marqué par l'arrivée dans notre laboratoire du Dr. André Phillion. J'ai eu la chance et le grand plaisir de partager mon bureau avec lui. Sa compagnie, sa sympathie et les nombreuses discussions que nous avons eues ont vraiment dopé ma thèse. Nous avons passé deux années fantastiques ensemble, et je l'en remercie de tout coeur.

Je voudrais aussi remercier le Prof. Jonathan Dantzig. Son oeil vif, sa vision extérieure et critique, ainsi que son humour et ses *tips* informatiques m'ont bien facilité les choses.

Merci aussi au Dr. Jean-Marie Drezet qui a toujours porté un regard externe et, de ce fait, riche à mon travail. Les nombreuses discussions avec lui ainsi que ses conseils pour les méthodes inverses m'ont bien aidé.

Un grand merci à Arlette Blatti et Anne Roy pour leur aide. Chaque fois qu'il y avait une difficulté administrative, elles étaient là pour trouver la solution: il aurait été difficile de finir ce travail sans leur aide.

Merci à la Dr. Emmanuelle Boehm pour son aide à la metallo et ses bons conseils pour la microscopie électronique. Par la même occasion, je voudrais remercier toute l'équipe du centre de microscopie, et notamment le Dr. Marco Cantoni, pour leur aide durant cette thèse.

Une collaboration particulièrement fructueuse a été développée entre le LSMX et le laboratoire SIMAP de Grenoble. J'ai été un des grands bénéficiaires de cette collaboration, puisque j'ai pu participer à de nombreuses expériences inédites de tomographie. Je voudrais tout particulièrement remercier le Prof. Michel Suéry, le Dr. Luc Salvo, le Dr. Sofiane Terzi, la Dr. Nathalie Limodin, ainsi qu'Elodie Boller (qui est, elle, à l'ESRF) pour leur aide, que ce soit pour les expériences de tomographie en soi, ou pour l'interprétation des résultats. Au même titre, je voudrais remercier le Prof. Marco Stampanoni et le Dr. Sam McDonald du SLS. Sans ces personnes, de nombreux résultats de cette thèse auraient été bien plus difficilement obtenus.

La vie au labo a été riche, non seulement en discussions fructueuses, mais aussi en rires et en émotions. Je voudrais donc tout particulièrement remercier *911* Gonzo, *Asu*Léa, Aurèle++, Christophe *Fantomette*, Denis *TicTac*, Fred *Kartman*, Jonathan *L'aviateur*, Jonas *Le haut-parleur*, Jonas *Feuille-cailloux-ciseaux*, Guven *Chromium*, Hossein *PHF*, Kamal *NPH*, Luc *Le pompier*, Ludwig *le Brésilien*, Mario *Mexico* Salgado, Meisam *3D*, Gui Pasche *Partout*, Stéphane *Le 'ouf*, *Vit*Amin, et Vincent *La grande Allemande*. Je crois qu'ensemble on a vraiment bien bossé, mais on a aussi bien ri!

J'aimerais aussi remercier les étudiants avec qui j'ai travaillé durant cette thèse: V. Chapuis, A. Waszyk, J. Roch, N. Ruffray, et E. Landry-Désy. Superviser leurs travaux a été une expérience très enrichissante, et les résultats en valaient la peine.

L'institut des matériaux ne se réduit pas qu'au LSMX, et l'aide que j'ai reçue tout au long de cette thèse est aussi venue d'autres labos. A ce titre, je voudrais remercier chaleureusement toute l'équipe de l'Atelier de l'IMX, particulièrement Pierre-André et Werner *Père Noël*. Par la force des choses, j'arrivais souvent à l'improviste pour réparer

un moule ou demander de tourner des échantillons “à faire pour hier”. A chaque fois j'étais accueilli avec un grand sourire et à chaque fois le travail était fait dans les règles de l'art.

Une grande complicité s'est développée entre le LSMX et le laboratoire “concurrent” du LMM (les deux laboratoires de métallurgie!), et je voudrais tout d'abord remercier le Dr. Ludger Weber pour ses conseils et son aide sur la théorie des milieux effectifs qui a été développée dans cette thèse. Mais aussi, que dire des moments passés en compagnie de Bacc, Vincent, Fred Diolo, Nico, Rando, JF, Yves, Doris, Edwina, Julien Perret, Noelia, Senad, Raph, Jérôme, Carmen... Quelle équipe! Que ce fût dans les labos, dans les couloirs, à la soud', à SAT ou ailleurs, j'ai des souvenirs inoubliables. Merci à vous tous!

Mais une si bonne ambiance au travail ne serait rien sans une vie à la maison remplie de bonheur. Mes pensées vont donc avec émotions à mes parents qui m'ont toujours soutenu, qui ont su me guider jusqu'où il fallait et me laisser voler de mes propres ailes quand il fallait. Merci à Isaline et Andrea, ainsi qu'à Laurent et à sa famille, qui m'ont toujours montré l'exemple, ont un peu fait de moi qui je suis.

Et puis enfin et surtout, merci à Stacey pour son éternel soutient tout au long de cette thèse. Elle est le rayon de soleil quand je rentre le soir à la maison. Et même s'il y a eu des moments plus difficiles que d'autres (en particulier lors de la rédaction...), une chose infaillible à laquelle j'ai toujours pu me raccrocher, c'est l'Amour. Et petit clin d'oeil à mon regretté Tonton Jörg qui *a passé* le jour où j'ai rendu ma thèse et qui aimait écouter Jacques Brel chanter: “Quand on a que l'Amour [...], Nous aurons dans nos mains, Amis le monde entier”.

Et maintenant, l'Australie!

Abstract

Porosity is one of the major defects in castings because it reduces the mechanical properties of a cast piece [1]. Porosity formation results from the effect of two concomitant mechanisms, namely solidification shrinkage and segregation/precipitation of gases [1]. A model for the prediction of microporosity, macroporosity and pipe shrinkage during the solidification of alloys has been developed at the Computational Materials Laboratory (LSMX-EPFL) [2]. This model has then been improved by taking into account the effect of various alloying elements and gases on porosity formation [3, 4, 5]. However, the modeling of two physical phenomena still needed to be improved: (i) the curvature influence and (ii) the hydrogen diffusion influence on the growth of pores. The effect of pinching, i.e. the pores are forced by the growing solid network to adopt a complex non spherical shape, induces curvature restriction to the pores. This pinching effect can be a limiting factor for the growth of pores and is too simply modeled in the model of Péquet *et al.* [2]. Several other pinching models exist, but a rigorous experimental study to validate either one of these models is needed. Additionally, Carlson *et al.* [6] have recently shown that hydrogen diffusion might also be a limiting factor for the growth of pores. In the model of Péquet *et al.* [2], this effect was not taken into account.

This thesis is mainly aimed to (i) provide experimental results that specifically validate the pinching model developed by Couturier *et al.* [4], (ii) investigate the influence of hydrogen diffusion on the growth of pores and (iii) provide a new model that takes into account the pinching effect and the hydrogen diffusion influence on the growth of pores.

At first, pores formed in aluminum-copper (Al-Cu) samples (cast under controlled conditions) have been analyzed using high resolution X-ray tomography. The influence of the alloy inoculant, copper content, cooling rate and initial hydrogen content on the morphology of pores has been investigated. The results show that the curvature of micropores pinched in either non-inoculated or inoculated Al-4.5wt%Cu alloys can be fairly well approximated to that of cylinders. The results also show that the pinching model must be function of (i) the volume fraction of the primary phase g_α and (ii) the secondary dendrite arm spacing λ_2. However, the influence of the initial hydrogen content appears to be negligible. The pinching model developed by Couturier *et al.* [4] accounts for these observations and their relation fits fairly well the average mean curvature value of our experimental data.

A new model has been developed to calculate an effective hydrogen diffusion coefficient $D_e(g_s)$, that is a function of the volume fraction of solid only. For that purpose,

in-situ X-ray tomography has been performed on Al-Cu alloys. For each volume fraction of solid $0.6 \leq g_s \leq 0.9$, a representative volume element of the microstructure has been obtained from the tomography data. Solid and liquid voxels being assimilated to solid and liquid nodes respectively, a hydrogen diffusion equation has then been solved numerically. Calculations have been run until steady-state was reached in order to deduce $D_e(g_s)$ and the simulation results were successfully compared with a new theory based on effective-medium approximations. Both approaches lead to the main conclusion that hydrogen diffusion through the solid phase cannot be neglected, unlike it is assumed in the model of Carlson *et al.* [6].

Next, using the pinching model of Couturier *et al.* [4] and the obtained $D_e(g_s)$, a new volume-averaged model has been developed in order to simulate the growth of pores limited by (i) the curvature of the pore phase and (ii) the diffusion of hydrogen. The results show that, although hydrogen diffusion can be a limiting factor for the growth of pores, the pinching effect has a much larger influence. Accordingly, any model for porosity prediction should carefully take into account the influence of curvature and hydrogen diffusion on the growth of pores.

In order to ripen this study at a refined scale, a 2D phase-field model has been developed to describe the complex shape of a pore formed within interdendritic liquid channels [7]. The influence of the solid, which can force the pore to adopt a non-spherical shape, is taken into account through the geometry of the domain and appropriate boundary conditions. This model accounts for curvature influence and hydrogen diffusion in the liquid, two of the main aspects governing the growth kinetics of a pore. However, the model still needs to be combined with a description of the liquid flow induced by the pore growth. Basically, this model should serve as a sound basis for further developments that might lead to more sophisticated pinching models.

Finally, an experimental study has been conducted in order to track the inoculant influence on the shape of pipe shrinkage. Simultaneously, pipe shrinkage calculations (using the model of Péquet *et al.* [2]) were performed in order to track the influence of the $g_{s,c}$ parameter on the shape of the pipe shrinkage. This $g_{s,c}$ parameter corresponds to the critical volume fraction of solid at which mass feeding stops. Comparisons between experimental and simulation results show that the $g_{s,c}$ parameter should be set equal to 0.6 or 0.1 for a casting simulation of an inoculated or non-inoculated alloy, respectively.

Keywords: Porosity, microporosity, solidification, defects, X-ray tomography, mean curvature, hydrogen diffusion, inoculant, pore morphology, phase-field modeling, pipe shrinkage.

Résumé

La porosité est un problème récurrent dans les alliages de coulée. On l'évite autant que possible, puisqu'elle abaisse les propriétés mécaniques d'une pièce [1]. La porosité résulte de l'action combinée de deux mécanismes: le retrait de solidification et la ségrégation/précipitation de gaz [1]. Un modèle prédisant la microporosité, la macroporosité et la retassure d'une pièce coulée a été développé au Laboratoire de Simulation des Matériaux (LSMX-EPFL) [2]. En prenant en compte l'influence d'éléments d'alliages et de différents gaz, Couturier *et al.* [3, 4, 5] ont alors amélioré ce modèle. Toutefois, l'influence de la courbure et l'influence de la diffusion de l'hydrogène sur la croissance des pores sont deux phénomènes qui doivent encore être pris en compte de façon plus rigoureuse. L'action du pincement des pores, i.e. le fait que les pores soient contraints d'adopter une forme non sphérique et complexe, implique une restriction de courbure des pores. Cette action de pincement peut être un facteur limitant pour la croissance des pores, et ceci a été implémenté de façon trop simple dans le modèle développé par Péquet *et al.* [2]. Plusieurs modèles empiriques de pincement existent déjà, mais il manque une étude rigoureuse qui validerait expérimentalement l'un ou l'autre de ces modèles. Par ailleurs, Carlson *et al.* [6] ont récemment montré que la diffusion de l'hydrogène pourrait aussi être un facteur limitant pour la croissance des pores. Ceci n'était pas pris en compte dans le modèle de Péquet *et al.* [2].

Ce travail de thèse propose donc trois choses : (i) des résultats expérimentaux qui valident spécifiquement le modèle de pincement des pores développé par Couturier *et al.* [4], (ii) une étude de l'influence de la diffusion de l'hydrogène sur la croissance des pores, et (iii) un nouveau modèle de porosité qui prend en compte l'influence de la courbure et de la diffusion de l'hydrogène sur la croissance des pores.

Tout d'abord, des alliages aluminium-cuivre (Al-Cu) ont été coulés de façon contrôlée. Ces échantillons ont ensuite été analysés par tomographie à rayons X à haute résolution pour déterminer l'influence de l'inoculant, de la teneur en cuivre, du taux de refroidissement et de la concentration initiale en hydrogène de l'alliage sur la morphologie des pores contenus dans ces échantillons. Les résultats montrent qu'indépendamment de l'inoculation de l'alliage, la courbure moyenne des pores contenus dans un alliage d'Al-4.5wt%Cu peut être assimilée à celles de cylindres. Les résultats montrent aussi que le modèle de pincement des pores doit être fonction de la fraction volumique de phase primaire g_α, ainsi que de l'espacement secondaire des bras de dendrites λ_2. En revanche, l'influence de la concentration initiale en hydrogène semble être minime. Le modèle de pincement des pores proposé par Couturier *et al.* [4] tient compte de toutes ces considérations et corrobore de manière satisfaisante nos résultats de tomographie.

Un coefficient effectif de diffusion de l'hydrogène $D_e(g_s)$ fonction de la fraction volumique de solide g_s uniquement a ensuite été calculé. Pour ce faire, des alliages Al-Cu ont été analysés *in-situ* par tomographie à rayons X. Un élément de volume représentatif de la microstructure de ces alliages a été extrait pour des fractions volumiques de solide comprises entre 0.6 et 0.9. Chaque voxel solide ou liquide a été ensuite utilisé comme noeud solide ou liquide pour résoudre numériquement l'équation de diffusion de l'hydrogène. Une fois l'état stationnaire atteint, les valeurs de $D_e(g_s)$ ont pu être déduites de ces simulations. Ces valeurs ont été ensuite comparées avec succès à des modèles de milieux effectifs, et il est montré que la diffusion de l'hydrogène à travers la phase solide ne peut pas être négligée comme il est supposé dans le modèle de Carlson *et al.* [6].

Ensuite, grâce au modèle de pincement de Couturier *et al.* [4] et en utilisant $D_e(g_s)$, un modèle de porosité a été développé pour simuler la croissance de pores limitée par l'action de la courbure et de la diffusion de l'hydrogène. Les résultats montrent que, même si la diffusion de l'hydrogène peut être un facteur limitant pour la croissance des pores, l'influence de la courbure due au pincement des pores est nettement plus importante. En conséquence, tout modèle de porosité devrait d'une part prendre en compte l'influence de la diffusion de l'hydrogène sur la croissance des pores et, d'autre part, utiliser un modèle de pincement des pores adéquat.

Pour étayer ce travail à plus fine échelle, un nouveau modèle de champ de phase bidimensionnel a été développé afin de tenter de prédire la forme complexe qu'adopte un pore lorsqu'il est pris dans un réseau inter-dendritique. L'influence du solide, lequel force le pore à adopter une forme non sphérique, est prise en compte par la géométrie du domaine et grâce à des conditions de bord appropriées. Ce modèle de champ de phase prend en compte l'influence de la courbure et celle de la diffusion de l'hydrogène, mais ne prend pas en compte, pour le moment du moins, la convection du liquide. Néanmoins, ce modèle est sujet à de nombreuses améliorations qui pourraient conduire aux développements de modèles de pincement des pores plus sophistiqués et réalistes.

Une étude expérimentale visant à déterminer quelle influence a l'inoculant sur la forme de la retassure d'une pièce coulée est finalement présentée. En parallèle sont présentés des calculs numériques (en utilisant le modèle de Péquet [2]) montrant l'influence du paramètre $g_{s,c}$ sur la forme de la retassure. Ce paramètre $g_{s,c}$ décrit la fraction de solide critique à laquelle le retrait de solidification n'est plus compensé par l'apport de matière. La comparaison des résultats expérimentaux avec ceux de la simulation montre que le paramètre $g_{s,c}$ devrait être fixé à 0.6 pour la simulation d'un alliage inoculé et à 0.1 pour un alliage non-inoculé.

Mots-clés: Porosité, microporosité, solidification, défauts, tomographie à rayons-X, courbure moyenne, morphologie des pores, inoculant, diffusion de l'hydrogène, champ de phase, retassure.

Contents

List of symbols

Principal nomenclature

Table 1: Roman alphabet

Symbol	Quantity Represented	Unit
A, B	species (component) A, B	-
A	area	m^{-2}
a_A	chemical activity of species A	-
A, B	constants	-
C_A	mass fraction of species A, mass of A / total mass	wt%
C_s^*, C_ℓ^*	mass fractions in the solid and liquid at the interface	wt%
c_p	specific heat at constant pressure	$\mathrm{J\,kg^{-1}\,K^{-1}}$
d	mesh size	m
D	chemical diffusivity of solute	$\mathrm{m^2\,s^{-1}}$
$\mathfrak{D}_{eff}$	general effective property	arbitrary
D_e	effective diffusion coefficient	$\mathrm{m^2\,s^{-1}}$
E	eigenvector matrix of the moment of inertia tensor	m^5
f_A	activity coefficient of the species A	-
g	acceleration due to gravity = 9.81	$\mathrm{m\,s^{-2}}$
g_α	volume fraction of phase α	-
G	temperature gradient; Gibbs free energy	$\mathrm{K\,m^{-1}}$; J
G_α^m	molar Gibbs free energy of phase α	$\mathrm{J\,mol^{-1}}$
G_A^o	standard Gibbs free energy of the pure component A	$\mathrm{J\,mol^{-1}}$
$\mathcal{G}$	Gauss curvature	m^{-2}
h	specific enthalpy	$\mathrm{J\,kg^{-1}}$
h_T	heat transfer coefficient	$\mathrm{W\,m^{-2}\,K^{-1}}$
H	enthalpy	J
$\mathbf{I}$	unit tensor (identity tensor); the ij component is δ_{ij}	-
I^{ND}	non-dimensionalized inertia tensor matrix	-
$\mathbf{J}_A$	mass fraction flux for species A	$\mathrm{m\,s^{-1}}$
$\mathcal{J}_A$	mass fraction flux for species A	$\mathrm{mol\,m^{-2}\,s^{-1}}$
k	thermal conductivity	$\mathrm{W\,m^{-1}\,K^{-1}}$
k_0	partition coefficient	-
k_B	Boltzmann's constant, 1.38×10^{-23}	$\mathrm{J\,K^{-1}}$
K	permeability	m^{-2}
$\mathcal{K}$	chemical reaction constant	-

Table 1: Roman alphabet (continued)

Symbol	Quantity Represented	Unit
L	length	m
L_f	latent heat of fusion	$\mathrm{J\,kg^{-1}}$
L_v	latent heat of vaporization	$\mathrm{J\,kg^{-1}}$
$\overline{M}_A$	mean mobility of species A	$\mathrm{mol\,m^2\,s^{-1}\,J^{-1}}$
$\mathcal{M}_A$	molecular weight of species A	kg
m_ℓ,m_S	slopes of the liquidus and solidus lines	$\mathrm{K\,wt\%^{-1}}$
N_0	Avagadro's number, 6.022×10^{-23}	$\mathrm{at\,mol^{-1}}$
N_A	total number of atoms of species A in a mixture	-
N_c	Number of components	-
N_g	number of grid points in a computational domain	-
N_ϕ	Number of phases	-
n	number of moles	-
$\mathcal{N}_p$	pore density	$\mathrm{m^{-3}}$
$\mathbf{n}$	unit vector normal to a surface	-
p	pressure	Pa
p_{atm}	atmospheric pressure	Pa
p_g	gas pressure, pressure inside a pore	Pa
p_ℓ	liquid pressure	Pa
p_0	standard pressure	Pa
q_b	boundary heat flux	$\mathrm{W\,m^{-2}}$
$\mathcal{R}$	gas constant = 8.31	$\mathrm{J\,mol^{-1}\,K^{-1}}$
R	radius	m
R_p	pore radius	m
R_{p0}	characteristic radius within which a pore can grow	m
R_p^{sph}	Radius of a spherical equivalent pore	m
$\dot{R}$	specific heat generation rate	$\mathrm{W\,m^{-3}}$
r, θ, z	cylindrical coordinates	-
r, θ, ϕ	spherical coordinates	-
$r^\dagger$	dimensionless radius	-
$R_p^{sph,\dagger}$	dimensionless pore radius	-
S	bounding surface; entropy; solid	- ; $\mathrm{J\,K^{-1}}$; -
S_ℓ	Sievert's constant	$\mathrm{mol\,m^{-3}}$
t_c	characteristic time	s
t	time	s
t_f	local solidification time	s
T	temperature	°C or K
$T^\star$	liquid-solid interface temperature	°C or K
T_b	boundary temperature	°C or K
T_{eut}	eutectic temperature	°C or K
T_f	equilibrium melting temperature	°C or K
T_{liq}	liquidus temperature	°C or K
T_p	melting point of a pure material	°C or K

Table 1: Roman alphabet (continued)

Symbol	Quantity Represented	Unit
T_{sol}	solidus temperature	℃ or K
U	electric potential	V
v	*vertex*; scalar velocity	- ; $\mathrm{m\,s^{-1}}$
$\mathbf{v}, v$	velocity vector, scalar magnitude	$\mathrm{m\,s^{-1}}$
v_n	velocity normal to the liquid-solid interface	$\mathrm{m\,s^{-1}}$
v_L	liquidus velocity	$\mathrm{m\,s^{-1}}$
$\mathbf{v}_\alpha$	velocity vector for species α	$\mathrm{m\,s^{-1}}$
V	volume	$\mathrm{m^3}$
V_{comp}	Volume of the calculation domain	$\mathrm{m^2}$
W	double-well in the phase-field method	$\mathrm{J\,m^{-3}}$
X_A	molar composition of species I, moles I / total moles	-
$\overline{X}_A$	average molar composition	-
$\langle X_H \rangle$	average molar composition of hydrogen in the mush	-
$X_{H\ell 0}$	initial hydrogen composition in the liquid	-
$X^\dagger_{H\ell}$	normalized hydrogen composition in the liquid	-
$X^\dagger_{H_2}$	normalized hydrogen composition in the gas phase	-
$\mathbf{x}$	position vector	m
x, y, z	Cartesian coordinates; also x_1, x_2, x_3	m
$\mathfrak{X}_A$	number of moles of A per cubic meter	$\mathrm{mol\,m^{-3}}$

Table 2: Greek alphabet

Symbol	Quantity Represented	Unit
α	thermal diffusivity $\equiv k/(\rho c_p)$	$\mathrm{m^2\,s^{-1}}$
β	solidification shrinkage coefficient	-
β_T	volumetric thermal expansion coefficient	$\mathrm{K^{-1}}$
β_C	volumetric solutal expansion coefficient	$\mathrm{wt\%^{-1}}$
β_p	compressibility coefficient	Pa
$\Gamma_{s\ell}$	Gibbs-Thomson coefficient, $\gamma_{sl} T_f/\rho L_f$	$\mathrm{K\,m}$
$\gamma_{f\ell}$	surface tension between foreign substrate and liquid	$\mathrm{N\,m}$
γ_{fs}	surface tension between foreign substrate and solid	$\mathrm{N\,m}$
$\gamma_{s\ell}$	surface tension between solid and liquid	$\mathrm{N\,m}$
ΔS_f	entropy of fusion, $\rho L_f/T_f$	$\mathrm{J\,m^{-3}\,K^{-1}}$
ΔS_f^{mA}	molar entropy of fusion of species A	$\mathrm{J\,K^{-1}\,mol^{-1}}$
ΔT_0	solidification interval	K
ΔT_k	kinetic undercooling	K
ΔT_R	curvature undercooling	K
ΔT_s	solutal undercooling	K
$\Delta x, \Delta y, \Delta z$	grid spacing in various coordinate directions	m
δ	interface thickness	m
δ_{ij}	unit tensor in indicial notation (the Kronecker delta)	-
θ	dimensionless temperature; angular coordinate	-

Table 2: Greek alphabet (continued)

Symbol	Quantity Represented	Unit
$\kappa_{1,2}$	principal curvatures	m^{-1}
$\bar{\kappa}$	mean curvature	m^{-1}
$\langle\bar{\kappa}\rangle_{tot}$	average value of the mean curvature	m^{-1}
$\langle\bar{\kappa}\rangle_{\geq 0}$	average value of the mean curvature for $\kappa_{1,2} \geq 0$ only	m^{-1}
λ_1, λ_2	primary, secondary dendrite arm spacing	m
μ	viscosity of a Newtonian fluid	Pa s
μ_A	chemical potential of species A	$\mathrm{J\,mol}^{-1}$
$\mu_{\ell g}$	mobility coefficient of the liquid-gas interface	$\mathrm{m}^4\mathrm{J}^{-1}\,\mathrm{s}^{-1}$
ν	phase (either solid or liquid)	-
π	3.14159 . . . or plane	
ρ	density	$\mathrm{kg\,m}^{-3}$
ρ_0	pore free density	$\mathrm{kg\,m}^{-3}$
Σ	arbitrary surface patch	
τ	dimensionless time	-
ϕ_A	fugacity coefficient for this component	Pa^{-1}
χ_A	molar fraction of the element A	-
ψ	order parameter of the phase-field method	-
Ω	regular solution parameter	$\mathrm{J\,mol}^{-1}$
ω	width of the liquid channel in the phase-field model	m

Table 3: Subscripts and superscripts

Symbol	Meaning
$*$	evaluated on the solid-liquid interface
$A, B, \ldots$	species A, B, . . .
ℓ	quantity in the liquid, e.g., ρ_ℓ
m	amount of a quantity per mole
n	component of vector evaluated normal to the interface
s	quantity in the solid, e.g., ρ_s
$s\ell$	property of the liquid-solid interface, e.g., $\gamma_{s\ell}$
$\alpha, \beta, \ldots$	quantity in phase α, β, . . .
x, y, z	x, y, z components of a vector

Dimensionless numbers

Table 4: Dimensionless numbers

Name	Expression
Biot no.	$\mathrm{Bi} = \frac{hL}{k}$
Fourier no.	$\mathrm{Fo} = \frac{\alpha t}{L^2}$
Péclet no.	$\mathrm{Pe} = \frac{vL}{\alpha}$
Reynolds no.	$\mathrm{Re} = \frac{\rho V L}{\mu}$
Stefan no.	$\mathrm{Ste} = \frac{c_p \Delta T}{L_f}$

Chapter 1

Introduction

1.1 Aluminum, history and costs

One often classifies human history by the so-called "three-age system", i.e., by three consecutive time periods named for their respective predominant tool-making technologies [8]. It is usually considered that the stone age begins about 2.5×10^6 years ago, when the humans first started to make tools. About 8000 to 4500 years ago, the bronze age started with As- and Sn- copper base alloys to make bronze tools and armors. Finally, a famous battle seeing the Achaeans (with bronze armors) defeated by the Dorians (equipped with much lighter and more resistant iron (Fe) armors) around 1200 BC marks the transition from the bronze age to the iron age [9]. Surely, there would have been an "aluminum" age if this metal had not such a stable oxide Al_2O_3 (called alumina), avoiding the possibility of reducing its ore by heating it with charcoal (which was the key concept for iron and copper extraction at that time). However, alumina was still known and used in the antiquity: Naxos (an island in the middle of the Aegean see) was very prosperous thanks to its marble and its emery, which was made of corrindon, i.e., a special phase of Al_2O_3 [10].

It is only in 1808 that Sir Humphrey Davy first concentrated what he thought to be a new metal mixed with iron from its natural ore. Davy named the new element *aluminum*, after alum, its bisulfate salt (which, by the way, was already known to the ancient Egyptians for its use in dyeing) [11]. Then, several scientists continued to write the history of aluminum: H. C. Ørsted was the first to produce aluminum in his lab in Denmark in 1825, followed by F. Wöhler in Germany some years later. Small scale production began in 1855 when H. St. Claire Deville produced aluminum through a chemical process. A first ingot was made (97 % pure) and presented at the World Exhibition in Paris in 1855. Seeing already the potential of such a light metal, Napoleon III hoped to equip his armies with aluminum and to repeat the Dorians superiority; but the metal was too expensive at that time (around 130 £/kg), and the "precious metal" was used instead of silver for his tableware [12]. The chemical process of Deville was then supplanted by the electrolytic process, which was discovered simultaneously but independently on opposite sides of the Atlantic: C. M. Hall in Ohio and P. T. Héroult in France both electrolyzed alumina dissolved in molten cryolite (which is a naturally sodium aluminum fluoride, that dissolves alumina above 900 °C). This electrolytic process was very much demanding of electric power; but the problem was at that time

already solved, since both Siemens and General Electric had simultaneously developed the dynamo and the price of aluminum sank down to 5.5 £/kg, then. Last but not least, the Austrian K. J. Bayer developed in 1892 an efficient process that used caustic soda to extract alumina from bauxite, a natural ore containing up to 50 % alumina. Taking the advantage of hydroelectric energy in the Alps, industrial production of aluminum was developed in Neuhausen (Switzerland) using the Héroult process, allowing the price of aluminum to drop down to around 0.5 £/kg, which was about five times larger than the price of steel used for railroads [13]. Nowadays, aluminum costs about 1 £/kg and steel about four times less. The ratio remains thus about the same, but it must be noted that the production of aluminum approaches nowadays 30×10^6 tons per year versus more than 1000×10^6 tons per year for steel. Even if steel is about three times heavier per unit volume than aluminum, this difference is huge; two reasons explain why steel production is still so much larger than aluminum: the first and main one is the enormous energy power required to produce aluminum: the approximate energy content of aluminum is about 50×10^9 joules per ton, two to three times more than steel [12]. The second reason is that the weight saving offered by aluminum is counterbalanced by a much lower elastic modulus. As a matter of fact, the ratio E/ρ, where E is the elastic modulus and ρ the density, is about the same for both metals.

However, for applications such as plane sheets for a floor or aircraft fuselage, the ratio of the Young's modulus to the square or even the cubic power of the specific mass must be maximized. This makes aluminum very competitive compared to other metals, since its density is very low ($\rho_{\mathrm{Al}} \approx 2.7 \times 10^3\,\mathrm{kg\,m^{-3}}$). Nowadays for example, Novelis (Novelis is a subsidiary of Hindalco Industries Ltd., part of the worldwide Aditya Birla Group) is making car bonnets 1 to 1.1 mm thick of aluminum alloy (compared to 0.7 to 0.8 mm thick of steel), which produces an interesting weight gain for only 10 to 15 % of extra costs. Aluminum and its alloys are thus very competitive for the transport industry. But the low density, low corrosion tendency, good formability and joining capability, so as its high thermal and electrical conductivities are also very appreciated in the construction, packaging, electricity or engineering processes.

1.2 Aluminum alloys

Aluminum is often alloyed with several elements in order to improve the physical properties. Two types of alloys are nowadays considered: alloys used for producing castings and alloys devoted to wrought products [12]. The alloys used for castings contain generally more alloying additions than those used for wrought products. The addition of alloying elements is multiple: in the first case, alloying elements mainly improve the castability, whereas they improve the mechanical properties for wrought products. Table 1 summarizes the different denominations for cast and wrought alloys. Four digits are used to identify aluminum alloys, the first digit being characteristic of the alloy group. For cast alloys, digits two and three indicate the aluminum purity or further identify the alloy. The digit after the comma indicates the product form, either a casting or an ingot. A serial letter before the numerical designation is sometimes used

Table 1.1: The aluminum association alloy designation system [1].

Cast alloys	**Series**	**Wrought alloys**	**Series**
Al $\geq$ 99.00 %	1xx.x	Al $\geq$ 99.00 %	1xxx
Alloys grouped by major alloying elements			
Cu	2xx.x	Cu	2xxx
Si + Cu or Mg	3xx.x	Mn	3xxx
Si	4xx.x	Si	4xxx
Mg	5xx.x	Mg	5xxx
Zn	7xx.x	Mg and Si	6xxx
Sn	8xx.x	Zn	7xxx
Other element	9xx.x	Other element	8xxx
Unused series	6xx.x	Unused series	9xxx

to indicate modifications to original casting alloys. For example, the capital A for the alloy A356.0 indicates a modification of alloy 356.0. The number 3 indicates that it is of the Si + Cu and/or Mg series. The 56 identifies the alloy within the 3xx.x series, and the .0 indicates that it is a final shape casting and not an ingot.
For wrought alloys, the second digit indicates modifications of the original alloy and the impurity limits. The last two digits serve to further identify individual aluminum alloys.

It is necessary to differentiate between cast and wrought alloys. Both types are subdivided into those alloys that are solution heat treatable and those that are not (heat treatment is commonly used to enhance the mechanical properties of the alloy [1]). Casting alloys are used for cast parts, whereas wrought alloys are generally used for further fabrication (rolling, forging, extrusion or drawing). Figure 1.1 summarizes the different operations and products in semi-fabricated products plants and foundries. There are three main aluminum casting processes: sand casting, permanent mold casting, and die casting, which produces finished pieces in generally one single step. Understanding the physical and chemical phenomena involved in the solidification process is thus very important. It is indeed only by proceeding in this way that defects in such parts will be avoided.

1.3 Casting defects

Compared to forming processes (like forging for instance), the solidification process enable the production of very complex shapes, and at relatively high industrial rates. For obvious costs reasons, it is highly important that cast parts contain as few defects as possible. In the casting process indeed, the phase transformation of the alloy from the liquid state to the solid state is accompanied with several defects formation; the origin and implications of these defects are summarized hereafter, whereas examples

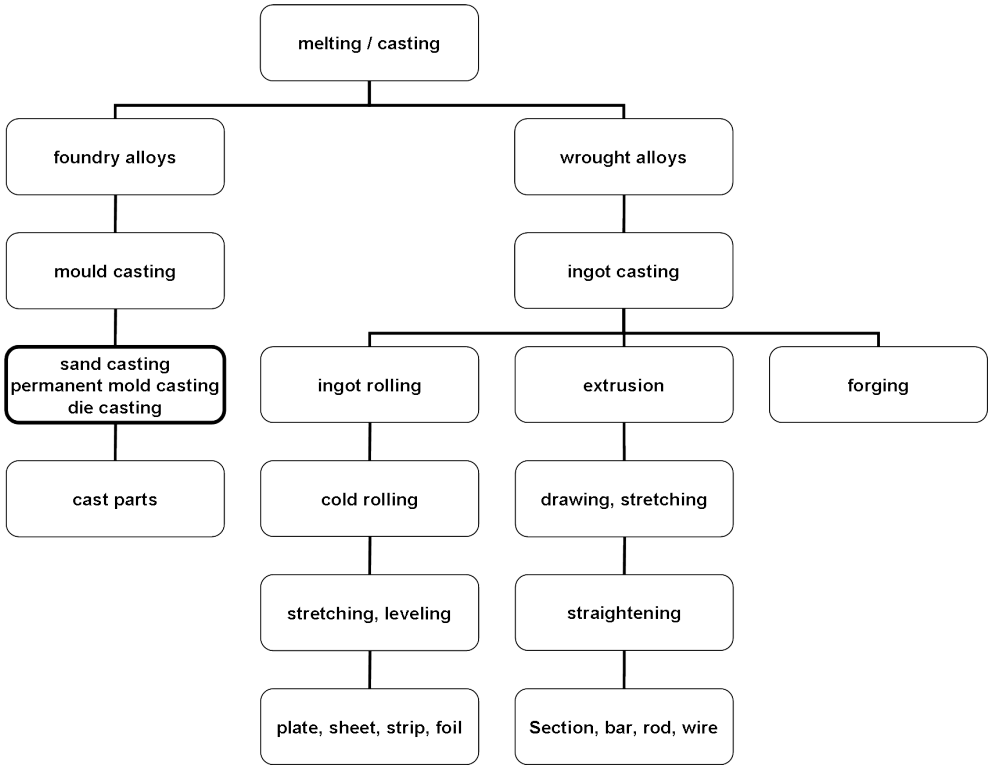

Figure 1.1: Operations and products in semi-fabricated products plants and foundries, after [12].

are given in Figs. 1.2 and 1.3.

- **Macrosegregation** is defined by inhomogeneous solute composition a the scale of a whole casting. Since the solid and liquid have different composition at the microscale, relative movement of the two phases by convection of the liquid, by grain movement or by deformation of the coherent solid induces such inhomogeneities [14].

- **Stresses and strains** In direct chill casting (DC casting) for example, deformation of the solid during cooling and stress build-up are important issues: deformation limits the heat extraction by the mold lateral surfaces or by the bottom block as well as modifies the shape of the ingot; compressive stresses expel the interdendritic liquid out of the mushy zone, leading to deformation-induced segregation; tensile stresses, finally, leads to an opening of the mushy zone, inducing segregation and hot tears [15]. To illustrate the influence of stresses, Fig. 1.2a (1) shows how the water cooled part of an ingot can be deformed due to thermal stresses.

- **Pipe shrinkage** Depending on the cooling conditions, solidification shrinkage can appear at a free surface of a casting, producing an external macroporosity. Figure 1.2a (2) shows a typical pipe shrinkage due to the radial cooling conditions of the cylindrical sample.

- **Hot tearing** Hot tears formation is due to a lack of feeding in the mushy zone

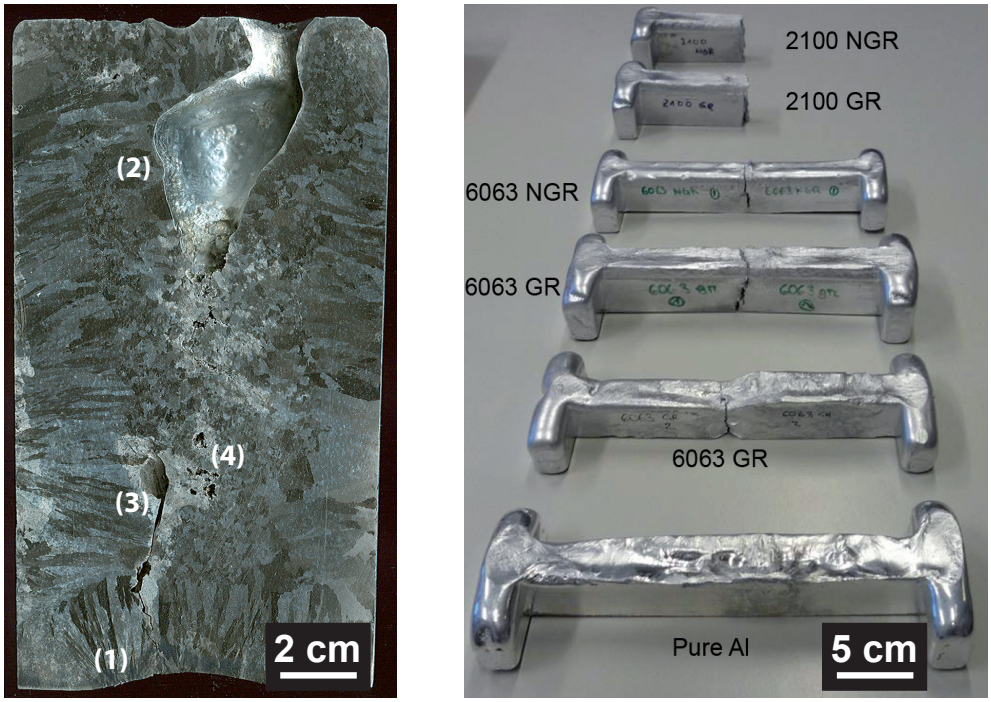

(a) (b)

Figure 1.2: (a) Typical cast ingots (radial + bottom cooling) produced in this thesis (polished and etched to reveal the microstructure). (b) Semester project performed at the Computational Materials Laboratory: Dog bone samples (last region to solidify (= hot spot) in the center of each sample), revealing the alloy tendency to crack due to hot tearing (GR: grain refined, NGR: non grain refined).

for specific regions where the dendritic network is submitted to shear or tensile stresses, which are induced by thermal contraction upon cooling. Deep in the mushy zone, where the permeability of the mush is very small and where the solid can transmit stresses, an opening of the dendritic network by tensile deformation cannot be compensated for by the liquid, leading to hot tears formation [16]. Figure 1.2a (3) shows a hot tear in a typical casting produced in this thesis, while Fig. 1.2b shows different alloys cast in a dog bone-shaped mold so that the center part of the casting is the last to solidify: pure aluminum, which has a negligible interval of solidification, is the only sample without any visible macro-crack in its center.

- **Inclusions** For products such as foil or computer discs, impurities in the melt prior to the casting process must be avoided because they are deleterious for the final product. For castings however, impurities such as carbides or borides may not be harmful; they are even sometimes wanted, as TiB_2 for example, which is conventionally used as grain refiner [1]. On the other hand, if the surface oxide layer is broken during the casting process, tiny air pockets encapsulated inside oxide "bifilms" can be entrapped in the melt, and later originate porosities as suggested by Campbell [17]. Figure 1.2a (4) is a typical view of pores that may have grown from bifilms.

- **Porosity** Because of a lack of mass feeding and due to hydrogen segregation,

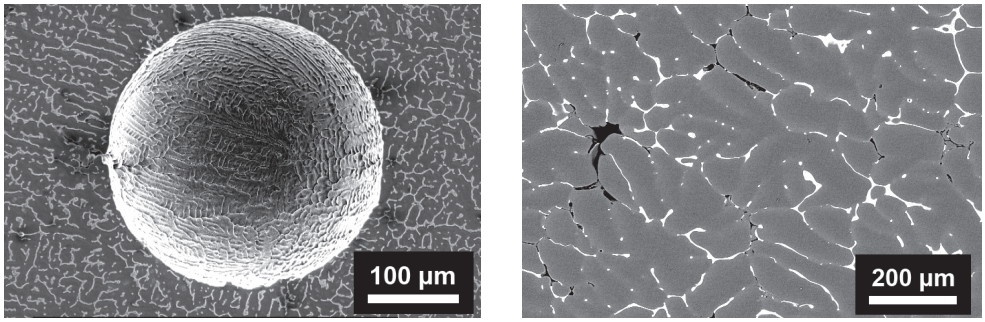

(a) (b)

Figure 1.3: (a) Gas porosity as observed by secondary electrons in scanning electron microscopy (SEM) in an Al-10wt%Cu alloy saturated in hydrogen. (b) Shrinkage porosity observed by back-scattered electron microscopy in an Al-4.5wt%Cu alloy.

voids appear during solidification processes. Since this defect is the main subject of this thesis, a more extended description of its features is given in the following.

1.4 Porosity in aluminum and its alloys

As we shall see, voids may appear in aluminum alloys due to different reasons. First, it must be noted that the surface of a casting is always covered with a thin aluminum oxide layer (even at a very low oxygen partial pressure); if this layer is broken (during pouring for example) air pockets (a mixture of oxygen and nitrogen) can be encapsulated in these oxide bifilms and entrapped in the casting. Since oxygen and nitrogen solubilities in liquid aluminum (at the melting point) are only about 3.0×10^{-8} and 1.0×10^{-11} at% respectively [18, 19], which is negligible, such air pockets never dissolve in the melt and hence produce holes in the casting. This is the mechanism of bifilms formation suggested by Campbell [17]. These bifilms act as ideal "nucleation" sites for pores, since a gaseous phase already exists in the melt. But even if the mold design and its filling are well controlled (bottom filling with slow rate, i.e., no pouring that would break the surface oxide layer and lead to further bifilms entrapment), there are evidences that porosity still occurs (see Fig. 1.3 or [20] for example). In that case, porosity is due to the result of two concomitant mechanisms, being namely solidification shrinkage and gas segregation/precipitation.

In order to compensate for solidification shrinkage – which is due to the (usual) negative volume change that occurs during the liquid → solid phase transformation – liquid must flow towards the root of the dendrites. This flow of liquid induces a pressure drop across the mushy zone, and liquid pressure as low as -200 kPa can be observed near the end of solidification [4] (i.e., depression in the liquid). On the other hand, because of the strong partitioning of hydrogen between solid and liquid aluminum, hydrogen is segregated as the alloy is solidifying[1]. Hence, once the actual gas concentration in the liquid exceeds the solubility limit, pores are likely to form and grow, relaxing in the mean time the stresses in the liquid.

[1]Hydrogen is the only gas soluble to an appreciable extent in aluminum, its solubility just above the melting point being about 1.5×10^{-3} at% [17].

Figure 1.3a shows a secondary electron microscope image of a spherical pore with dendrites growing around it, indicating that the pore existed before the development of the dendritic network; this is typical of "gas porosity". On the other hand, Fig. 1.3b shows several fine pores (in black) appearing between the primary dendrites (in grey). The Al-Al_2Cu eutectic (much denser) appears in white on this figure taken by back-scattered electron microscopy. During the solidification of an Al-Cu alloy, the last liquid to solidify has generally the eutectic composition. The liquid near the end of solidification has a density of about $3200\,\mathrm{kg\,m^{-3}}$, whereas the solid Al-$Al_2Cu$ eutectic has a density of about $3400\,\mathrm{kg\,m^{-3}}$ [21]. Hence, when the eutectic is forming, solidification shrinkage cannot be compensated for anymore (since liquid feeding is hindered) and holes appear in the casting, typically a few tens of microns in size, but usually interconnected in a complex network, as described later on in this document.

1.5 Objectives and outline

Modeling solidification processes is a powerful tool to prevent defect formation in castings. It improves the yield rate and is readily affordable with the cost and power of nowadays computers together with the availability of dedicated softwares. However porosity modeling is a complex problem, since many physical phenomena have to be taken into account. As we shall see in chapter 2, all the following time-dependent phenomena should be taken into account (they can even interact one with another):

(i) The thermal field,

(ii) The flow field,

(iii) The solute concentration field of each species,

(iv) The solidification path of the alloy,

(v) The nucleation and growth of pores,

(vi) The pinching of pores by the growing solid network inducing curvature restriction on the pore phase.

A model for the prediction of microporosity, macroporosity and pipe shrinkage during the solidification of alloys has been developed at the Computational Materials Laboratory (LSMX-EPFL) [2] and implemented in the commercial softwares CalcoSOFT® and ProCAST® (both are registered trademarks of ESI Group, Paris, France). This model is used as a post-processing of thermal results, i.e., it is a "module" that uses the calculated thermal field to solve the conservation equations that predict porosity. This porosity module has then been improved by taking into account the effect of various alloying elements and gases on porosity formation [3, 4, 5] to become the *"Advanced Porosity Module"*, or *APM* as it will be denoted from now on.

However, this model has some limits:

- The **pinching model** to describe the growth of pores restricted by the growing solid network – inducing curvature restriction to the pore phase – is very simple and needs to be improved.

- The growth of pores is considered not to be limited by **hydrogen diffusion**, since the lever rule is used for hydrogen mass conservation. However Lee *et al.* [22], as well as Carlson *et al.* [6] later on, have shown that hydrogen diffusion can be a limiting factor for pore growth.

- Experimental validations of pipe shrinkage calculations performed with the softwares CalcoSOFT® or ProCAST® need to be carried out.

Moreover, recent advances in high resolution techniques of 3D reconstruction, such as X-ray tomography, offer tremendous possibilities of sample analysis [23]: three dimensional observation with micrometer range resolution [24], or even *in-situ* observation (i.e., at high temperature) and full 3D reconstruction of a 4 mm^3 solidifying aluminum-copper sample [25].

In this work, simulation results are combined with X-ray tomography data to solve the problems enumerated above. Accordingly, here are the following goals of this thesis:

(i) Investigate the curvature influence of the pore phase on microporosity formation using high resolution X-ray tomography in order to develop a new pinching model from these results.

(ii) Develop an effective hydrogen diffusion coefficient, that is function of the volume fraction of solid only,

(iii) Analyze through X-ray tomography the behavior of a 300 μm wide pore during an isothermal holding at high temperature and during a solidification experiment,

(iv) Develop and test a new volume-averaged model for pore growth that takes into account curvature restriction of the pore phase (with the results obtained form the first point) and hydrogen diffusion (with the results obtained from the second point),

(v) Develop and test the bases of a new phase-field model that describes the equilibrium shape of micropores constrained by a solid network,

(vi) Develop a new and simple set-up to validate pipe shrinkage calculations performed with the softwares CalcoSOFT® and ProCAST®.

The outline of this thesis was chosen as follows. In Chapter 2, the fundamentals of solidification are recalled: they will be used in order to model the different phenomena involved in porosity formation. An overview of the existing models of porosity formation is also provided.

In chapter 3, we describe the experimental methods used to produce the samples. In particular, we show how we tried to avoid microporosity formation originating from bifilms. Then, we describe the analysis techniques that we used with a special focus on X-ray tomography, since this technique was widely used for this thesis.

We show in the first part of chapter 4 how very large three-dimensional X-ray tomography data can be handled with a conventional computer to extract not only

qualitative but also quantitative results. In the second part of this chapter, the model developed to extract an effective hydrogen diffusion coefficient for solidifying aluminum alloys is presented. We then show how this effective hydrogen diffusion coefficient can be used to model the growth of pores limited by diffusion. Next, the bases for the development of a new phase field model for a geometrical description of a pore constrained by a solid network is presented. Finally, the description of the pipe shrinkage calculations are given at the end of this chapter.

Chapter 5 is dedicated to the experimental and numerical results. This chapter is separated into six parts, following the enumerated goals of the thesis. Finally, conclusions and perspectives of future work are presented in chapter 6.

Chapter 2

Literature review

The purpose of this chapter is to introduce the basics of solidification needed for studying porosity nucleation and growth in aluminum alloys. As the microstructure – and hence the alloy macroscopic properties – forms within the mushy zone, we will first focus our attention on this region. We will then focus more on porosity and develop the governing equations underlying the phenomena involved in porosity formation. Finally, a literature review of the existing models for porosity prediction will be presented.

2.1 Mushy zone morphology

In a casting process, a liquid alloy of composition C_0 is poured into a mold where it cools down and solidifies. In order to characterize how the alloy changes from the liquid to the solid state, it is necessary to start with the phase diagram of the alloy. A phase diagram indicates which phase is thermodynamically stable as a function of temperature and composition for a fixed pressure. Usually, the pressure is assumed to be 1 atm since most casting processes are conducted under normal conditions. Figure 2.1 is a simple phase diagram showing at which temperatures and compositions the stable state is either a solid phase (s), a liquid phase (ℓ), or a mixing of these two phases ($s + \ell$). In this work, we will mainly focus on the Al-Cu or Al-Si alloys and both assessed phase diagrams are given in Fig. 2.2 [26].

Let us consider an alloy of composition C_0 at an elevated temperature which is then cooled down. Once the alloy temperature falls below the liquidus temperature T_{liq}, it is thermodynamically favorable for the solid phase to form. The volume fraction of solid g_s increases progressively as the temperature decreases and $g_s = 1$ at the solidus temperature T_{sol}. Under equilibrium conditions, the thermodynamic evolution of g_s as a function of temperature over the solidification interval (or freezing range $\Delta T_0 = T_{liq} - T_{sol}$) is dependent on several parameter: the melting temperature of the pure element T_f, the alloy nominal composition C_0, the slope of the liquidus line m, and the partition coefficient $k_0 = \frac{C_s}{C_\ell}$. Non-equilibrium effects related to the finite solidification time also influence the extent of the freezing range, in particular finite diffusion in the solid or the growth kinetics of the dendrite tips. However, it is important to note that there is a representative volume element (RVE) in which solidification can

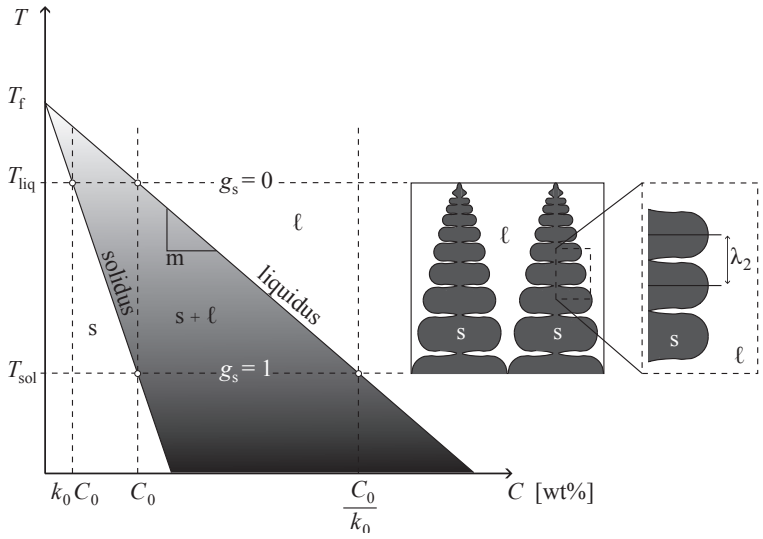

Figure 2.1: Solidification of a binary alloy. Between T_{liq} and T_{sol}, the alloy is solidifying by usually forming dendrites. Above T_{liq}, the volume fraction of solid $g_s = 0$; below T_{sol}, $g_s = 1$; between these two temperatures g_s progressively increases from 0 to 1.

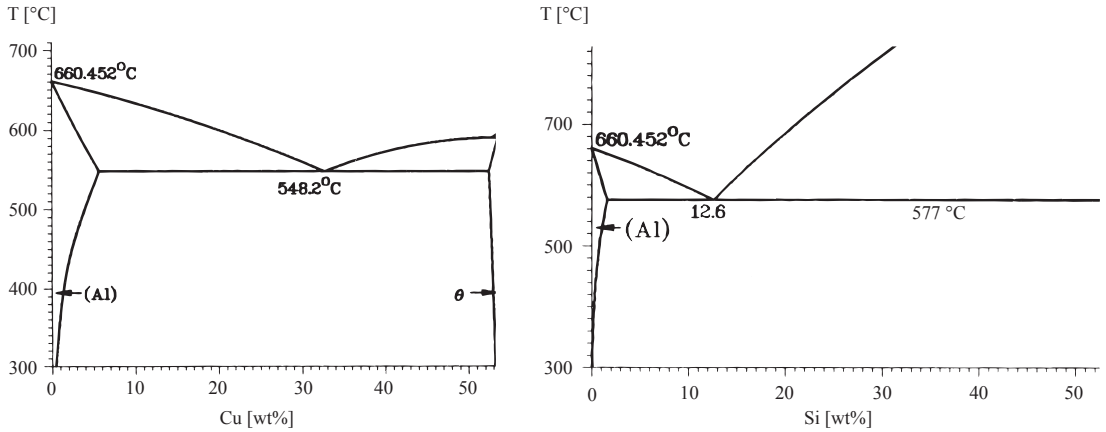

Figure 2.2: Al-rich part of the assessed phase diagrams for the Al-Cu and Al-Si binary alloys [26].

be modeled. This volume element has a typical size of λ_2 (the secondary dendrite arm spacing, see Fig. 2.1), and is commonly used in order to derive the solidification path $g_s(T)$.

Let us assume first that the liquid and solid densities are constant, i.e. their volume and mass fractions are equal. At equilibrium, i.e., when complete mixing in both the liquid and solid phases is achieved, the volume fraction of solid g_s and solid composition at the solid-liquid interface (C_s^*) are given by the lever rule. For a linearized phase diagram, we have:

$$\begin{aligned} g_s(T) &= \frac{1}{1-k_0}\left(\frac{T_{liq}-T}{T_f-T}\right) \\ C_s^*(g_s) &= \frac{k_0 C_0}{g_s(k_0-1)+1} \end{aligned} \tag{2.1}$$

On the other hand, solute diffusion in the solid is much lower than in the liquid and in many cases, it is a better approximation to assume that $D_s = 0$. This case is known as Scheil-Gulliver's approximation:

$$\begin{aligned} g_s(T) &= 1-\left(\frac{T-T_f}{T_{liq}-T_f}\right)^{\frac{1}{k_0-1}} \\ C_s^*(g_s) &= k_0 C_0 \left(1-g_s\right)^{k_0-1} \end{aligned} \tag{2.2}$$

This approximation leads to a divergence of C_ℓ^* (or C_s^*) as $g_s \to 1$ when $k_0 < 1$, and thus g_s is set to 1 when the eutectic temperature T_{eut} is reached.

In real cases, diffusion is possible in both solid and liquid phases. Up to now, Eqs. 2.1 and 2.2 were only temperature dependent, and no influence of time or space was introduced. However, models that describe back-diffusion (i.e. infinitely fast diffusion in the liquid combined with $D_s \neq 0$) must take into account the effect of both time and scale. This is why Brody and Flemings [27] developed in 1966 a model based on the solute Fourier number in the solid $\mathrm{Fo}_s = 4\frac{D_s t_f}{\lambda_2^2}$, where t_f is the local solidification time. Their analysis lead to the following expression:

$$\begin{aligned} g_s(T,\mathrm{Fo}_s) &= \frac{1}{1-2k_0\mathrm{Fo}_s}\left[1-\left(\frac{T-T_f}{T_{liq}-T_f}\right)^{(1-2k_0\mathrm{Fo}_s)/(k_0-1)}\right] \\ C_s^*(g_s) &= k_0 C_0 \left[1-(1-2k_0\mathrm{Fo}_s)g_s\right]^{(k_0-1)/(1-2k_0\mathrm{Fo}_s)} \end{aligned} \tag{2.3}$$

Clyne and Kurz in 1981 [28] introduced an empirical expression based on Brody and Fleming's work. They replaced the Fourier number in Eq. 2.3 by:

$$f(\mathrm{Fo}_s) = \mathrm{Fo}_s\left[1-\exp\left(-\frac{1}{\mathrm{Fo}_s}\right)\right] - 0.5\exp\left(-\frac{1}{2\mathrm{Fo}_s}\right) \tag{2.4}$$

Replacing Fo_s by $f(\mathrm{Fo}_s)$ in Eq. 2.3 improves Brody-Fleming's model in the sense that not only the Scheil approximation is retrieved when $\mathrm{Fo}_s \to 0$, but also the lever rule is

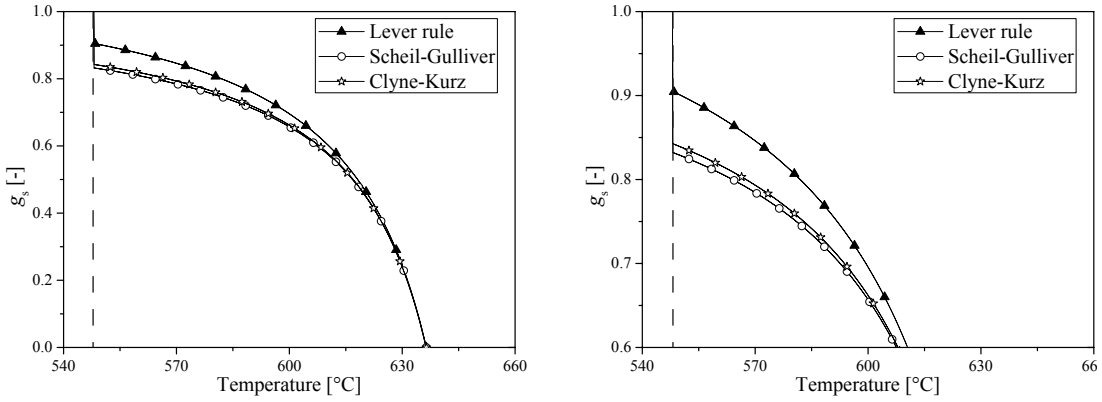

Figure 2.3: Solidification paths predicted by the different models for an Al-10wt%Cu alloy (t_f = 500 s). The graph on the right hand side is a zoom of the left graph that emphasizes the differences at high solid fractions.

retrieved when $\mathrm{Fo}_s \to \infty$, which was not the case in Brody-Fleming's model. Figure 2.3 shows the difference between the various models that predict the solidification path. Whereas few variations are observed at low solid fractions, up to 10 % difference are observed for the eutectic fraction $g_{eut} = 1 - g_s(T_{eut})$.

The formation of dendrites and the evolution of the fraction of solid is illustrated on Fig. 2.4. This figure shows a sequence of 2D cross-sections obtained via in-situ X-ray tomography at the European Synchrotron Radiation Facility in Grenoble (ESRF) for an Al-10wt%Cu [25]. As the cooling rate was relatively low (about $-3\,^{\circ}\mathrm{C\,min^{-1}}$), and as the copper diffusion coefficient in solid aluminum is relatively high ($D_s^{Cu} \approx 7 \times 10^{-13}\,\mathrm{m^2\,s^{-1}}$ at 612 °C [29]), the lever rule is well followed in that case [25]. We can see on the four first images of Fig. 2.4 that the secondary dendrite arm spacing λ_2 evolves with decreasing temperature (and hence time) and we use in this thesis the coarsening law derived by [30] to describe the evolution of λ_2 with time:

$$\begin{aligned} \lambda_2(t) &= \left[\lambda_{2,0}^3 + M(t)(t - t_{liq})\right]^{1/3} \\ &\text{with} \\ M(t) &= \frac{\gamma_{s\ell} T_f D_\ell}{\rho L_f (1 - k_0) m} \frac{\ln C_i(t) - \ln C_{i,0}}{C_A(t) - C_{i,0}} \end{aligned} \tag{2.5}$$

where $\lambda_{2,0}$ is the secondary dendrite arm spacing before ripening (i.e., close to the dendrite tip) and is in the order of twice the tip radius. M is the coarsening factor written here for a binary alloy, but a similar law can be deduced for a multi-component system [31]. The time t_{liq} corresponds to the instant when the temperature reaches the liquidus (i.e., beginning of solidification), and thus $(t - t_{liq})$ is the time elapsed since the local temperature became lower than the liquidus. The parameters of the coarsening factor are: the interfacial solid-liquid energy $\gamma_{s\ell}$, the diffusion coefficient of solute in the liquid D_ℓ, the volumetric latent heat of fusion ρL_f, the current and the nominal compositions of solute in the liquid, $C_i(t)$ and $C_{i,0}$, respectively. As an example, Fig. 2.5 shows the evolution of the secondary dendrite arm spacing as a

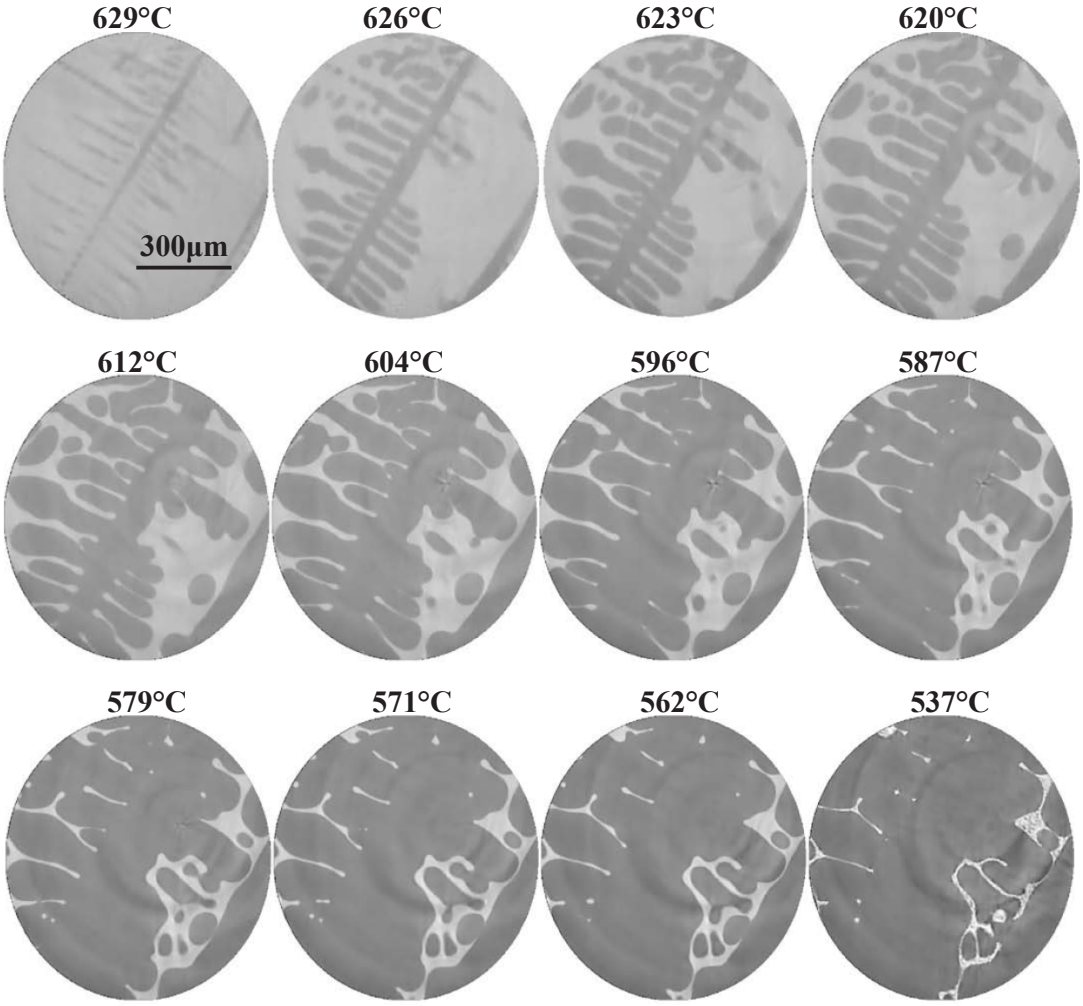

Figure 2.4: 2D cross-section of a dendrite (Al-10wt%Cu alloy) observed via in-situ X-ray tomography [25].

function of temperature for three different alloys: Al-1wt%Cu, Al-4.5wt%Cu, and Al-10wt%Cu. The solidification paths were calculated using the improved solution of the

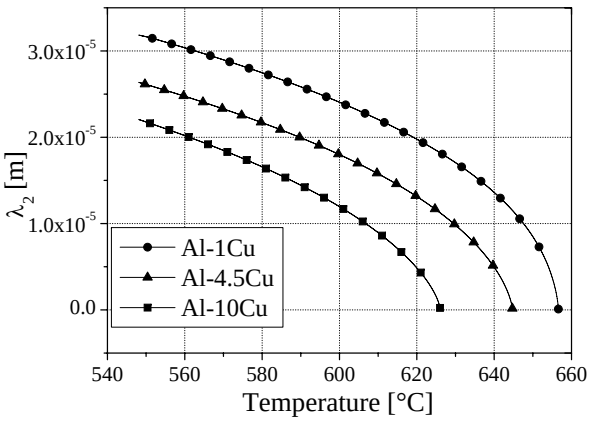

Figure 2.5: Copper content influence on the λ_2 spacing as a function of temperature in three different Al-Cu alloys for a solidification time $t_f = 20\,\mathrm{s}$.

Brody-Fleming's model developed by Clyne-Kurz with a local solidification time of 20 s.

Now that we have introduced the relation between volume fraction of solid and temperature, let us see – by using continuity equations – why porosity must occur in an RVE if the solid density ρ_s is larger than the liquid density ρ_ℓ, which is usually the case for a solidifying metallic alloy.

2.2 Conservation equations

Let us consider an RVE of the mushy zone in which the solid, liquid and pore phase can coexist. Each of these phases has a volume fraction g_s, g_ℓ, and g_p with the condition:

$$g_s + g_\ell + g_p = 1 \tag{2.6}$$

The average mass conservation equation for such an RVE is given by [32]:

$$\frac{\partial \langle \rho \rangle}{\partial t} + \nabla \cdot \langle \rho \mathbf{v} \rangle = 0 \tag{2.7}$$

where $\langle \rho \rangle$ is the density averaged over all the phases:

$$\langle \rho \rangle = \rho_s g_s + \rho_\ell g_\ell + \rho_p g_p \tag{2.8}$$

As we shall see, hydrogen is the main gas present in pores for aluminum alloys. At normal temperature and pressure, hydrogen density is about $0.09\,\mathrm{kg\,m^{-3}}$, about 30×10^3 times less than the density of aluminum. We can thus legitimately neglect the density of pores in Eq. 2.8. In order to simplify the following equations, we introduce the *pore*

free density $\langle\rho_0\rangle(T)$ of a sound RVE, i.e., without any pore. The latter could be measured for example by densitometric measurements or calculated using a solidification model for $g_s(T)$ as described in section 2.1. This would lead to the following equation:

$$\langle\rho_0\rangle(T) = \frac{\rho_s g_s + \rho_\ell g_\ell}{g_s + g_\ell} \tag{2.9}$$

Combining Eqs. 2.6, 2.8 and 2.9, one gets:

$$\langle\rho\rangle = \langle\rho_0\rangle(1 - g_p) \approx \langle\rho_0\rangle - \rho_\ell g_p \tag{2.10}$$

Following the same procedure and neglecting the mass transport of the gas phase, the average mass flow $\langle\rho\mathbf{v}\rangle$ is given by:

$$\langle\rho\mathbf{v}\rangle = \rho_\ell g_\ell \langle\mathbf{v}\rangle_\ell + \rho_s g_s \langle\mathbf{v}\rangle_s \tag{2.11}$$

where $\langle\mathbf{v}\rangle_\ell$ and $\langle\mathbf{v}\rangle_s$ are the intrinsic velocities of the corresonding phase. Combining Eqs. 2.7, 2.10 and 2.11, one gets [33]:

$$\frac{\partial\langle\rho_0\rangle}{\partial t} - \rho_\ell\frac{\partial g_p}{\partial t} + \nabla\cdot(\rho_\ell g_\ell\langle\mathbf{v}\rangle_\ell) + \nabla\cdot(\rho_s g_s\langle\mathbf{v}\rangle_s) = 0 \tag{2.12}$$

We have here neglected the term $g_p\partial\rho_\ell/\partial t$ since it is much smaller than the other ones. The various terms appearing in this equation are clear: solidification shrinkage or contraction of the solid and liquid phases (first term) are compensated either by porosity formation in the liquid (second term), interdendritic liquid flow (third term), or deformation of the solid phase (fourth term). This last term will be left aside in this work, since it is mainly responsible for hot tears formation, which is beyond the scope of the subject.

Before considering the thermodynamic conditions that govern pore formation, we first develop Eq. 2.12 further in relation with the interdendritic fluid flow.

2.3 Pressure drop and liquid feeding

Solidification of an aluminum alloy is accompanied by shrinkage. For example, the density an Al-10wt%Cu alloy will vary from $2580\,\mathrm{kg\,m^{-3}}$ in the liquid state to $2650\,\mathrm{kg\,m^{-3}}$ in the solid state [21]. This volume change can be compensated, at least partially, by the interdendritic liquid flow. The "easiness" of this liquid to flow between the dendrites is dictated by the permeability of the microstructure. It is usual to consider that the liquid flowing within a porous solid matrix is similar to the water flowing through a packed bed of sand, a problem considered by Darcy in 1856 [34]. Darcy showed that there is a simple proportional relationship between the superficial velocity of the liquid through a porous medium $\langle\mathbf{v}_\ell\rangle = g_\ell\langle\mathbf{v}\rangle_\ell$, the viscosity of the fluid μ_ℓ and the pressure drop over a given distance:

$$\langle\mathbf{v}_\ell\rangle = g_\ell\langle\mathbf{v}\rangle_\ell = -\frac{K}{\mu_\ell}(\nabla p_\ell - \rho_\ell\mathbf{g}) \tag{2.13}$$

where p_ℓ is the pressure in the liquid and $\mathbf{g}$ the gravity vector. Nielsen *et al.* [35] showed that, for Al-Cu alloys, the permeability K as a function of the solid fraction g_s can be well approximated by the famous Carman-Kozeny relationship given by:

$$K = \frac{(1-g_s)^3}{5(\mathcal{S}_V^{s\ell})^2} \tag{2.14}$$

where $\mathcal{S}_V^{s\ell}$ is the solid-liquid surface over volume ratio which can be approximated by $\mathcal{S}_V^{s\ell} \approx 6g_s/\lambda_2$ [36]. Note that the secondary dendrite arm spacing evolves within the mushy zone and Eq. 2.5 is used for that purpose. Figure 2.6 shows the evolution of the permeability as a function of temperature for the same alloys as in Fig. 2.5. Note

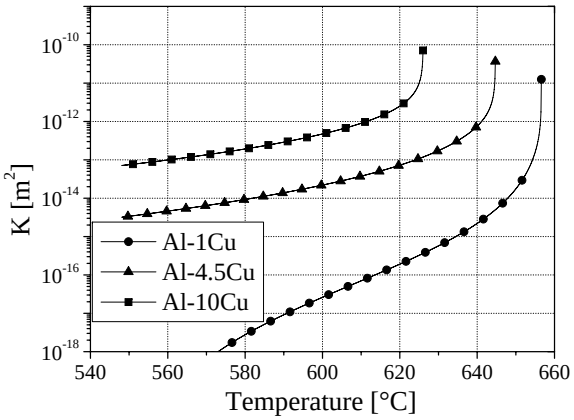

Figure 2.6: Copper content influence on the permeability as a function of temperature for three different Al-Cu alloys.

the logarithmic scale of the permeability in Fig. 2.6, emphasizing the importance of the liquid pressure drop induced by the Darcy's equation near the end of solidification. Combining Eqs. 2.12 and 2.13 and by neglecting the strains in the solid, one gets:

$$\nabla \cdot \left(\rho_\ell \frac{K}{\mu_\ell} \left(\nabla p_\ell - \rho_\ell \mathbf{g} \right) \right) + \rho_\ell \frac{\partial g_p}{\partial t} = \frac{\partial \left\langle \rho_0 \right\rangle}{\partial t} \tag{2.15}$$

Two scalar fields appear in this equation: the pressure in the liquid p_ℓ and the volume fraction of porosity g_p. This elliptic-type equation can only be solved with a supplementary equation of state. In the case of aluminum alloys, this additional equation is given by the segregation and precipitation of hydrogen, namely a gas mass balance equation.

2.4 Thermodynamics of gases in solution

2.4.1 The Al-H phase diagram

The Al-H system can be fairly well described by a regular solution model [37]. Considering either the solid or the liquid ($\nu = s$, or ℓ, respectively), the molar Gibbs free

energy of each phase G_ν^m is then described by [38]:

$$G_\nu^m = \underbrace{X_A G_{A\nu}^o + X_B G_{B\nu}^o}_{G_{\text{ideal}}} + \underbrace{\Omega_\nu X_A X_B}_{\Delta H_{\text{mix}}^m} + \underbrace{\mathcal{R}T\left(X_A \ln X_A + X_B \ln X_B\right)}_{-T\Delta S_{\text{mix}}} \tag{2.16}$$

where X_A and X_B are the molar fraction of each component, G_A^o and G_B^o the standard Gibbs free energy of the pure components, Ω the interaction parameter describing the enthalpy of mixing, $\mathcal{R}$ the perfect gas constant, and ΔS_{mix} the entropy of mixing.

Qiu et al. [37] assessed the thermodynamic properties of the Al-H system using such an approach (their model parameters were obtained by fitting experimental data), whereas the gas phase H_2 was assimilated to a perfect gas. Figure 2.7 shows the Al-

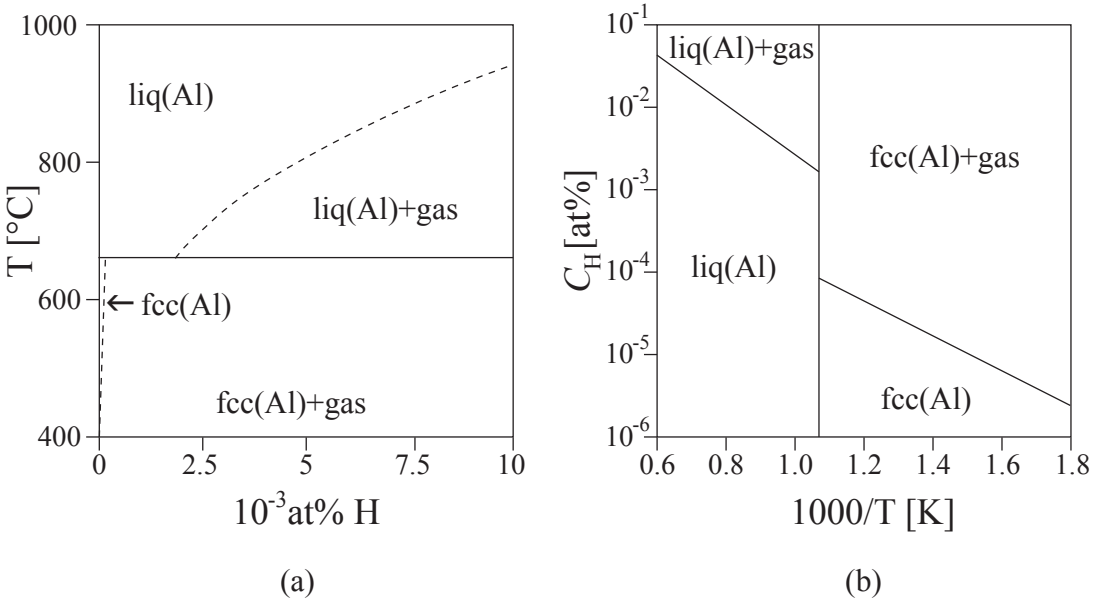

Figure 2.7: (a) Al-H phase diagram calculated at 1 atm. (b) Arrhenius plot of the Al-H diagram showing hydrogen solubility in the two condensed phases as a function of temperature at 1 atm [37].

H binary phase diagram determined by these authors, as well as the solubility of H as a function of $1/T$. Please note that this Al-H phase diagram is similar to that of eutectics, but the "mushy zone" is almost reduced to $\Delta T_0 = 0$. The dashed lines in Fig. 2.7a show limits of hydrogen solubility in the Al-H system. Experimentally, they correspond to solubility values of dissolved hydrogen in a solid or liquid aluminum, both in contact with a H_2 reservoir at $p_{H_2} = 1$ atm, which is analogous to Sievert's experiment. Let us see then how Sievert got around phase diagrams in order to deduce the solubility of a diatomic gas in a melt.

2.4.2 Hydrogen solubility

The equilibrium between dissolved hydrogen and gaseous hydrogen as depicted in Fig. 2.8 is given by the following reaction:

$$\underline{\text{H}} + \underline{\text{H}} \rightleftarrows \text{H}_2 \ \text{(g)} \tag{2.17}$$

The underlined symbol H denotes hydrogen dissolved in aluminum (and its alloys). In other words, the reaction is a balance between:

- Vaporization of dissolved hydrogen to gaseous hydrogen,
- Dissolution of gaseous hydrogen into atomic hydrogen within the melt.

Note that dissolved hydrogen is atomistic (H) rather than molecular (H_2). For such a

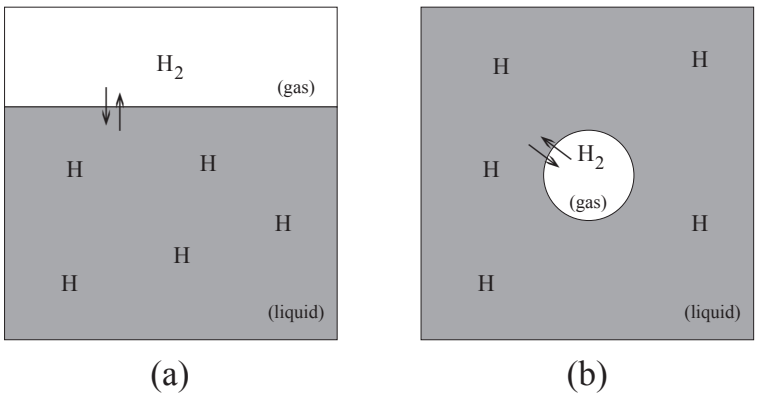

Figure 2.8: (a) Equilibrium between the atmospheric hydrogen partial pressure and its solubility in a liquid. (b) Equilibrium between the pressure inside a gas bubble and hydrogen solubility in the surrounding liquid.

chemical equilibrium, the reaction constant $\mathcal{K}$ is defined by [39]:

$$\mathcal{K} = \frac{\text{activity of the products}}{\text{activity of the reactants}} \tag{2.18}$$

It is indeed conventional to put the activities of the products in the numerator and those of the reactants in the denominator. For equilibria in a gas phase, the activity of a gaseous component A is the product of the component's partial pressure p_A with the fugacity coefficient for this component ϕ_A [39]. The activity a_A is then dimensionless as fugacity has the dimension of inverse pressure. On the other hand, for equilibria in solution, the activity is the product of composition X_A with the activity coefficient f_A^o [39]. Considering hydrogen as a perfect gas ($f_H^o = 1$), the equilibrium constant of the reaction described by Eq. 2.17 is then given by:

$$\mathcal{K} = \frac{p_g/p_0}{a_{H\ell}^2} \tag{2.19}$$

We used here p_g instead of p_{H_2} to describe the gas pressure. We will see later on the reason of this choice. Note that the sum of all the partial pressures is equal to the atmospheric pressure p_0. As in standard thermodynamics, we can relate the constant of reaction with the change in Gibbs free energy of reaction described by Eq. 2.17 [38]:

$$\Delta G^m = -\mathcal{R}T \ln \mathcal{K} \tag{2.20}$$

We know that we have a dilute solution of H in Al, and thus by Henry's law, the chemical activity is approximated by $a_{H\ell} = f_H^o X_H^{eq}$, where f_H^o is the activity coefficient of hydrogen in pure aluminum. Thus:

$$\Delta G^m = \Delta H^m - T\Delta S^m = -\mathcal{R}T \ln \mathcal{K} = -\mathcal{R}T \ln \left(\frac{p_g/p_0}{(f_H^o X_{H\ell}^{eq})^2} \right) \tag{2.21}$$

or:

$$\frac{p_g}{p_0} = (f_H^o X_{H\ell}^{eq})^2 \exp\left(-\frac{\Delta H^m}{\mathcal{R}T}\right) \exp\left(\frac{\Delta S^m}{\mathcal{R}}\right) \tag{2.22}$$

where ΔH^m is the enthalpy of dissolution and ΔS^m the entropy of dissolution. In other words, we retrieve here the well-known Sievert's law:

$$X_{H\ell}^{eq} = \frac{1}{\sqrt{A_{H_2}}} \exp\left(\frac{\Delta H^m}{2\mathcal{R}T}\right) \left(\frac{p_g}{p_0}\right)^{1/2} \tag{2.23}$$

with

$$A_{H_2} = \exp\left(\frac{\Delta S^m}{\mathcal{R}}\right) (f_H^o)^2 \tag{2.24}$$

Sievert's law states that the composition of a dissolved gas in a liquid varies with the square root of the diatomic gas partial pressure. Sigworth and Engh [40] have reported a temperature-dependent expression for the constant of reaction $\mathcal{K}$ in pure aluminum. Similar expressions were reported by Sung *et al.* [41] for both hydrogen and nitrogen in α, δ, γ, and liquid iron. The expressions for the reaction constant $\mathcal{K}$ as a function of temperature allows us to derive the enthalpy (ΔH^m) and entropy term (A_{H_2}). For pure aluminum, we have $\Delta H^m = -97645\,\mathrm{J\,mol^{-1}}$ and $A_{H_2} = 10000\,[\text{-}]$.

For binary Al-H alloys, which contain no more than a few ppm of hydrogen, the activity coefficient f_H^o can be assumed equal to 1. In the case of ternary alloys (Al-Cu-H for example), the presence of a third element changes the hydrogen solubility. For this reason, it is common to use the "interaction coefficients" first used by Wagner in 1962 [42], and summarized by Sigworth and Engh in 1982 for aluminum alloys [40]. The interaction coefficients are based on Taylor series expansion of the excess Gibbs free energy of solution of the element under consideration. For hydrogen we have:

$$f_{H\ell} = f_{H\ell}^o 10^c \tag{2.25}$$

with

$$c = \sum_{B=1}^{N_s} \left(e_H^B C_{B\ell} + r_H^B (C_{B\ell})^2 \right) \tag{2.26}$$

where e_H^B and r_H^B are the first- and second-order interaction coefficients between solute element B (Cu for instance) and the gas respectively, and N_s is the number of solute components. Experimentally determined first- and second-order interaction coefficient are shown in Table 1. Higher order terms are assumed to be zero, since they can seldom be calculated with any degree of certainty [40].

Table 2.1: First and second order interaction coefficients for Al-H-I alloys.

Solute element I	e_H^I [wt%$^{-1}$]	r_H^I [wt%$^{-1}$]
Copper	0.03	-0.0004
Iron	0.0	0.0
Magnesium	-0.01	0.0
Manganese	0.06	0.0
Silicon	0.03	-0.0008

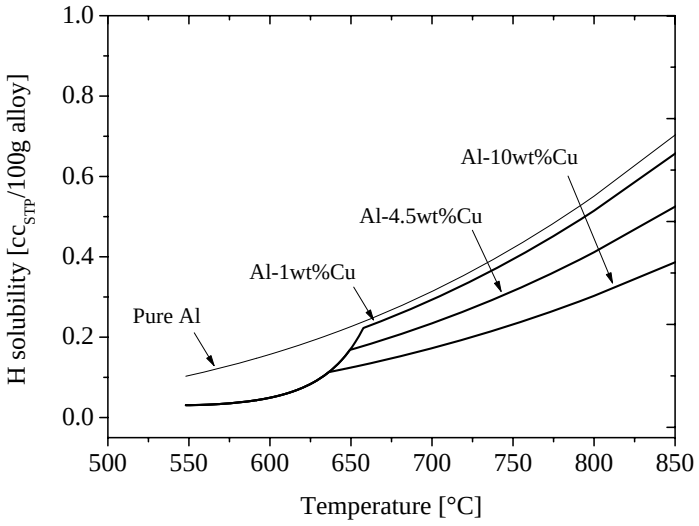

Figure 2.9: Alloy copper content influence on hydrogen solubility as a function of temperature for a hydrogen partial pressure $p_{H_2}/p_0 = 0.1$.

Figure 2.9 shows the influence of copper content on the solubility of hydrogen. For comparison, the curve for pure aluminum is also shown. The copper concentration in the liquid was estimated by the Clyne-Kurz model (see Eq. 2.4). Note the non trivial unit of "$\mathrm{cc}_{STP}/100\mathrm{g}$ of alloy" used on the graph. This is the common industrial unit used to describe the solubility of a gaseous element. The conversion between this unit into mass fraction or mole fraction is given by:

$$\begin{aligned} \frac{1\mathrm{cc_{STP}}}{100g} &\rightarrow C_{H\ell} = \frac{N_H}{22400(\mathrm{cm^3/mol})}\frac{\mathcal{M}_H(\mathrm{g/mol})}{100g} \\ \frac{1\mathrm{cc_{STP}}}{100g} &\rightarrow X_{H\ell} = \frac{N_H}{22400(\mathrm{cm^3/mol})}\frac{\mathcal{M}_\ell(\mathrm{g/mol})}{100g} \end{aligned} \tag{2.27}$$

where $\mathcal{M}_H = 1\ \mathrm{g\,mol^{-1}}$, $N_H = 2$ for aluminum, and $\mathcal{M}_\ell$ is the liquid molecular weight. This means that 1 $\mathrm{cc_{STP}}/100\mathrm{g}$ is equivalent to 0.89×10^{-6}, i.e., about 1 ppm by weight; in aluminum, this corresponds to 24 hydrogen atoms dissolved in 1×10^6 atoms of Al! Although this seems to be very small, we shall see how an alloy containing only $0.3\,\mathrm{cc_{STP}}/100\mathrm{g}$ can develop gas porosity.

The composition of hydrogen in the solid alloy has not yet been considered. Although the same formalism could be used, one usually assumes during solidification that the solubility in the solid is related to the solubility in the liquid and to the partition coefficient of pure Al:

$$X_{Hs}^{eq} = k_{0H} X_{H\ell}^{eq} \tag{2.28}$$

where $k_{0H} = 0.07$ for aluminum [43]. Thus, the partitioning is independent of the alloy composition.

Let us see now a practical example by considering a pure aluminum melt in contact with a normal atmosphere. We consider then the following reaction of aluminum with the humidity present in the atmosphere:

$$2\mathrm{Al} + 3\mathrm{H_2O} \rightarrow \mathrm{Al_2O_3} + 3\mathrm{H_2} \tag{2.29}$$

According to the Ellingham diagram, the reaction $4/3\mathrm{Al} + \mathrm{O_2} \rightarrow 2/3\mathrm{Al_20_3}$ has a $\Delta G^m \approx -210$ kcal, whereas the reaction $2\mathrm{H_2} + \mathrm{O_2} \rightarrow 2\mathrm{H_2O}$ has a $\Delta G^m \approx -90$ kcal at 1000 K [44]. The reaction described by Eq. 2.29 is thus favorable and goes from the left to the right. Consider a normal day with 30 % relative humidity and a temperature of 30 °C. The saturating water vapor pressure in such conditions is about 42 mbar [39]. The water partial pressure is given by $p_{H_2O} = 0.3 \times 42 \times 10^{-3} \times p_0$, where p_0 is the atmospheric pressure. Assuming all the water is transformed into hydrogen via the above reaction, and according to Eq. 2.23, a pure aluminum melt at 700 °C contains about $0.11\,\mathrm{cc_{STP}}/100\mathrm{g}$ of dissolved hydrogen in such conditions. This value is tolerable for most applications but increases up to $0.2\ \mathrm{cc_{STP}}/100\mathrm{g}$ for a pure aluminum melt at 800 °C. Increasing the temperature by 100 °C doubles the liquid hydrogen concentration in that case. This is why in practice casting temperature must be kept as low as possible.

Now that we have seen how to handle the conservation of hydrogen, we have the supplementary equation needed to solve Eq. 2.15. Let us see now how we can employ Sievert's law (Eq. 2.23) to model nucleation and growth of pores.

2.5 Pore curvature

Before describing pore nucleation and growth, let us summarize the different mechanisms that promote porosity formation:

- Solidification shrinkage and thermal contraction induce a liquid flow towards the root of the mushy zone, producing a pressure drop in the liquid.
- Hydrogen segregation occurs since the partition coefficient between the solid and liquid alloy is much smaller than 1 ($k_{0H} = 0.07$ [43]).
- Hydrogen solubility in the liquid decreases with temperature and liquid pressure.

Using a solidification model as described in section 2.1, we can calculate at which temperature (or solid fraction) the actual hydrogen composition of the liquid is higher than the solubility limit, considering a complete mixing of hydrogen segregated in the liquid given by the lever rule. If no pores have formed, the gas spieces conservation equation becomes [33]:

$$C_{H\ell}^{eq} = \frac{\langle \rho_0 \rangle C_{H0}}{g_s \rho_s k_{0H} + g_\ell \rho_\ell} \tag{2.30}$$

Whereas if pores have already formed, we simply add the contribution of the gas phase [33]:

$$\langle \rho_0 \rangle C_{H0} = (g_s \rho_s k_{0H} + (1 - g_s)\rho_\ell) C_{H\ell}^{eq} + 2\frac{g_p p_g}{\mathcal{R}T} \tag{2.31}$$

But since we do not know the pressure inside the gas p_g, we will treat first Eq. 2.30 to deal only with the case where no pores have formed and we will come back to Eq. 2.31 later on.

Equations 2.4 and 2.30 have been combined in order to produce Fig. 2.10. This figure shows the hydrogen segregation in the liquid as a function of the solid fraction for two different initial hydrogen contents (0.05 and 0.15 $\mathrm{cc_{STP}}/100\mathrm{g}$) in an Al-4.5wt%Cu alloy. The solubility limit of hydrogen in the liquid is also plotted on this graph, which shows that for values of g_s where $C_{H\ell} > C_{H\ell}^{eq}$, the melt is supersaturated with hydrogen, making it possible to precipitate pores. However, as in conventional nucleation theory, the appearance of porosity has to overcome curvature restrictions due to the Laplace-Young overpressure.

Indeed, in the case of a liquid forming a meniscus between two solid surfaces as depicted in Fig. 2.11, the balance of forces is given by the well-known Young-Dupré equation:

$$\gamma_{sg} = \gamma_{s\ell} + \gamma_{\ell g} \cos\theta \tag{2.32}$$

For aluminum, we have $\gamma_{\ell g} \approx 0.87\,\mathrm{J\,m^{-2}}$ [1] and $\gamma_{s\ell} \approx 0.15\,\mathrm{J\,m^{-2}}$ [45]. It is generally observed that the gas exhibits a positive curvature, which implies a θ value less than

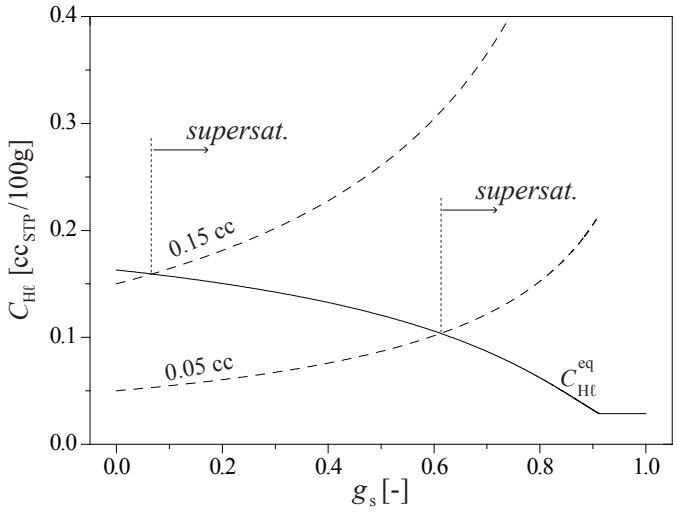

Figure 2.10: The evolution of the hydrogen composition in the liquid, $C_{H\ell}(g_s)$, as a function of the volume fraction of solid for an Al-4.5wt%Cu alloy, for two different initial composition, $C_{H0} = 0.05$ and 0.15 $\mathrm{cc_{STP}}/100\mathrm{g}$. The continuous solid curve corresponds to the equilibrium saturation composition $C^{eq}_{H\ell}(T(g_s))$ for $p_0 = 1\,\mathrm{atm}$. The arrows indicate the point at which the liquid becomes supersaturated. The copper concentration and the solid fraction were calculated using Eq. 2.4, whereas the hydrogen segregation was calculated using Eq. 2.30.

$\pi/2$ in Eq. 2.32. This in return implies that $\gamma_{sg} < 1.02\,\mathrm{J\,m^{-2}}$. However, a value of $\gamma_{sg} \approx 1.10\,\mathrm{J\,m^{-2}}$ is reported by Hatch [1], meaning that a thin film of liquid would be always present between the solid and the gas. But due to the fact that there are large uncertainties for this γ_{sg} value, and that we generally observe that $\theta < \pi/2$, it will be assumed that no liquid film exists between the gas and the solid phase. Thereof, there is a pressure difference between the gas and the liquid given by the well-known Laplace-Young equation:

$$\Delta p = 2\gamma_{\ell g}\bar{\kappa} \tag{2.33}$$

where $\bar{\kappa}$ is the local mean curvature defined by the local principal radii of curvature R_1 and R_2:

$$\bar{\kappa} = \frac{1}{2}\left(\frac{1}{R_1} + \frac{1}{R_2}\right) \tag{2.34}$$

(Note that more details are given in section 4.1.2 concerning the mean curvature $\bar{\kappa}$.) Accordingly, a bubble that exists in a liquid as depicted on Fig. 2.8b has an internal pressure given by $p_g = p_\ell + 2\gamma_{\ell g}/R_p$ where R_p is the radius of the bubble (the mean curvature of a sphere equals $1/R$). As the liquid composition at the surface of the bubble is still given by Eq. 2.23, the latter is dependent on the pore pressure. Accordingly, a smaller pore will nucleate at a higher hydrogen concentration in the liquid. This effect is shown in Fig. 2.12 where the curvature influence on pore nucleation is emphasized. Note that this figure is similar to Fig. 2.10; however, we now take into account the curvature influence on pore nucleation. If the influence of curvature is not taken into account (as in Fig. 2.10) pores are likely to form already from $g_s = 0.08$ or $g_s = 0.61$ for an initial hydrogen content of 0.15 or 0.05 $\mathrm{cc_{STP}}/100\mathrm{g}$, respectively. However, if the curvature influence of the pore radius is taken into account, a supersaturation is

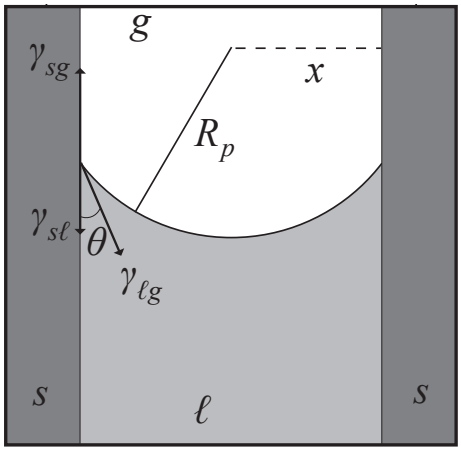

Figure 2.11: Schematic of a liquid forming a meniscus between to solid surfaces with the corresponding interfacial energies given by the Young-Dupré equation (Eq. 2.32).

needed. This supersaturation is represented by dotted lines in Fig. 2.12 for two different initial pore radii (100 and 10 μm).
Here is a short summary of Fig. 2.12:

- The black continuous line is the solubility limit of dissolved hydrogen in the liquid as a function of g_s.
- The two dashed lines are the actual hydrogen concentration in the alloy as a function of g_s for two initial hydrogen concentration (0.05 and 0.15 $\mathrm{cc_{STP}}/100\mathrm{g}$) assuming complete mixing of segregated hydrogen.
- The two dotted lines represent the solubility limit of dissolved hydrogen in the liquid alloy considering the influence of surface tension to nucleate a pore with a radius of 100 μm or 10 μm.
- $\Delta C_{H\ell}^{100\mu m}$ and $\Delta C_{H\ell}^{10\mu m}$ represent the supersaturation required in order to nucleate a pore with a radius of 100 μm and 10 μm, respectively.

Table 2.2: Curvature influence upon pore nucleation. The table gives the solid fraction at which a pore of radius R_p can nucleate in a melt which has an initial hydrogen concentration $C_{H\ell}^0$. These values correspond to Fig. 2.12.

$C_{H\ell}^0$ [$\mathrm{cc_{STP}}/100\mathrm{g}$]	g_s if $R_p \to \infty$	g_s if $R_p = 100$ [μm]	g_s if $R_p = 10$ [μm]
0.05	0.61	0.74	0.88
0.15	0.16	0.41	0.72

Table 2.2 summarizes the curvature influence upon pore nucleation. For example, a pore nucleates in a melt containing 0.15 $\mathrm{cc_{STP}}/100\mathrm{g}$ not at $g_s = 0.16$ but rather at $g_s = 0.72$ to overcome surface energy costs due to curvature.

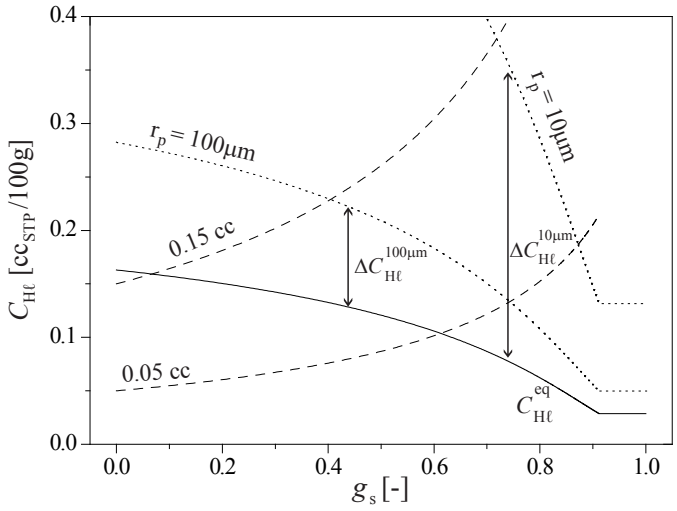

Figure 2.12: The evolution of the hydrogen composition in the liquid, $C_{H\ell}(g_s)$, as a function of the volume fraction of solid for an Al-4.5wt%Cu alloy, for two different initial compositions, $C_{H0} =$ 0.05 and 0.15 cc$_{\mathrm{STP}}$/100g. The continuous solid curve corresponds to the equilibrium saturation composition $C_{H\ell}^{eq}(T(g_s))$ for $p_0 = 1$ atm. The two dotted lines represent the solubility limit of dissolved hydrogen in the liquid alloy considering the influence of surface tension to nucleate a pore with a radius of 100 μm and 10 μm. $\Delta C_{H\ell}^{100\mu m}$ and $\Delta C_{H\ell}^{10\mu m}$ represent the supersaturation required in order to nucleate a pore with a radius of 100 μm and 10 μm, respectively. Note that the copper composition as well as the solid fraction were calculated using Eq. 2.4, whereas the hydrogen segregation was calculated using Eq. 2.30.

Note finally that composition departure from equilibrium and pressure difference between the bubble and the liquid are in fact related:

$$\begin{aligned} \Delta C_{H\ell} &= C_{H\ell}^{eq}(p_g, T) - C_{H\ell}^{eq}(p_\ell, T) \\ &= C_{H\ell}^{eq}(p_\ell + \frac{2\gamma_{\ell g}}{R_p}, T) - C_{H\ell}^{eq}(p_\ell, T) \end{aligned} \tag{2.35}$$

Given this relation, some models define a nucleation criterion in terms of a critical pressure difference, or a critical nucleus size. As shows Eq. 2.35, they are in fact linked via Eqs. 2.23 and 2.33.

Once a pore has nucleated, it will grow and its growth is influenced by curvature on one hand and by diffusion on the other. Of course, a pore completely surrounded by the liquid adopts a spherical shape. In this case, the pore fraction g_p is given by:

$$g_p = \mathcal{N}_p \frac{4}{3} \pi R_p^3 \tag{2.36}$$

where $\mathcal{N}_p$ is the pore density and R_p the mean pore radius. In many situations, the pore has to develop in a mushy region and cannot displace the solid network. Therefore, it is forced to adopt a non-spherical shape if the solid fraction is high enough. On the other hand, as shown in Fig. 2.13, regions of a pore which are in contact with the liquid must exhibit the same mean curvature values, as the latter is directly related to

the pressure inside the pore[1]. Since we know the pressure of the gas is related to the

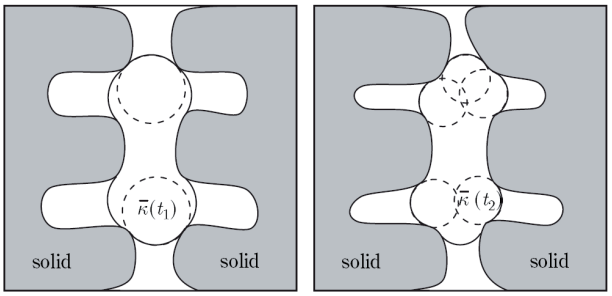

Figure 2.13: A 2D schematic view of pore growth between dendrite arms at two solidification times, $t_1 < t_2$. The mean curvature $\bar{\kappa}(t)$ of the pore in contact with the liquid is uniform at any instant and increases with time (after [33]).

pore curvature, we can now combine Eqs. 2.31 and 2.33:

$$\langle \rho_0 \rangle C_{H0} = (g_s \rho_s k_{0H} + (1 - g_s)\rho_\ell) C^{eq}_{H\ell} + 2\frac{g_p}{\mathcal{R}T}\left(p_\ell + 2\gamma_{\ell g}\bar{\kappa}\right) \tag{2.37}$$

Even Eq. 2.36 can be introduced here if spherical pores are considered. Note that Eq. 2.37 is written for a Eulerian frame; in practice, the volume fractions are almost always calculated on a fixed mesh. As we saw, solidification shrinkage can be compensated for either by liquid flow or porosity formation. The presence of porosity implies that less liquid will flow into the volume element. In fact, liquid might even be pushed out if the volume fraction of porosity is larger than shrinkage. This effect is less pronounced for aluminum alloys than for steels for example, as the liquid density is lower ($\rho_{Al,\ell} \approx 2400\,\mathrm{kg\,m^{-3}}$, whereas $\rho_{Fe,\ell} \approx 7230\,\mathrm{kg\,m^{-3}}$ [46]).

Because of the complexity of the pore shape when it is constrained to grow within the solid network, porosity models approximate the pore radius to be a function of the solid fraction g_s instead of the pore fraction g_p (Eq. 2.36). Péquet *et al.* [2] (as well as many authors, [6] in particular) keep the radius constant until the volume fraction of pores corresponds to that of spherical pores. From then on, the average radius of curvature is a function of g_s and λ_2 in order to express the increasing difficulty for the pores to grow in between the dendritic network (open triangles in Fig. 2.14). Couturier *et al.* [4] developed a refined geometrical model by approximating the dendrite arms or globulitic grains to a regular arrangement of cylinders or spheres, respectively. A simple geometry calculation gives the $R_p(g_s)$ relationship given in Fig. 2.14, when it is normalized by the secondary dendrite arm spacing λ_2 or the grain diameter R_g, respectively. The latter development is compared with a simpler model of hexagonal arms arranged in a hexagonal network, as suggested in [47]. One of the goals of the present study is to challenge these different models of pore growth restriction with experimental curvature data obtained by 3D reconstruction of the surface of a pore.

[1] A small perturbation inducing an increase, locally, of the mean curvature at the liquid-gas interface will affect each other point of this liquid-gas interface at the speed of sound (it is a mechanical effect), and the curvature will be equilibrated almost immediately.

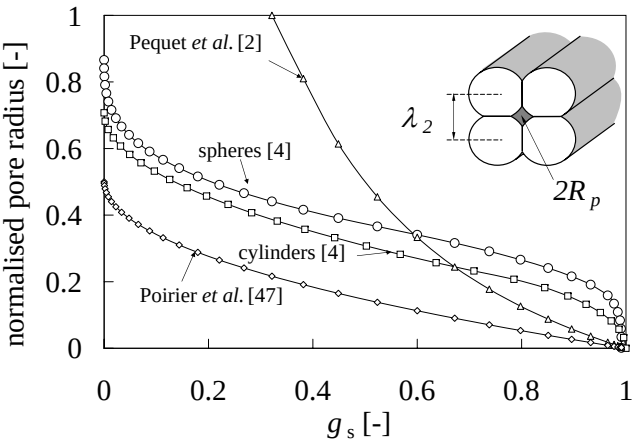

Figure 2.14: The pore radius R_p normalized by the secondary dendrite arm spacing (dendrite morphology)[4], grain diameter (globular equiaxed structure)[4], or following the developments of [2] or [47] as a function of the solid fraction g_s. The insert shows the geometry for the first case.

2.6 Pore nucleation

Homogeneous nucleation of voids is similar to that of a solid phase in a liquid: a nucleation barrier associated with a critical nucleation radius must be overcome so that it can form and then grow. Making a balance between the volumetric energy and surface energy, one can derive very simply the free energy change for the nucleation of a (spherical) pore as a function of the pore radius R_p, in the bulk (homogeneous) or with the help of a foreign substrate (heterogeneous) [33]:

$$\Delta G = \left(-\frac{4\pi R_p^3}{3} \Delta G_V + 4\pi R_p^2 \gamma_{\ell g} \right) f(\theta) \tag{2.38}$$

where ΔG_V is the free energy per unit volume of the bulk, i.e., $\Delta G_V = G_\ell - G_s$ for the solid-liquid system and $\Delta G_V = p_g - p_\ell$ for the liquid-gas system, and $f(\theta)$ a geometrical factor equal to 1 for homogeneous nucleation. The well-known Laplace-Young equation is then retrieved if one solves this equation for the critical radius of nucleation (with $f(\theta) = 1$ for homogeneous nucleation). Taking $\gamma_{\ell g} \approx 1\,\mathrm{J\,m^{-2}}$ and a typical radius of a nucleating bubble of a few nanometer, the pressure difference $(p_g - p_\ell)$ is in the GPa range. As the pressure in the void must be positive (say on the the order of the atmospheric pressure), this means that the liquid just next to the pore must exhibit a significant negative pressure. Although negative pressure in liquid are legitimate (inside a 100 m high redwood tree, the pressure of the water is 1 bar at ground level, but decreases down to -9 bars near the top of the tree), values in the GPa range are certainly much too high [17]. As a consequence, porosity must nucleate heterogeneously with the help of a foreign substrate.

Here must be mentioned the mechanism suggested by Campbell [17], who considers a nucleation-free mechanism for pore formation based on the concept of double oxide films, or *bifilms*. In this scenario, turbulent pouring of the liquid in a casting process makes the liquid surface of the alloy, which is covered by an oxide film, to fold upon

itself (like if one scrunches a sheet of paper). This folding action leads to bifilms, which are entrained into the bulk melt as a pocket of air enclosed by the bifilm. The bifilm with its air pocket is then the natural seed of a pore, since oxygen and nitrogen solubilities in liquid aluminum (at the melting point) are only about 3.0×10^{-8} and 1.0×10^{-11} at% respectively [18, 19]. Further pore growth can occur by simple action of unfurling of the bifilms, with or without the aid of hydrogen diffusion.

2.6.1 Evidences of microporosity non induced by bifilms

Although the heterogeneous nucleation mechanism proposed by Campbell is valid, it is important only when the liquid feeding system is not carefully designed and/or in the absence of filters (which is normally not the case in industry nowadays). Although some experiments reported in the literature do show this nucleation mechanism, there are significant evidences in the literature that show that Campbell's mechanism for pore formation is not universal. Let us see two examples.

The first one is the work by Prasad *et al.* [48] who used 1μm resolution X-ray tomography to produce 3D-images of Al-4.3wt%Cu and Al-17wt%Cu atomized droplets (660 and 450 μm of diameter for the first and second alloy, respectively). Based on the observation of microstructural features in the 3D images, physical phenomena of rapid solidification such as nucleation and initial growth, recalescence, and porosity distribution could be investigated. The Al-4.3wt%Cu droplet had a porosity homogeneously distributed throughout the droplet volume, whereas the Al-17wt%Cu one exhibited a highly heterogeneous porosity distribution concentrated near the periphery. Because of the principles of the atomization process, no dissolved gas was considered by these authors and shrinkage driven porosity was assumed to be the only mechanism. For a given undercooling, the growth rate of the dendrites in Al-4.3wt%Cu alloys is higher than in Al-17wt%Cu alloys. Therefore, the Al-17wt%Cu liquid has time to reach the interdendritic regions, whereas cavities are formed in the Al-4.3wt%Cu droplet, explaining the homogeneous dispersion of porosity in the Al-4.3wt%Cu sample. In both cases, porosity is not linked with oxide bifilms. The porosity distribution within the droplets could be explained by the importance of recalescence and the growth rate of the dendrites. High growth rates during recalescence developed an even distribution of porosity, whereas lower growth rates but larger recalescence volume segregated the porosity to the periphery of the droplet.

The second example is the work presented by Zhao *et al.* [49], who developed a set-up very similar to that one used in this thesis (see the $DS_{\mathrm{1D-ATM}}$ set-up described in section 3.2.2). These authors performed a vertical 1D solidification experiment with an Al-4.5wt%Cu alloy that was melted directly in the solidification set-up. An induction crucible heater was used to melt the alloy and melt stirring was performed for ten minutes, time after which the induction was turned off and the bottom copper chill was cooled down with a water flow. No liquid metal pouring was necessary in this experiment and yet, porosity was found after solidification mainly with round shapes, suggesting early nucleation of gas porosities.

2.6.2 Heterogeneous nucleation

As shown previously, homogeneous pore nucleation is not legitimate in most casting processes, because of the very large Laplace-Young overpressure it involves.

In conventional nucleation theory, where the process is thermally activated, the rate of formation of critical nuclei depends on temperature and time [33]. The mechanism of heterogeneous nucleation (see Fig. 2.15a) is easier than homogeneous nucleation by the presence of a wetting substrate via the factor $f(\theta) \leq 1$ appearing in Eq 2.38 :

$$f(\theta) = \frac{(2 + \cos\theta)(1 - \cos\theta)^2}{4} \tag{2.39}$$

where θ is the wetting angle satisfying the Young-Dupré equation (Eq. 2.32).
In this case of conventional heterogeneous nucleation, the number of nuclei is almost immediately increased from zero to its maximum number of sites as soon as the necessary undercooling is reached [33]. One often considers the nucleation process to be then *instantaneous*. Accordingly, one can treat the nucleation of voids as instantaneous, since the same mechanism of heterogeneous nucleation can be considered (note that this hypothesis is common but not universal, since [50, 51, 52, 53] developed non instantaneous relationships for the nucleation rate). This is represented schematically in Fig. 2.15 where a pre-existing nucleus, either on a substrate ((a) gas adsorbed on a particle, for example, or (b) in a groove (analogous to Campbell mechanism)), can be assumed. Nevertheless, a small supersaturation is still required in both cases for the

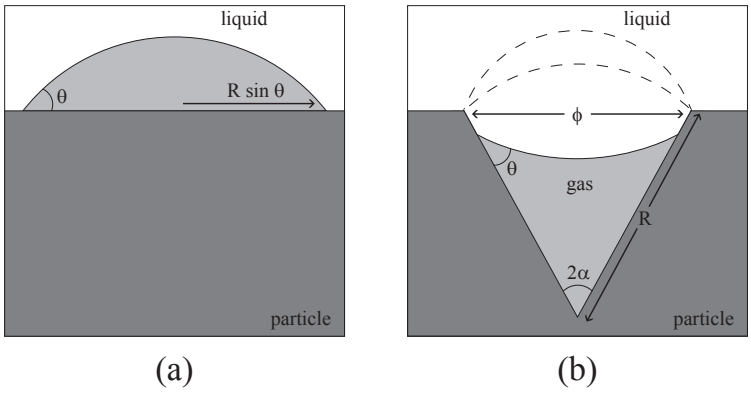

Figure 2.15: Schematic of heterogeneous nucleation on a foreign particle (a) and in a groove (b).

bubble to grow by hydrogen diffusion. In this scenario, the smallest radius of curvature associated to a hemispherical cap might be in the order of 10 to 100 μm, which is quite realistic with the range of values encountered in the mushy zone [33].

To illustrate this mechanism of heterogeneous nucleation, Fig. 2.16 shows a time sequence obtained via X-ray radiography of the directional solidification of a 200 μm-thick Al-30wt%Cu alloy contained between two quartz plates [54]. Regions of low Cu concentration appear white, whereas regions with high concentration appear dark. In this experiment, columnar dendrites grew downward with an angle of about $\pi/6$ from the vertical thermal gradient. Let us focus on the bottom left part of the images: a small pore is trapped between the dendrite arms in the last image, originating from

a tiny groove, as shown in the first image. As the dendrite front approaches the groove, the air entrapped in the groove escape from it, probably because of the density difference and hydrogen segregation, illustrating the mechanism shown in Fig. 2.15b.

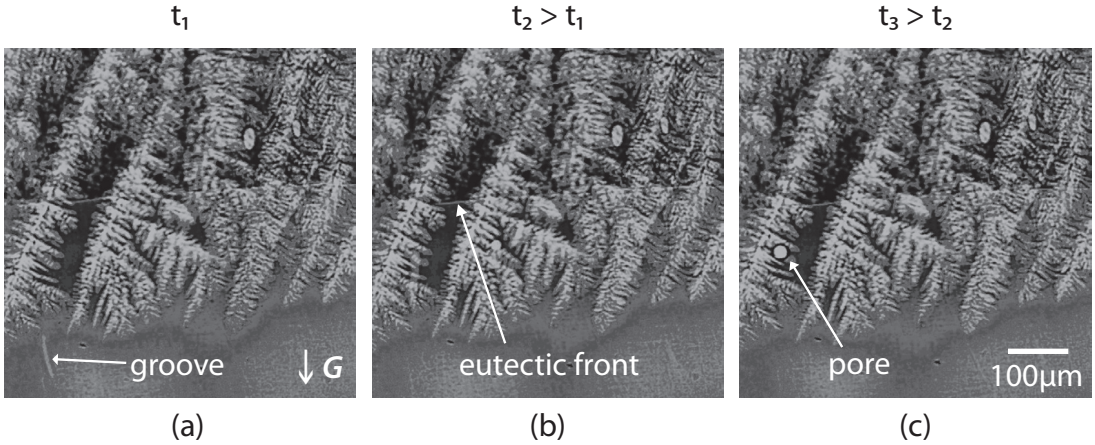

Figure 2.16: Sequence of three X-ray radiographs showing the formation of gas porosity in a directionally solidified Al-30wt%Cu alloy (after [54]).

Now that we have introduced the main mechanisms of pore nucleation, let us see how hydrogen diffusion can influence its growth.

2.7 Diffusion of gases and pore growth

Once a pore has nucleated, it is a sink for dissolved hydrogen. Dissolved atomic hydrogen must hence diffuse through the solidifying alloy to the pore so that it can grow. Since hydrogen diffuses very rapidly (the liquid hydrogen diffusion coefficient $D_{\ell H} \approx 10^{-7}$ m^2/s at the melting point [43]), most models assume a lever rule for the hydrogen mass balance conservation equation (see Eq. 2.30) and pore growth is thus not limited by hydrogen diffusion [2, 3, 55]. However, it has been shown that pore growth can be limited by hydrogen diffusion [22, 6], a concept already taken into account in the models of Fredriksson in 1976 [56]. Whether or not diffusion is a limiting factor depends actually on the Fourier number $D_{\ell H} t_f / L^2$ associated with the diffusion process (where L is half of the typical distance between pores). If the density of pores is low and the solidification time is short, this effect is important (small values of the Fourier number). This is why recent models have tried to account for the influence of hydrogen diffusion upon pore growth. However, pore "feeding" in hydrogen was supposed to happen only at the liquid-gas interface [6, 57]; hence, for pores growing in the mushy zone, where both solid and liquid are in contact with the pore, a pore-liquid interfacial area "fraction" must be estimated. This parameter is difficult to assess since many parameters must be adjusted, as it appears in Carlson's paper [6]. Also, although hydrogen has a solubility 15 times lower in solid aluminum compared to the liquid, the diffusion coefficient in the solid is only 2.5 times lower than that in the liquid. Hence, at high solid fraction, pore "feeding" in hydrogen through the solid-pore interface cannot be neglected anymore. This is why a new approach based on the effective medium

theory [58] correlated to simulation results performed on real microstructures has been developed in this work.

2.7.1 Hydrogen diffusion in a two-phase medium

In the diffusion process, thermodynamic equilibrium is achieved when the chemical potential of each species is the same everywhere. Atom migration – namely diffusion – will occur until thermodynamic equilibrium is satisfied. Hence, the flux of atoms A $\mathcal{J}_A$ at any point in the lattice is proportional to the chemical potential gradient $\nabla\mu_A$. Fick's first law stating that $\mathcal{J}_A$ is proportional to the composition gradient ∇C_A is a simplification to describe the flux of atoms. A more accurate one relates the flux of atoms to the chemical potential gradient [38]:

$$\mathcal{J}_A = -M_A C_A \nabla\mu_A \tag{2.40}$$

where M_A is the mobility coefficient of A. Combining Eq. 2.40 with the Gibbs-Duhem relationship, and introducing the molar volume $V_m = X_A/C_A$ (where X_A is the molar fraction of A), the following equation is obtained [38]:

$$\mathcal{J}_A = -M_A \frac{X_A}{V_m}\frac{RT}{X_A}\left(1 + \frac{\mathrm{d}\ \ln f_A}{\mathrm{d}\ \ln X_A}\right)\nabla X_A \tag{2.41}$$

where f_A is the activity coefficient of the component A ($f_A = \frac{a_A}{X_A}$, where a_A is the activity of A). Comparing the latter equation with Fick's first law, we obtain a relationship between the diffusion coefficient and the atomic mobility of component A.

$$D_A = M_A RT\left(1 + \frac{\mathrm{d}\ \ln f_A}{\mathrm{d}\ \ln X_A}\right) \tag{2.42}$$

For dilute solutions such as the Al-H system, $X_A \to 0$ and $f_H = a_H/X_H \approx$ constant (Henry's law) the term in brackets is equal to 1. The diffusion coefficient is thus simply linked to the atomic mobility M_H via the following relationship:

$$D_H = M_H RT \tag{2.43}$$

In order to solve the diffusion equation in a heterogeneous material, a quantity must be continuous at the interface between the two phases: this quantity is the chemical potential. Thus, in order to properly calculate the diffusion of hydrogen across a representative volume element of the mushy zone, the following generalized Fick's equation must be applied:

$$\boldsymbol{J}_H = -M_H X_H \nabla\mu_H \tag{2.44}$$

This equation is similar to Eq. 2.40, but both parts of the equation have been divided by the molar volume, so that the flux $\boldsymbol{J}_H$ is given in $[\mathrm{m\,s^{-1}}]$ (whereas the flux $\mathcal{J}_H$ in Eq. 2.40 is given in $[\mathrm{mol\,m^{-2}\,s^{-1}}]$), the composition X_H in mole fraction, and the chemical potential μ_H in $[\mathrm{J\,mol^{-1}}]$. Fick's second law is thus adapted accordingly:

$$\frac{\partial X_H}{\partial t} = -\nabla\cdot\boldsymbol{J}_H = \nabla\cdot(M_H X_H \nabla\mu_H) \tag{2.45}$$

This equation will be used and further developed in section 4.3 to model hydrogen diffusion through a mushy zone microstructure obtained via *in-situ* X-ray tomography. Once a steady state will be reached, an overall hydrogen diffusion coefficient function of g_s only will be deduced and compared with effective medium approximations.

2.7.2 Effective medium approximations

Effective-medium theories rely on the fact that there is a linear relationship between an average generalized flux $\boldsymbol{F}$ and an average (or applied) generalized intensity $\boldsymbol{G}$ whose quantity is constant at the interface between the different phases [58]. The coefficient of proportionality is then the general effective property $\mathfrak{D}_{eff}$. In the thermal (electrical) problem for instance, the heat flux (current density) is equal to the temperature gradient (electric field) $\times$ the effective thermal (electrical) conductivity. The temperature (electric potential) is continuous across the interface and the generalized Fourier's (Ohm's) law is retrieved.

For a composite sphere made of spherical particles (phase 2) in a matrix (phase 1), there are numerous ways of calculating $\mathfrak{D}_{eff}$, the most important ones being:

- the self-consistent approximation (SC) [59]:

$$\mathfrak{D}_{eff}^{SC} = \frac{1}{6}\left(\mathfrak{D}_1(3g_1-1)+\mathfrak{D}_2(3g_2-1)+\sqrt{\mathfrak{D}_1(3g_1-1)+\mathfrak{D}_2(3g_2-1)+8\mathfrak{D}_1\mathfrak{D}_2}\right) \tag{2.46}$$

- the Maxwell-type approximation for spherical inclusions [60] which coincides with the Hashin-Shtrikman (HS) upper bond:

$$\frac{\mathfrak{D}_{eff}^{HS}-\mathfrak{D}_1}{\mathfrak{D}_{eff}^{HS}+2\mathfrak{D}_1} = g_2\left(\frac{\mathfrak{D}_2-\mathfrak{D}_1}{\mathfrak{D}_2+2\mathfrak{D}_1}\right) \tag{2.47}$$

- the differential effective-medium approximation (DEM) [61]:

$$\frac{\mathfrak{D}_2-\mathfrak{D}_{eff}^{DEM}}{\mathfrak{D}_2-\mathfrak{D}_1}\left(\frac{\mathfrak{D}_1}{\mathfrak{D}_{eff}^{DEM}}\right)^{1/3} = 1-g_2 \tag{2.48}$$

The SC approximation is implicit: it requires solving implicit equations for the effective properties and it treats each phase symmetrically: both phases are considered as inclusions in a composite matrix. Hashin and Shtrikman [62], on the other hand, derived explicit relationships for the best possible bounds on the effective conductivity of two-phase isotropic three-dimensional composites given just the volume fraction information [58]. Finally the DEM implicit approximation scheme lies between the HS lower and upper bounds and is supposed to be a better approximation in the case of a two-phase material with high phase contrast ratio $\mathfrak{D}_2/\mathfrak{D}_1$ (more than 4 typically [63]).

In the diffusion process, the quantity which must be continuous at the interface is the chemical potential (or the activity alternatively, they are directly linked via $\mu_A = \mu_A^o + \mathcal{R}T\ln a_A$). In that prospect, we will derive in section 4.2.3 a linear relationship between the gradient of a quantity continuous across the interface and the flux of atoms

to use the common models for establishing effective properties of heterogeneous media as described by Eqs 2.46 to 2.48. In that way, an effective hydrogen diffusion coefficient D_e will be deduced and compared with simulation results.

Atwood *et al.* [64] were the first to introduce an effective hydrogen diffusion coefficient $D_{e,H}$ function of the local volume fraction of solid:

$$D_{e,H} = D_{\ell H}\frac{D_{\ell H}(1-g_s)+D_{sH}(1+g_s)}{D_{\ell H}(1+g_s)+D_{sH}(1-g_s)} \tag{2.49}$$

This approximation is based on an effective-medium theory applied to transverse thermal conductivity of a unidirectional fibre composite with fibre-matrix debonding [65], i.e., these authors directly replaced the phase conductivities by the diffusion coefficient in Markworth's formula [65]. However this equation is valid only at low solid fractions (up to $g_s \approx 0.6$) and for solid cylinders only. A freezing aluminum alloy can be considered as a solid-liquid composite which undergoes a topological change near $g_s = 0.9$ typically, solid fraction at which the solid cannot be approximated by cylinders anymore. Moreover, replacing directly the phase conductivities by their corresponding diffusion coefficient turns out to be wrong, since the influence of both diffusion coefficients and solubilities must be taken into account.

We will thus see in section 4.2 how an effective hydrogen diffusion coefficient function of the volume fraction of solid only can be obtained from real microstructures. In section 4.3, we will see how this effective hydrogen diffusion coefficient can be applied to a consistent model that simulate pore growth limited by hydrogen diffusion.

2.8 Boundary conditions

We have seen through this chapter that in order to model pore nucleation and growth, the following aspects must be interpreted:

(i) The thermal field [33]:

$$\frac{\partial(\rho h)}{\partial t} + \nabla\cdot(\rho h\mathbf{v}) = \nabla\cdot(k\nabla T) + \rho\dot{R}_q \tag{2.50}$$

where k is the thermal conductivity and $\dot{R}_q$ is the specific heat generation rate.

(ii) The flow field for the pressure, heat and mass transport (cf. Eq. 2.13):

$$\langle\mathbf{v}_\ell\rangle = g_\ell\langle\mathbf{v}\rangle_\ell = -\frac{K}{\mu_\ell}(\nabla p_\ell - \rho_\ell\mathbf{g}) \tag{2.51}$$

(iii) The solidification path (cf. Eqs. 2.1, 2.2, or 2.4):

$$g_s = 1 - \left(\frac{T_f - T_{liq}}{T_f - T}\right)^{\frac{1}{1-k_0}} \quad \text{(Scheil rule here)} \tag{2.52}$$

(iv) The composition distribution of dissolved gases (cf. Eqs. 2.30 or 2.31):

$$C_{H\ell}^{eq} = \frac{\langle\rho_0\rangle C_{H0}}{g_s\rho_s k_0 H + g_\ell\rho_\ell} \tag{2.53}$$

(v) The nucleation of pores (cf. Eq. 2.35):

$$C_{H\ell} = C_{H\ell}^{eq} + \Delta C_{H\ell} \tag{2.54}$$

(vi) The equilibrium between gas porosity and pressure given by Eq. 2.37:

$$\langle \rho_0 \rangle C_{H0} = (g_s \rho_s k_{0H} + (1 - g_s)\rho_\ell) C_{H\ell}^{eq} + 2\frac{g_p}{\mathcal{R}T}\left(p_\ell + 2\gamma_{\ell g}\bar{\kappa}\right) \tag{2.55}$$

(vii) The growth of pores limited or not by hydrogen diffusion,

(viii) The impingement of pores upon the growing solid network inducing pore curvature restriction (see Fig. 2.14).

Moreover, the appropriate boundary conditions required for the modeling of porosity formation depend on the location of the mushy zone within a casting. Whereas four important cases are shown on Fig 2.17 and described below, the reader can refer to [2] for more details.

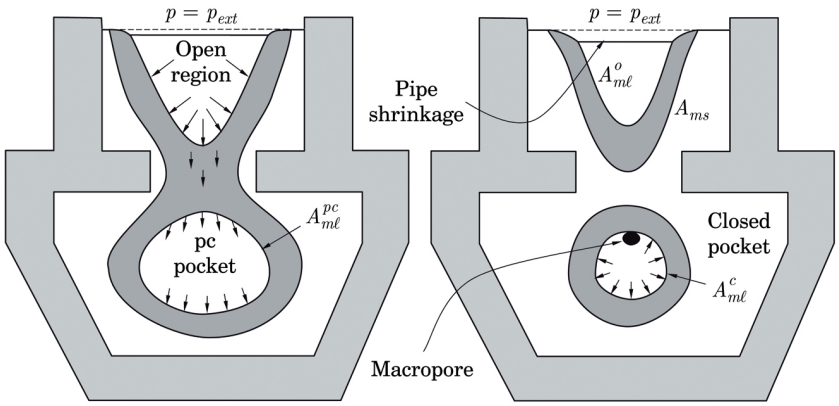

Figure 2.17: (left) Schematic view of an alloy solidifying in a mold and having a partially-closed (pc) region of liquid connected via the mushy zone to an open pocket. (right) As solidification proceeds, the partially closed region becomes a closed one. A_{ms} is the boundary separating the mushy zone and the fully solid region, whereas $A_{m\ell}$ separates the fully liquid and mushy regions (after [33]).

- For a boundary of the mushy zone in contact with the liquid, such as at the surface $A_{m\ell}$ corresponding to the liquidus (see Fig. 2.17), a pressure boundary condition can be imposed if the pressure in the liquid is known. This is the case when an open region of liquid is in contact with external air, and the pressure in the liquid is simply given by the atmospheric pressure + the metallostatic pressure.

- For a closed liquid pocket (a liquid pocket totally surrounded by the solid phase and/or the mold), no feeding is possible and a macropore will form at the highest point ($\rightarrow$ lowest pressure) of $A_{m\ell}^{c}$ (see Fig. 2.17, right image), and a cavitation pressure condition $p_\ell = p_c$ must then be applied.

- When the liquid pocket is partially closed (pc), i.e., connected to an open region of liquid through the mushy zone (see Fig. 2.17, left image), an integral boundary condition is applied before cavitation occurs. A pressure $p_{\ell z_0}$ must apply at height z_0 of this partially closed liquid pocket, and the pressure at the other points of this region is given by $p_\ell(\mathbf{x}) = p_{\ell z_0} + \rho_\ell \, \mathbf{g}(z_0 - z)$. The pressure $p_{\ell z_0}$ is in fact unknown, but since any flow that enters the partially closed pocket must also exit, its value must produce a velocity field at $A^{pc}_{m\ell}$ satisfying the overall mass balance equation:

$$\int_{A^{pc}_{m\ell}} \rho_\ell \mathbf{v}_\ell \cdot \mathbf{n} dS = 0 \tag{2.56}$$

  If $p_{\ell z_0} < p_c$, a pressure condition corresponding to that of a closed pocket must be applied and a macropore forms.

- At the boundary of the mushy region directly in contact with the ambient air, two situations might arise:

  (i) When the volume fraction of the solid g_s at a point of the surface is smaller than a critical value $g_{s,c}$, mass feeding occurs and the whole surface can move downward in order to compensate for solidification shrinkage.

  (ii) For $g_s > g_{s,c}$, the velocity at the free surface is set to zero, which is the same case as for a mold wall boundary condition. Note that this $g_{s,c}$ value is critical and difficult to assess; it is usually set at a very small value ($g_s = 0.01$) for columnar dendritic alloys or $g_s = 0.5$ for a globular-equiaxed solidification.

Validation of the $g_{s,c}$ parameter as a function of the microstructure has not been performed, yet. This is why one goal of this thesis is to make casting experiments (with an inoculated alloy or not) and to try to correlate these experimental data with simulation results by varying the $g_{s,c}$ parameter.

2.9 Phase-field simulation

Up to now, we have assumed that the shape of the pore is known *a priori*, i.e., a sphere for gaseous porosity (with a fraction given by Eq. 2.36) or a complex morphology for shrinkage porosity (with a fraction given by Eq. 2.37). However, near the end of the solidification process, we know that the pore is constrained to grow in between the solid network, inducing a curvature that is function of g_s and λ_2. The shape of the pore becomes thus very complex and cannot be predicted in a simple way.

The phase-field method is a robust modeling technique that can handle arbitrary complex interface shapes [66]. Indeed, the phase-field method provides an effective means for solving, on a fixed or adaptive grid [67], a complete set of equations governing both diffusion and the evolution of the interface, without tracking the latter explicitly.

It is not our purpose to develop the whole theory of the phase-field method, and we just summarize its main features. Because the theory was first developed for two incompressible phases, e.g., the solid and the liquid, we will shortly introduce this case to then adapt this theory to the liquid-gas system in section 4.4.

The phase-field method introduces an order parameter $\psi \in [0,1]$ to identify the phase, where $\psi = 1$ is the liquid, and $\psi = 0$ corresponds to the solid phase. Intermediate values of ψ represents the solid-liquid interface and a value of $\psi = 0.5$ defines the location of the interface. Thus, the usual "sharp" interface between liquid and solid becomes diffuse, and the order parameter continuously changes from 0 to 1 across the diffuse interface which has a thickness δ and a mobility $\mu_{s\ell}$.

The key parameter of this model is the free energy, which must be chosen so that:

- The integration of the free energy over a volume that includes an interface gives the correct value for the surface energy,
- There are two stable states, corresponding to $\psi = 0$ and $\psi = 1$,
- The preferred state is coupled to the temperature field so that the transition occurs at the equilibrium melting point for a flat surface.

Considering a domain containing both solid and liquid phases, we state that the overall energy of the system is given by the following functional $\mathcal{F}(T, C, \psi)$ [66]:

$$\mathcal{F}(T, C, \psi) = \int_V \left(F(T, C, \psi) + \frac{\varepsilon_\psi^2}{2} |\nabla \psi|^2 \right) dV \tag{2.57}$$

where $\varepsilon_\psi = \delta\sqrt{2W}$ (with the relationship $\gamma_{\ell g} = \delta W/3$) and F is the volumetric local free energy based on the free energies of the individual elements in both the liquid and solid phases and can be expressed as:

$$F(T, C, \psi) = F_s(T, C) - p(\psi)[F_s(T, C) - F_\ell(T, C)] + W g(\psi) \tag{2.58}$$

where F_s or F_ℓ are given by Eq. 2.16 for a regular solution. The $p(\psi)$ function is chosen to comply with the evolution of the order parameter along the solid-liquid interface. The $g(\psi)$ function is chosen so that the double-well potential $W g(\psi)$ is used to partially account for the excess free energy at the interface. In a non-stationary situation, the interface $\psi(\mathbf{x}, t)$ must move in such a way to minimize the overall energy of the system and the simplest equation that guarantees a decrease in total free energy with time is given by [66]:

$$\frac{\partial \psi}{\partial t} = -\mu_{\ell g} \frac{\delta \mathcal{F}}{\delta \psi} = -\mu_{\ell g} \left[\frac{\partial F}{\partial \psi} - \nabla \cdot (\varepsilon_\psi^2 \nabla \psi) \right] \tag{2.59}$$

where $\mu_{\ell g}$ is the mobility coefficient of the liquid-gas interface. This equation represents the evolution of the interface as a function of the free energy densities. We will see in section 4.4 how the concentration, which influences directly the free energy density, is coupled to this phase equation, and how to adapt this theory to the liquid-gas system to obtain the equilibrium shape of a pore constrained by a solid network.

2.10 Overview of the existing porosity models

2.10.1 Analytical models

Nowadays, state-of-the-art computer models describing the formation of microporosity on the scale of the casting process are based on volume-averaging methods for the

calculation of the local temperature and pressure fields in the interdendritic liquid, as described in section 2.3. These quantities are then used to estimate the level of gas segregation and to determine if conditions for the nucleation of a pore are met.

Almost all these approaches originate from the work of Piwonka and Flemings, dating back to 1966, these authors being the first to take into account both shrinkage and gas porosity [68]. Their 1D analytical developments were based on the assumptions of a constant solidification velocity together with a constant thermal gradient assuming: (i) the mushy zone is made of n tubes, where n was the reciprocal of the square of the primary dendrite arm spacing, (ii) a tortuosity factor was introduced in order to compensate for the fact that the liquid channels were not straight, and (iii) the flow was laminar, given by Hagen-Poiseuille's solution. With these assumptions, Piwonka and Flemings compared their results with experimental data, and concluded that they always under-predicted the pore size. They decided then to include the effect of dissolved gases on the pressure when pores form. They used the lever rule for the gas partitioning between liquid and solid and for calculating the supersaturation of the gas. Using Laplace-Young's equation to estimate the pressure in the pore, they predicted larger pores, in reasonable agreement to experimental results.

2.10.2 Criteria function

Before the work of Piwonka and Flemings arose the need for useful and practical rules that relate the local conditions (cooling rate, solidification velocity, thermal gradient, etc.) to porosity formation. Back to the 1950's, criteria functions were developed for dimensioning the size of risers and prevent interdendritic centerline shrinkage and porosity in steel plates [69]. Numerous criteria functions were then proposed by different authors, and among those by Niyama [70]. His criterion is widely used, because it is one of the fewest that holds any physical reasoning.

It is well established that a mass balance at the solidifying interface requires that the liquid must have a normal velocity ($v_{\ell n} = -\beta v_n^*$) to compensate for solidification shrinkage, where v_n^* is the velocity of the solidification front and β the solidification shrinkage ($\beta = (\rho_s - \rho_\ell)/\rho_\ell$). Interestingly, this relation is still valid for a steady-state columnar solidification of dendrites with $\rho_s = \text{cte}$ and $\rho_\ell = \text{cte}$: the microscopic velocity of the fluid $\langle v \rangle_{\ell x}$ in the mushy zone is uniform under such conditions and only the superficial velocity varies, $\langle v_{\ell x} \rangle = g_\ell \langle v \rangle_{\ell x}$, which is proportional to the mass flow rate. After having derived this key relationship, Niyama used Darcy's law (without considering gravity) to derive the pressure difference between the tip of the dendrite to any point $x(T)$ in the mushy zone:

$$\Delta p = p_\ell(T_{liq}) - p_\ell(T) = \frac{\beta \mu_\ell v_T}{G} \int_{g_\ell}^{1} \frac{g_\ell}{K(g_\ell)} \frac{dT}{dg_\ell} dg_\ell \tag{2.60}$$

Since the isotherms are difficult to measure, Niyama replaced v_T by $-\dot{T}/G$, and the pressure difference becomes thus proportional to $|\dot{T}|/G^2$. Niyama then performed experiments on cylindrical steel castings of various diameters and observed that porosity occurs when $G/\sqrt{-\dot{T}} < 1\ \sqrt{\text{K min}}/\text{cm}$. It should be noted that this criterion was developed specifically for shrinkage porosity in steels. This specific value of $1\ \sqrt{\text{K min}}/\text{cm}$

would of course vary if one considers other alloys, a fact that is ignored by many users. But more important, this criterion is valid for shrinkage porosity only, and does not account for gas porosity.

Nevertheless, the pressure drop at any point of the mushy zone is accessible with these derivations. Equation 2.60 states that the pressure difference is proportional to the solidification shrinkage, the viscosity, and to the ratio v_T/G. Indeed, it seems obvious that an increase of the isotherms velocity induces a faster interdendritic liquid flow, whereas a larger thermal gradient reduces the extent of the mushy zone, and thus facilitates feeding. Carlson and Beckermann [71] integrated numerically Eq. 2.60 using measured $g_s(T)$ curves to deduce a dimensionless value of the Niyama criterion. Here we use a Scheil-Gulliver microsegregation model and the Carman-Koseny relationship for the permeability in order to integrate Eq. 2.60 analytically[2] as suggested by [33]. Taking the same condition as in Fig. 2.5, the pressure drop in the mushy zone can be calculated for Al-Cu alloys of different compositions. This is shown in Fig. 2.18.

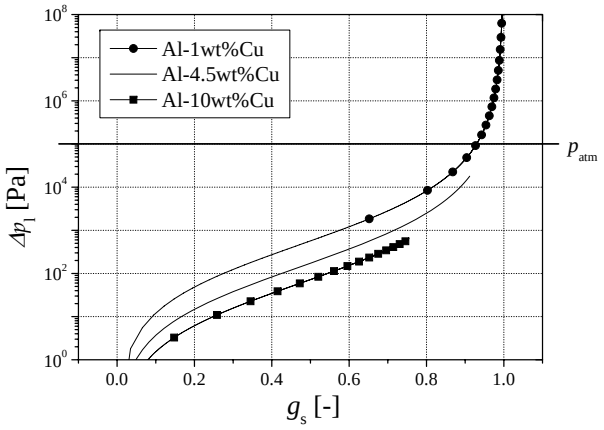

Figure 2.18: Pressure drop in the liquid as a function of g_s for three different Al-Cu alloys. Note that the pressure drop can easily reach equivalent atmospheric pressure values when the eutectic forms at 548 °C, thus inducing tension stresses in the liquid

2.10.3 Numerical models

In 1985, Kubo and Pehlke [20] published the first 2D model for porosity predictions. Assuming a solidification path given by the Scheil approximation, they calculated the fluid flow by coupling Darcy's law (see Eq. 2.13) to the mass conservation equation (Eq. 2.7), and constructed a relationship between the fraction of porosity and the pressure. They calculated first the change in solid fraction to deduce the fluid velocity via Darcy's equation. The local pressure in the liquid was obtained from the mass conservation equation. Assuming that the pores nucleate at the solid-liquid interface

[2]Using a Clyne-Kurz approximation (see Eqs. 2.3 and 2.4) is also possible, but gives much more complicated results (hypergeometric functions must then be used), without bringing significant improvement to the solution.

with a diameter equals to the secondary dendrite arm spacing, they used the Laplace-Young equation to deduce the gas pressure in the pore. If the latter was higher than a critical pressure, the pore would nucleate and a gas-conservation equation was then solved using Sievert's law (see Eq. 2.23).
As can be seen, Kubo and Pehlke had pretty much incorporated all the necessary ingredients for the modeling of porosity, even if some aspects related to nucleation and growth of pores are arguable. In particular, because a liquid wets generally well its own solid, the solid-liquid interface is not a favorable site for pore nucleation (a fact not taken into account by these authors). Nevertheless, it is fair to say that state-of-the-art models for porosity predictions are based on Kubo and Pehlke's developments.

Since only about three groups in the solidification community incorporate in their models all the aspects enumerated at the beginning of section 2.8, we will present briefly their contributions, whereas the reader is referred to the reviews of Lee *et al.* [72] or Stefanescu [73] for other, maybe more pragmatic approaches.

The first group is that of Peter Lee at Imperial College (UK). Lee and Hunt [50], then at Oxford, experimentally observed porosity formation in Al-Cu alloys using an X-ray temperature gradient stage. They found the pressure drop caused by shrinkage to be negligibly small. Then, using previous results, they simulated the growth of a population of pores due to hydrogen diffusion in Al-Cu alloys, using a 2D continuum-diffusion model, combined with a *stochastic* model of pore nucleation [74] (note that they are one of the few groups to handle stochastic aspects of nucleation). In a way similar to cellular automata developed for dendritic solidification [75], potential pore sites are randomly placed within the domain, each being attributed a stochastically chosen supersaturation threshold at which nucleation occurs. Their model did not include the effect of pressure drop due to shrinkage, although it showed good correlation with in situ observations of pore growth. In a more recent paper, Lee *et al.* [77] developed a multiscale model of solidification microstructures in an Al-Si-Cu alloy, including microsegregation and microporosity. A comparison of these simulations with X-ray tomography data was performed for different alloys and is shown in Fig. 2.19 [76]. ProCAST® was used to solve the energy, momentum and continuity equations to determine the heat and momentum equations. The temperature and pressure from these calculations were then coupled to a mesoscale model for microstructure formation via the enthalpy and pressure. The solid phase nucleation and growth was solved using a stochastic nucleation model with a combined cellular automaton-finite difference model (the grain velocity was estimated via the KGT model [78] and the grain envelope was tracked using Gandin and Rappaz' technique [75]). Pore formation was simulated using a finite difference solution of the diffusion equation for hydrogen (using Eq. 2.49) with a stochastic location of pores nucleation sites. The pinching of pores by the solid – inducing non-spherical pore shapes and growth restrictions – as well as the influence of shrinkage were taken into account. Their effective diffusion coefficient is empirical, as their curvature restriction law (see [79] for details). Finally the influence of the local solute content is not well taken into account (in comparison to Sigworth and Engh available data [40]).

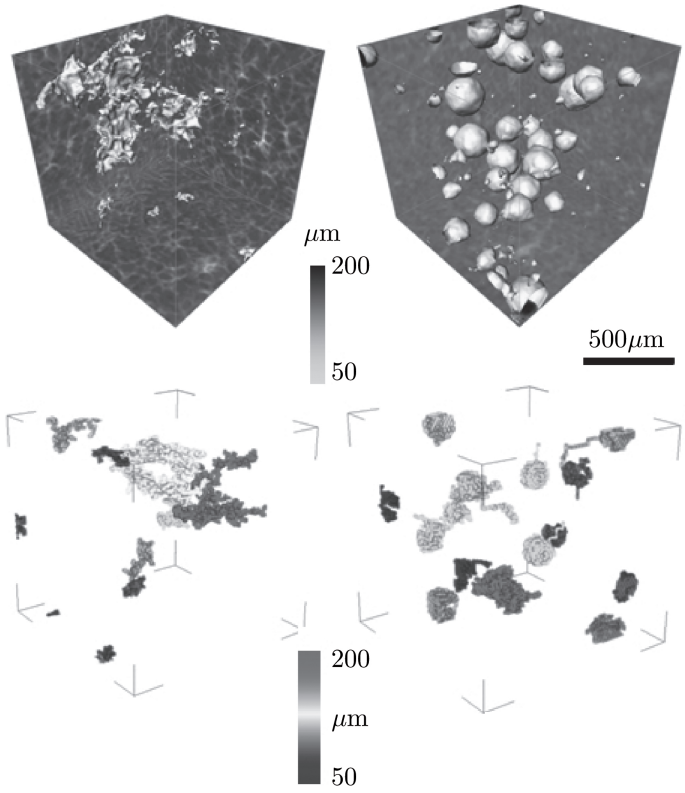

Figure 2.19: Comparison of (top) experimentally observed and (bottom) simulated pore formation in binary (left) Al-4wt%Cu and (right) Al-7wt%Si alloy, respectively. The domain size is 1.2 mm^3 and the grey level in the simulated pores represents the equivalent pore diameter. The nominal hydrogen content was set at 0.24 $cc_{STP}/100g$ (after [76]).

The second group is that of Christoph Beckermann at the University of Iowa (US). In a recent study, this group developed a volume-averaged model for finite-rate diffusion of hydrogen in aluminum alloys [6]. They coupled the calculation of the micro-/macro-scale gas species transport in the melt with a model for the feeding, flow and pressure field. They showed that the rate of pore growth is influenced by the local level of gas supersaturation in the melt, as well as various microstructural parameters. Figure

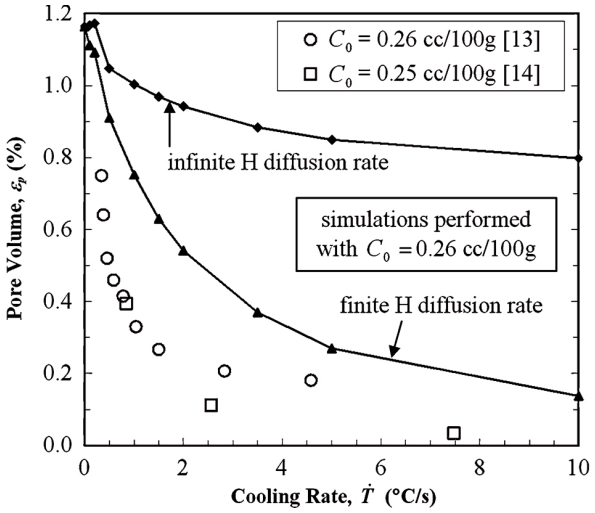

Figure 2.20: Simulations with initial hydrogen concentrations of 0.26 $cc_{STP}/100g$, with both finite and infinite hydrogen diffusion rates. Results shown use a temperature gradient $G = 3265\dot{T}^{0.512}$ K/m, a pore density $\mathcal{N}_p = 1 \times 10^{11}\,m^{-3}$, and a capillary pressure at nucleation of 1.6 bar. Experimental results of [80, 81] ($\equiv$ [13] and [14] on the figure legend) are shown for comparison (after [6]).

2.20, taken from their article [6], shows the influence of hydrogen diffusion on the pore volume as a function of the cooling rate. These authors were in fact the first to account for hydrogen diffusion in the growth of pores for 3D calculations. However, as pointed in section 2.7, only diffusion through the liquid-gas interface was considered. Finally, the influence of the growing solid network on the curvature of the pore phase was taken from the model of Péquet *et al.* [2], which is fairly inaccurate (see Fig. 2.14).

The last group is that of Michel Rappaz at EPFL (CH). This group has developed a 3D microporosity model based on the solution of Darcy's equation and microsegregation of gas [2]. They were the first to couple microporosity with macroporosity and pipe-shrinkage predictions in a coherent way, with appropriate boundary conditions. In order to accurately calculate the pressure drop within the mushy zone, they developed a dynamic mesh refinement technique (see Fig. 2.21): a fine and regular finite volume (FV) grid is superimposed onto the finite-element (FE) mesh used for the heat-flow computations. For each time-step, the cells which fall in the mushy zone are activated, and the governing equations of microporosity formation are solved only within this domain, with appropriate boundary conditions as described in section 2.8. In the same group, Couturier *et al.* [4, 3, 5] then improved the model by developing a porosity model for multi-gas systems in multi-component alloys in a way analogous to that

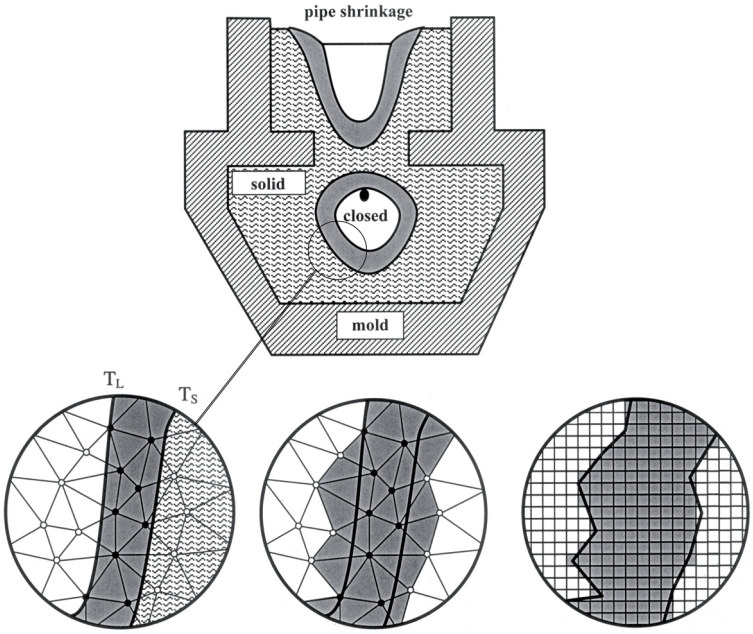

Figure 2.21: Up: schematic representation of a casting. Bottom: (left) A magnified view of the mushy zone shows that only few FE nodes fall within its thickness (filled circles). (right) The FE elements are refined into small regular squares or cells, and those falling within mushy elements (gray elements in the middle figure) are activated (after [2]).

described in section 2.4.2. They also introduced a simple, but realistic model for pore pinching. Considering the pinching of cylindrical dendrite arms arranged in a square lattice, the evolution of the maximum radius of curvature of a perfectly non-wetting pore is computed as a function of the solid fraction, as shown in Fig. 2.14. However this porosity model, which is implemented in ProCAST®, does not take into account the effect of hydrogen diffusion; moreover, the curvature influence has never been validated by any experimental data; and last but not the least, the influence of the pore curvature has never really been separated from the hydrogen diffusion influence.

Chapter 3

Experimental methods

In this chapter, we first describe which materials were investigated in this study and how they were prepared. Then, we present the 2-dimensional (2D) solidification set-up that we developed for the understanding of the inoculant influence on the pipe shrinkage shape. 1D Directional Solidification (DS) set-ups were also use to investigate the morphology of pores non-induced by bi-films, as well as the influence of alloy copper content, cooling rate and initial hydrogen concentration on the morphology of pores.

Finally, the different analysis techniques that were used in this study are detailed at the end of this chapter, with a focus on X-ray tomography, since this technique was widely used for this thesis.

3.1 Materials

Three alloy compositions were investigated in this study:

- Al-1wt%Cu
- Al-4.5wt%Cu (with or without inoculant)
- Al-10wt%Cu

Prior to casting, pure Al and Al-4.5wt%Cu ingots (both coming from Alcan, Voreppe, France) were sawed with a conventional band saw (Daiß and Partner HBS 500G). The resulting pieces were then sandblasted and washed with soap and water, whereas OFHC (Oxygen Free High conductivity) copper pieces (typically 10 g each) were washed with sulfuric acid. All these pieces of metal were then placed in an ultra-wave acetone-alcohol bath for final cleaning and then dried in a conventional drying oven at 120 °C for 1 hour. The alloys were then prepared by mixing appropriate amounts of these base materials in the devices described in the following sections.

3.2 Solidification experiments

3.2.1 2D-Directional solidification

In order to investigate the influence of the inoculant on the shape of pipe shrinkage, two Al-4.5wt%Cu alloys (one with, the other without inoculant) have been solidified under

the same cooling conditions. To do so, a new bi-directional solidification apparatus – denominated D_2S set-up – has been developed. Adapted and improved from the experimental set-up of Grasso [82], it is made of a cylindrical (slightly conical) 60 mm ∅ by 110 mm height stainless steel mold covered with boron nitride (BN) to avoid chemical reaction with the melt. At the bottom, a coated stainless steel sheet (2 mm thick) is mechanically fixed to the cylindrical mold as shown in Fig. 3.1. A cover holding several thermocouples can be placed at the top of the mold. Temperatures were recorded before and during solidification by K-type thermocouples (chromel-alumel), located at different heights within the mold (at typically 6, 8, and 52 mm from the bottom), and connected to a NetDAQ Data Acquisition system (FLUKE Corporation, Everett, WA). The entire system can be taken out of the heating furnace where the metal was molten and directly clamped onto a platform having a hole in the center. At the bottom of this hole, a water jet spray can be turned on to directly cool the thin bottom sheet of the mold. Additionally, eight water jet spray noses located around the mold (see Fig. 3.1) can be activated to have a radial solidification. Note that the room temperature and relative humidity were recorded with a conventional hygrometer.

The experimental procedure was as follows. 850 g of Al-4.5wt%Cu (inoculated or not) was melted directly inside the mold in a resistance furnace at about 50 °C above the liquidus. The metal was kept for 1 hour at this temperature in order to ensure a uniform temperature in the mold, as well as equilibrium with the ambient humidity (i.e. hydrogen contained in the water partial pressure). Note that the oxide skin at the top of the melt was mechanically removed every ten minutes. The mold was then taken out of the furnace and directly fixed onto the solidification set-up. The water cooling was then activated until solidification is complete (typically 80 s). A constant flow rate of 300 L/h for both vertical and radial water jets was used ($\frac{300}{8}$ L/h for each radial nose) to ensure both upward and radial solidification. The solidified specimens were then cut into two halves using the same conventional band saw used previously. Conventional grinding with SiC papers (500 to 4000 grade) was performed before chemical etching of the surface for a couple of seconds only using a "Keller" agent (25 mL HNO_3, 15 mL HCl, 10 mL HF, and 900 mL H_2O).

3.2.2 1D-Directional solidification

Two different 1-D DS set-ups were used in this study. The first one – denominated DS_{1D-ATM}, for atmospheric conditions – was designed so that the oxide skin at the surface of the melt is never broken. However, the atmosphere cannot be controlled with this apparatus, and the solidification process is thus performed under conventional atmospheric conditions.
The second directional set-up – denominated DS_{1D-AC}, for atmosphere controlled set-up – is a 1D-DS set-up mounted inside a vacuum induction furnace so that the atmosphere can be controlled. However, melt pouring into a copper mold is obligatory in this case, leading to possible oxide entrapment during the casting process.

The main purpose of the DS_{1D-ATM} is to produce samples without breaking the

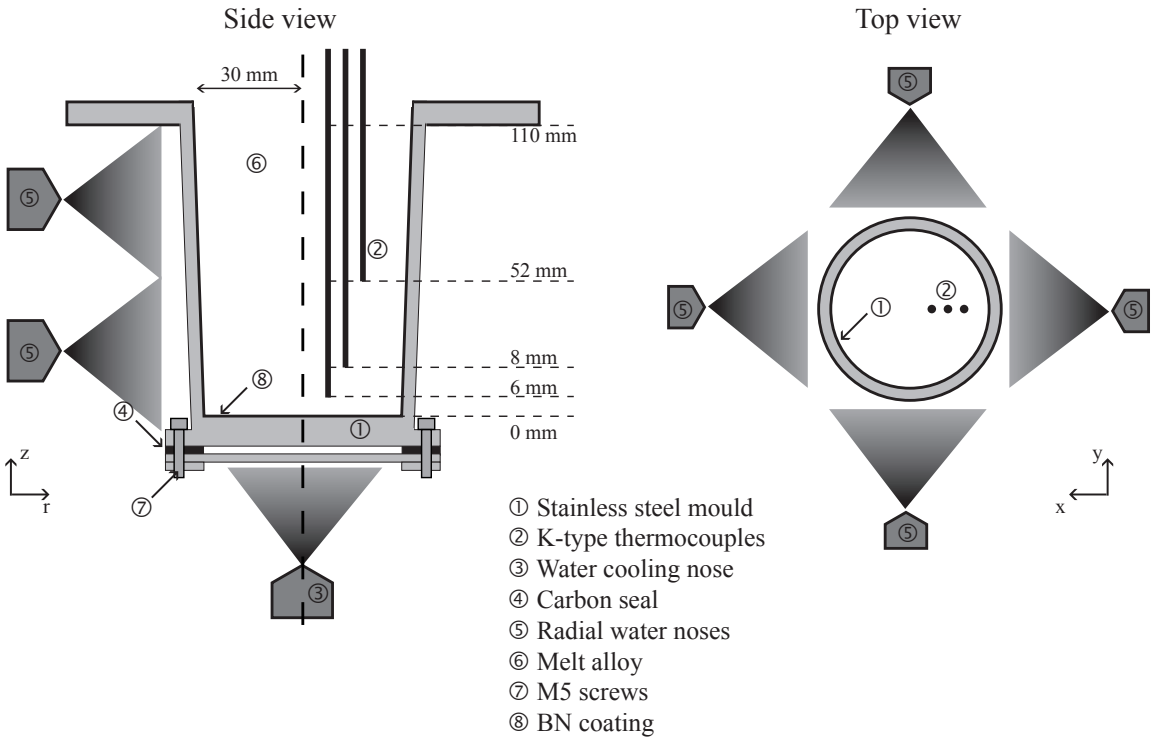

Figure 3.1: Schematic of the D_2S set-up.

oxide skin and thus to avoid melt pouring and further oxide bifilms entrapment in the casting. The only alloy that was solidified with this device was an Al-4.5wt%Cu (with and without inoculant). This DS apparatus is very similar to the D_2S set-up, the only significant change being the radial cooling conditions. Indeed, in order to have 1D upward solidification conditions, the lateral and top surfaces of the mold were wrapped with a thick quartz wool layer (and of course the 8 radial noses were not activated for this experiment, see Fig. 3.2). To test the adiabatic radial condition of the mold lateral surface, three K-type thermocouples were placed at the same hight, but at different radii during a 1D upward solidification experiment. A temperature difference smaller than 1 °C was observed between the three thermocouples during the entire experiment, proving the efficiency of the quartz wool layer for lateral insulation. Alternatively, for further determination of the longitudinal heat flux, the thermocouples were typically placed at 8, 55, and 90 mm from the bottom of the mold (see Fig. 3.2).

The experimental procedure was the same as for the D_2S set-up. The only significant change was related to the cooling conditions. Whereas the eight radial noses were not activated, a vertical flow with a constant rate of 400 L/h was used. Typical experimental results showing the thermal evolution for the three different thermocouples are presented in Fig. 3.3a.

The thermal gradient G and the liquidus velocity v_L were determined using a 1D inverse modeling technique [83] using the software CalcoSOFT® (Calcom ESI Group,

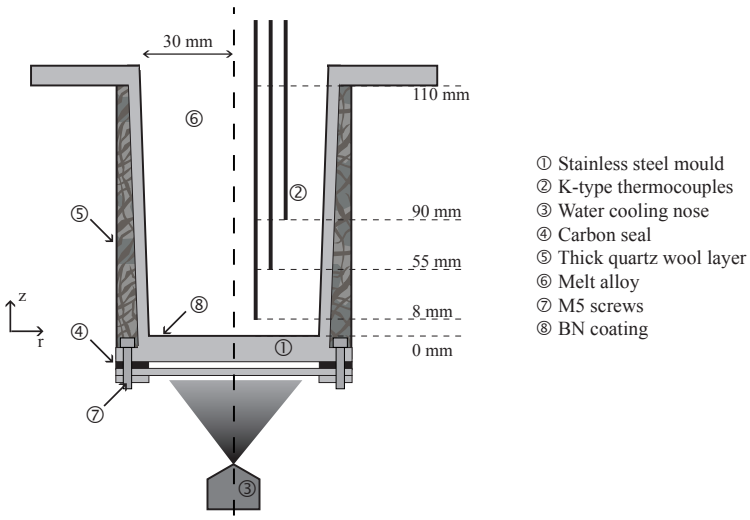

Figure 3.2: Schematic of the DS_{1D-ATM}.

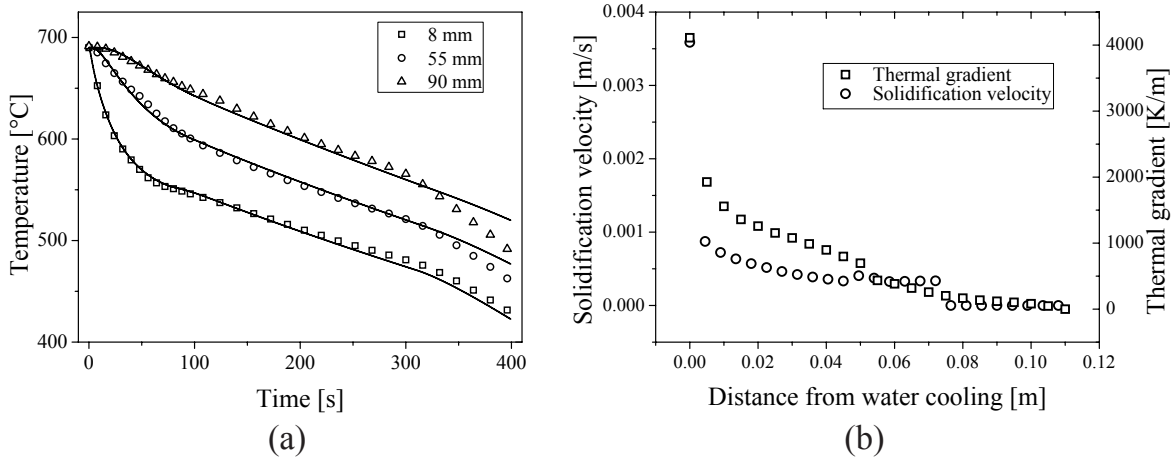

Figure 3.3: (a) Typical recorded temperatures during a 1D upward solidification experiment of an Al-4.5wt%Cu alloy performed with the DS_{1D-ATM}. Three thermocouples were placed at different heights (symbols) and inverse modeling was performed to fit the experimental data (continuous lines). (b) Liquidus velocity and thermal gradient as a function of the sample height obtained via inverse modeling [83].

Lausanne, Switzerland). After convergence to a minimal error between measured and calculated temperatures, the temperature is known at each height within the specimen and for each time, from which $G(z)$ and $v_L(z)$ can be calculated. The results of these simulations are shown in Fig. 3.3b. A thermal gradient of about $3000\,\mathrm{K\,m^{-1}}$ is achieved near the bottom of the mold, whereas $G \to 0$ around $z = 0.07\,\mathrm{m}$. The first value indicates strong directional solidification conditions at the bottom, whereas the last one shows a good thermal insulation at the top. The velocity of the liquidus v_L decreases rapidly to stay at a constant speed of about $0.5\,\mathrm{mm/s}$. This will allow us to use the conventional solidification theories for microsegregation (see Eq. 2.4) and for the secondary dendrite arm spacing (λ_2) as a function of the height (see Eq. 2.5).

In order to control the atmosphere and thus the initial hydrogen content in the melt, a $DS_{\mathrm{1D-AC}}$ set-up was developed inside a vacuum induction furnace (see Fig. 3.4). Note that all three alloy compositions, Al-1wt%Cu (non-inoculated), Al-4.5wt%Cu (both inoculated or not), and Al-10wt%Cu (non-inoculated) were investigated with this device. The main purposes of these experiments were to investigate the influence

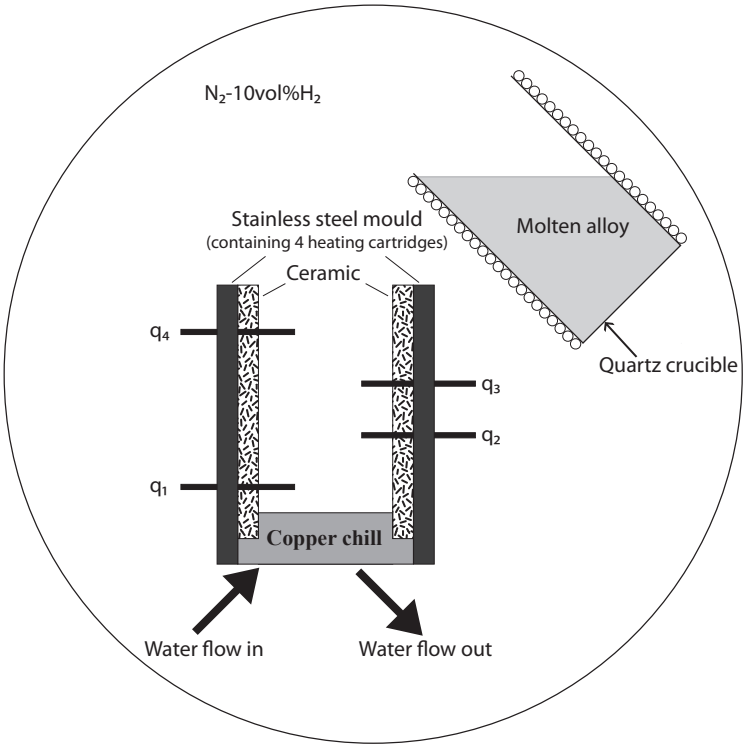

Figure 3.4: Schematic of the $DS_{\mathrm{1D-AC}}$.

of the alloy copper content, cooling rate and initial hydrogen content on the pore morphology.

The mold consists of two cylinders in close contact with each other. The inner one is made of ceramic (3 mm thick). The outer one is made of stainless steel in which four heating cartridges were introduced, allowing to control the mold surface temperature and to reduce radial heat transfer. The dimensions of the specimens are 40 mm in

diameter and about 70 mm in height and the bottom of the mold consists in a copper chill cooled down by a continuous flow of water. The temperatures before and during solidification were recorded by four K-type thermocouples (chormel-alumel) located at different heights within the mold and connected to the NetDAQ Data Acquisition system described previously.

The experimental procedure was as follows: the proper amount of materials (Al + Cu) was introduced in the quartz induction crucible, where they were first melted under vacuum. When the alloy was completely melted, proper amount of N_2-10vol%H_2 was introduced in the chamber for 20 min, time during which the induction was kept on in order to stir the melt and to allow equilibration with the hydrogen partial pressure (20 min waiting time seemed adequate compared to [84] (5 min for aluminum based alloys) and [56] (25 min for steel alloys)). The alloy was then poured in the mold and solidified in the cylindrical ceramic mold preheated at the initial melt temperature.

First the influence of the alloy copper content and cooling rate on porosity was investigated. For that purpose, Al-1wt%Cu, Al-4.5wt%Cu, and Al-10wt%Cu samples have been solidified under the same hydrogen partial pressure from an initial melt temperature of 800 °C. Here again, inverse modeling was performed in order to deduce the thermal gradient G and liquidus velocity v_L at each point in the casting. Figure 3.5 shows a typical result for an Al-4.5wt%Cu casting experiment.

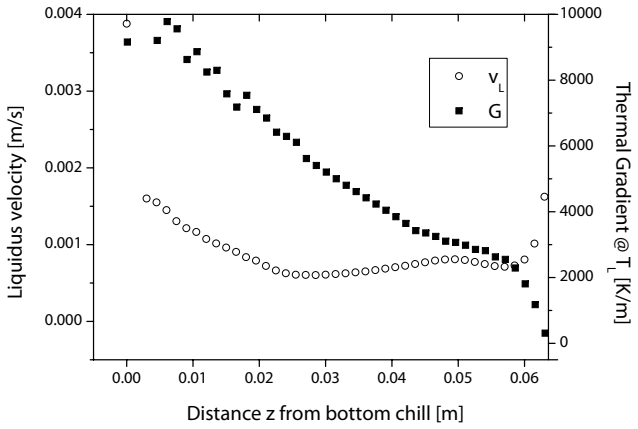

Figure 3.5: Thermal gradient and liquidus velocity for an Al-4.5wt%Cu casting experiment performed under 800 mbar of N_2-10vol%H_2, with an initial temperature of 800 °C.

The influence of the initial hydrogen concentration on pore morphology in the melt was analyzed in a second stage. Since the formation of a gaseous phase in a liquid is governed by Sievert's law as we saw in section 2.4.2, samples of identical composition (Al-4.5wt%Cu) have been solidified under the same hydrogen partial pressure, but with a different initial casting temperature. Samples with three different hydrogen content have then been produced (0, 0.23 and 0.41 $cc_{STP}/100g$). A sample without hydrogen (or minimum) was cast under Ar from an initial temperature of 800 °C. Two others

were cast under 800 mbar of N_2-10vol%H_2 at 700 and 800 °C, so that their initial hydrogen content was calculated to be 0.41 and 0.23 $cc_{STP}/100g$, respectively.

To sum up, we have first cast Al-4.5wt%Cu alloys (inoculated or not) in the DS_{1D-ATM} in order to investigate the morphology of microporosity in a quiescent melt, probably free of any oxide bifilms. Second, in order to investigate the influence of the copper content and cooling rate on pore morphology, Al-Cu specimens of different compositions were cast under the same conditions in the DS_{1D-AC} set-up. Finally, the influence of hydrogen content on pore morphology was investigated for a non-inoculated Al-4.5wt%Cu alloy solidified in the DS_{1D-AC} set-up.

After solidification, the obtained specimens were cut in two halves using the same conventional band saw used previously; one half was dedicated to further machining for X-ray tomography experiments, whereas the other half was characterized using liquid penetrant testing, optical and electronic microscopy. These techniques are briefly described in the next section.

3.3 Analysis techniques

3.3.1 Liquid penetrant testing

Liquid penetrant testing (LPT) is a method that is used to reveal surface breaking flaws by bleedout of a colored or fluorescent dye from the flaw [85]. Although this method dates back to the early ages of the railways to inspect their surface defects, it is still widely used nowadays. The main advantage of this method is its simplicity; indications can be shown to third parties without a lot of explanations. However, in order to have reliable results, much care must be taken. In order to perform LPT via a standardized procedure (ASTM E1417 (revised in 2005) [86], following the Qualified Product List QPL-AMS-2644 [87]), the Al-Cu alloys produced via the DS_{1D-AC} set-up were analyzed by an industrial company (*Quality Control NDT S.A.*, 1072 Forel, Switzerland). The general procedure of the LPT was as follows and a schematic is given in Fig. 3.6.

1– Milling the surface at a cutting speed of 128 m min^{-1} and 0.04 mm/tooth (without any further grinding and/or polishing),

2– Chemical etching of the surface for 30 s to clean it,

3– Cleaning in ultra-wave acetone-alcohol bath,

4– Samples drying at 120 °C for 1 hour,

5– Cooling of the samples at room temperature,

6– Immersing the samples into the penetrant liquid for 10 min,

7– Samples draining for 10 min,

8– Excess penetrant removal (water spray),

9– Drying,

10– Application of the developer,

11– Inspection (photo camera).

The chemical etching solution consisted of 50 vol% nitric acid, 25 vol% sulfuric acid, 25 vol% water, and 60 g/L ammonium bifluoride. Note that much care must be taken with this solution since it produces a lot of HF.
LPT is a powerful qualitative technique, but barely a quantitative one: the information on the shape of the surface defect (either rounded or elongated) is reliable, as well as the density of surface defects, if the pores are not too close from one another. However, there are too many uncertainties to make quantitative comparison between two samples.

Figure 3.6: Principle of liquid penetrant testing: (a) surface defect, (b) application of the penetrant, (c) excess penetrant removal, (d) application of the developer.

3.3.2 Scanning electron and optical microscopy

Scanning electron microscopy (SEM) was performed on polished sections of the different specimens. To avoid closing or widening of the pores, the specimen surfaces were milled as opposed to being ground with coarse SiC papers. After milling, the specimen preparation was completed using fine SiC papers from 1000 to 2400 grade, followed by polishing with 5- and 1-μm AP-A alpha alumina polishing suspension on DP-Nap clothes (Struers GmbH, Willich, Germany) using distilled water as lubricant. Finally, the same chemical etching as for LPT was performed for approximatively 30 s in order to clean the surface and remove the imperfections that could possibly close the pores.

The SEM images were acquired using a PHILIPS® (Philips Electronics Instruments Corp., Mahwah, NJ.) XL30-FEG SEM microscope (typically 10 kV, spot size of a few nanometers, and working distance of 10 mm) using a secondary electron (SE) detector and/or a backscattered (BSE) electron detector. EDX (Energy-dispersive X-ray spectroscopy) was used to identify and quantify the chemical composition of the samples with a typical resolution of 1 μm that can be achieved with the conventional parameters of the XL30-FEG SEM. Finally, optical microscopy was performed using a Leica microscope coupled to a data acquisition system. In order to reveal the microstructure, the surfaces of the Al-Cu samples were chemically etched using the "Keller" agent described previously. Typical samples obtained via the D_2S, $DS_{\mathrm{1D-ATM}}$ and $DS_{\mathrm{1D-AC}}$ set-ups are shown in Fig. 3.7a, b and c, respectively.

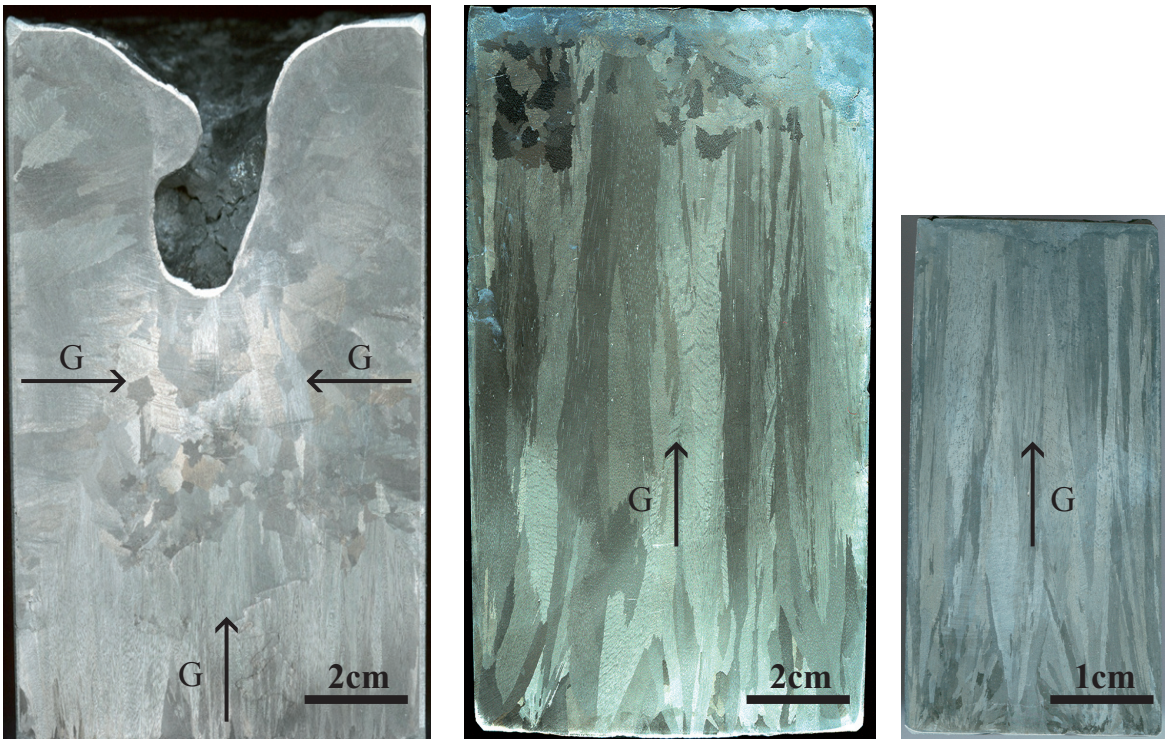

(a) (b) (c)

Figure 3.7: Al-4.5wt%Cu alloy samples cast with (a) the D_2S set-up, (b) the DS_{1D-ATM} set-up, and (c) DS_{1D-AC} set-up.

3.4 X-Ray tomography

X-ray tomography enables 3D reconstruction of a sample from a sufficiently large number of projection radiographies (see Fig. 3.8). Its theory relies on two basic principles, the Lambert-Beer law and the Radon theorem [88].
The Lambert-Beer law stipulates that, for a given beam parallel to the x-axis, the transmitted energy E is linked to the initial photon energy E_0 via the following attenuation law [89]:

$$\frac{E(x)}{E_0} = \exp\left(-\int_0^x \frac{B\rho(x')Z^4(x')}{E_0^3}dx'\right) \tag{3.1}$$

where B is a constant, x the local position, $\rho(x)$ the local density, and $Z(x) = \sum_A Z_A\chi_A$, where χ_A is the molar fraction of the element A.
The Radon theorem establishes the possibility to reconstruct an object from all its projections [90] (of course only a finite number of projections can be recorded, so that interpolation between two steps is required). The Radon transform is the mathematical formulation of a projection, and hence the reconstruction of the function $\rho(x, y, z)$ can be performed via the inverse Radon transform. This transformation is obtained using an appropriate algorithm based on the filtered back-projection theory [91].

The X-ray tomography experiments performed in this study have been conducted at the European Synchrotron Radiation Facility (ESRF) in Grenoble (France) under the project ANR-05-BLAN-0286-01 TOMOSOLIDAL supported by the "Agence Nationale

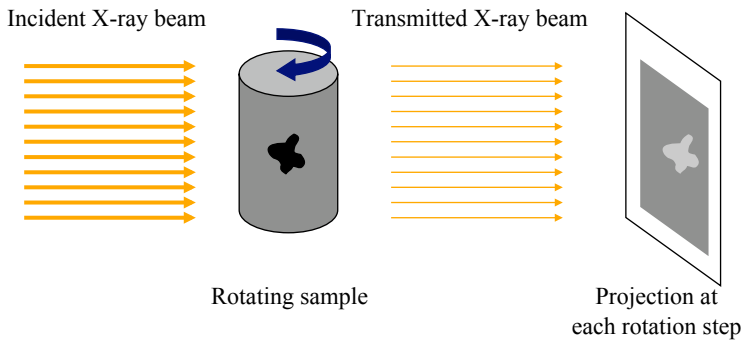

Figure 3.8: Schematic of an X-ray tomography experiment.

de la Recherche", and at the Swiss Light Source (SLS) in Villigen (Switzerland) under the project ID20090118.
In a synchrotron, X-rays are produced by relativistic electrons that are accelerated by a magnetic field in a storage ring (*Bremsstrahlung* effect). The resulting polychromatic X-ray beam (tangential to the storage ring) passes through a monochromator and has then the main advantages to be highly coherent and to possess an exceptional brightness compared to commercial tomography devices. The ID19 beam line at ESRF and the TOMCAT beamline at SLS are devoted to high-resolution tomographic imaging and have an energy-tunable X-ray beam. The advantage of the ESRF beamline is its large energy range (from a few keV up to 100 keV theoretically). We observed indeed a stainless steel crack filled with gold at 60 keV [92] at ESRF, which was impossible to achieve at the SLS, since the energy there can go only up to 40 keV. However for aluminum rich alloys, because of their low densities, lower energy (around 20 keV) is required and both ESRF and SLS beamlines can be used. The dedicated micro-tomographic set-up either at the ESRF or at the SLS consists of a precision mechanical sample stage (rotation and translation in the three directions are possible) combined with a fast, high-resolution detector system. The latter consists of a fluorescent screen (YAG:Ce), which transforms the X-rays into visible light, combined with microscope optics to project the image on 14 bit dynamic CCD camera that has a 2048×2048 pixel chip. The 14 bit projections are transformed into 16 bit images and after processing and 3D reconstruction, the resulting stack of images is coded on 32 bit (32 bit are necessary for the reconstruction and ring artefact correction algorithms). In order to reduce the size of the files (note that a stack of 2048 images of 2048×2048 pixels coded on 8 bit has already a file size of $2048^3 \approx 8$ Gb), the stack is then transformed from 32 to 8 bit (i.e., 256 grey levels).

Two main different sets of experiments have been performed:

- The samples were analyzed *ex-situ*: small samples of 1 mm in diameter and 3 mm in height were machined from the specimens obtained from the DS_{1D-AC} and DS_{1D-ATM} and observed at room temperature via X-ray tomography.

- The samples were analyzed *in-situ*: samples of about 1.4 mm in diameter and 3 mm in height were machined from specimens supersaturated in hydrogen obtained via the DS_{1D-AC}. These small samples were then heated up in a resistance

furnace to a temperature within the mushy zone and directly observed by X-ray tomography, which was thus performed *in-situ*, i.e., typically for $0 \leq g_s \leq 1$.

Figure 3.9 shows the rotating stage at ESRF (left image) with its resistance furnace, as well as the rotating stage at SLS (right image). Note finally that all the experiments were performed via absorption contrast only, and phase contrast was avoided as much as possible (the camera position was as near as possible from the sample, as shown in Fig. 3.9b).

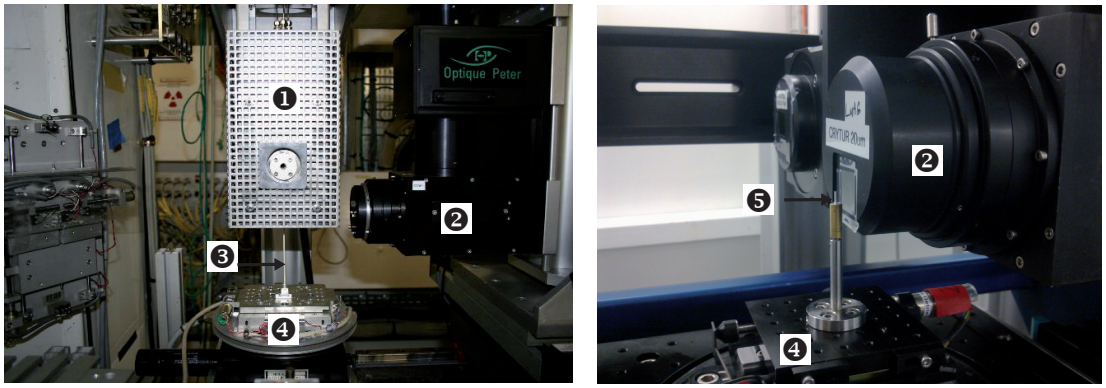

(a) (b)

Figure 3.9: X-ray tomography set-up at ESRF (a) and SLS (b). In both cases the X-rays are coming from the left. The numbers represent (1) the furnace, (2) the camera, (3) the alumina rod, (4) the rotating stage, and (5) the sample.

3.4.1 Ex-situ experiments

First, Al-4.5wt%Cu specimens (with or without inoculant) were cast with the $DS_{\mathrm{1D-ATM}}$. One sample (1 mm in diameter, 3 mm in height) of each casting were extracted at 8 mm from the bottom chill. The shape of micropores non-induced by oxide bifilms was investigated in this experiment. The samples were analyzed through X-ray tomography at ESRF with a typical pixel size of 0.7 μm. Please note that the resolution should be given as twice the pixel size, since 2 pixels are needed to visualize an edge. This is a common error found in the literature.

Second, Al-Cu samples (1, 4.5, or 10wt%Cu) were cast in the $DS_{\mathrm{1D-AC}}$ under different hydrogen partial pressures. Two samples (1 mm in diameter and 3 mm in height) were then machined from these specimens at 10 and 40 mm from the bottom chill. The influence of (i) the alloy copper content, (ii) the initial hydrogen content, and (iii) the λ_2 spacing on porosity was investigated in this series of experiments. These samples were analyzed at the SLS with a typical pixel size of 0.7 μm.

3.4.2 In-situ experiments

Under special conditions, it is possible to perform an X-ray tomography scan in less than a minute at the ESRF (400 projections on an 512×512 ROI (Region Of Interest)

with a camera readout time of 9.1×10^{-3} s). These conditions enable the observation of the 3D microstructure evolution during coarsening [25] or even inhomogeneous deformation in semi-solid aluminium alloys [93].

The set-up used in this study is similar to the one of Limodin *et al.* [25]. To sum up, a sample of 1.4 mm diameter and 3 mm height was extracted from the casting and then glued with a zirconia paste onto the top of an alumina rod, which was then placed on the rotating stage. This rotating sample was inserted into a fixed resistive furnace through a small hole at the bottom. The furnace has two windows on the sides to allow X-rays to pass through. The projection size of the X-ray images was set at 512×512 pixels and the scan time for a full rotation was about 51 s. The resulting pixel size is 2.8 μm and scan was taken every 1.28 min to characterize the microstructural evolution (radiographies without samples as well as without X-rays (i.e., flat field and dark field images) were recorded during the 26 remaining seconds for further image processing). Note finally that the sample was supported by its own oxide skin during the whole experiment.

Two main sets of experiments were then conducted. In the first one (denoted *in-situ_A* from now on), the 3D mushy zone morphologies of an Al-4.5wt%Cu and of an Al-10wt%Cu alloy were analyzed during solidification. For that purpose, each sample was gradually heated to a temperature slightly above the liquidus, where it was maintained in the liquid state for a few minutes to allow alloy homogenization and diffusion of hydrogen out of the sample (this was required to produce a pore-free specimen). Next, the specimen was cooled at a controlled rate of $-2.5\,^{\circ}\mathrm{C\,min^{-1}}$ while the microtomography experiment was carried out; this low cooling rate was necessary to ensure that the microstructure did not evolve too much during the image acquisition.

Next, the morphology of gas porosity was analyzed at high temperature (i) during isothermal holding at $g_s = 0.49$ and (ii) during a solidification experiment. First, the sample was heated (at $20\,^{\circ}\mathrm{C\,min^{-1}}$) up to 612 °C, temperature at which the sample was hold for 37 min, while the microtomography experiment was carried out; this sequence will be denoted *in-situ_B1* from now on. After this isothermal holding, the sample was cooled form 612 °C down to 540 °C at $-2.5\,^{\circ}\mathrm{C\,min^{-1}}$; this solidification sequence, during which X-ray tomography analysis was also performed, will be denoted *in-situ_B2* hereafter.

We have introduced in this chapter the methodology used to characterize our samples. Unlike liquid penetrant testing, optical and electronic microscopy that do not need further processing, X-ray tomography data does. Hence, the first part of next chapter is dedicated to image processing of X-ray tomography data in order to deduce important characteristics of microporosity. The second part of the chapter will then present the models that were developed, sometimes based on tomography data, in order to address porosity issues such as gas diffusion and curvature contribution.

Chapter 4

Data analysis and model developments

The purpose of this chapter is to detail the different modeling methods and post-processing techniques of the X-ray tomography data that have been developed or used in this study.

The first part is dedicated to X-ray tomography data analysis. We first show in section 4.1 how a 3D pore can be isolated in an X-ray tomography stack in order to: (i) describe the overall shape factor of a pore by calculating the moment of inertia tensor and its principal values, (ii) calculate the two principal curvatures at each point of the surface of the pore, and (iii) correlate the local mean curvature to the adjacent material. As the curvature calculations are quite sensitive to the method used, two different techniques are detailed and compared in sections 4.1.4.

The second part of this chapter is dedicated to modeling. We describe in section 4.2 how *in-situ* X-ray tomography data performed on Al-Cu alloys can be used in order to deduce an effective hydrogen diffusion coefficient D_e, that is function of the volume fraction of solid g_s only. This effective diffusion coefficient is then used in section 4.3 in a model for predicting porosity formation. This new model accounts for limited hydrogen diffusion in addition to the influence of curvature, as limiting factors to the growth of pores.

At a refined scale, both curvature and hydrogen diffusion are taken into account in a 2D phase-field model that describes the complex shape of a pore constrained to grow in a solid network. This model is described in section 4.4.

Finally, the description of the pipe shrinkage calculations are given in the end of this chapter.

4.1 Pore morphology and curvature analysis

An X-ray tomography stack is a file containing the information of the grey value (integer from 0 to 255) as a function of the pixel position (x, y, z). This grey value represents in fact the local absorption of a small voxel located at this position. As we saw in section 3.4, the absorption is function of the local density and atomic number of the elements present in the considered voxel. A typical 2D cross-section of such a stack is

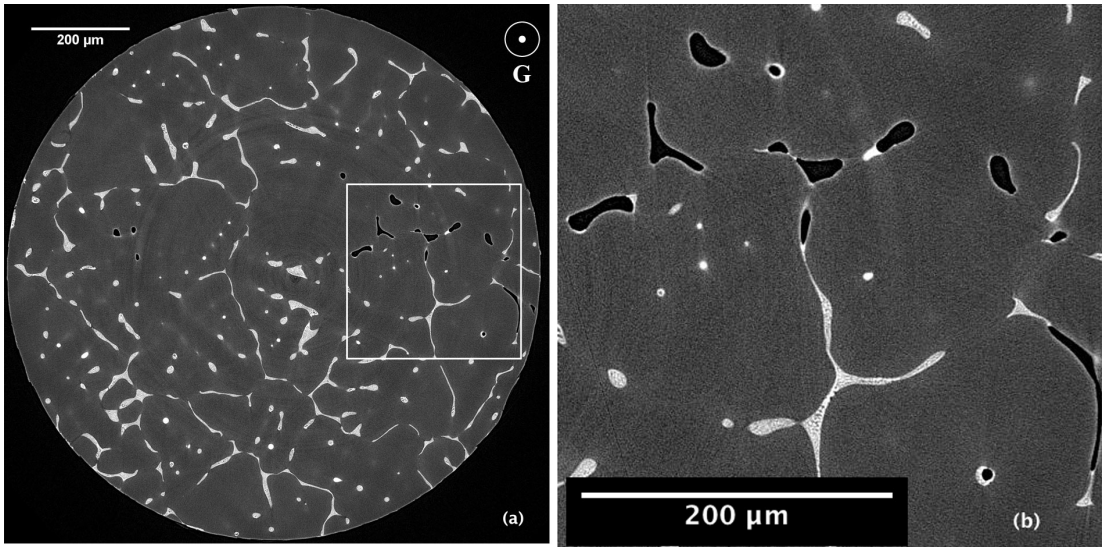

Figure 4.1: (a) Cross section of a typical Al-4.5wt%Cu sample observed by X-ray tomography (after reconstruction), with (b) an enlarged region. White regions correspond to the eutectic, dark grey regions to the Al-matrix and black regions to the pore phase. The thermal gradient G points out in the third dimension.

given in Fig. 4.1. In this reverse-contrast figure, black regions correspond to a local absorption close to 0, and thus represent the pore phase. White regions correspond to high absorption voxels, the Al-Al_2Cu eutectic in that case. Please note that the fine eutectic structure is barely resolved as seen in the enlarged view of Fig. 4.1b. Finally, the grey regions correspond to the Al-matrix phase in that case. Note that the thermal gradient G is perpendicular to the figure, i.e., parallel to the z axis (convention used throughout this work). To validate these assumptions, the different phases have been identified using electron microscopy and compared to the X-ray tomography data (see Fig. 4.2). Similar contrast are obtained using both techniques proving the ability of X-ray tomography to identify the different phases with their respective densities and atomic number. Looking at Fig. 4.1b, several isolated pores can be seen in this cross-section, but they are in fact interconnected in 3D. In order to have the three dimensional information on the pore phase, the stack of images is first binarized so that the grey Al matrix and the eutectic regions are turned white while the pore remains black. This *threshold* operation is a standard procedure which is implemented in the freeware ImageJ [94]. Next, a 3D median filter is applied on the volume in order to suppress isolated noise without blurring sharp edges. (Specifically, the median filter replaces a pixel by the median of all pixels in the neighborhood.) The result of such an operation is given in Fig. 4.3a. The volume fraction of the pore phase is now accessible by counting the number of black voxels in the whole sample and dividing this value by the total number of voxels. We have then:

$$g_p = \frac{\sum \text{pore voxels}}{\sum (\text{solid voxels} + \text{pore voxels})} \tag{4.1}$$

In order to visualize the shape of a pore in 3D, we either use *VTK/Paraview* (Paraview is the graphical user interface of the open-source visualization toolkit (VTK)

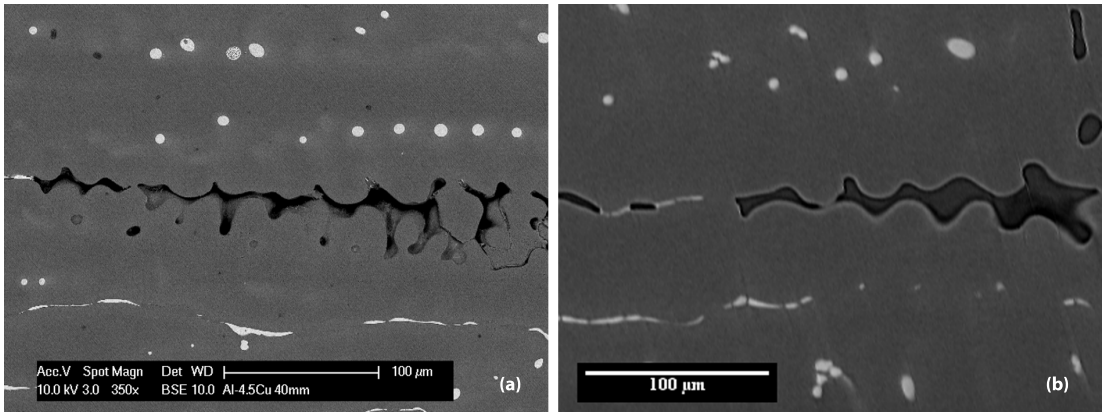

Figure 4.2: (a) Back-scattered electron microscopy image and (b) X-ray tomography cross-section of a pore constrained in a non inoculated Al-4.5wt%Cu matrix. The images come from the same sample but taken at locations that differ by about 1 mm. Using electron microscopy, the different phases were identified. As for image (b), black regions in image (a) correspond to the pore phase, white regions to the Al-Al_2Cu eutectic and grey regions to the Al-matrix phase.

program) or *Avizo* (Avizo is a registered trademark of Mercury Computer Systems, Chelmsford, Massachusetts). However, the surface has still a "stair-like" shape, which is inappropriate for further processing (like curvature calculations for instance). In order to produce a polygonal mesh from voxels, we use a conventional marching cubes filter, implemented in both software VTK and Avizo. A marching cubes filter is a com-

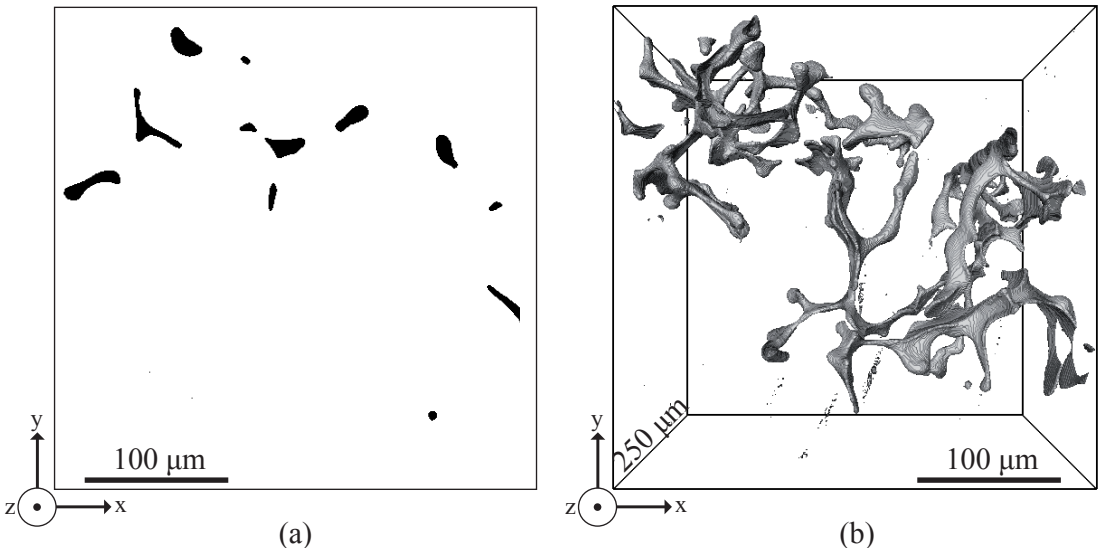

Figure 4.3: (a) Binarization of Fig. 4.1b to reveal the pore phase only (2D cross-section view). (b) 3D volume rendering of the pore phase.

puter graphics algorithm for extracting a polygonal mesh of an isosurface (produced by a threshold operation only) from a three-dimensional scalar field at voxel positions [95] (see Fig. 4.4). Using such a filter, Figure 4.3b can be obtained using either VTK or Avizo. Whereas Figure 4.3a is a 2D cross-section in the xy plane, Figure 4.3b is a

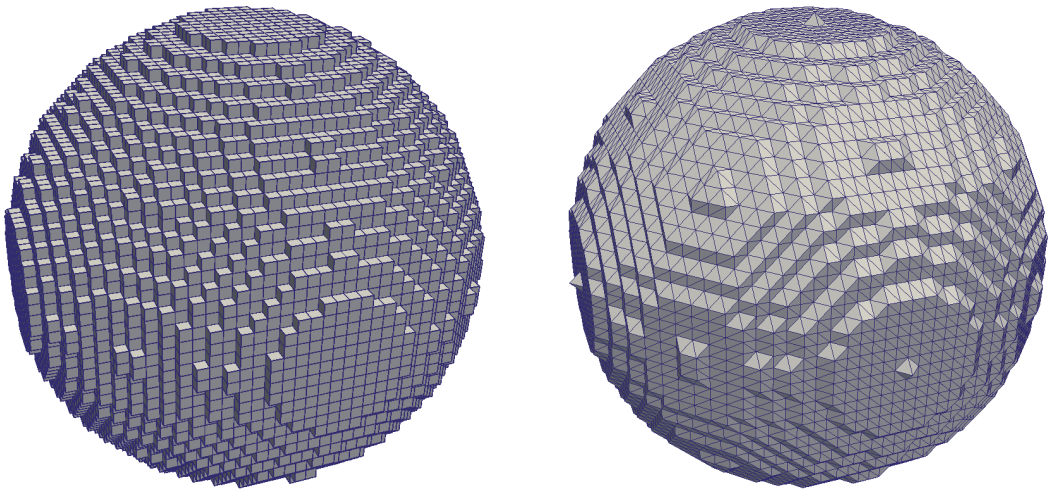

(a) (b)

Figure 4.4: 3D volume rendering of a sphere made of voxels. (a) Threshold representation: no filter has been used and the sphere is made of cubic voxels. (b) A marching cubes filter has been used, producing a sphere with its surface made of a polygonal mesh.

top view of the 3D volume rendering of the pore phase, showing the interconnectivity of the "isolated" pores of Fig. 4.3a.

To summarize, the image processing of the X-ray tomography data was performed as follows. First the 8-bit grey scale reconstructed volumes were cropped to a typical final size of minimum 50×10^6 voxels and then binarized in order to isolate the pore phase. A 3D median filter was then applied to reduce noise. The final result, called V_{init}, is now a set of $(N_x N_y N_z)$ binary values $\{I(x,y,z); I = 0,1; x = 1, N_x; y = 1, N_y; z = 1, N_z\}$.

Now that we have introduced how to obtain the 3D shape of a pore, let us see first how its shape can be characterized in terms of moments of inertia, and then how its principal curvature values can be extracted.

4.1.1 Pore morphology

In order to determine whether a pore is elongated or has rather an "equiaxed" shape, the moments of inertia tensor matrix, together with its principal directions, have been calculated. Following a method similar to that developed by Doube *et al.* [96], the moments of inertia tensor matrix (with a gravity center that coincides with the origin) for a pore made of N_k voxels is given by:

$$I \ [\mu\mathrm{m}^5] = \sum_{k=1}^{N_k} V_k \begin{pmatrix} {y_k}^2 + {z_k}^2 & -x_k y_k & -x_k z_k \\ & {x_k}^2 + {z_k}^2 & -y_k z_k \\ \text{sym} & & {x_k}^2 + {y_k}^2 \end{pmatrix} \tag{4.2}$$

where x_k, y_k, z_k and V_k are the x, y and z coordinates of the voxel k that has a volume V_k (z is parallel to the thermal gradient). This tensor has 3 eigenvectors with their 3 associated eigenvalues. Since the moments of inertia tensor is given in $\mu\mathrm{m}^5$, it has been

non-dimensionalized to give the tensor I^{ND}, by normalizing by the pore volume and by an average distance to its center. This ensures I^{ND} to be influenced by the pore shape only and not by its volume. In other words for a spherical body, I^{ND}_{zz} would be equal to:

$$\begin{aligned} I^{ND}_{zz} &= \frac{\sum_k (x_k^2 + y_k^2) \cdot V_k}{\sum_k (x_k^2 + y_k^2 + z_k^2) \cdot V_k} = \frac{\sum_k x_k^2 + y_k^2}{\sum_k x_k^2 + y_k^2 + z_k^2} \\ &\overset{\text{Sphere}}{=} \frac{\int_0^R \left(\int_0^{2\pi} \left(\int_0^{\pi} r^2 \sin^2\theta \; r^2 \sin\theta \; d\theta \right) \; d\phi \right) \; dr}{\int_0^R \left(\int_0^{2\pi} \left(\int_0^{\pi} r^2 \; r^2 \sin\theta \; d\theta \right) \; d\phi \right) \; dr} = \frac{\frac{8 \; \pi \; R^5}{15}}{\frac{4 \; \pi \; R^5}{5}} = \frac{2}{3} \end{aligned} \tag{4.3}$$

where r is the distance to the pore gravity center, ϕ the azimuthal angle, and θ the polar angle. Finally, the tensor I^{ND} has been multiplied by 3/2 in order to have 1 on the diagonal terms and zero for the off-diagonal terms for the case of a sphere.

It will be seen in section 5.1.1 that the principal moments of inertia are quite different for porosity formed in columnar or equiaxed Al-Cu alloys.

4.1.2 Curvature calculations

Consider any reference frame attached to the point p of a surface patch Σ such that: (i) the z axis coincides with the normal $\mathbf{n}$ to the surface and (ii) the x and y axes are in the tangent plane (see Fig. 4.5). The shape of the surface near p can be approximated locally by the following quadratic equation:

$$z(x, y) = ax^2 + by^2 + cxy + dx + ey + f \tag{4.4}$$

Since we have stated that $z = 0$ at $x = y = 0$, we have $f = 0$. On the other hand, we have:

$$\frac{\partial z}{\partial x}|_{x=y=0} = \frac{\partial z}{\partial y}|_{x=y=0} = 0 \rightarrow d = e = 0 \tag{4.5}$$

and the approximated surface can now be written as:

$$z(x, y) = ax^2 + by^2 + cxy \tag{4.6}$$

By making a rotation of an angle θ around the z axis such that:

$$\begin{aligned} x &= x' \cos\theta + y' \sin\theta \\ y &= -x' \sin\theta + y' \cos\theta \\ \text{with} \quad \tan 2\theta &= \frac{-c}{a - b} \end{aligned} \tag{4.7}$$

the surface approximation becomes then:

$$z(x', y') = a'x'^2 + b'y'^2 \tag{4.8}$$

The two directions x' and y' are the principal curvature directions and the two principal curvatures are given by [97]:

$$\begin{aligned} \kappa_1 &= \frac{\partial^2 z / \partial x^2}{\sqrt{(1 + (\partial z / \partial x)^2)^3}}|_{x=y=0} = 2a' \\ \kappa_2 &= \frac{\partial^2 z / \partial y^2}{\sqrt{(1 + (\partial z / \partial y)^2)^3}}|_{x=y=0} = 2b' \end{aligned} \tag{4.9}$$

Hence, in the coordinate system of the principal curvature vectors, a surface patch Σ near p can be approximated with a paraboloid given by [97]:

$$z = \frac{1}{2}(\kappa_1 x'^2 + \kappa_2 y'^2) \tag{4.10}$$

Note that if the signs of κ_1 and κ_2 are the same, the local surface is an elliptic

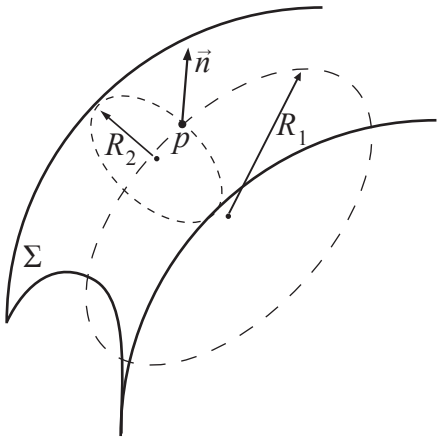

Figure 4.5: Schematic of a surface patch Σ. The two osculating circles in p have a radius R_1 (maximal radius of curvature in p) and R_2 (minimum radius of curvature in p). The normal $\mathbf{n}$ points outwards of the surface and is perpendicular to the tangent plane (which is not shown here) of Σ in p.

paraboloid (see Fig. 4.6a), whereas the surface is an hyperbolic paraboloid if the signs of the principal curvatures are different (see Fig. 4.6b).

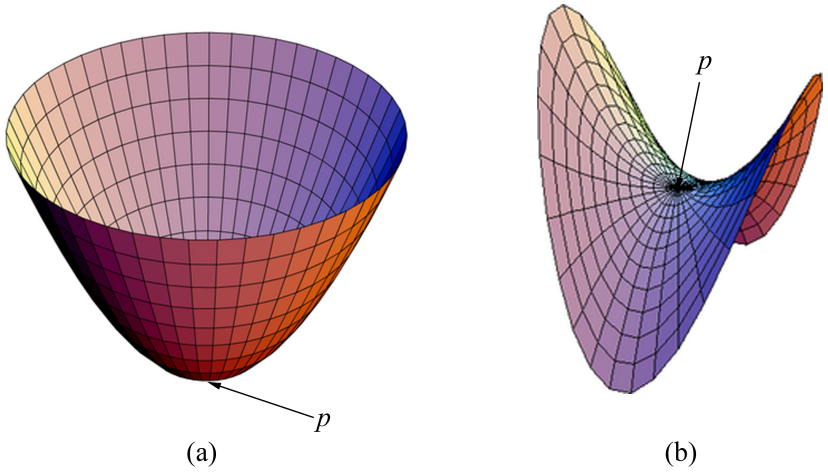

Figure 4.6: The local shape of a surface near a point p can be approximated either by (a) elliptic paraboloid or (b) hyperbolic paraboloid.

The product and the average of the two principal curvatures of the curvature tensor are two invariants and are equal to the Gauss curvature $\mathcal{G}$ and to the mean curvature $\bar{\kappa}$, respectively [97]:

$$\mathcal{G} = \kappa_1 \kappa_2 \tag{4.11}$$

$$\bar{\kappa} = \frac{1}{2}(\kappa_1 + \kappa_2) \tag{4.12}$$

This means that κ_1 and κ_2 can be deduced from both the Gauss and the mean curvatures via the following relationship.

$$\kappa_{2,1} = \bar{\kappa} \pm \sqrt{\bar{\kappa}^2 - \mathcal{G}} \tag{4.13}$$

In other words, if one finds a way of calculating $\bar{\kappa}$ and $\mathcal{G}$ at each point on the surface of a pore *independently* of κ_1 and κ_2, it is then possible to extract the principal curvatures at each point on its surface using Eq. 4.13.

We have described two different ways of finding κ_1 and κ_2 at each point on a surface:

- Approximate locally the surface by a paraboloid with Eq. 4.10,
- Calculate $\bar{\kappa}$ and $\mathcal{G}$ locally (independently of κ_1 and κ_2) and apply Eq. 4.13.

Because of the complexity of the pore-solid interface (see Fig. 4.3b), the curvature calculations were performed using these two different techniques. Let us describe them briefly.

Surface reconstruction algorithms such as a marching cubes filter produce a surface as a set of triangles in space as shown in Fig. 4.4b. This is a piecewise linear surface. The computation of curvatures theoretically requires a twice differentiable surface (see Eq. 4.9). We therefore need to modify either the surface or the curvature computations. Often, the first approach is used, i.e., a twice differentiable local patch is fitted around every vertex. This is the approach which is implemented in the software Avizo and described by Eq. 4.10.

The second approach, implemented in the software VTK, is much more efficient in terms of CPU time, but appears to be less accurate. In this approach, curvatures are calculated directly from the geometric data contained in the triangular mesh (see [98] for more details): both Gauss and mean curvatures are directly evaluated from the triangular mesh (i.e., without calculating κ_1 and κ_2). The Gauss curvature is obtained at a vertex by the angle defect (Descartes' theorem). Therefore, the Gauss curvature at vertex v is $\mathcal{G}(v) = 2\pi - \sum(\text{angles at } v)$ (see Fig. 4.7 for the definition of this angle for a simple pyramid).
To calculate the mean curvature $\bar{\kappa}$ at a vertex v, we average the mean curvature calculated at each edge e connected to v. The mean curvature $\bar{\kappa}$ can be approximated at an edge e by the product of the length with the dihedral angle at this edge. The dihedral angle is the oriented angle between the planes of the facets, and is calculated from the facet surface normals. The mean curvature at an edge is therefore given by $\bar{\kappa}(e) = \text{length}(e) \times$ dihedral angle at e, and divided by one third of the area of the

two adjacent facets[1]. The mean curvature at a *vertex* is then calculated by averaging the curvature along each edge connected to the vertex [98]. Once the mean curvature

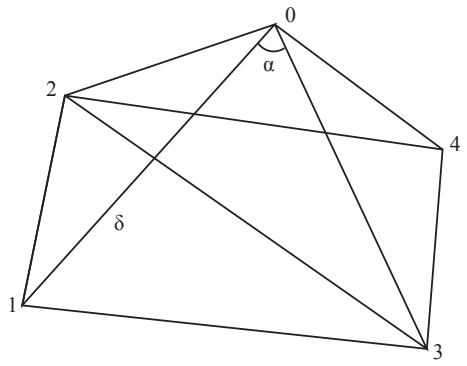

Figure 4.7: Example of the computation of curvatures for a simple square pyramid: the base $\{1, 2, 3, 4\}$ is a square of side 1, the vertex 0 is at height 0.5 above the center of the square, the area of the side triangle is $\sqrt{2}/4$, and the angle is here the same in every facet, i.e., $\alpha = 2 \arctan \sqrt{2}/2$, and thus $\mathcal{G} = 2\pi - 4\alpha$ (Descartes' theorem). On the other hand, the mean curvature at an edge is $(\sqrt{3}/2)(\pi/3)$, since the dihedral angle $\delta = \pi/3$.

$\bar{\kappa}$ and the Gauss curvature $\mathcal{G}$ are known at each vertex v, both principal curvatures κ_1 and κ_2 are calculated using Eq. 4.13. Note that an example of a script that calculates both principal curvatures using either Avizo or VTK is given in Appendix D and E, respectively.

After having calculated κ_1 and κ_2 at each point of the surface of the pore, the pairs of $(\kappa_1; \kappa_2)$ values are sorted as follows. Assume the voxel size is set at $0.74 \times 0.74 \times 0.74\,\mu\text{m}^3$, the pairs of $(\kappa_1; \kappa_2)$ that exhibit a local mean curvature higher than $\frac{1}{2 \cdot 0.74} \mu m^{-1}$ or less than $-\frac{1}{2 \cdot 0.74}\,\mu\text{m}^{-1}$ are excluded. As a rule of thumb indeed, the resolution is generally estimated as twice the camera pixel size. Then, each pair of $(\kappa_1; \kappa_2)$ is counted and set into classes of curvature in order to produce the Interfacial Shape Distribution (ISD) plots as described by Kammer *et al.* [99]. ISD are shown as contour plots of equal probability to find a pair of $(\kappa_1; \kappa_2)$. These contour plots are generated by 3D probability functions and both $\bar{\kappa}$ and $\mathcal{G}$ can be directly seen on the same graph, as schematized on Fig. 4.8. Note that the influence of the corresponding triangle surface has also been taken into account (the bigger the surface triangle, the more "weight" this pair of $(\kappa_1; \kappa_2)$ has in the statistics). Finally, the average values of κ_1, κ_2 and $\bar{\kappa}$ are calculated for all the $(\kappa_1; \kappa_1)$ pairs (denoted $\langle \kappa_1 \rangle_{tot}$, $\langle \kappa_2 \rangle_{tot}$, and $\langle \bar{\kappa} \rangle_{tot}$ hereafter) or only for $\kappa_1, \kappa_2 \geq 0$ (denoted $\langle \kappa_1 \rangle_{\geq 0}$, $\langle \kappa_2 \rangle_{\geq 0}$, and $\langle \bar{\kappa} \rangle_{\geq 0}$ hereafter).

[1]Picture an edge e is smoothed and replaced by a sector of cylinder; its cross section is thus an arc of circle with a small radius ε, a dihedral angle δ, and has a length l. The two principal curvatures of this sector of cylinder are 0 and $1/\varepsilon$. The mean curvature $\bar{\kappa} = \frac{1}{2 \cdot \varepsilon}$ is constant over this region and is thus integrated over the smoothed region. We thus get $Area \cdot \frac{1}{2 \cdot d\epsilon} = \frac{l \cdot \delta \cdot \varepsilon}{2 \cdot \varepsilon} = \frac{l \cdot \delta}{2}$, which is independent of ε. The value $\frac{l \cdot \delta}{2}$ is thus attributed to that edge and must now be normalized by the surface area. A facet is shared between 3 edges and each edge has two vertices. Thus the curvature along an edge is scaled by $\frac{3 \cdot 2}{A_f}$, with A_f being the total area of the neighboring triangles that have the common edge e (see [98] for more details).

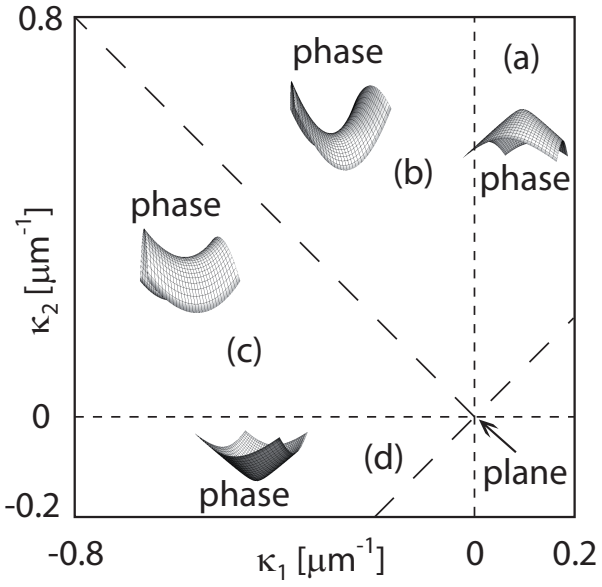

Figure 4.8: $\kappa_2 - \kappa_1$ graph used for representing the interfacial shape distribution (ISD) contour plot. Region (a) represents fully convex interfacial shapes, (b) and (c) saddle shapes with either $-\kappa_1 < \kappa_2$ or $-\kappa_1 > \kappa_2$, and (d) totally concave.

Now that we have seen how pore curvatures can be calculated, let us see how one can correlate the local mean curvature to the adjacent material.

4.1.3 Relationship between local mean curvature and adjacent material

The last liquid to solidify has the composition of the eutectic in most Al-Cu alloys. Because of the Laplace-Young law and considering the values of $\gamma_{s\ell}$, $\gamma_{\ell g}$, and γ_{sg}, the local pore mean curvature should be positive at each point where the pore is in contact with the last liquid to solidify, i.e., the eutectic. To assess this (non trivial) concept, the local grey value of the region next to the pore surface has been put in relationship with the local mean curvature of the pore. For that purpose, the coordinates of the surface of the pore contained in V_{init} has been extracted (white regions in Fig. 4.9b). Then, the eutectic present in V_{init} has been isolated (black regions in Fig. 4.9c). Knowing the coordinates of the pore surface, the average local grey value (in a small sphere of 5 voxels radius) has been evaluated (see Fig. 4.9c) for each coordinate of the pore surface. Then, knowing (i) the local mean curvature for each coordinate of the pore surface and (ii) the local average grey value for each coordinate of the pore surface, the local mean curvature could be put in direct relationship with the local average grey value. For that purpose, a java plug-in for *ImageJ* has been developed (see Appendix B for details).

Figure 4.9: (a) Initial volume. (b) Binarization to extract the pore phase coordinates, and calculations of the local mean curvature of the pore surface. (c) Binarization to extract the eutectic phase only. The local average grey value in a small sphere of 5 voxels radius is then calculated at each point on the pore surface.

4.1.4 Validation of curvature calculations

To validate our curvature calculation techniques, both methods implemented in Avizo and VTK are now compared. For that purpose, "spheres" (made of cubic voxels) with different radii R (with a mean curvature $\bar{\kappa}_{\text{ideal}} = R^{-1}$) have been created and the local mean curvature $\bar{\kappa}$ has been calculated at each point of the surface following the same procedure as described in section 4.1.2. Then, each mean curvature value of the surface falling between $\bar{\kappa} - 2.5 \times 10^{-3} \leq \bar{\kappa} \leq \bar{\kappa} + 2.5 \times 10^{-3}$ (in voxel^{-1} unit) has been counted in order to produce a probability density function (whose integral equals 1). The results for six different spheres radii are given in Fig. 4.10. Each graph corresponds to one sphere with a particular radius of 10, 20, 40, 80, 160, or 250 voxels and the dashed vertical line corresponds to the value of $\bar{\kappa}_{\text{ideal}}$. The thick black curve on each graph corresponds to the probability density function of curvatures calculated with the software VTK, whereas the thin dashed curve represent the probability density function of curvatures calculated with the software Avizo. Accordingly, in bold on the left and in regular typeface on the right hand side of each graph are given the average value $\langle\bar{\kappa}\rangle$ of the distribution together with its standard deviation σ. Finally, the full width of the distribution at half maximum value, or full-width half-maximum FWHM is given for each distribution. For that purpose, a gaussian fit (whose area still equals to 1) has been performed on each curve.

It is clear form Fig. 4.10 that curvatures are better estimated for large spheres, independently of the used software. We observe indeed that:

- $\langle\bar{\kappa}\rangle$ (as well as the mode of the distribution) gets nearer to $\bar{\kappa}_{\text{ideal}}$ as the sphere radius increases,
- The standard deviation decreases as the sphere radius increases,
- The full-width half-maximum value decreases as the sphere radius increases.

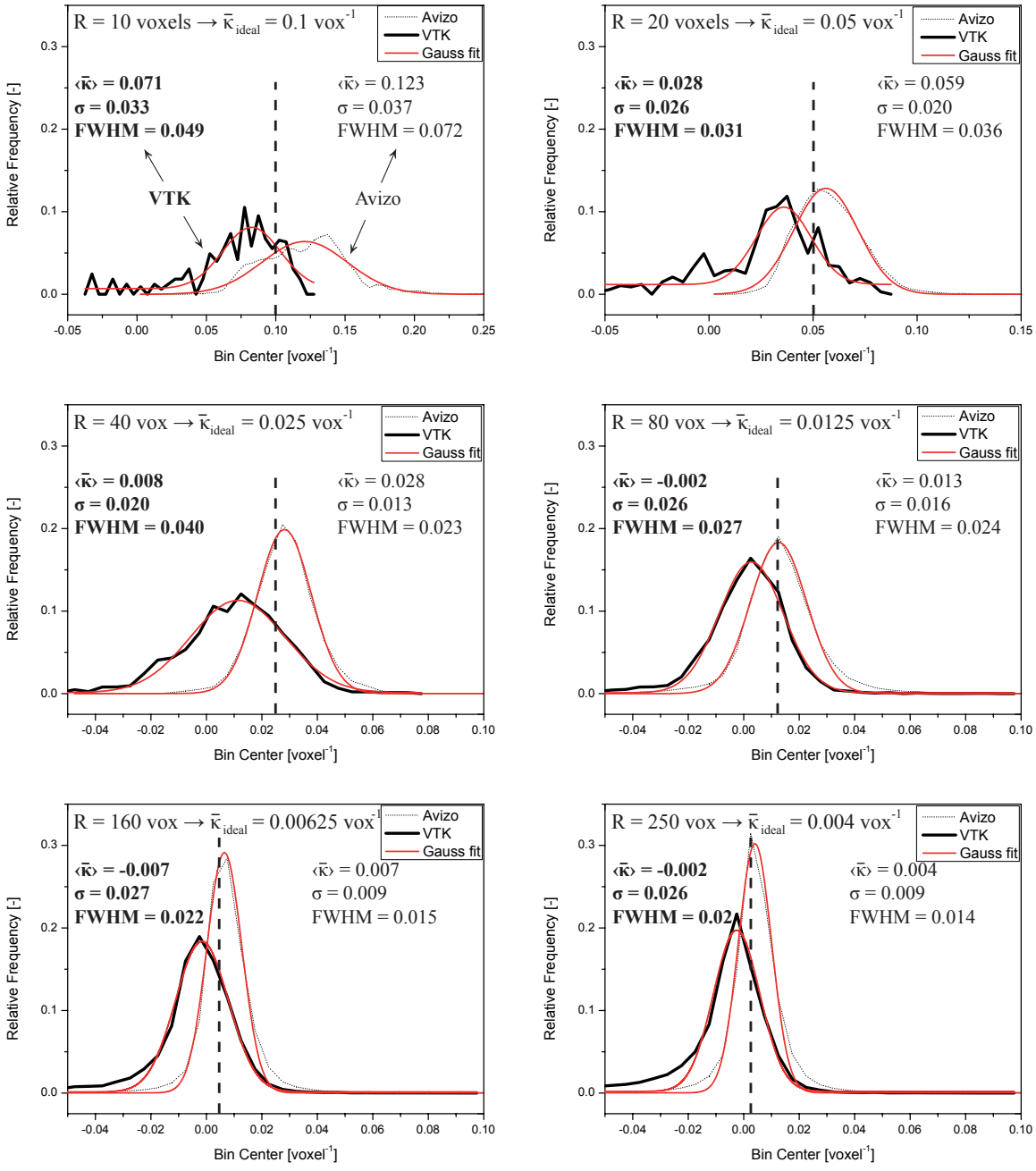

Figure 4.10: Mean curvature distribution of a spheres with different radii. Note the dashed line representing the theoretical mean curvature in each case.

All these observations are due to the fact that creating a sphere with voxels becomes a poor approximation as the sphere radius decreases, especially for spheres of small radii. On the other hand for larger spheres, the curvature calculations are fairly accurate, especially if one uses the Avizo software. There are two reasons for that: (i) the interface between white and black voxels is much better approximated with Avizo than with VTK (producing a "good" surface is actually the key for curvature calculations) and (ii) the curvature calculation method implemented in Avizo (based on a local paraboloid approximation of the surface shape) is more accurate and more direct as compared with the angle defect approximation perfomed in VTK. This is why the Avizo method will be used preferably in this study. Nevertheless, pore curvature results calculated with both methods will also be presented to show that similar results are achieved.

We have presented all the useful tools for the post-processing of X-ray tomography data. Let us now describe how these data can be used in order to improve the modeling and understanding of porosity formation.

4.2 Effective hydrogen diffusion coefficient

The purpose of this section is to describe how an effective hydrogen diffusion coefficient, that is function of g_s only, can be calculated based on *in-situ* X-ray tomography data. This diffusion coefficient will then be used in the next section in order to develop a new model for pore growth influenced by hydrogen diffusion.
To deduce this effective hydrogen diffusion coefficient, *in-situ* X-ray tomography has been performed at the European Radiation Synchrotron Facility (ESRF) in Grenoble (France) on Al-4.5wt%Cu and Al-10wt%Cu samples (see the experiment *in-situ_A* described in section 3.4.2).
From the reconstructed 3D stack of images acquired at different temperatures, a pore-free RVE has been isolated in which the solid and the liquid have been extracted. The phase number ψ was set to $\psi = 1$ if the voxel is solid and $\psi = 0$ if it is liquid. Figure 4.11a shows the volume rendering of a reconstructed Al-10wt%Cu alloy with $g_s = 0.8$. From this reconstructed volume, an RVE of $200 \times 200 \times 200$ voxels has been extracted (see Fig. 4.11b) and binarized. We have defined then a realistic "mesh" of finite volumes corresponding to the voxels of the X-ray tomography data. Based on this "mesh", a time-explicit finite volume element method has been used to solve the hydrogen diffusion equation (see Eq. 2.45), from which an *effective diffusion coefficient* D_e function of the solid fraction only has been extracted. This procedure has been applied on two different samples (Al-4.5wt%Cu and Al-10wt%Cu) for each solid fraction $0.6 \leq g_s \leq 0.9$.
Let us see now in details how the calculations were performed.

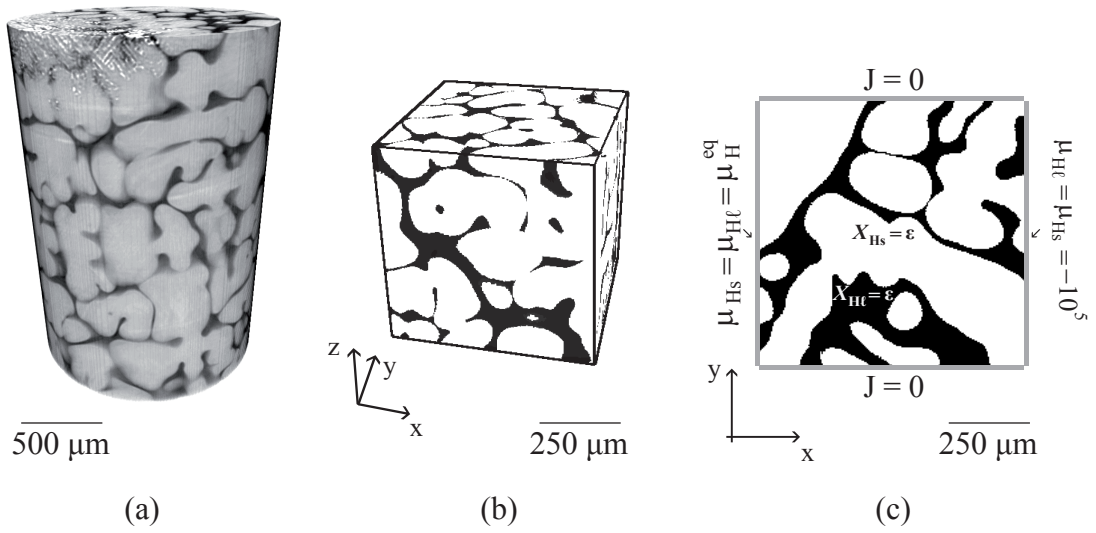

Figure 4.11: (a) 3D volume rendering of a reconstructed solidifying Al-10wt%Cu sample ($g_s = 0.8$). (b) Representative volume element (RVE). Solid regions are white ($\psi = 1$), whereas black represents liquid regions ($\psi = 0$). (c) 2D cross-section with the applied boundary conditions.

4.2.1 Discretization

Let us first recall the time-explicit equation that must be solved (Eq. 2.45):

$$\frac{\partial X_A}{\partial t} = -\nabla \cdot \boldsymbol{J}_A = \nabla \cdot (M_A X_A \nabla \mu_A) \tag{4.14}$$

We saw in section 2.4.1 that Qiu *et al.* [37] assessed the thermodynamic properties of the Al-H system using a regular solution as described by Eq. 2.16 for the liquid and solid phases. This will be used in order to have a direct relationship between X_H and μ_H in both phases (which is required in order to solve the above equation). For a regular solution, we have indeed the following relationship (for the liquid phase) [38]:

$$\mu_{H\ell} = G^o_{H\ell} + \Omega_\ell (1 - X_{H\ell})^2 + \mathcal{R}T \ln X_{H\ell} \tag{4.15}$$

Unfortunately, the same procedure cannot be applied to the solid mixture, because G^o_{Hs} is unknown. However, the Gibb's free energy curve of the solid mixture G^m_s is known from [37]. As shown in Fig. 4.12, it is possible to extrapolate μ_{Hs} (at $X_H = 1$). Estimating the slope of G^m_s by a small variation ΔX_H, μ_{Hs} can be calculated from the following equation:

$$\frac{\partial G^m_s}{\partial X_H} \approx \frac{\Delta G^m_s}{\Delta X_H} = \frac{\mu_{Hs} - G^m_s(X_H)}{1 - X_H} \tag{4.16}$$

Therefore, $\mu_{H\ell}(X_H)$ being given by Eq. 4.15 and $\mu_{Hs}(X_H)$ by Eq. 4.16, both hydrogen chemical potentials as a function of the composition X_H are known.

The mobility and composition in the solid and liquid phases being known from the diffusion coefficient and the phase diagram, the average values at the interfacial cells must be estimated. They have to be calculated along each direction in order to take them out of the divergence term. Equation 2.45 can be rewritten as follows (note that

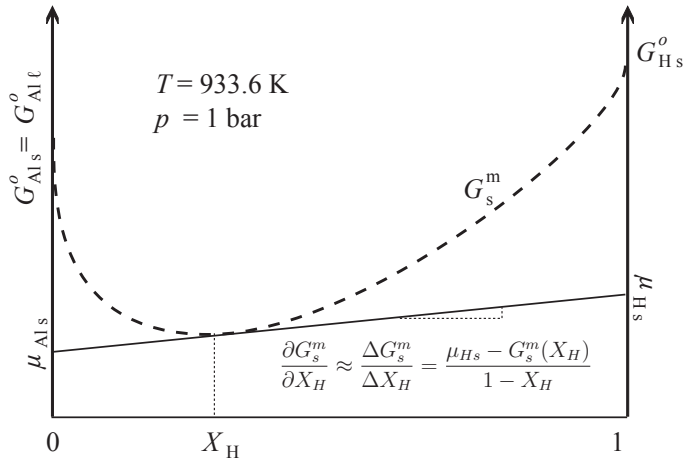

Figure 4.12: Graphical representation of the thermodynamic equilibrium.

in the next equations, because each quantity X_A, M_A, μ_A, $\boldsymbol{J}_A$ refers to hydrogen, the subscript H has been omitted).

$$\frac{\partial X}{\partial t} = -\nabla \cdot \boldsymbol{J} = \overline{M}\ \overline{X}\nabla^2\mu \tag{4.17}$$

where $\overline{M}$ and $\overline{X}$ are the mean "conductance" (mobility in fact) and composition of hydrogen along each direction, respectively[2]. Between a node j and a node $j+1$ (East to node j) for example, the mean composition X^j_E is then given by:

$$\overline{X}^j_E = \frac{X^j + X^{j+1}}{2} \tag{4.18}$$

The mobility can be related to the "conductance" of the solvant (aluminum) for the diffusing species (hydrogen). As the conductances are connected in series, the resulting average mobility between two nodes is given by:

$$\overline{M}^j_E = 2\frac{M^j M^{j+1}}{M^j + M^{j+1}} \tag{4.19}$$

For every node, the mobility is calculated only once via Eq. 4.19 (in each direction) since the microstructure is fixed. From now on, the hydrogen flux (to the East for example) can be calculated as in Eq. 2.44:

$$\boldsymbol{J}^j_E = -\ \overline{M}^j_E \cdot \overline{X}^j_E \cdot \left(\frac{\mu^{j+1} - \mu^j}{d}\right) \tag{4.20}$$

where d is the mesh size ($= 2.8\,\mu$m). The hydrogen fluxes in the 6 directions (*East*, *West*, *North*, *South*, *Front*, and *Back*, denoted *E, W, N, S, F, B* hereafter) around node j are calculated similarly, and the new hydrogen composition at the next time step is obtained via the following explicit time-discretization scheme:

$$X^j(t + \Delta t) = X^j(t) - \frac{\Delta t}{d}\left(J^j_E(t) - J^j_W(t) + J^j_N(t) - J^j_S(t) + J^j_F(t) - J^j_B(t)\right) \tag{4.21}$$

[2] Rigorously, Eq. 4.17 gives: $\partial X/\partial t = MX\nabla^2\mu + \nabla\mu \cdot \nabla(MX)$. However, the only nodes where the second term is important are those located at the solid-liquid interface (a low number compared to the whole volume). Tests have shown that using equation 4.17 as given here gives is appropriate.

The algorithm can thus be summarized as follows:

1– Calculate the mean mobility at each node in every direction using Eq. 4.19,

2– Calculate the chemical potential at each node using Eqs. 4.15 and 4.16 for all the nodes,

3– Calculate the mean composition at each node in every direction using Eq. 4.18,

4– Calculate the flux at each node in every direction using Eq. 4.20,

5– Calculate the new composition at each node using Eq. 4.21,

6– Restart at step 2 until the end of the time steps (typically when steady-state is reached).

Equation 4.21 is typical of an explicit time-discretization scheme. It is easy to program it, but not very efficient in terms of CPU time. A more elegant way to calculate the steady-state would be to use an implicit time-discretization scheme. But then, it would be required to invert a $200 \times 200 \times 200$ matrix at each time step, which is a rather complicated and time consuming operation. For simplicity, we decided to use Eq. 4.21.

4.2.2 Boundary conditions

Since the $560 \times 560 \times 560$ μm^3 volume is supposed to be a representative volume element of the solidifying microstructure, a zero flux condition is applied on the *Front*, *Back*, *North*, and *South* frontiers of the volume. Dirichlet boundary conditions are then considered for the *West* and *East* frontiers (see Fig. 4.11):

- $\mu_W^s = \mu_W^\ell = \mu^{eq}$, where μ^{eq} corresponds to the equilibrium chemical potential of hydrogen at 933.6 K and 1 bar,
- $\mu_E^s = \mu_E^\ell = -10^5\,[\mathrm{J\,mol^{-1}}]$

Even if REVs are for different solid fractions, i.e., at different temperatures for Al-Cu alloys, the temperature and the pressure of the system are supposed to remain fixed at 933.6 K and 1 bar, respectively. Then, only the influence of the microstructure is taken into account, and the solid and liquid solubilities are considered unaffected by the temperature. Note also that the curvature influence on hydrogen solubility has been neglected (in both phases), since the voxel size of the X-ray tomography data was set at 2.8 μm/pixel (the curvature influences the solubility limit for nanoscale structures only). The chemical potential at the *East* frontier of the domain corresponds to a very low composition of $\varepsilon = 10^{-10}$ [-] in the solid and $\varepsilon = 10^{-10}/k_{0H}$ [-] in the liquid, where k_{0H} is the partition coefficient of hydrogen in aluminium. Finally, the initial conditions are fixed as follows: the composition is set to $\varepsilon = 10^{-10}$ [-] everywhere in the RVE except at the *East* and *West* frontiers.

These developments will allow us to deduce an effective diffusion coefficient D_e (function of g_s only), that will be normalized by the liquid diffusion coefficient D_ℓ for convenience.

4.2.3 Effective medium approximations

In the diffusion process and under steady state conditions, the activity a or the chemical potential μ of each component at an interface in the system must be equal in the two phases [38]. Using Fick's first law in each phase separately (which is valid as long as one phase only is considered), but replacing the composition by the chemical activity and assuming Henry's law, we can introduce a quantity $\mathfrak{D}_\nu = \frac{D_\nu}{f_\nu}$ ($\nu = s$ or ℓ) in both the solid and liquid phases so that:

$$\boldsymbol{J}_\nu = -D_\nu \nabla X_\nu = -D_\nu \nabla \left(\frac{a_\nu}{f_\nu}\right) \overset{\text{Henry}}{\cong} -\frac{D_\nu}{f_\nu} \nabla a_\nu = -\mathfrak{D}_\nu \nabla a_\nu \tag{4.22}$$

where $f_\nu = a_\nu / X_\nu$ is the chemical activity coefficient of hydrogen in the phase ν. Note that we have omitted the subscript H, since each parameter refers to hydrogen only. $\mathfrak{D}_\nu$ is sometimes called the "phase contrast" of the phase ν and represents in this case the ability of the phase to transport hydrogen. We see that not only the diffusion coefficient, but also the solubility must be taken into account if one wants to derive effective properties for the diffusion in a multiphase material.

Now that we have a linear relationship between the flux $\boldsymbol{J}_\nu$ and the gradient of a continuous quantity across the interface (the activity a_ν), which is a necessary condition, we can use common models for establishing effective properties of heterogeneous media, e.g. $\mathfrak{D}_{eff}$ in section 2.7.2, in order to derive the flux not only in each phase separately, but in the entire two-phase system. We will then use the fact that there is a linear relationship between the overall flux of atoms and the gradient of activity in order to deduce an effective diffusion coefficient D_e, assuming that we have an overall linear relationship between the flux and the composition, so that $\boldsymbol{J} = -D_e \nabla \langle X \rangle$, where $\langle X \rangle = g_s X_s + g_\ell X_\ell$. In other words, we have:

$$\boldsymbol{J} = -\mathfrak{D}_{eff} \nabla a = -D_e \nabla \langle X \rangle \tag{4.23}$$

Note that we have *assumed* that $\boldsymbol{J} = -D_e \nabla \langle X \rangle$. The justification will be given in section 5.2.
The relationship between the activity and the composition is given by:

$$\nabla \langle X \rangle = \nabla \left(\frac{\langle a \rangle}{\langle f \rangle}\right) \overset{\text{Henry}}{\cong} \frac{1}{\langle f \rangle} \nabla a = \left(\frac{g_s}{f_s} + \frac{g_\ell}{f_\ell}\right) \nabla a \tag{4.24}$$

since we have:

$$\langle X \rangle = X_s g_s + X_\ell g_\ell = \frac{a_s}{f_s} g_s + \frac{a_\ell}{f_\ell} g_\ell = a \left(\frac{g_s}{f_s} + \frac{g_\ell}{f_\ell}\right) \tag{4.25}$$

and we have thus:

$$D_e = \mathfrak{D}_{eff} \cdot \frac{\nabla a}{\nabla \langle X \rangle} = \mathfrak{D}_{eff} \left(\frac{g_s}{f_s} + \frac{g_\ell}{f_\ell}\right)^{-1} \tag{4.26}$$

Three ways of calculating $\mathfrak{D}_{eff}$ were described in section 2.7.2 and we will use these different effective medium approximations, described by Eqs. 2.46 to 2.48, to deduce an effective diffusion coefficient D_e function of the solid fraction g_s only, and compare them with the simulation results. Note that the percolating phase being always the

liquid one, the latter will be considered as the matrix phase. On the other hand, as the liquid has larger inclusions of solid as g_s increases, the solid phase will be treated as phase 2, as described in section 2.7.2. The best approximation of this effective diffusion coefficient will then be used in order to derive a new gas species conservation equation for a model of the growth of pores limited by hydrogen diffusion.

4.3 Hydrogen diffusion modeling

4.3.1 Model

Assume that we have an effective hydrogen diffusion coefficient, that is function of the volume fraction of solid g_s only. We will now see how pore growth can be influenced by hydrogen diffusion in a supersaturated mushy zone. To construct a simple model, we replace the tortuous morphology of the pore by a sphere, i.e., the pore has an equivalent spherical radius R_p^{sph}. This is valid as long as the actual extension of the tortuous pore is much smaller than the distance between two pores, i.e., $R_p^{sph}/R_{p0} \ll 1$. R_p^{sph} is the equivalent radius of the pore, i.e., $\frac{4}{3}\pi(R_p^{sph})^3 = V_p$, where V_p is the volume of a pore and R_{p0} is the size of the domain associated with a pore, i.e., $\frac{4}{3}\pi R_{p0}^3 = \mathcal{N}_p^{-1}$, where $\mathcal{N}_p$ is the pore density (see Fig. 4.13). Assuming spherical diffusion, the diffusion equation

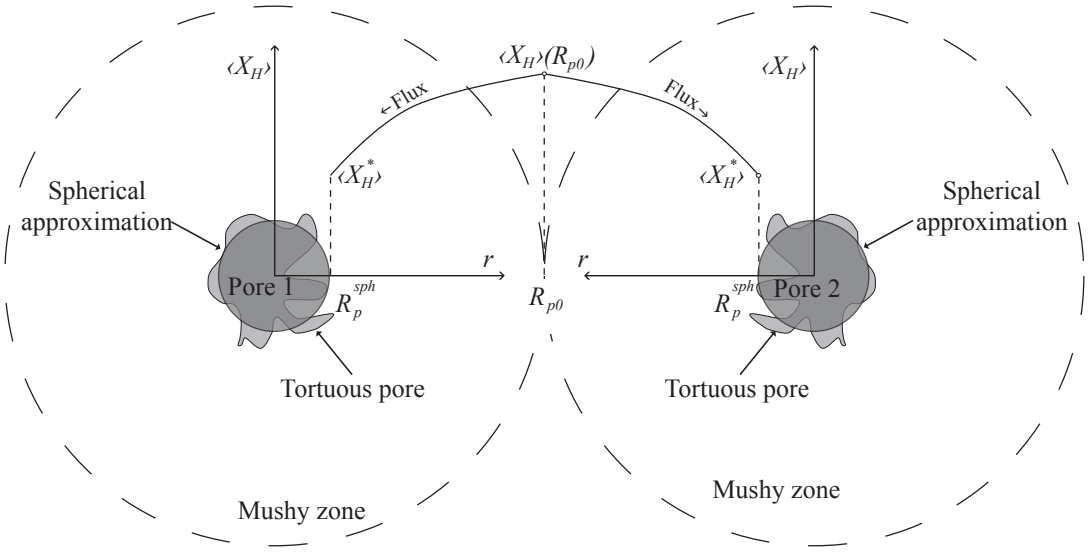

Figure 4.13: Schematic profile of hydrogen during pore growth.

can be written in terms of the radial coordinate r only:

$$\frac{\partial \langle X_H \rangle}{\partial t} = D_e \left(\frac{\partial^2 \langle X_H \rangle}{\partial r^2} + \frac{2}{r} \frac{\partial \langle X_H \rangle}{\partial r} \right) \tag{4.27}$$

where $\langle X_H \rangle$ is the local average hydrogen composition:

$$\langle X_H \rangle = X_{H\ell} g_\ell + X_{Hs} g_s = X_{H\ell}(1 - g_s + k_{0H} g_s) \tag{4.28}$$

As for the determination of the hydrogen diffusion coefficient, we use the hydrogen molar fraction and the fact that $\boldsymbol{J}_H = -D_e \nabla \langle X_H \rangle$ (see Eq. 4.23). Please note that there is no source term on the right hand side of Eq. 4.27 as would be the case if only diffusion in the liquid would be considered. Indeed we treat the mush as an effective medium in which the local average hydrogen composition is $\langle X_H \rangle$, and whose effective hydrogen diffusion coefficient is $D_e(g_s)$.
This problem is in fact very similar to the solidification of a sphere in an undercooled melt: the hydrogen pressure inside the pore is nearly constant if one neglects curvature (as the temperature inside a solid sphere which is growing in an undercooled melt is constant and uniform under the same assumption) and the growth is governed by the flux (of hydrogen or heat, respectively). We know that in the case of a solidifying sphere in an undercooled melt, the temperature distribution in the melt can be approximated by the steady-state solution of the diffusion equation only if the interface moves slowly in comparison with the diffusion of heat [33]. This means that the characteristic time for diffusion needs to be much smaller than the characteristic time for the velocity of the interface. The proof of that assumption can be found in Appendix C, where we have non-dimensionalized the following equations to show that the velocity of the pore surface is slow compared to the diffusion of hydrogen, with the only assumption that $R_p^{sph}/R_{p0} \ll 1$ (note that this assumption was already made in the first paragraph of this section).

Assuming that the diffusion in the sphere of radius R_{p0} can be approximated by the steady-state solution, one has in spherical coordinates:

$$\frac{1}{r^2}\frac{\partial}{\partial r}\left(r^2 \frac{\partial \langle X_H \rangle}{\partial r}\right) = 0 \tag{4.29}$$

The solution of this equation is given by:

$$\langle X_H \rangle(r) = \frac{A}{r} + B \tag{4.30}$$

Two conditions are required to determine the constants A and B. The first one is provided by the interfacial composition $\langle X_H \rangle(r = R_p^{sph}) = \langle X_H^* \rangle$ obtained from Sievert's law (see Eq. 2.23), corrected by the pore curvature if needed. For the second condition, one could impose $\langle X_H \rangle(r = R_{p0}) = \langle X_{H0} \rangle$, the initial hydrogen content of the alloy. If this condition might be valid at the nucleation of the pore, this is no longer the case during growth as the overall mixture composition must decrease. Instead, the second condition is replaced by an integral hydrogen balance over the entire domain (see below). This procedure also corrects the fact that the hydrogen flux at $r = R_{p0}$ is not zero when using the steady state solution.

The amount of hydrogen that diffuses into the pore per unit time can be calculated by multiplying the molar flux by the surface area of the pore. Obviously, the hydrogen content at the surface of the pore must be less than $\langle X_{H0} \rangle$, so that a concentration gradient is established (see Fig. 4.13). The latter is the driving force for hydrogen diffusion from the mush to the pore. Neglecting the transport of hydrogen by liquid advection during pore growth, the variation in the sphere of radius R_{p0} of dissolved

hydrogen in the mush (= solid + liquid, domain $[R_p^{sph}, R_{p0}]$) is equal to the increase of hydrogen in the pore. In other terms, we must conserve hydrogen in the sphere of radius R_{p0} at all time:

$$\frac{\partial}{\partial t}\int_{R_p^{sph}(t)}^{R_{p0}} \langle\rho\rangle \frac{\langle X_H\rangle}{\mathcal{M}_{Al}} 4\pi r^2 dr = \frac{\partial}{\partial t}\left(\frac{4}{3}\pi (R_p^{sph})^3 \frac{2p_g}{\mathcal{R}T}\right) \tag{4.31}$$

where $\langle\rho\rangle = \rho_\ell g_\ell + \rho_s g_s$. Neglecting temperature variation and using the composition profile given by Eq. 4.30:

$$\frac{\partial}{\partial t}\int_{R_p^{sph}(t)}^{R_{p0}} \langle\rho\rangle \left(\frac{A}{r}+B\right)\frac{4\pi}{\mathcal{M}_{Al}} r^2 dr = \underbrace{\frac{8\pi}{3\mathcal{R}T}\left(3(R_p^{sph})^2\, p_g\, \frac{\partial R_p^{sph}}{\partial t} + (R_p^{sph})^3\, \frac{\partial p_g}{\partial t}\right)}_{RHS} \tag{4.32}$$

with the two "constants" given by:

$$\langle X_H\rangle(R_{p0}) = \frac{A}{R_{p0}} + B \qquad \langle X_H^*\rangle = \frac{A}{R_p^{sph}} + B \tag{4.33}$$

On the other hand, we have the mechanical equilibrium of the pore given by Eq. 2.33, together with the equilibrium of the chemical potential at the pore interface given by Eq. 2.23. Finally, the variation of hydrogen entering the pore (= RHS in Eq. 4.32) is given by Fick's first law. Neglecting temperature variation, we have then:

$$RHS = D_e \frac{\rho}{\mathcal{M}_{Al}} \nabla\langle X_H\rangle \times 4\pi (R_p^{sph})^2 = -D_e \frac{\rho}{\mathcal{M}_{Al}} \frac{A}{(R_p^{sph})^2} 4\pi (R_p^{sph})^2 = -4\pi \frac{\rho}{\mathcal{M}_{Al}} A D_e \tag{4.34}$$

As already explained, the two "constants" A and B are function of (i) the pore radius R_p^{sph}, (ii) the hydrogen composition in the liquid at the interface $\langle X_H^*\rangle$, and (iii) the hydrogen concentration $\langle X_H\rangle(R_{p0}) \neq \langle X_{H0}\rangle$. We will see in the next section how this problem can be solved using an integral hydrogen balance over the entire domain.

4.3.2 Implementation

We consider the solidification of an Al-7wt%Si alloy following a Scheil behavior (see Eq. 2.2). This alloy has a certain initial hydrogen composition in the liquid $\langle X_{H0}\rangle$. We know that a certain supersaturation of hydrogen in the liquid is required so that a pore nucleates in this phase (see Eq. 2.35) and we set the critical nucleation radius equal to 10 μm. To determine the gas concentration profile in the liquid phase – given by the two "constants" A and B in Eq. 4.30 – we first calculate the gas partial pressure at the current step from the pore mechanical equilibrium equation. However, as the pore curvature radius at the current step t is unknown, we will assume it is equal to the pore curvature radius at the previous step $t - \Delta t$:

$$p_g(t) \cong p_\ell(t) + \frac{2\gamma_{\ell g}}{R_p^{sph}(t-\Delta t)} \tag{4.35}$$

From Sievert's law (see Eq. 2.23), we can deduce the gas molar concentration in the liquid at the interface with the pore at the current step t.

$$X^*_{H\ell}(t) \propto \sqrt{\frac{p_g(t)}{p_0}} \tag{4.36}$$

where the proportionality constant can be deduced from Eq. 2.23. From the perfect gas law, we can determine the mole number of gas in the pore of volume V_p at the previous step $t - \Delta t$.

$$n_p(t - \Delta t) = \frac{2p_g(t - \Delta t)V_p(t - \Delta t)}{\mathcal{R}T} \tag{4.37}$$

From the latter, the number of moles of hydrogen in the solid-liquid mixture at the previous step $n_{\text{mush}}(t - \Delta t)$ can be deduced.

$$n_{\text{mush}}(t - \Delta t) = n_{p0} - n_p(t - \Delta t) \tag{4.38}$$

where n_{p0} is the initial number of moles of hydrogen in the sphere of radius R_{p0}. $n_{\text{mush}}(t - \Delta t)$ is also equal to the integration of the hydrogen profile in the domain $[R_p^{sph}, R_{p0}]$. From the following spherical integration of the concentration profile:

$$\int_{R_p^{sph}(t)}^{R_{p0}} \langle\rho\rangle \left(\frac{A}{r} + B\right) \frac{4\pi}{\mathcal{M}_{Al}} r^2 dr = n_{\text{mush}} \tag{4.39}$$

and the boundary condition:

$$B = \langle X^*_H \rangle - \frac{A}{R_p^{sph}(t - \Delta t)} \tag{4.40}$$

we can deduce A:

$$A = \frac{-3n_{\text{mush}}\mathcal{M}_{Al}R_p^{sph} + 4\pi R_p^{sph}\left(-(R_p^{sph})^3 + R_{p0}^3\right)\langle X^*_H\rangle\langle\rho\rangle}{2\pi(R_p^{sph} - R_{p0})^2(R_p^{sph} + 2R_{p0})\langle\rho\rangle} \tag{4.41}$$

where R_p^{sph} is the radius at the previous step ($R_p^{sph}(t - \Delta t)$), $\langle X^*_H\rangle$ the gas molar concentration at the interface deduced from Eqs. 4.28 and 4.36, and n_{mush} the number of moles of hydrogen in the mush deduced from Eq. 4.38.

Now that the hydrogen profile in the mush is known, we can determine the porosity fraction at the current step. One can indeed determine the number of moles of hydrogen passing from the liquid to the pore using Eq. 4.34. Combining the latter equation with the perfect gas law and assuming the pore is not constrained by the solid phase, the pore volume increment during Δt can be evaluated and the pore radius at the current step $R_p^{sph}(t)$ is known. The latter multiplied by the pore density $\mathcal{N}_p$ gives then the pore volume fraction at the current step t. Part the C++ code developed to calculate both A and B coefficients (as well as g_p and R_p^{sph}) is given in Appendix F.

The shape of the pore was prescribed until now, either as a sphere or as an entity whose curvature is given by the remaining space. Let us see then how the phase-field method can be applied to the liquid-gas system in order to derive the complex equilibrium shape of a pore constrained by a solid network.

4.4 Equilibrium shape of a pore using the phase-field method

A 2D phase-field model has been developed in order to describe the equilibrium shape of a pore forming within interdendritic liquid channels [7]. The problem is solved in a domain that is representative of a small section of an interdendritic liquid channel. In this preliminary approach, only the evolution of the liquid-gas interface is considered. The influence of the solid, which can force the pore to adopt a non-spherical shape, is taken into account through the geometry of the calculation domain and the boundary conditions, considering that the exterior of the domain corresponds to solidified regions. The evolution of the liquid-gas interface is described with a phase equation using a similar approach as in solidification phase-field models [66]. The major difference lies in the driving force, which is given here by the pressure difference between the interior of the pore and the surrounding liquid indeed. In conventional solidification models, the driving force for solidification is given by the change in free energy between the liquid and solid phases. By analogy, we saw that this driving force is translated in the liquid-gas system by the pressure difference between the liquid and the pore (see Eq. 2.38). Conventional phase-field models use the following equation to describe the shape of a solid nucleus [66]:

$$\frac{\dot{\psi}}{\mu_{s\ell}} = \gamma_{s\ell}\left(\nabla^2\psi - \frac{\psi\left(1-\psi\right)\left(1-2\psi\right)}{\delta^2}\right) - \frac{5\psi^2\left(1-\psi\right)^2}{\delta} \times \underbrace{\Delta G_{s\ell}}_{\text{driving force}} \tag{4.42}$$

with $\psi = 1$ is the liquid and $\psi = 0$ is the solid. $\mu_{s\ell}$ is the mobility of the solid-liquid interface, $\gamma_{s\ell}$ the interfacial energy, δ the thickness of the diffuse solid-liquid interface and $\Delta G_{s\ell}$ is the volumetric Gibbs free energy difference between the solid and liquid phases, i.e., $\Delta G_{s\ell} = (\rho L_f / T_f)\Delta T$, where ΔT is the undercooling, T_f the melting point, and L_f the latent heat.

In the following developments, we replace the driving force by the pressure dependance term:

$$\frac{\dot{\psi}}{\mu_{\ell g}} = \gamma_{\ell g}\left(\nabla^2\psi - \frac{\psi\left(1-\psi\right)\left(1-2\psi\right)}{\delta^2}\right) - \frac{5\psi^2\left(1-\psi\right)^2}{\delta} \times \underbrace{\Delta p}_{\text{driving force}} \tag{4.43}$$

with $\Delta p = p_g - p_\ell$ and $\psi = 1$ is still the liquid. Rearranging terms, the following phase equation has been used:

$$\dot{\psi} = \frac{\mu_{\ell g}}{6\delta}\left[\varepsilon_\psi^2\nabla^2\psi - 2W\psi(1-\psi)(1-2\psi) - 30\psi^2\left(1-\psi\right)^2\left(p_g - p_\ell\right)\right] \tag{4.44}$$

with $\varepsilon_\psi = 6\gamma_{\ell g}\delta$ and the double-well potential $W = 3\gamma_{\ell g}/\delta$. By solving the steady-state form of Eq. 4.44 in cylindrical coordinates, the Laplace pressure condition $p_g - p_\ell = \gamma_{\ell g}/R_p$ (in 2D) is recovered for a given pore radius R_p justifying in this way the form of this equation.

In this preliminary approach, the growth kinetics of the pore is assumed to be governed by hydrogen diffusion in the liquid, which, as pointed out by Lee *et al.* and Carlson *et al.* [22, 6], can be the limiting factor. As in conventional phase-field models,

a local volumetric molar concentration of hydrogen $\mathfrak{X}_H$ is introduced based on an averaging procedure and considering as a local volume fraction of phase:

$$\mathfrak{X}_H = \psi \mathfrak{X}_{H\ell} + (1-\psi)\,\mathfrak{X}_{Hg} \tag{4.45}$$

where $\mathfrak{X}_{H\ell}$ and $\mathfrak{X}_{Hg}$ [$\mathrm{mol\,m^{-3}}$] are the concentration of hydrogen in the liquid and in the gas, respectively. Assuming thermodynamic equilibrium at the interface, $\mathfrak{X}_{H\ell}$ can be expressed as a function of p_g using Sievert's law (cf. Eq. 2.23). Combining the latter with the perfect gas law and Eq. 4.45, one has:

$$\mathfrak{X}_H = \psi S_\ell \sqrt{\frac{p_g}{p_0}} + (1-\psi)\,\frac{2p_g}{\mathcal{R}T} \tag{4.46}$$

where S_ℓ is the Sievert's constant. A hydrogen conservation equation is then solved, neglecting any hydrogen concentration gradient in the gas phase and any hydrogen transport in the liquid due to flow:

$$\frac{\partial \mathfrak{X}_H}{\partial t} + \nabla \cdot (\psi D_{H\ell} \nabla \mathfrak{X}_{H\ell}) = 0 \tag{4.47}$$

The resolution of Eq. 4.43 and 4.47 is performed using a finite difference method and an explicit time-discretization scheme. At each time-step, the solution of Eq. 4.47 is used to calculate the driving force term of the phase equation. This requires solving the second-order polynomial expression of Eq. 4.46 to obtain p_g from $\mathfrak{X}_H$. Note that an averaging procedure eliminating any concentration gradient in the pore is applied at every time-step, since any concentration gradient in the pore is purely a numerical artefact[3].

To sum up, a flow chart of the phase-field model is as follows:

1– Initialization of the model (ψ, $\mathfrak{X}_{H0}$, $\mathfrak{X}_{H\ell}$, $\mathfrak{X}_{Hg}$).

2– Resolution of the hydrogen conservation equation and redistribution of $\mathfrak{X}_{Hg}$ in the gas phase

$$\frac{\partial \mathfrak{X}_H}{\partial t} + \nabla \cdot (\psi D_{H\ell} \nabla \mathfrak{X}_{H\ell}) = 0 \tag{4.48}$$

3– Calculate the liquid and gas concentration

$$\mathfrak{X}_{H\ell} = S_\ell \sqrt{\frac{p_g}{p_0}} \tag{4.49}$$

$$p_g V = n_{H_2} \mathcal{R}T \rightarrow p_g = \frac{\mathfrak{X}_{Hg}\mathcal{R}T}{2} \tag{4.50}$$

$$\mathfrak{X}_H = \psi S_\ell \sqrt{\frac{\frac{1}{2}\mathfrak{X}_{Hg}\mathcal{R}T}{p_0}} + (1-\psi)\mathfrak{X}_{Hg} \tag{4.51}$$

4– Resolution of the phase equation:

$$\dot{\psi} = \frac{\mu_{\ell g}}{6\delta}\left[\varepsilon_\psi^2 \nabla^2 \psi - 2W\psi(1-\psi)(1-2\psi) - 30\psi^2\,(1-\psi)^2\right] \times \left(\frac{1}{2}\mathfrak{X}_{Hg}\mathcal{R}T - p_\ell\right) \tag{4.52}$$

[3]Indeed, any pressure variation in the pore (or concentration difference) is equilibrated with the speed of sound in a gas phase

5– Return to step 2.

Finally, in order to take into account the solid phase, the contact angle between the liquid-gas interface and the domain border (i.e. with the solid) is prescribed via the Young-Dupré equation (see Eq. 2.32). The wetting angle of the pore is introduced in the phase-field model with a Dirichlet boundary condition, using the approach developed by Sémoroz *et al.* [100]. Once steady state is achieved, the average mean curvature of the pore-liquid interface is calculated using the following expression:

$$\bar{\kappa} = \frac{\int\limits_{\Omega} \psi^2 \left(1-\psi\right)^2 \nabla \cdot \left(\frac{\nabla\psi}{|\nabla\psi|}\right) \mathrm{d}\Omega}{\int\limits_{\Omega} \psi^2 \left(1-\psi\right)^2 \mathrm{d}\Omega} \tag{4.53}$$

since $\mathbf{n} = \nabla\psi/|\nabla\psi|$ is the normal to the interface and $\nabla \cdot \mathbf{n}$ represents the mean curvature of a sharp interface. Calculations performed with different geometries of the solid (i.e., for different secondary dendrite arm spacings) are presented in section 5.5, where it will be shown how the λ_2 spacing influences (i) the shape of the pore, (ii) its volume and (iii) its internal pressure.

4.5 Pipe shrinkage modeling

Until now, we were only interested in microporosity. This section describes how external macroporosity (i.e., pipe shrinkage) simulations were carried out.
The pipe shrinkage calculations were performed with ProCAST® 2008.0. With this software, the porosity calculations result from a post-processing treatment of the thermal results. The underlying physical model of this module can be found in the references of Péquet *et al.* [2] and Couturier *et al.* [3, 4, 5]. A good estimation of the thermal field is thus necessary for porosity calculations. The boundary conditions, especially where the water flow cools down the mold, are critical (see section 3.2.1 for the experiments related to macroporosity). Hence, in order to evaluate the heat flux resulting from the water cooling, inverse 1D modeling has been first performed, as described in section 3.2.1. Then, the resulting calculated time dependent heat flux was used for the direct 3D calculations of the thermal field. Finally, the porosity calculations were performed as a post-processing of these direct 3D thermal calculations.

It is well known that a solidifying piece deforms as solidification occurs. As a consequence, the thermal contact between the mold and the sample changes with time, making this boundary condition difficult to estimate, unless thermo-mechanic calculations are performed. Hence, inverse modeling has been performed first in order to estimate the heat flux due to water cooling. For that purpose, using the D_2S set-up (see Fig. 3.1), three thermocouples have been placed at the same height (90 mm from the bottom chill), but at different radii (see Fig. 4.14a). 1D inverse calculations were made then following the method of Drezet *et al.* [83]. After convergence to a minimal error between calculated and measured temperatures, the heat fluxes as a function

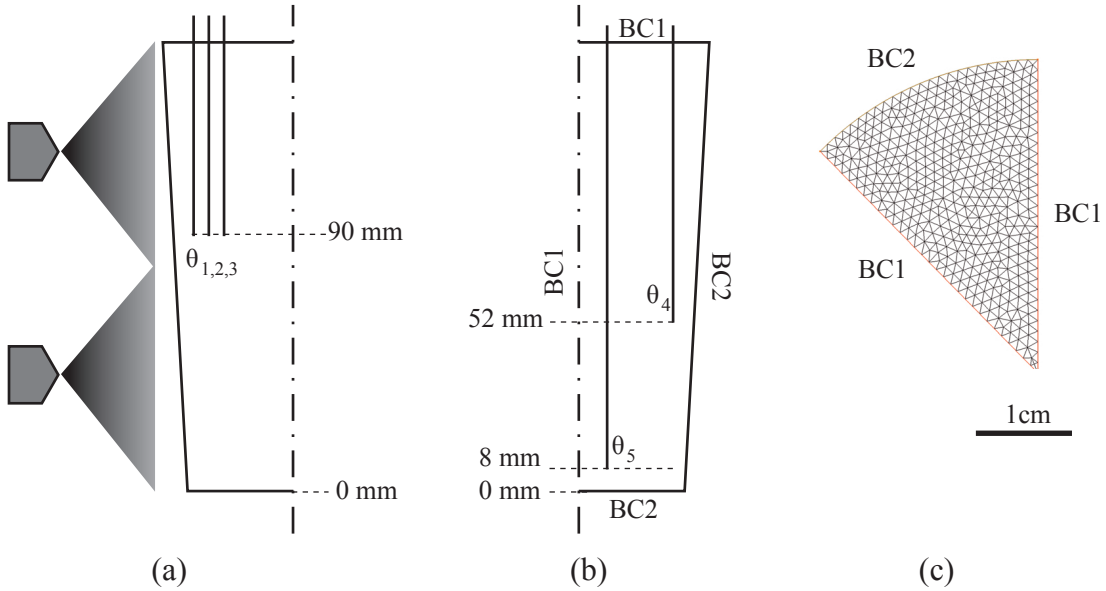

Figure 4.14: (a) Schematic of the experiment for the 1D modeling calculations. (b) Boundary conditions (BC1 = adiabatic, BC2 = Heat flux from Table 4.1). (c) Top view of the mesh for the direct 3D thermal calculations. The thermocouples $\theta_1 - \theta_3$ were used for the inverse modeling, and thermocouples θ_4 and θ_5 were used for validation of the 3D direct calculations.

of time were obtained (see Table 4.1). Note that the provided tabulated physical

Table 4.1: Calculated heat fluxes by inverse modeling.

Time [s]	Heat flux [$\mathrm{W\,m^{-2}}$]
0	-2.3×10^5
10	-4.8×10^4
40	-4.6×10^5
60	-3.4×10^5
120	-1.8×10^5

values of the Al-4.5wt%Cu alloy implemented in ProCAST® 2008.0 were used for all the calculations and are given in Appendix A. The fluxes given in Table 4.1 were then used for the 3D (direct) thermal field calculations performed with an enthalpy method (see Eq. 2.50). Comparisons between calculated and measured temperatures of two thermocouples placed within the casting (see Fig. 4.14b) are given in Fig. 4.15.

Note that the finite element mesh for the direct 3D thermal calculations consisted of 51504 nodes and 277860 tetrahedra (~ 0.15 mm^3 per element) and that a finer mesh had no effect on the thermal results. Figure 4.15 shows comparisons between calculated and measured temperature profiles. The larger discrepancy is observed for the thermocouple θ_5 located near the bottom of the casting where the boundary condition is not well represented (faster cooling than predicted). Nevertheless, a fair correlation between measured and estimated temperatures using the values of Table 4.1 is obtained

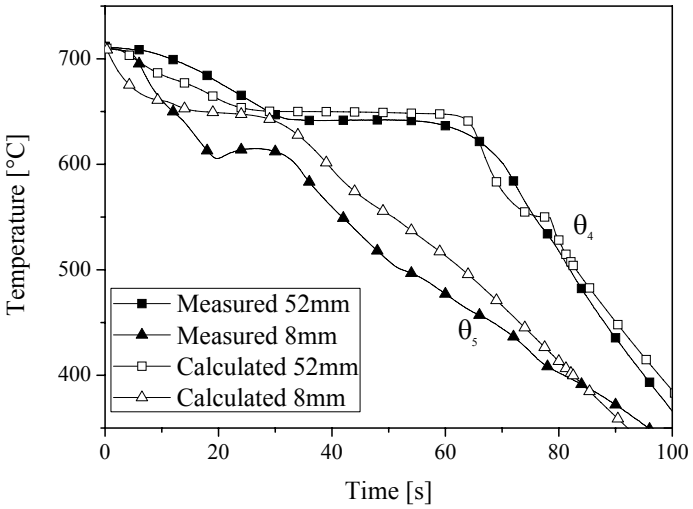

Figure 4.15: Measured and calculated temperature profile of two points within the casting performed with the D_2S set-up. Black symbols represent measured temperatures, whereas open symbols represent calculated temperatures obtained with the heat fluxes given in Table 4.1.

and this thermal field was thus used as input for the porosity calculations.

The "Advanced Multi-Gas Porosity Solver" of ProCAST® (version 2008.0) was used to perform the pipe shrinkage simulations. As a post-processing of the thermal results, the porosity calculations were performed with the default parameters (see Table 4.2) and a grid spacing of 0.5 mm was chosen. Only the mobility limit was varied, i.e., the $g_{s,c}$ parameter, which represents the critical volume fraction of solid at which the surface of the casting cannot move anymore, i.e., when mass feeding is stopped. Comparison between experimentally observed and calculated pipe shrinkage shapes for an Al-4.5wt%Cu casting (inoculated or not) are given in section 5.6.

Table 4.2: Parameters used for the pipe shrinkage calculations.

Parameter	Value
Liquid viscosity	0.001 [Pa s]
Typical λ_2 spacing	100 [μm]
Pore nucleation radius	10 [μm]
Pore density	1×10^9 [m^{-3}]
Liquid-gas interface energy	0.1 [$N\,m^{-1}$]
Cavitation pressure	10000 [Pa]
Hydrogen nominal concentration	0.1 [$cc_{STP}/100g$]
Mobility limit	$0.01 \leq g_{s,c} \leq 0.9$

Chapter 5

Results and discussion

This chapter is divided in six sections. In section 5.1 are presented the X-ray tomography results of the experiments carried out to investigate the influence of the inoculant, copper content, cooling rate and initial hydrogen content on the curvature of the pore phase. Next, an effective hydrogen diffusion coefficient, that is function of the volume fraction of solid only, is obtained in section 5.2. The latter is used in section 5.3 to explain the behavior of a macropore observed at high temperature by X-ray tomography. It is used as well in section 5.4 for the model of pore growth limited by (i) hydrogen diffusion and (ii) curvature restriction by the growing solid network. Section 5.5 presents the results of the new phase-field model developed to simulate the equilibrium shape of a pore constrained by a solid network. Finally, comparisons between experimentally observed and calculated shapes of the pipe shrinkage are presented in section 5.6.

5.1 Casting parameters influences on microporosity

5.1.1 Inoculant influence on pore morphology

The first goal of this study was to investigate the 3D morphology of microporosity formed in a quiescent melt, which was probably free of any oxide bifilms. For that purpose, Al-4.5wt%Cu alloys (inoculated or not) have been solidified with the $DS_{\mathrm{1D-ATM}}$ set-up (see Fig. 3.2). During both experiments (conducted the same day), a room temperature of 25 °C and a relative humidity of 40 % were measured. Following the developments presented in section 2.4.2, this leads to an initial hydrogen concentration of about 0.1 $\mathrm{cc_{STP}}/100\mathrm{g}$ for both alloys if one considers equilibrium between the melt and the ambient relative humidity.

After solidification, samples have been machined from these castings and observed through X-ray tomography with a pixel size of 0.7 μm. After having isolated pores, both principal curvatures at each point on their surface have been calculated with Avizo or VTK, as described in section 4.1.2.

The results are shown in Fig. 5.1, where the two pores are colored with their local mean curvature (red = positively curved regions, blue = negatively curved regions).

After nucleation in the liquid, the pore grows by gradually replacing and pushing away the liquid phase, while the solid grows where the liquid remains and pinches the

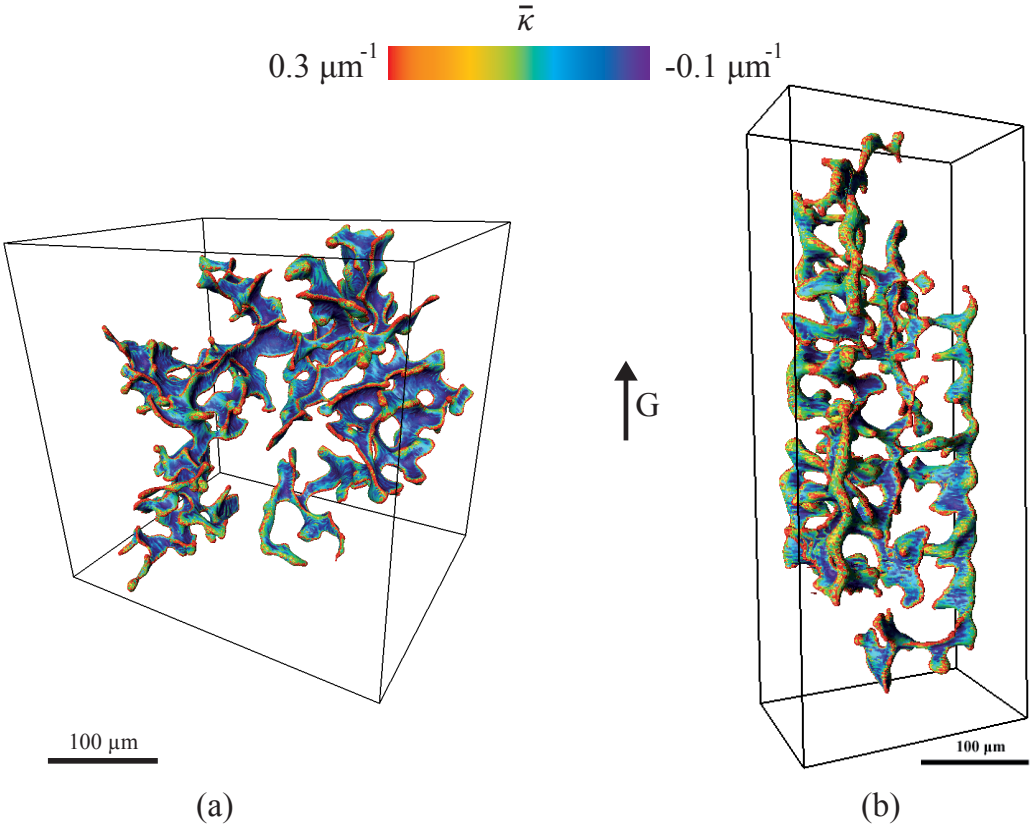

Figure 5.1: Morphologies of pores constrained in (a) an inoculated Al-4.5wt%Cu network and (b) a non-inoculated Al-4.5wt%Cu network. In both cases, the secondary dendrite spacing is similar ($\lambda_2 \approx 20$ μm), i.e., nearly identical thermal conditions ($\dot{T} \approx -2\,^{\circ}\mathrm{C\,s^{-1}}$) and the eutectic volume fraction is similar ($g_{eut} \approx 9\,\%$). Highly positively curved regions are shown in red, whereas negatively curved regions are colored in blue.

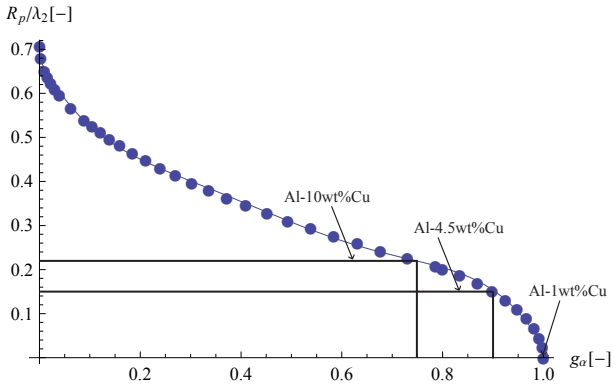

Figure 5.2: Pinching model giving the pore radius of curvature normalized by the λ_2 spacing as a function of g_α as developed by Couturier and Rappaz (symbols = solution from [4], line = fit using Eq. 5.1).

pore. Consequently, the pore shape is the "negative" of the dendritic network. This can be seen in Fig. 5.1, where we can clearly distinguish the characteristic length of the microstructure, i.e., the λ_2 spacing.

We remind here that Couturier and Rappaz [4] developed a simple pinching model to calculate the radius of a non-wetting pore as a function of the volume fraction of solid for a dendritic network assimilated to cylinders of radius $\sqrt{g_\alpha}\lambda_2/2$ (see Fig. 2.14). This model has never been validated, but we will see that it gives a fairly good estimation of the pore radius as a function of g_α and λ_2. For that purpose, we have fitted the relationship developed in [4] with an analytical solution given by (see Fig. 5.2):

$$R_p(g_\alpha, \lambda_2) = \lambda_2 \times (0.678 - 2.167 g_\alpha + 8.122 g_\alpha^2 - 18.545 g_\alpha^3 + 20.086 g_\alpha^4 - 8.151 g_\alpha^5) \quad (5.1)$$

where $g_\alpha = g_s(T_{eut}) = 1 - g_{eut}$. Knowing the λ_2 value and the volume fraction of primary phase g_α from the X-ray tomography data, we can directly calculate the pore radius using this model and compare it with curvatures obtained via tomography.

The characteristic length scales of the microstructures shown in Fig. 5.1 are similar, but the pore of the inoculated alloy (see Fig. 5.1a) seems to exhibit more negatively curved regions (more blue is visible as compared with Fig. 5.1b). To verify this assumption, we have calculated the following characteristic values of the (κ_1, κ_2) distribution as described in section 4.1.2:

(i) The average values of both principal curvatures $\langle\kappa_1\rangle_{tot}$ and $\langle\kappa_2\rangle_{tot}$ calculated on the total set of the (κ_1, κ_2) pairs,

(ii) The average values of both principal curvatures $\langle\kappa_1\rangle_{\geq 0}$ and $\langle\kappa_2\rangle_{\geq 0}$ calculated on the positive values of the (κ_1, κ_2) pairs only,

(iii) The surface over volume ratio of each pore[1].

The results are listed in Table 5.1 and are compared with the results obtained using Eq. 5.1. Looking at the three first lines of this table, it can be seen that $\langle\kappa_1\rangle_{tot} < 0$ and $\langle\kappa_2\rangle_{tot} > 0$ for both alloys. On the other hand, $\langle\kappa_1\rangle_{tot}^{\text{Inoculated}} < \langle\kappa_1\rangle_{tot}^{\text{NonInoculated}}$ and $\langle\kappa_2\rangle_{tot}^{\text{Inoculated}} < \langle\kappa_2\rangle_{tot}^{\text{NonInoculated}}$, thus explaining the pore in Fig. 5.1a is more blue than that in Fig. 5.1b. Therefore, a pore constrained to grow in an inoculated alloy exhibits more negatively curved regions than a pore constrained to grow in a non-inoculated alloy, for otherwise similar thermal conditions and secondary dendrite arm spacing.

Looking at the next three lines of Table 5.1, we can see that $\langle\bar{\kappa}\rangle_{\geq 0}$ is similar for the two alloys. As stated earlier, the last liquid to solidify has the eutectic composition, and hence highly curved regions of a pore should be in contact with the last liquid to solidify, i.e., the eutectic. To prove this assumption, the local mean curvature $\bar{\kappa}$ of a pore has been put into relation with its surrounding local grey value, as described

[1]It must be noted that the approximation of S_V using Carman's formula $S_V = 6(1 - g_s)/\lambda_2$ does not fit well the results, probably because the microstructure has already too much coarsened.

Table 5.1: Inoculant influence on the pore morphology in Al-4.5wt%Cu alloys (same pores as the ones in Fig. 5.1). The last line gives the surface over volume ratio S_V of the pore and all the data are given in μm^{-1}. The typical cooling rate of $-2\,^{\circ}C\,s^{-1}$ and thermal gradient of about $1000\,K\,m^{-1}$ lead to a typical λ_2 spacing of about 20 μm. Note finally that $g_{eut} \approx 9\,\%$ and that $C_{H0} = 0.1\,cc_{STP}/100g$ in both cases.

	Inoculated	Non-inoculated
$\langle\kappa_1\rangle_{tot}$	-0.104	-0.080
$\langle\kappa_2\rangle_{tot}$	0.267	0.344
$\langle\bar{\kappa}\rangle_{tot}$	0.081	0.132
$\langle\kappa_1\rangle_{\geq 0}$	0.060	0.062
$\langle\kappa_2\rangle_{\geq 0}$	0.574	0.546
$\langle\bar{\kappa}\rangle_{\geq 0}$	0.317	0.304
$1/R$ (via Eq. 5.1)	0.333	0.333
S_V	0.517	0.465

in section 4.1.3. The results for a pore constrained to grow in a non-inoculated alloy are shown in Fig. 5.3, but similar results are obtained for each pore studied in this thesis. This figure is a plot that represents with various grey levels the probability of

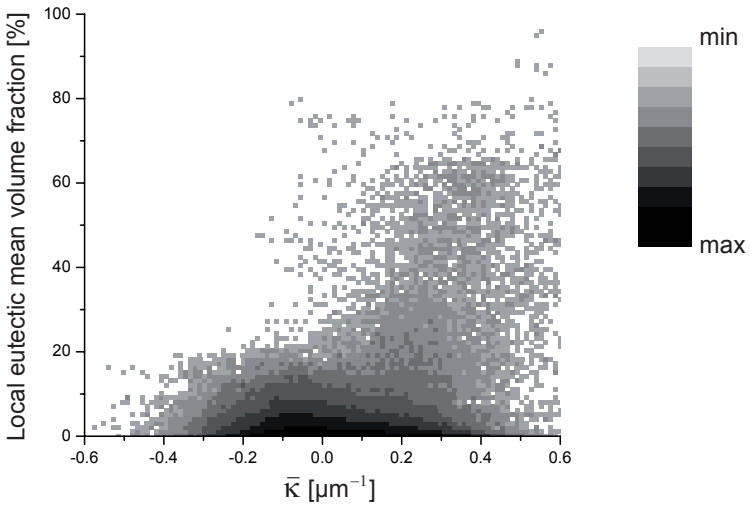

Figure 5.3: Probability, indicated with various grey levels, of having a point at the surface of a pore with a given local mean curvature and eutectic fraction.

finding (on the surface of a pore) a given local mean curvature $\bar{\kappa}$ in contact with a given eutectic percentage present in the adjacent material. We see that negative values of $\bar{\kappa}$ have a high probability of being in contact with the aluminum primary phase, whereas positive values of $\bar{\kappa}$ have an increasing probability of being in contact with the interdendritic eutectic.

However, it is difficult to extract from Table 5.1 an overall shape of a pore growing in inoculated and non-inoculated alloys. We have seen in section 4.1.2 that the Interfacial Shape Distribution (ISD) is a useful tool for representing the shape of a body (see Fig. 4.8). Figure 5.4 shows the calculated ISD plots of these two pores, with a grey level indicating the probability of finding a pair of (κ_1, κ_2) values (the darker the local grey value, the higher the probability). We can see that for a non-inoculated alloy (right

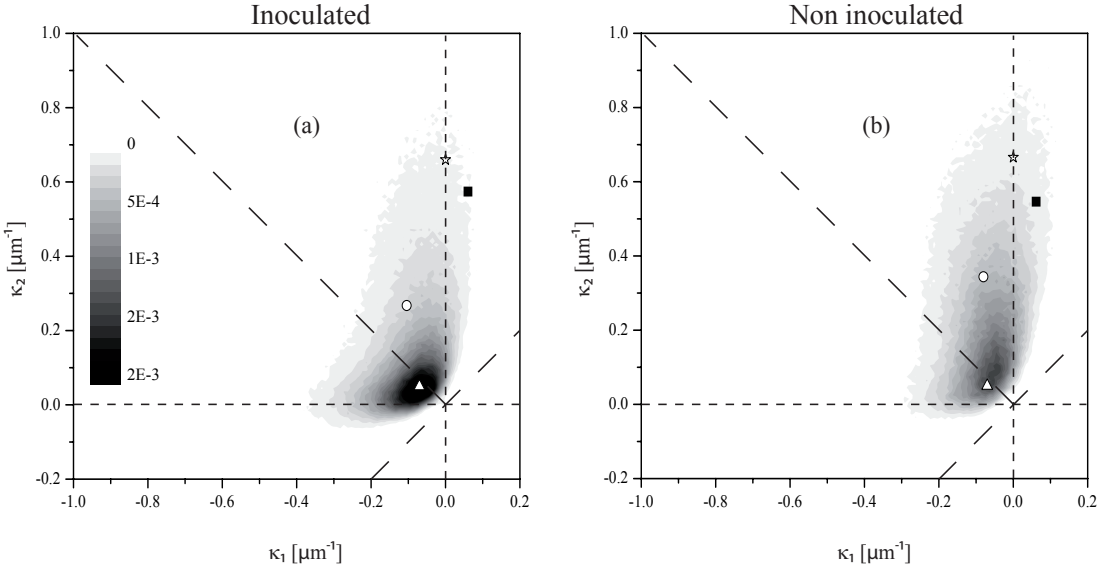

Figure 5.4: Interfacial shape distribution of pores constrained in (left) an inoculated Al-4.5wt%Cu network and (right) a non-inoculated Al-4.5wt%Cu network (same pores as the ones in Fig. 5.1 $\rightarrow g_{eut} \approx 9\,\%$ in both cases). The white circle represents the mean of the distribution and the triangle its maximum. The black square represent the mean of the distribution if one considers only positive values of both κ_1 and κ_2. The star finally represents the value of the curvature as calculated with the pinching model of [4].

plot), the distribution is elongated along one axis only ($\kappa_1 \approx 0$ and $\kappa_2 \geq 0$), indicating that a large portion of the pore surface is well represented by cylinders. This behavior is similar for a pore constrained to grow in an inoculated alloy, even if more negatively curved regions are observed with $\kappa_2 \approx 0$ and $\kappa_1 \leq 0$. This was actually already visible in Table 5.1: $\langle\kappa_1\rangle_{tot}$ is smaller for a pore constrained to grow in an inoculated alloy than in a non-inoculated one, hence more "blue" in Fig. 5.1a than in Fig. 5.1b.
As a first conclusion, the ISD plots indicate that the curvature of pores can be well approximated to that of cylinders independently of the inoculation condition.

On these graphs, we have also represented the following characteristic values:

- Average value of the mean curvature $\langle\bar{\kappa}\rangle_{tot}$ calculated on the total set of the (κ_1, κ_2) pairs (white circle),
- Average value of the mean curvature $\langle\bar{\kappa}\rangle_{\geq 0}$ calculated on the positive values only of the (κ_1, κ_2) pairs (black square),
- Maximum value of the distribution (white triangle).

- The mean curvature value $1/R$ obtained via Eq. 5.1 (white star).

We can see that the black square and the white star are almost aligned on the $\kappa_1 = 0$ axis, and that their κ_2 value are very similar. This means that the positive curved regions of a pore are well approximated by the simple model developed by Couturier and Rappaz [4]. This was actually already visible on Table 5.1, since the mean curvature calculated with Eq. 5.1 is close to the measured $\langle\bar{\kappa}\rangle_{\geq 0}$ value in both cases.

It should be noted that looking at the ISD plots, it is not obvious that the black square in Fig. 5.4 represents $\langle\bar{\kappa}\rangle_{\geq 0}$. However these plots show the ISDs based on all the curvature values, not for positive values only. To clarify this fact, Fig. 5.5 shows the ISD of a non-inoculated alloy (same as Fig. 5.4b), but based on positive values only. In this figure, it is now clear that the black square represents the mean value of the distribution. Then, the black square in Fig. 5.4 is at the right place, and the $\langle\bar{\kappa}\rangle_{\geq 0}$ value seems to be truncated only because the ISD is based on all the curvature data, and not on positive values only.

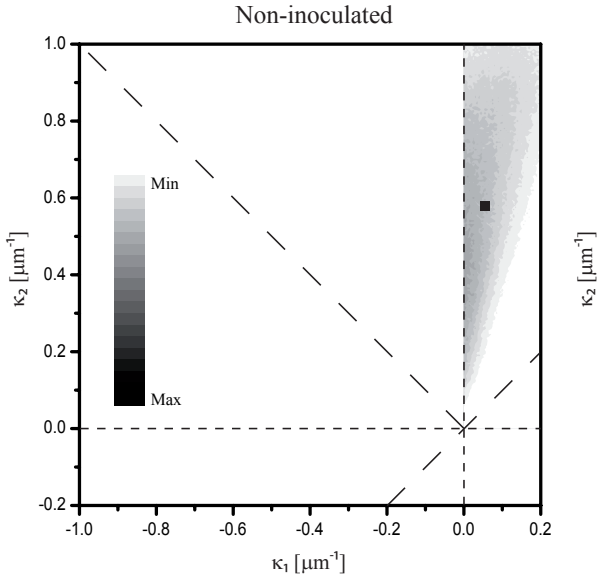

Figure 5.5: Similar to Fig. 5.4b, but ISD for positive curvature values only. The black square, representing the average value of the mean curvature calculated on the positive values only, represents now clearly the mean value of the distribution.

In the next part of this section, we analyze the shape of a pore constrained to grow in a dendritic network (inoculated or not) in terms of moments of inertia as described in section 4.1.1. Interestingly, the pore shape is well elongated in Fig. 5.1 for the non-inoculated alloy, whereas it is nearly independent of the thermal gradient direction for the inoculated alloy. The non-dimensionalized moments of inertia tensor I^{ND} and the corresponding eigenvector matrix E for the pore pinched in an inoculated alloy (Fig. 5.1a) are equal to:

$$I^{ND} = \begin{pmatrix} 0.81 & 0.00 & 0.00 \\ 0.00 & 0.82 & 0.00 \\ 0.00 & 0.00 & 1.37 \end{pmatrix} \qquad E = \begin{pmatrix} -0.99 & -0.01 & 0.00 \\ -0.01 & 0.99 & 0.00 \\ 0.00 & 0.00 & 1.00 \end{pmatrix} \tag{5.2}$$

whereas for a pore constrained in a non-inoculated network (Fig. 5.1b), we have:

$$I^{ND} = \begin{pmatrix} 1.29 & -0.12 & 0.02 \\ -0.12 & 1.13 & 0.02 \\ 0.02 & 0.02 & 0.59 \end{pmatrix} \qquad E = \begin{pmatrix} -0.07 & -0.49 & -0.86 \\ -0.08 & -0.86 & 0.49 \\ 0.99 & -0.11 & 0.02 \end{pmatrix} \tag{5.3}$$

The first vector (column) of E corresponds to the lowest eigenvalue of I^{ND}. One can see that the non-inoculated alloy has its lowest moment of inertia well aligned along z, which means that the pore is elongated along the thermal gradient. As a matter of fact, it grows in between the columnar dendrites which are themselves more or less aligned along the thermal gradient.
On the opposite, the equiaxed pore in Fig. 5.1a is already diagonal in the xyz-reference frame and has the largest value along the thermal gradient. The tensor I^{ND} is nearly degenerated in the xy-plane, i.e., perpendicular to G. This is probably due to the growth mode of equiaxed grains growing in a thermal gradient. The pore is more or less following the grains boundaries in this case, as can be guessed from Fig. 5.1a.

In summary, the principal aspects resulting from the analysis of the experiments performed with the $DS_{\mathrm{1D-ATM}}$ set-up are:

(i) The positively curved regions of a pore are primarily in contact with the last liquid to solidify, i.e., the eutectic.

(ii) Approximating the pores curvature by that of cylinders is a fair approximation for pores in both non-inoculated alloy and inoculated alloys since the ISDs are mainly elongated along $\kappa_1 = 0$ and $\kappa_2 > 0$. The characteristic value of the pore overpressure $\langle\bar{\kappa}\rangle_{\geq 0}$ is also similar in both cases. The pinching model must be then independent of the alloy inoculation. The simple model of pinching developed in [4] and described by Eq. 5.1 gives results that have the right order of magnitude as compared with the value of $\langle\bar{\kappa}\rangle_{\geq 0}$.

(iii) $\langle\bar{\kappa}\rangle_{\geq 0}$ gives a fair estimation of the overpressure inside the pore near the end of solidification, since the mean curvature is directly linked to the pressure via the Laplace-Young's equation. With a value of $\gamma_{\ell g} = 0.87\,\mathrm{N\,m^{-1}}$ [1] and using Eq. 2.33, a pore curvature overpressure of about 550 kPa is achieved near the end of solidification in that case.

(iv) The pore is well elongated along the thermal gradient for non-inoculated alloys, whereas it is nearly equiaxed in inoculated alloys.

It should be noted that the calculations and results presented in this section were performed for a certain characteristic length of the microstructure ($\lambda_2 \approx 20\ \mu$m). However, similar findings and conclusions in terms of: (i) cylindrical approximation of the

pore curvature and (ii) moments of inertia with corresponding eigenvalues and eigenvectors have been made for a coarser microstructure, i.e., $\lambda_2 \approx 40$ μm. However, the curvature values are influenced by the λ_2 spacing. We will see how hereafter.

But before coming to this point, we present in Fig. 5.6 the ISD plot of the eutectic phase of an inoculated and non-inoculated alloy (taken from the same samples of Fig. 5.4). Surprisingly, these ISD plots do not differ much from those of Fig. 5.4: the curvature of the eutectic can also be approximated by cylinders, since the ISDs are elongated along $\kappa_1 = 0$ and $\kappa_2 > 0$, and $\langle \bar{\kappa} \rangle_{\geq 0}$ represented by the black square has a value of the same order of magnitude as the pores in Fig. 5.4. It seems then that the shape of the

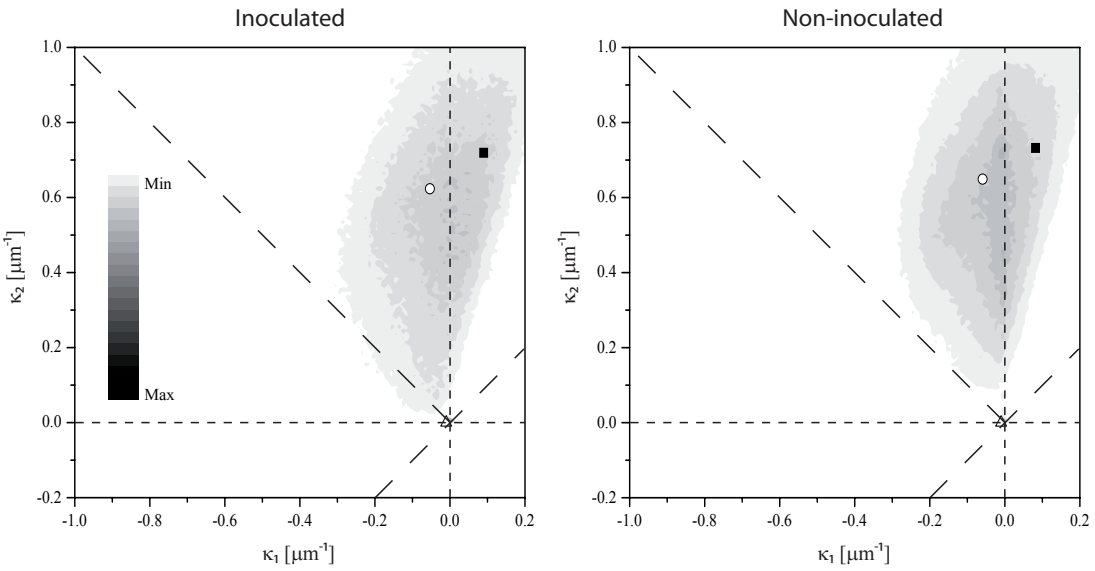

Figure 5.6: Interfacial shape distribution of the eutectic phase in (left) an inoculated Al-4.5wt%Cu network and (right) a non-inoculated Al-4.5wt%Cu network ($g_{eut} \approx 9\,\%$ in both cases). The white circle represents the mean value of the distribution and the black square the mean value of the distribution if one considers only positive values of both κ_1 and κ_2. The triangle represents the maximum value of the distribution. Note that this value is close to the one of a plane, probably because microstructure coarsening occurred, leading to more planar-like solid-liquid interfaces. This phenomenon could barely happen for a non-condense phase like the gas phase.

phase growing in between the primary dendrites is ruled mainly by the place left by the primary α-phase. Accordingly, assuming the pore phase is a condensed phase but with a lower interfacial energy than the solid-liquid one, it could be then possible to run "conventional" phase-field calculations (i.e., of *condensed* phases only) of a ternary alloy with appropriate interfacial energies and compare them with X-ray tomography data. This is however beyond the scope of this work, and is left as a suggestion of possible future work.

Until now, we have analyzed two pores in castings performed with the $DS_{\mathrm{1D-ATM}}$ set-up, and the level of hydrogen could not be directly controlled. We analyze now the samples cast with the $DS_{\mathrm{1D-AC}}$ set-up, from which the level of hydrogen could be directly controlled. First, the liquid penetrant testing results are presented. Then,

we compare the shape of pores produced with the DS_{1D-AC} and DS_{1D-ATM} set-ups. Finally, the influence of the alloy copper content, cooling rate and hydrogen partial pressure on the pore curvature is analyzed.

5.1.2 Liquid penetrant testing results

According to Sievert's law (Eq. 2.23), the higher the hydrogen partial pressure in the atmosphere, the higher the hydrogen content in the melt. This, combined with the strong partitioning of hydrogen between solid and liquid aluminum ($k_{0H} \approx 0.07$ [43]) leads to a pore fraction g_p increasing with the hydrogen content. This behavior is well verified in our castings made with the DS_{1D-AC} set-up, as shown by the liquid penetrant testing (LPT) results shown in Fig. 5.7. This figure shows the influence of the initial hydrogen content on the density of pores in Al-4.5wt%Cu alloys. Note that the big "hole" on each photograph is produced by the thermocouple and thus must be ignored in the interpretation. Clearly, no pore can be seen if $C_{H0} = 0\,\mathrm{cc_{STP}}/100\mathrm{g}$, proving the efficiency to cast aluminum alloys under argon. Then, as C_{H0} increases (Figs. 5.7b and 5.7c) more pores are visible. They are clearly elongated in the thermal gradient direction, as in Fig. 5.1b, since these alloys were non-inoculated. The influence of the inoculant can be seen in Fig. 5.7d: for the same hydrogen content, the pores have a more "equiaxed" shape in Fig. 5.7d as compared with Fig. 5.7c. This confirms the fact that the thermal gradient influences the pore shape only if the alloy is not inoculated. These results also show that the developed DS_{1D-AC} set-up does indeed produce cast samples with a porosity which is dependent on the hydrogen partial pressure.
But before further evaluating the influence of C_{H0} on the curvature of the pore phase, we will see first the difference between pores obtained with the DS_{1D-ATM} and DS_{1D-AC} set-ups.

5.1.3 Bifilms

The main difference between the two 1D-DS set-ups is that melt pouring is not required with the DS_{1D-ATM} set-up but necessary with the DS_{1D-AC} set-up, leading possibly to oxide bifilm entrapment. Figure 5.8 shows the volume rendering of a pore constrained to grow in columnar and equiaxed Al-4.5wt%Cu dendritic networks. These castings were produced using the DS_{1D-AC} set-up and no significant difference can be seen between this figure and Fig. 5.1 in terms of pore shape. Here again, the pore is well elongated along the thermal gradient if the alloy is non-inoculated, whereas it is equiaxed if the alloy is inoculated. Similar moment of inertia tensors as previously found (see Eqs. 5.2 and 5.3) were obtained for these two pores, and no evidence of bifilm can be seen here. We will thus assume in the results of the next sections that the pores obtained in the castings performed with the DS_{1D-AC} set-up do not originate from oxide bifilms.

However, we have also observed pores originating from oxide bifilms (but very few of them) in castings produced with the DS_{1D-AC} set-up, especially those with a low initial hydrogen content. Figure 5.9 shows a typical entrapped oxide bifilm from which

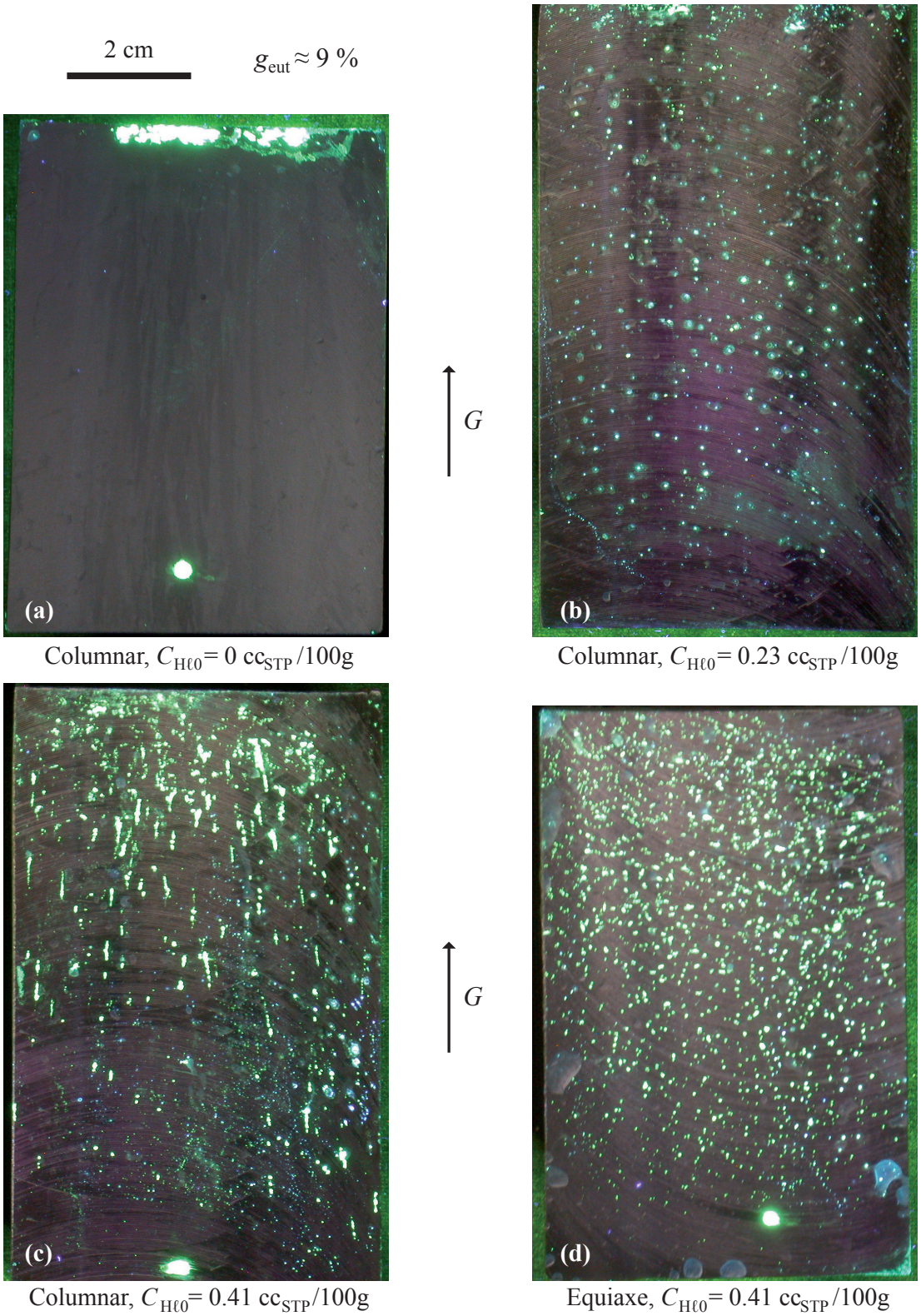

Columnar, $C_{H\ell 0}$= 0 cc_{STP}/100g

Columnar, $C_{H\ell 0}$= 0.23 cc_{STP}/100g

Columnar, $C_{H\ell 0}$= 0.41 cc_{STP}/100g

Equiaxe, $C_{H\ell 0}$= 0.41 cc_{STP}/100g

Figure 5.7: Hydrogen content influence on pore density in Al-4.5wt%Cu alloys.

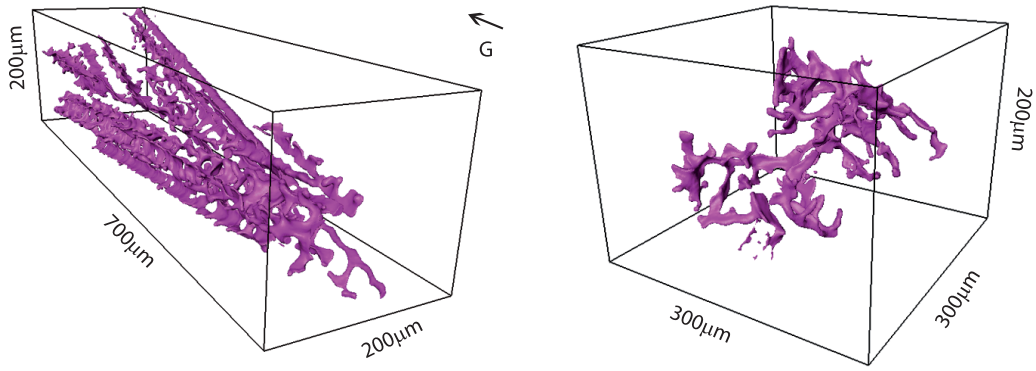

Figure 5.8: Volume rendering of pores constrained in (a) a columnar and (b) an equiaxed Al-4.5wt%Cu dendritic network (castings performed with the DS_{1D-AC} set-up, $g_{eut} \approx 9\,\%$ in both cases).

an interdendritic pore has grown. To the author's knowledge, it is the first time that the 3D volume rendering of such an interdendritic pore, originating from an entrapped oxide bifilm, is reported with such a high resolution (0.7 μm/voxel). Note that this kind of bifilm was only observed in castings produced with the DS_{1D-AC} set-up, and never with the DS_{1D-ATM} set-up. Note also the small dimensions of the bifilm and the even finer shape of the interdendritic microporosity originating from it.

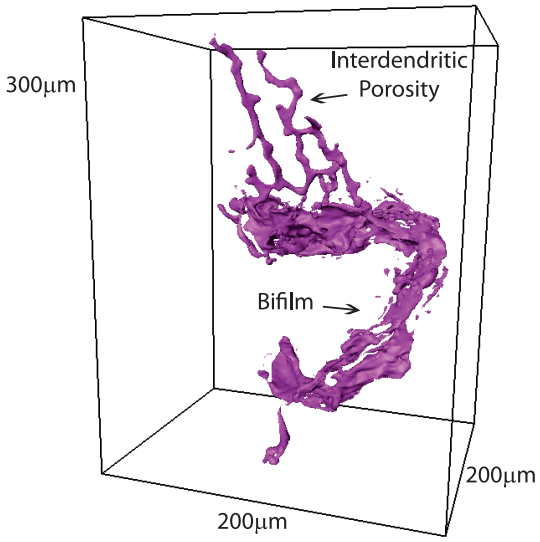

Figure 5.9: Interdendritic microporosity originating from an oxide bifilm.

This result confirms the mechanism of pore nucleation by oxide bifilms proposed by Campbell [17], when melt pouring is not properly done. However, very few of these pores have been observed: less than 5 % of them originated from bifilms and were thus not further analyzed. This proves that the Campbell's mechanism is not

universal. Consequently, assuming the pore surface is not in contact with a bifilm, the pore curvature values that we calculate (typically $\langle\bar{\kappa}\rangle_{\geq 0}$) fairly represent the local mechanical equilibrium described by the Laplace-Young's equation.

5.1.4 Influence of the copper content and cooling rate

As pores grow in between dendrite arms of the primary phase, their curvature must be influenced by (i) the secondary dendrite arm spacing λ_2 and (ii) the amount of liquid left in between when they form. Therefore, we treat in this section the influence of the copper content of the alloy and of the cooling rate on the pore curvature. We remind here that $DS_{\mathrm{1D-AC}}$ castings with three different copper contents were produced, and that a sample was machined from each casting at 10 and 40 mm from the bottom copper chill in order to investigate the microstructure coarseness influence on pore curvature.
The results are presented in the same way as in section 5.1.1: a table gives the main characteristic values of the (κ_1, κ_2) distributions, and these values are then reported on the ISD plots of each pore. Besides, the microstructure coarseness is taken into account by specifying the λ_2 spacing in each case.

We remind here that several examples of quantities evolving during solidification as a function of temperature or volume fraction of solid were given in Chapter 2:

- Figure 2.3 shows the evolution of the volume fraction of solid with temperature,
- Figures 2.5 and 2.6 show the copper content influence on the λ_2 spacing and permeability, respectively, as a function of temperature for the three considered Al-Cu alloys,
- Figure 2.9 shows the copper content influence on hydrogen solubility as a function of temperature.
- Figure 2.12 shows the evolution of the hydrogen composition in the liquid as a function of the volume fraction of solid for an Al-4.5wt%Cu alloy.

All these figures correspond precisely to the cases analyzed in this section, especially for the samples taken at 10 mm from the copper chill.

Figure 5.10 shows the volume rendering of two pores (colored by their local mean curvature, with the same scale) in (a) an Al-4.5wt%Cu sample taken at 10 mm from the copper chill and (b) an Al-10wt%Cu sample taken at 40 mm from the copper chill (both alloys were non-inoculated). It appears that the λ_2 spacing is about the same in both cases, as the copper content is increased (reduced solidification interval ($T_{liq} - T_{eut}$)), while the cooling rate is decreased. The measured λ_2 values as a function of the alloy copper content are compared with coarsening calculations in Table 5.2. The λ_2 measurements were directly performed on the X-ray tomography stacks, whereas the coarsening calculations were performed using a simple 1-D model using Eqs. 2.4 and 2.5, together with the measured values of the thermal gradient and liquidus velocity

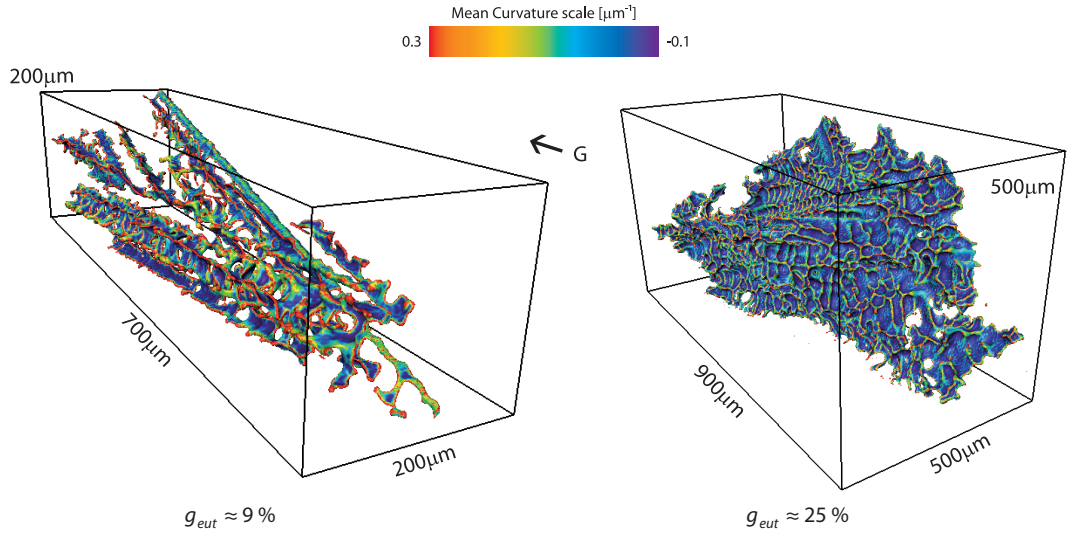

Figure 5.10: Volume rendering of a pore (colored by its local mean curvature) in a columnar (a) Al-4.5wt%Cu (sample taken at 10 mm from the copper chill) and (b) Al-10wt%Cu alloy (sample taken at 40 mm from the copper chill).

given in Fig. 3.5 (see Fig. 2.5 for the details). A fairly good agreement is observed between measured and calculated values. Yet, looking at Fig 5.10, the pore on the

Table 5.2: Measured and calculated λ_2 values for the samples extracted at 10 and 40 mm from the copper chill, as a function of the alloy copper content. The mean value of the measured cooling rate $|\dot{T}| = \frac{T_{liq}-T_{eut}}{t_{liq}-t_{eut}}$ is also given for each case.

	Al-1wt%Cu $g_{eut} \approx 0\,\%$		Al-4.5wt%Cu $g_{eut} \approx 9\,\%$		Al-10wt%Cu $g_{eut} \approx 25\,\%$	
Distance from Cu chill	10 mm	40 mm	10 mm	40 mm	10 mm	40 mm
Cooling rate $\lvert\dot{T}\rvert$	$6\,\mathrm{K\,s^{-1}}$	$1\,\mathrm{K\,s^{-1}}$	$7\,\mathrm{K\,s^{-1}}$	$1.5\,\mathrm{K\,s^{-1}}$	$10\,\mathrm{K\,s^{-1}}$	$2\,\mathrm{K\,s^{-1}}$
Measured λ_2 [μm]	26	38	23	32	14	26
Calculated λ_2 [μm]	31	40	23	32	19	27

left looks more "red" than the one on the right. Since the λ_2 spacings are similar (see Table 5.2), this means that the curvature of a pore does not depend on the secondary dendrite arm spacing λ_2 only.

Table 5.3 summarizes the influence of the copper content and cooling rate on the pore curvature values. The surface over volume ratio is also given for each pore at each composition. Here again, calculations with the relationship $6(1-g_\alpha)/\lambda_2$ does not fit well the data, probably because the microstructure has too much coarsened. These values are nevertheless given as information. For comparison, we have given in Table 5.4 the results obtained with VTK (curvatures are obtained via the angle defect method). Although the angle defect method implemented in VTK gives values about 20% lower than those obtained Avizo, the results are quite close. However we will focus

on the results obtained with the Avizo software, since they appear to be more accurate, as shown in section 4.1.4.

Note that the influence of the the copper content on hydrogen solubility has been taken into account as described in section 2.4.2, reason why even if the casting temperature as well as the hydrogen partial pressure are the same for all these castings, the initial hydrogen concentrations are different. We know however that these samples are saturated in hydrogen and we will treat them as so.

Table 5.3: Copper and cooling rate influence on pore curvatures calculated with Avizo (data given in $[\mu m^{-1}]$). The values under the composition are the initial hydrogen concentrations. The last line gives the surface volume ratio of each pore.

	Al-1wt%Cu 0.51 $cc_{STP}/100g$ $g_{eut} \approx 0\,\%$		Al-4.5wt%Cu 0.41 $cc_{STP}/100g$ $g_{eut} \approx 9\,\%$		Al-10wt%Cu 0.30 $cc_{STP}/100g$ $g_{eut} \approx 25\,\%$	
	10 mm	40 mm	10 mm	40 mm	10 mm	40 mm
$\lvert\dot{T}\rvert$ $[K\,s^{-1}]$	6	1	7	1.5	10	2
λ_2 $[\mu m]$	26	38	23	32	14	26
$\langle\kappa_1\rangle_{tot}$	-0.076	-0.071	-0.127	-0.098	-0.136	-0.139
$\langle\kappa_2\rangle_{tot}$	0.444	0.242	0.389	0.253	0.403	0.170
$\langle\bar{\kappa}\rangle_{tot}$	0.184	0.086	0.131	0.077	0.134	0.015
$\langle\kappa_1\rangle_{\geq 0}$	0.066	0.047	0.064	0.051	0.068	0.051
$\langle\kappa_2\rangle_{\geq 0}$	0.629	0.415	0.654	0.483	0.674	0.503
$\langle\bar{\kappa}\rangle_{\geq 0}$	0.348	0.231	0.359	0.267	0.371	0.277
$1/R$ (via Eq. 5.1)	1.538	1.053	0.289	0.208	0.325	0.175
S_V	0.790	0.444	0.862	0.488	0.605	0.177

Let us enumerate the conclusions that can be drawn from Table 5.3:

(i) $\langle\bar{\kappa}\rangle_{tot}$ and $\langle\bar{\kappa}\rangle_{\geq 0}$ increase with a decreasing λ_2 for a given copper content, i.e., nearly equal fraction of primary phase. This means that the λ_2 spacing does have an impact on the pore curvatures. However it is not the only parameter,

(ii) $\langle\kappa_1\rangle_{\geq 0} \approx 0$ and $\langle\kappa_2\rangle_{\geq 0} \gg 0$ in each case, leading to a possible approximation of the pore curvatures by that of cylinders,

(iii) For identical λ_2 spacings, e.g. Al-4.5wt%Cu at 10 mm ant Al-10wt%Cu at 40 mm ($\lambda_2 = 26$ μm), the mean positive curvature $\langle\bar{\kappa}\rangle_{\geq 0}$ decreases as the copper content increases. Indeed, the space remaining in between dendrite arms are larger as g_{eut} increases with the copper content.

As in section 5.1.1, we have calculated the ISD plots for all these pores to see if a general trend concerning their overall shape can be obtained. We can see in Fig. 5.11 that for each pore, we have a main "tail" along the $\kappa_1 = 0$ axis, which means

Table 5.4: Copper and cooling rate influence on pore curvatures calculated with VTK (data given in $[\mu m^{-1}]$). The values under the composition are the initial hydrogen concentrations. The last line gives the surface volume ratio of each pore.

	Al-1wt%Cu 0.51 $cc_{STP}/100g$ $g_{eut} \approx 0\,\%$		Al-4.5wt%Cu 0.41 $cc_{STP}/100g$ $g_{eut} \approx 9\,\%$		Al-10wt%Cu 0.30 $cc_{STP}/100g$ $g_{eut} \approx 25\,\%$	
	10 mm	40 mm	10 mm	40 mm	10 mm	40 mm
$\lvert\dot{T}\rvert$ $[K\,s^{-1}]$	6	1	7	1.5	10	2
λ_2 $[\mu m]$	26	38	23	32	14	26
$\langle\kappa_1\rangle_{tot}$	-0.045	-0.063	-0.091	-0.133	-0.145	-0.192
$\langle\kappa_2\rangle_{tot}$	0.329	0.197	0.279	0.235	0.342	0.196
$\langle\bar{\kappa}\rangle_{tot}$	0.142	0.067	0.094	0.051	0.099	0.002
$\langle\kappa_1\rangle_{\geq 0}$	0.106	0.078	0.099	0.085	0.112	0.087
$\langle\kappa_2\rangle_{\geq 0}$	0.445	0.318	0.463	0.385	0.511	0.408
$\langle\bar{\kappa}\rangle_{\geq 0}$	0.276	0.198	0.281	0.235	0.311	0.247
$1/R$ (via Eq. 5.1)	1.538	1.053	0.289	0.208	0.325	0.175
S_V	0.790	0.444	0.862	0.488	0.605	0.177

that once more the approximation of the pores curvature by that of cylinders is a fair estimation. The symbols in Fig. 5.11 are the same as those described for Fig. 5.4 and we can see that here again, $\langle\kappa_2\rangle_{\geq 0} \gg 0$ (represented by the black square) is near the $\kappa_1 = 0$ axis and that for Figs. 5.11c to 5.11f, the mean curvature value estimated via Eq. 5.1 (represented by the white star) well approximates that one represented by the black square. This tendency is inverted if one considers an Al-1wt%Cu alloy, but since $g_{eut} = 1 - g_\alpha \to 0$ for this alloy, this model cannot be valid anymore.

We have shown that the pinching model developed by Couturier and Rappaz [4] (and approximated by Eq. 5.1) gives the right order of magnitude for the pore radius as a function of g_α and λ_2. Let us see now if the initial hydrogen content must also be taken into account.

5.1.5 Influence of the hydrogen partial pressure

Using the DS_{1D-AC} set-up, the influence of the initial hydrogen concentration on the pore morphology has been investigated. We remind here that three similar Al-4.5wt%Cu samples have been cast under different hydrogen partial pressures, leading to three different hydrogen contents: 0, 0.23, and 0.41 $cc_{STP}/100g$. A sample was extracted from each casting at 10 and 40 mm from the bottom copper chill in order to investigate also the microstructure coarseness influence on the pores curvature.
Table 5.5 summarizes the results, whereas Fig. 5.12 shows the ISD plots of pores contained in these castings. Looking at Table 5.5, we can see a non-monotonic behavior of the curvature values as a function of the initial hydrogen content, and peak values are

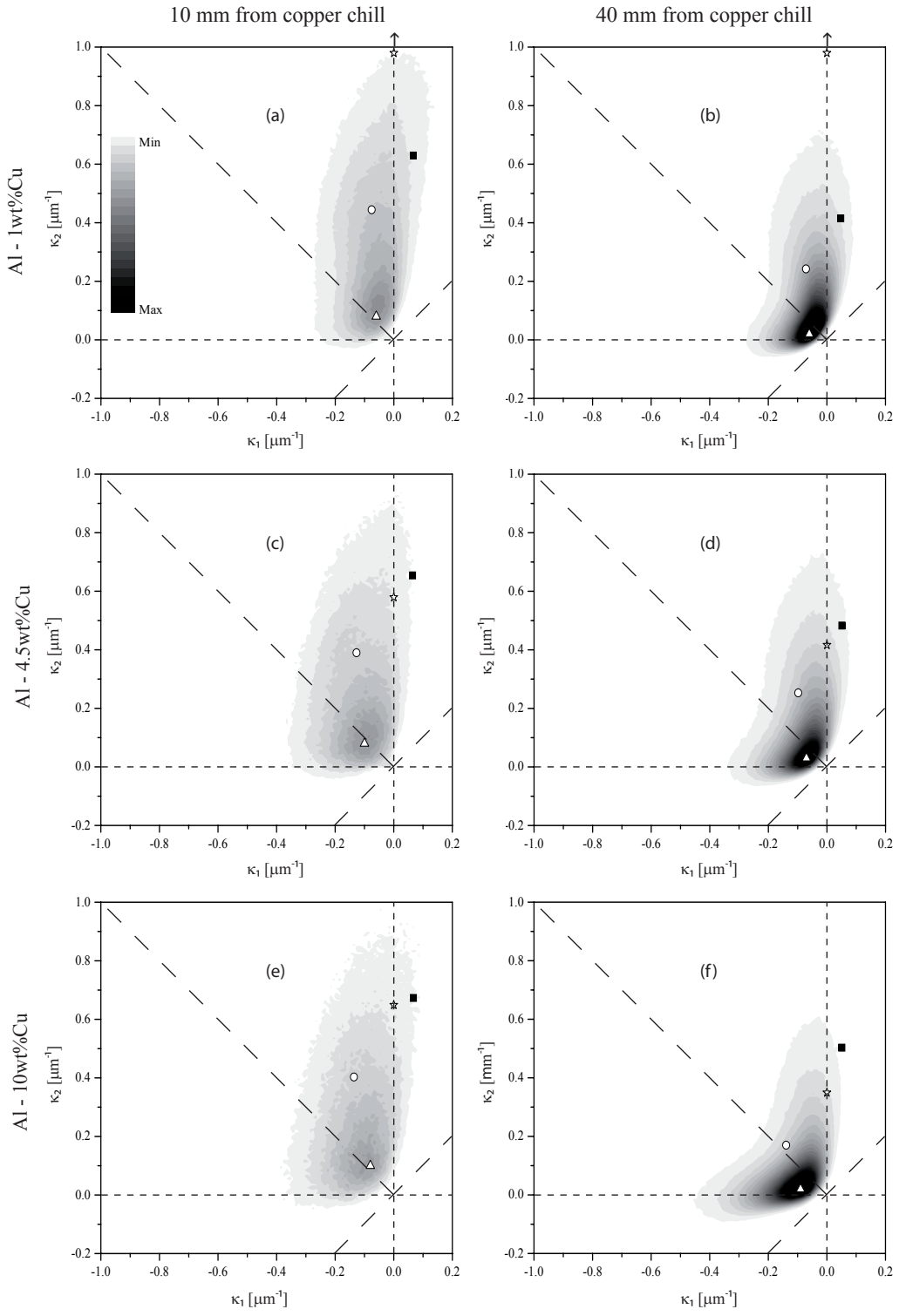

Figure 5.11: Coarseness and copper content influence on the interface shape distribution of the pore phase. The white circle represents the mean of the distribution and the triangle its maximum. The black square represent the mean of the distribution if one considers only positive values of both κ_1 and κ_2. The star finally represents the value of the curvature as calculated with the pinching model of [4].

obtained for an intermediate initial hydrogen content of 0.23 $cc_{STP}/100g$. These results

Table 5.5: Initial hydrogen content influence on pore curvatures calculated with Avizo (data given in [μm^{-1}], values under the composition being the initial hydrogen concentration) for an Al-4.5wt%Cu alloy ($g_{eut} \approx 9\,\%$). The last line gives the surface over volume ratio of each pore considered.

	0.00 $cc_{STP}/100g$		0.23 $cc_{STP}/100g$		0.41 $cc_{STP}/100g$	
	10 mm	40 mm	10 mm	40 mm	10 mm	40 mm
$\lvert\dot{T}\rvert$ [K s^{-1}]	7	1.5	7	1.5	7	1.5
λ_2 [μm]	23	32	23	32	23	32
$\langle\kappa_1\rangle_{tot}$	-0.017	-0.078	-0.084	-0.083	-0.127	-0.098
$\langle\kappa_2\rangle_{tot}$	0.591	0.318	0.754	0.415	0.389	0.253
$\langle\bar{\kappa}\rangle_{tot}$	0.287	0.120	0.335	0.166	0.131	0.077
$\langle\kappa_1\rangle_{\geq 0}$	0.077	0.051	0.079	0.059	0.064	0.051
$\langle\kappa_2\rangle_{\geq 0}$	0.648	0.520	0.868	0.587	0.654	0.483
$\langle\bar{\kappa}\rangle_{\geq 0}$	0.362	0.285	0.474	0.323	0.359	0.267
$1/R$ (via Eq. 5.1)	0.289	0.208	0.289	0.208	0.289	0.208
S_V	0.939	0.676	0.533	0.542	0.862	0.488

are difficult to explain, since there is a compromise between the pore pressure due to high hydrogen content, and pore pressure due curvature restriction by the solid phase: a pore nucleates later if the initial hydrogen concentration is lower. At this point, the microstructure has already evolved and the place left for the pore to expand is small, resulting in high pore curvature values. Moreover, if the initial hydrogen content tends to zero (as for the sample cast under argon for instance), no pore nucleates before the formation of the eutectic and only shrinkage porosity is then considered. This results in the formation of several small micropores that nucleate to compensate for the solidification shrinkage associated with the appearance of the eutectic. These pores are very small, at the limit of technique. But interestingly, they are always in contact with both the eutectic and the primary phase and are never surrounded by the eutectic only. This is shown in Fig. 5.13 where a pore (in pink) is represented with the eutectic (in yellow), the rest (invisible) being the primary aluminum phase.

On the other hand, a pore nucleates earlier if the initial hydrogen content is higher. But the higher the hydrogen concentration, the higher the pore pressure (due to the perfect gas law), and we assume that the sample containing a "high" initial hydrogen content (0.41 $cc_{STP}/100g$) results in gas porosity only. But there is surprisingly no significant difference between the $\langle\bar{\kappa}\rangle_{\geq 0}$ value of the sample cast under argon and the one having an initial hydrogen content of 0.41 $cc_{STP}/100g$.
Concerning the sample containing an intermediate initial hydrogen content (0.21 $cc_{STP}/100g$), it is likely that both mechanisms of shrinkage and gas porosity are involved in this sample, leading to a possible, yet low, increase of the curvature values.

As a conclusion, no significant influence of the initial hydrogen content on $\langle\bar{\kappa}\rangle_{\geq 0}$ can

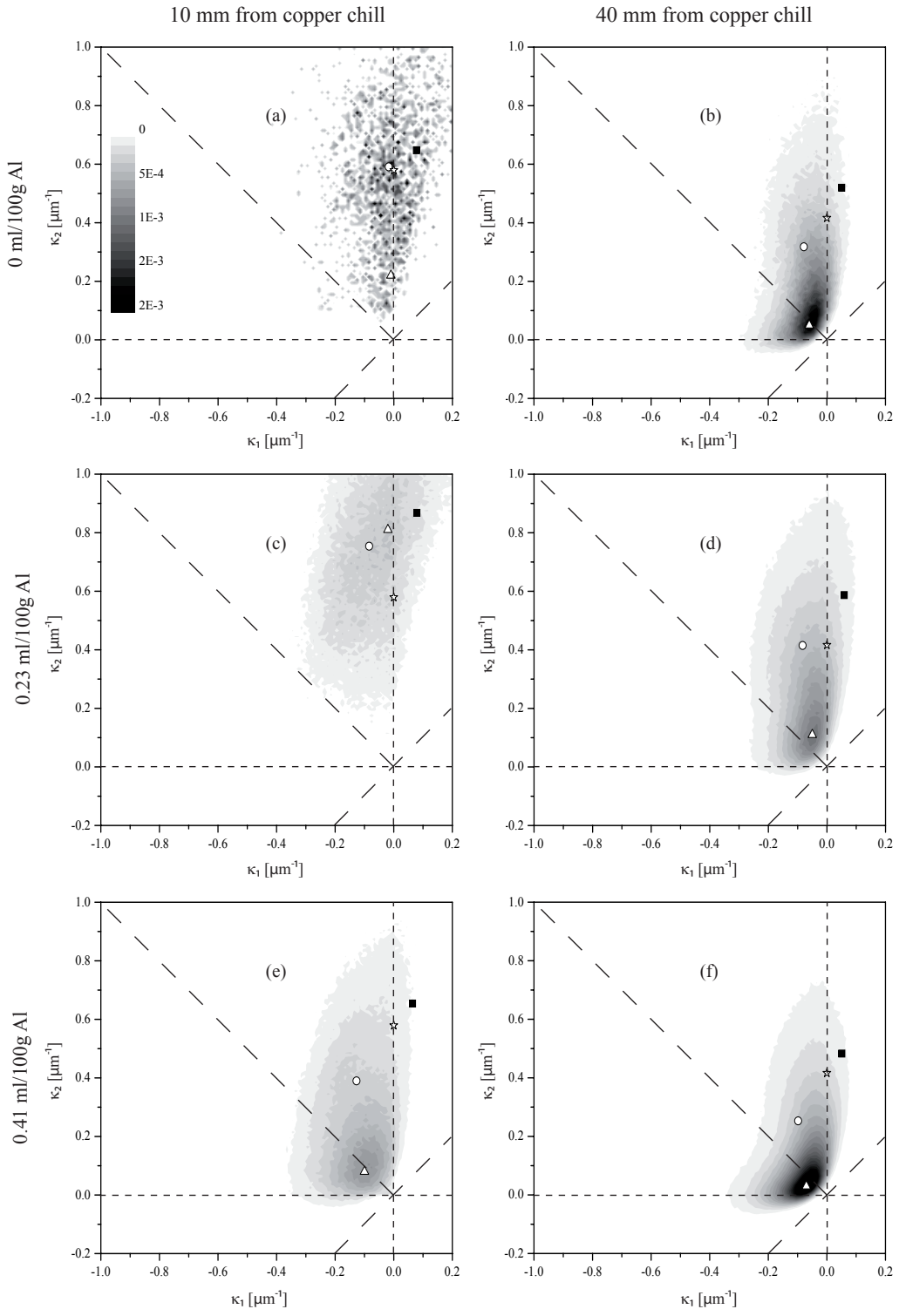

Figure 5.12: Interfacial shape distribution of pores constrained in a non-inoculated Al-4.5wt%Cu network for (left) a fine microstructure and (right) a coarser one. The white circle represents the mean of the distribution and the triangle its maximum. The black square represent the mean of the distribution if one considers only positive values of both κ_1 and κ_2. The star finally represents the value of the curvature as calculated with the pinching model of [4].

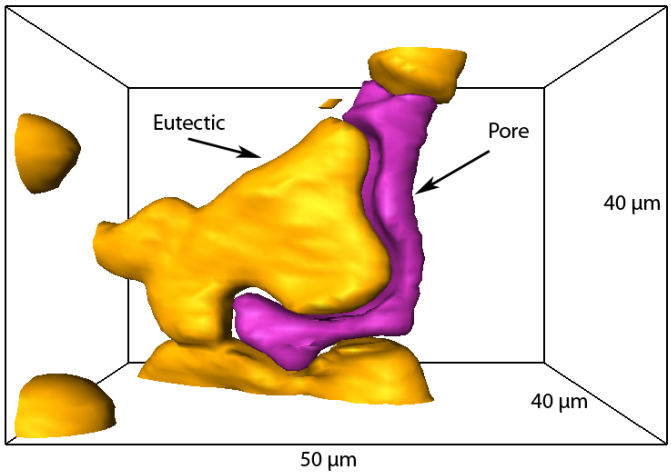

Figure 5.13: 3D volume rendering of a pore (pink) in contact with the eutectic (yellow), the rest of the volume being the primary aluminum phase. Al-4.5wt%Cu alloy cast under argon, i.e., no hydrogen dissolved in the liquid.

be observed and the approximation using Eq. 5.1 fits fairly well the results. Moreover, the sample represented by Fig. 5.4a is very similar to those of Figs. 5.12a, c, and e: the only significant change is the initial hydrogen content (they have about the same thermal conditions), and the fact that the curvature estimated by Eq. 5.1 is a good approximation to the measured $\langle\bar{\kappa}\rangle_{\geq 0}$ value is valid in each case.

5.1.6 Conclusions

In summary, the following conclusions can be drawn from the curvature results:

(i) The curvatures of micropores pinched either in non-inoculated and inoculated alloys can be fairly well approximated to that of cylinders ($\kappa_1 \approx 0$ and $\kappa_2 > 0$),

(ii) The pinching model to account for pore curvature restriction by the solid phase must be dependent on the volume fraction of the primary phase g_α and on the secondary dendrite arm spacing λ_2. However the influence of the initial hydrogen content appears to be negligible,

(iii) The model of a non-wetting pore pinched by a pack of cylinders developed by Couturier and Rappaz [4] gives a fairly good and simple approximation to the curvature distribution of actual pores in Al-Cu alloys. Equation 5.1 is a simplified polynomial approximation to the model developed in [4] that can speed up microporosity calculations,

(iv) High values of the local mean curvature of a pore are in contact with the eutectic, meaning that the value $\langle\bar{\kappa}\rangle_{\geq 0}$ is characteristic of the overpressure inside the pore near the end of solidification.

(v) A pore is elongated along the thermal gradient only if the alloy is non-inoculated.

5.2 Effective hydrogen diffusion coefficient

In this section, we will extract an effective hydrogen diffusion coefficient $D_e(g_s)$ from both X-ray tomography and simulation results. We first validate the model developed in section 4.2 using two simple test cases, before applying it to real microstructures obtained via in-situ X-ray tomography. Finally, the simulation results are compared with effective medium approximations.

5.2.1 Simple test cases

At first, a fictitious 3D microstructure ($60\times60\times60$ nodes (= voxels), i.e. $168\times168\times168$ μm^3) consisting of two layers was considered: a liquid one ($g_\ell = \frac{1}{3}$) and a solid one ($g_s = \frac{2}{3}$). These two layers were then connected either in parallel or in series (see Fig. 5.14), with the boundary conditions described in section 4.2.2. In each case, the mass flux, composition and chemical potential profiles are extracted in both solid and liquid phases as a function of the distance along the x axis, i.e., parallel to the chemical potential gradient. The calculations have been run until a steady-state was achieved and the results are shown in Figs. 5.15 and 5.16. For the parallel mode, it was checked

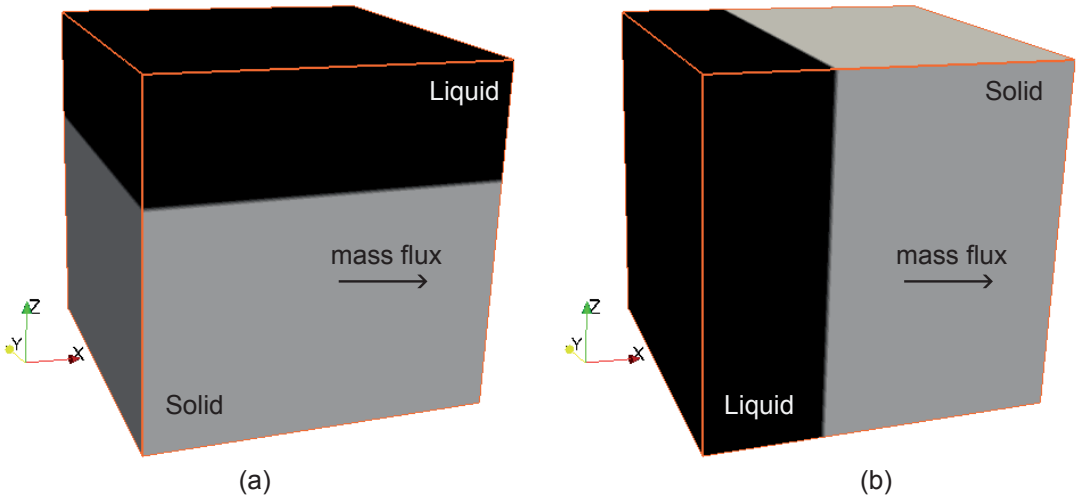

Figure 5.14: Volumes used to validate the hydrogen diffusion model. The solid and liquid layers are connected (a) in parallel and (b) in series.

that the total flux is given by the well known mixture rule, i.e., $J_{Total} = g_s J_s + g_\ell J_\ell$, whereas the flux in the series mode is unique and has a uniform value. Let us focus first on the parallel mode. Figure 5.16a shows the composition profiles in both the solid and liquid phases. By dividing in each phase the flux by its corresponding composition gradient, the solid and liquid diffusion coefficients are of course retrieved. But if we divide the total flux ($J_{Total} = 3.66 \times 10^{-9}\,\mathrm{m\,s^{-1}}$) by the slope of the total average composition profile $\nabla\langle X_H\rangle = \nabla(g_s X_{Hs} + g_\ell X_{H\ell}) = -3.57 \times 10^{-2}\ \mathrm{m^{-1}}$ (see Fig. 5.15), we obtain an average diffusion coefficient, which is not equal the the arithmetic average

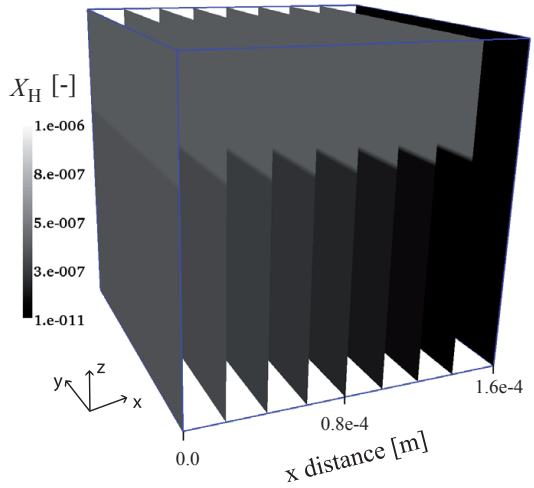

Figure 5.15: On each slice normal to the x-axis, the average composition $\langle X_H \rangle = g_s X_{Hs} + g_\ell X_{H\ell}$ is calculated to deduce the total composition gradient $\nabla \langle X_H \rangle$. The grey scale on the left hand side gives the local hydrogen composition, reason why the liquid layer is brighter than the solid layer in this test-case system connected in parallel. Note that the last slice ($x = 1.6 \times 10^{-4}$ m) seems to have a uniform composition. This is however only an artifact due to the chosen grey scale and the solid and liquid compositions are indeed different (see the last triangle on Fig. 5.16, which is slightly above the last circle).

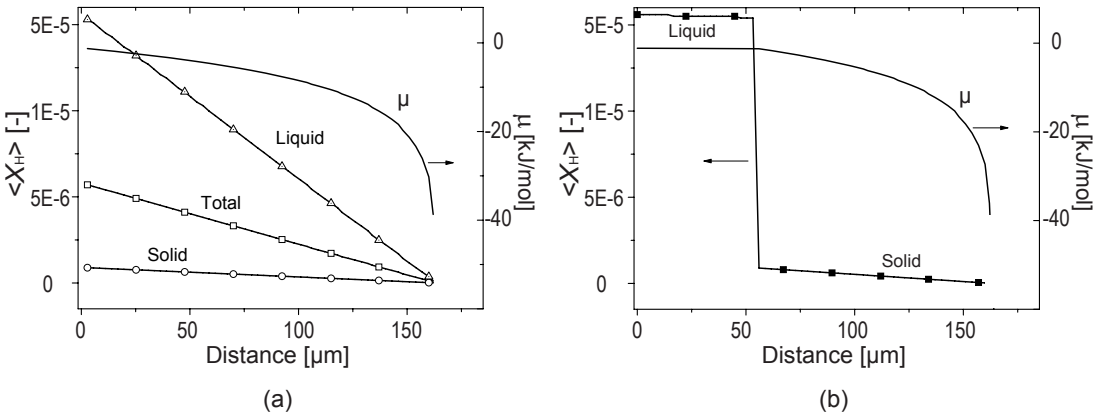

Figure 5.16: Hydrogen molar fraction and chemical potential profiles along the x-axis for the parallel mode (a) and the series mode (b). Note that the chemical potential profile is unique in both cases and is represented by the continuous line (without symbol).

of its components:

$$D_e = -\frac{J_{Total}}{\nabla\langle X_H\rangle} = 1.02\times10^{-7} \neq g_s D_s + g_\ell D_\ell = 6.62\times10^{-8} \tag{5.4}$$

Because we have:

$$\begin{aligned} J_{Total} &= J_s g_s + J_\ell g_\ell \\ &= (D_s\nabla X_s)g_s + (D_\ell \nabla X_\ell) g_\ell \\ &= D_s\nabla(g_s X_s) + D_\ell\nabla(g_\ell X_\ell) \\ &= D_e\nabla(g_s X_s + g_\ell X_\ell) \\ \rightarrow D_e &= \frac{D_s\nabla(g_s X_s) + D_\ell\nabla(g_\ell X_\ell)}{\nabla(g_s X_s + g_\ell X_\ell)} \neq D_s g_s + D_\ell g_\ell \end{aligned} \tag{5.5}$$

Indeed, in order to find an effective diffusion coefficient given by the arithmetic average of the diffusion coefficients, the composition gradient must be the same in both phases. This is not the case in this situation, where the chemical potential and not the composition gradient has been applied between the *East* and *West* frontiers of the domain, as described in section 4.2.2. This situation is similar inside a mushy zone: the hydrogen composition is never the same in the liquid and in the solid, but the chemical potential is. It is thus wrong to solve the problem of finding an effective diffusion coefficient for hydrogen inside a mushy zone by assuming a constant composition gradient, because it is not only a physical problem (diffusion of hydrogen, tortuosity), but also a chemical problem (different solubilities in the solid and in the liquid).

In the series mode, the flux is constant and uniform along the x axis after having reached a steady-state, as the electric current is the same before and after two resistances for an electronic system connected in series. By dividing this flux by the slope of the composition gradient in each phase, once again the solid and liquid diffusion coefficients are retrieved. But due to the configuration of this problem, it is not anymore possible to extract an effective diffusion coefficient, because the solid and liquid fluxes are connected in series and not in parallel.

5.2.2 Real microstructures

In order to deduce an effective diffusion coefficient for hydrogen in a solidifying aluminum alloy, computations have been run on RVEs of microstructures obtained via in-situ X-ray microtomography. The easiness of the explicit model described in section 4.2.1 finds its drawback in the computation time: about 10 days are needed on a Intel Xeon CPU @ 2.5 GHz to reach a steady-state on a single $200\times200\times200$ volume with the initial and boundary conditions described in section 4.2.2. Computations have been run on two different alloys (Al-4.5wt%Cu and Al-10wt%Cu) for four different volume fractions ($g_s = 0.6 \rightarrow 0.9$). Figure 5.17 shows the results (composition map on a cross-section in the xy plane for each g_s) of 3D calculations after a steady-state has been reached. On this figure, the brighter the grey level, the higher the hydrogen molar fraction. Obviously liquid regions are the brightest, and have only very small composition gradients (almost invisible on these figures because of the logarithmic gray

scale). On the other hand, the iso-compositions in the solid are clearly visible and are not perpendicular to the x axis, because of the influence of the 3D microstructure. Please note that the iso-values of the chemical potential would result in straight lines normal to the x axis. Note also that at $x = 0$, the composition in the solid and in the liquid are unequal, since the same equilibrium chemical potential has been applied in both phases.

Then, the composition has been average on each plane x = constant as in Fig. 5.15. Figure 5.18 shows the average composition $\langle X_H \rangle$ as a function of the distance from the plane $x = 0$ for each solid fraction g_s of an Al-4.5wt%Cu alloy (note that a similar trend is obtained for the Al-10wt%Cu alloy). The composition profiles appear all to be linear, which allows to make a linear regression for all the volume fractions of solid. From the test case, we know that such a linear profile shape is characteristic of a system connected in parallel, so that $J_{Total} = g_s J_s + g_\ell J_\ell$. But unlike in the parallel mode test-case, the points do not lie exactly on one single line, because of the intricate shape of the mushy zone and because some small liquid pockets exist, perturbing the latter equation. Also, the solid fraction in each plane x = constant differs slightly from the volumetric fraction of solid, skewing the results. Nevertheless, a correlation coefficient $R^2 \geq 0.99$ was always obtained, which allows us to divide the calculated total flux by the average composition gradient $\nabla \langle X_H \rangle$ (= slope of the linear fit) in order to extract an effective diffusion coefficient for each alloy at each solid fraction, as already done for the parallel test-case. The results are summarized in Tables 5.6 and 5.7.

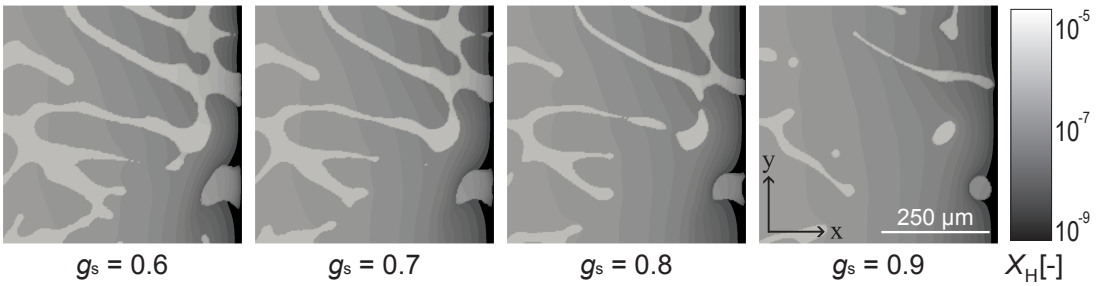

Figure 5.17: Cross-sections in the xy plane of the steady-state hydrogen composition maps as a function of the solid fraction g_s. Note the logarithmic grey scale for the composition and the coordinate system on the right hand side.

These effective diffusion coefficients were then compared to effective-medium theories for the three different approximations described in section 2.7.2. The results are shown in Fig. 5.19. As already mentioned in section 2.7.2, the self-consistent theory treats each phase symmetrically; this is why D_e can be much lower than D_s. In our case, this approximation is poor and hence the phases cannot be treated symmetrically, even if both phases are percolated in the considered solid fractions. On the other hand, the Hashin-Shtrikman upper bond deals clearly (as the DEM) with one phase

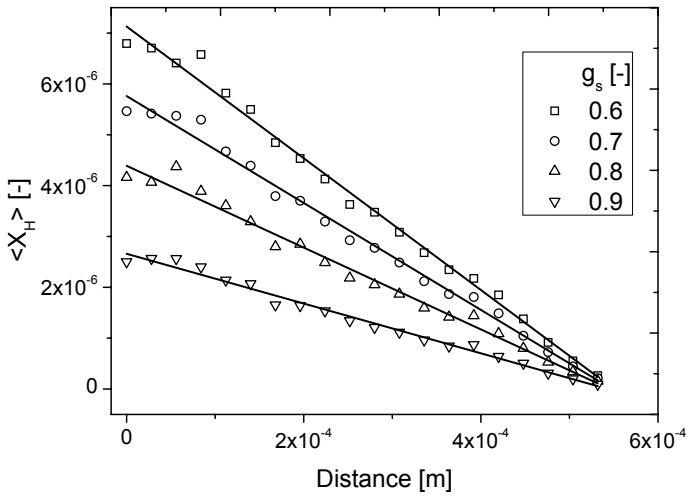

Figure 5.18: Average hydrogen molar fraction profile along the x axis for various volume fractions of solid in an Al-4.5wt%Cu alloy. Each black line shows a linear fit with a correlation coefficient of 0.99. A similar profile is obtained for a Al-10wt%Cu.

Table 5.6: Effective hydrogen diffusion coefficient for an Al-4.5wt%Cu alloy at four different volume fractions of solid.

g_s [-]	$\mathbf{J}_{Total}$ [m/s]	$\nabla\langle X_H\rangle$ [1/m]	D_e [m^2/s]	$g_s D_s + g_\ell D_\ell$
0.6	8.49 10^{-10}	-1.29 10^{-2}	6.55 10^{-8}	7.05 10^{-8}
0.7	6.39 10^{-10}	-1.05 10^{-2}	6.08 10^{-8}	6.41 10^{-8}
0.8	4.46 10^{-10}	-8.04 10^{-3}	5.55 10^{-8}	5.76 10^{-8}
0.9	2.21 10^{-10}	-4.89 10^{-3}	4.52 10^{-8}	5.12 10^{-8}

Table 5.7: Effective hydrogen diffusion coefficient for an Al-10wt%Cu alloy at four different volume fractions of solid.

g_s [-]	$\mathbf{J}_{Total}$ [m/s]	$\nabla\langle X_H\rangle$ [1/m]	D_e [m^2/s]	$g_s D_s + g_\ell D_\ell$
0.6	8.72 10^{-10}	-1.16 10^{-2}	7.53 10^{-8}	7.05 10^{-8}
0.7	6.07 10^{-10}	-8.98 10^{-3}	6.76 10^{-8}	6.41 10^{-8}
0.8	3.90 10^{-10}	-6.53 10^{-3}	5.97 10^{-8}	5.76 10^{-8}
0.86	2.44 10^{-10}	-4.66 10^{-3}	5.24 10^{-8}	5.38 10^{-8}

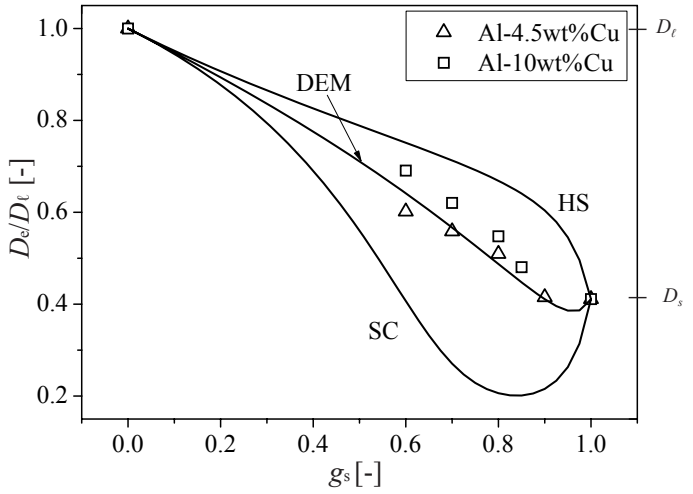

Figure 5.19: Computation results and effective medium approximations for an effective diffusion coefficient (normalized by the liquid diffusion coefficient) as a function of the solid volume fraction.

considered as the matrix, the other as inclusions. The HS approximation shows better agreements than the SC approximation, but it has been observed that when the phase contrast is high (here we have a "conductivity" ratio ($= \mathfrak{D}_\ell/\mathfrak{D}_s$) of 7.5 between the liquid and the solid), the DEM approximation gives better results than the Hashin-Shtrikman relationship [63]. This very large phase contrast is the reason why the DEM approximates closely the simulation results. Interestingly, D_e can decrease under D_s in this case too, because the remaining liquid droplets at high volume fractions of solid may act as sink for hydrogen and "pump" the hydrogen from the solid, reducing further the overall diffusion coefficient. Note also that the considered effective medium theories

Table 5.8: Surface volume ratio as a function of the solid volume fraction for both Al-4.5wt%Cu and Al-10wt%Cu alloys. The values are given in [m^{-1}].

g_s [-]	S_V Al-4.5wt%Cu		S_V Al-10wt%Cu	
	Measured	$6g_s/\lambda_2$	Measured	$6g_s/\lambda_2$
0.6	3.64×10^4	3.35×10^4	3.87×10^4	5.82×10^4
0.7	2.60×10^4	3.63×10^4	3.13×10^4	6.18×10^4
0.8	2.11×10^4	3.79×10^4	2.39×10^4	5.25×10^4
0.9 (0.86)	1.27×10^4	4.09×10^4	1.69×10^4	5.20×10^4

are valid for isotropic RVEs only. Although RVEs of $560 \times 560 \times 560$ μm^3 could be extracted from the tomography experiments, they may not be exactly representative or even isotropic. Moreover, the latter theories are based on volume fraction information only, and do not include any tortuosity or surface over volume ratio (S_V) influence. Indeed, the value of S_V theoretically decreases as solidification proceeds [35]. Table 5.8 gives the measured and calculated values of S_V for both alloys. To measure S_V, we have divided the area of the solid-liquid interface (defined by the sum of the triangles describing this interface) by the some of the solid voxels. The calculated values were

obtained using the relationship developed by Carman [36], $S_V = 6g_s/\lambda_2$, where λ_2 is the measured λ_2 spacing. Although S_V decreases as g_s increases for the measured values, it is not the case for the calculated ones. This is probably due to the large incertitude of the λ_2 spacing measurements. It is indeed difficult to estimate the λ_2 spacing from the X-ray tomography data. However the relationship $S_V = 6g_s/\lambda_2$ should give theoretically the right trend, since g_s varies with $1 - t^{1/(k_0-1)}$ (if a Scheil approximation is assumed), whereas λ_2 varies proportionally to $t^{1/3}$ (which is larger). Nevertheless, good agreement is found between measured and calculated values. (Note that these values have the same order of magnitude than that reported by [101] for a solidified Al-10wt%Cu alloy that encountered different cooling conditions ($S_V = 3.5 \times 10^4$ m^{-1} in their case).)
In our experiments, S_V(Al-10wt%Cu) $\approx 2 \times S_V$(Al-4.5wt%Cu). This could explain the small discrepancies in the effective diffusion coefficients between the two alloys. Nevertheless, for a given volume fraction of solid, the values of the effective hydrogen diffusion coefficient of both alloys are close and they are well fitted by the DEM approximation.

It must be noted that the DEM approximation is quite heavy to use (solving analytically Eq. 2.48 is not straightforward at all) and surprisingly, we can see that taking $D_e = g_s D_s + g_\ell D_\ell$ is actually already a good approximation. Good agreement is indeed observed between this relationship and the simulation results, as shown in Tables 5.6 and 5.7. Because of the simplicity of this result, we recommend to use the linear approximation $D_e(g_s) = g_s D_s + g_\ell D_\ell$ to deduce an effective diffusion coefficient, even if this relationship does not have any physical background.

5.3 Behavior of a macropore observed by in-situ XRT

The purpose of this section is to present the X-ray tomography results of the evolution of a macropore observed *in-situ* at high temperature. We remind here that the Al-10wt%Cu sample, saturated in hydrogen, was heated up inside an induction furnace and observed at high temperature through X-ray tomography. The experiment was separated into two phases. First the sample was observed at a constant temperature of 612 °C (see section 5.3.1). Then, while the X-ray tomography data were acquired, the sample was cooled down to 540 °C at a constant rate of -2.5 °C min^{-1} (see section 5.3.2).

5.3.1 Phase I: Isothermal holding

During phase I of this experiment, the sample was held at 612 °C for 37 minutes. We will first see that the lever rule can be applied to the Al-Cu system over this period of time.
The upper part in Fig. 5.20 shows the evolution (in 2D) of the sample microstructure as a function of time. It is a set of reconstructions taken at different times, i.e., 2D cross-sections of the mushy sample, taken at about mid-height. In this figure, the solid is represented in light grey, whereas white represents the liquid and dark grey the

pore phase. Looking at this figure, it seems that the volume fraction of solid does not evolve. Indeed the copper diffusion coefficient D_{Cu} in primary solid aluminum at 612 °C is about $7 \times 10^{-13}\,\mathrm{m^2\,s^{-1}}$ [29]. Taking a characteristic length L of the microstructure of $20 \times 10^{-6}\,\mathrm{m}$, the characteristic time for diffusion L^2/D_{Cu} is about 10 min. On the other hand, it took about 15 min to reach 612 °C (the furnace temperature was kept at 400 °C before the experiment was running) and to launch the data acquisition. The volume fraction of solid (calculated via Eq. 4.1) should thus be given by the lever rule during this isothermal holding. The solid, liquid and pore voxels have been counted in order to deduce their respective volume fractions, and a volume fraction of solid $g_s = 0.49$ was measured on all the X-ray tomography scans for $0 \leq t \leq 37$ min using Eq. 4.1. According to lever rule, $g_\alpha = 0.49$ for an Al-10wt%Cu alloy at 612 °C. (Note that we have used the values given in [21] to convert mass fraction of solid to volume fraction of solid.) The lever rule can thus be applied with no doubt to the Al-Cu system in this case.

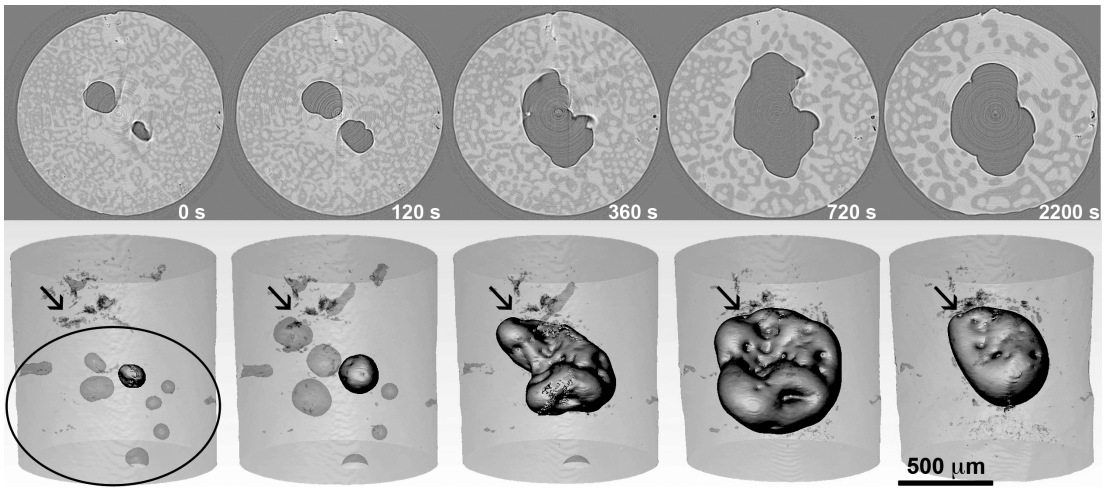

Figure 5.20: Coalescence of pores during isothermal holding at $T = 612$ °C $\rightarrow g_s = 0.49$; The upper part of the figure shows 2D cross-sections (taken at mid-height) of the reconstructed microstructures at different times. White, light grey, and dark grey regions correspond to the liquid, solid and pore phases, respectively. The lower part of the figure shows corresponding 3D views of the pore phase. Finally, the arrow shows where the pore is attached after coalescence.

On the other hand, even if the volume fraction of solid remains constant, we can clearly see an evolution of the microstructure. We remind here that, prior to the X-ray tomography experiments, the alloy was quenched from the liquid state in order to saturate the alloy with hydrogen. The microstructure is thus initially very fine and coarsens during isothermal holding to reduce the energy of the system, as described by Limodin *et al.* [25].

Let us focus now on the pore phase. The upper part of Fig. 5.20 shows the evolution of the morphology of the pore phase as a function of time in 2D. The first image shows that two pores have already nucleated at the onset of the isothermal holding because the cast sample was initially saturated with hydrogen. Because it is thermodynamically favorable for the hydrogen to be in the pore phase than in a dissolved state, these

two pores then grow (second image) and coalesce (third image). After 720 s (fourth image), the maximum pore size is reached and from then on, the pore size decreases (fifth image) by loosing hydrogen to the atmosphere through the mushy alloy. There is indeed a gradient of hydrogen partial pressure (and hence of hydrogen chemical potential) between the interior of the pore phase (p_{H_2} high) and the ambient partial pressure (p_{H_2} low), leading to a net flux of hydrogen from the pore to the outside of the sample through the mush.
The bottom part of Fig. 5.20 shows the pore shape in 3D for each corresponding microstructure (both solid and liquid phases are thus invisible here). It reveals that at the beginning of the experiment, not only 2 pores, but about 8 small spherical pores (encircled on the first image, the rest being artifacts or small oxide skins) have already nucleated and further grow to coalesce and form one "macropore". The arrows on the images show the point where the pore is attached. Because of a hydrogen flux from the pore to the outside of the sample, the pore size then decreases as function of time as shown in Fig. 5.21. It must be noted that, to the author's knowledge, it is the first time that real-time pore coarsening could be observed in 3D with a resolution that is high enough to capture the details of the morphology.

Following the developments presented in section 2.4.2, an Al-10wt%Cu alloy would have a hydrogen concentration of 0.31 $\mathrm{cc_{STP}}/100\mathrm{g}$ at 833 °C, whereas the hydrogen solubility limit in the liquid phase equals 0.20 $\mathrm{cc_{STP}}/100\mathrm{g}$ at 612 °C. Assume the sample mass mass is

$$m = \rho_s V_s = 2.7 \times 10^{-3}\ \mathrm{g\,mm^{-3}} \times \pi \left(\frac{1.4\ \mathrm{mm}}{2}\right)^2 3\ \mathrm{mm} \approx 12.5 \times 10^{-3}\,\mathrm{g}$$

and that the quench was fast enough so that the sample has an overall hydrogen composition of 0.31 $\mathrm{cc_{STP}}/100\mathrm{g}$. There is thus 38.75×10^{-3} $\mathrm{mm^3_{STP}}$ of hydrogen dissolved initially. On the other hand, the sample can dissolve $\frac{m}{2}(1 + k_{0H})0.20 \approx 13.375 \times 10^{-3}$ $\mathrm{mm^3_{STP}}$ of hydrogen at 612 °C. This difference of 25.375×10^{-3} $\mathrm{mm^3_{STP}}$ of dissolved hydrogen corresponds to a volume of 0.08 $\mathrm{mm^3}$ of hydrogen at 612 °C. However we measured a peak value of the pore volume (≈ 0.26 $\mathrm{mm^3}$) more than three times this number as shown in Fig. 5.21. It is suspected that the zirconia paste – having some hydrogenated component – is responsible for this discrepancy, the hydrogen contained in the paste diffusing through the sample to the pore. Nevertheless, after 720 s, all the available hydrogen has diffused to the pore (and simultaneously into the ambient atmosphere) and from then on, the pore can only loose hydrogen and decrease in size.

We have calculated an effective hydrogen diffusion coefficient function of g_s only (see Fig. 5.19). At 612 °C, the hydrogen diffusion coefficients in the solid and in the liquid are respectively $3.07 \times 10^{-8}\,\mathrm{m^2\,s^{-1}}$ and $7.43 \times 10^{-8}\,\mathrm{m^2\,s^{-1}}$ [43], leading to an effective hydrogen diffusion coefficient $D_e \approx 5.30 \times 10^{-8}\,\mathrm{m^2\,s^{-1}}$. Taking a typical length of 300 μm (= distance between the surface of the pore and the surface of the sample), the characteristic time for diffusion of hydrogen is about 2 s. This proves that hydrogen diffusion does indeed occurs and is responsible for the decrease of the pore size.

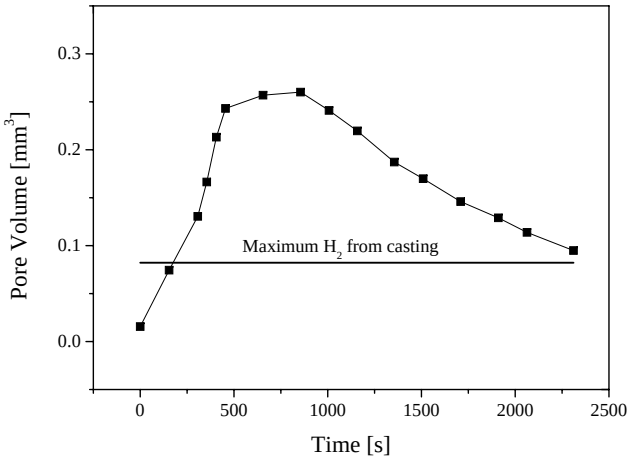

Figure 5.21: Pore volume evolution during isothermal holding at 612 °C → $g_s = 0.49$. The horizontal line gives the volume that a pore would have at 612 °C if it resulted from the hydrogen solubility difference between 833 °C and 612 °C.

5.3.2 Phase II: solidification

After 37 min of isothermal observation, a cooling rate $\dot{T} = -2.5\,^{\circ}\mathrm{C\,min^{-1}}$ has been imposed. It is easy to verify that the temperature distribution is uniform during this solidification process and is equal to the furnace temperature[2]. Once again, before analyzing the pore phase, let us see if the lever rule or the Scheil approximation is applicable during the solidification experiment.
Figure 5.22 shows the volume fraction of solid g_s as a function of the temperature using both models, as well as the experimental X-ray tomography data. Again, the solid and liquid densities were calculated using the values of [21]. Figure 5.22 shows that the lever rule fits well the experimental data. Another behavior would have been odd, since the cooling rate is slow and the characteristic diffusion time of copper associated with λ_2 (about 10 min) is smaller than the solidification time (about 25 min). The first scan of phase II was taken about 2 min after the last scan of phase I. It is shown in the first image of Fig. 5.23. On the upper part of this figure (which has the same contrast as the upper part in Fig. 5.20), 2D cross-sections of the reconstructed sample (taken at mid-height) indicates that the volume fraction of solid g_s increases as the temperature decreases. Also, as the liquid becomes richer in copper as solidification proceeds, it absorbs more the X-rays and becomes brighter in reverse contrast. The bottom part of the figure shows the 3D volume rendering of the pore (corresponding to the upper microstructure) colored by its local mean curvature (calculated with Avizo); green regions correspond to locally spherical regions, whereas blue and red regions

[2]Taking the Biot number $Bi = \frac{h\Delta x}{k} = \frac{200 \cdot 0.5 \times 10^{-3}}{100} = 1 \times 10^{-3}$, where $h = 200\,\mathrm{W\,m^{-2}\,K^{-1}}$ is an estimated convective heat transfer coefficient, Δx the radius of the sample and k the thermal conductivity of the sample, the temperature difference between the center of the sample and its surface, ΔT_{int}, is given by $\Delta T_{int} = Bi \Delta T_{ext}$. On the other hand, ΔT_{ext} is given by $\Delta T_{ext} = \frac{|\dot{T}|\rho c_p V}{hS} = 0.6\,^{\circ}\mathrm{C}$, where ρc_p is the volumetric heat capacity of the alloy, V the sample volume and S its surface.

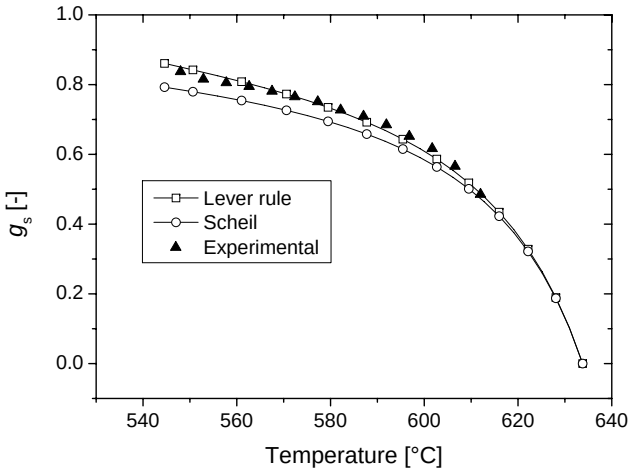

Figure 5.22: Comparison of the Scheil and lever rule with the experimental data for the Al-10wt%Cu specimen observed in-situ by X-ray tomography.

exhibit locally highly negative, respectively positive, mean curvature values (neither the solid nor the liquid phase is shown). As the volume fraction of solid g_s increases, the pore volume decreases (because the pore still looses hydrogen) down to 564 °C (second image in Fig. 5.23); from then on, the pore size increases (the pore is larger at 551 °C than at 564 °C) and reaches its final shape and size at the eutectic temperature (the sample was scan down to 530 °C, but no significant changes have been observed at temperatures below T_{eut}).

Figure 5.24 represents the sample volume, with and without the pore, together with the pore volume as a function of temperature. As the temperature decreases, the

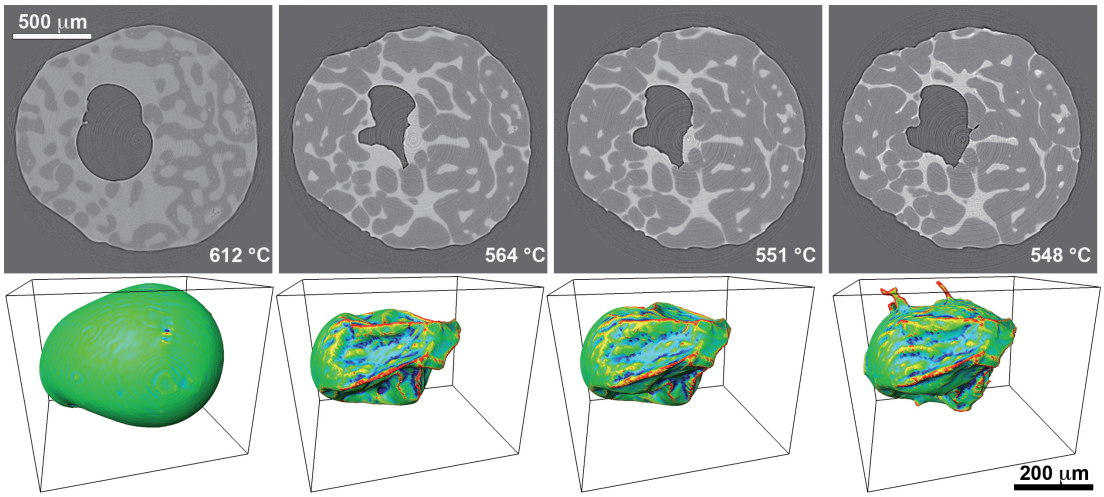

Figure 5.23: Upper part: 2D cross-sections of the pore evolution during solidification with the same contrast as in Fig. 5.20. Lower part: 3D representation of the pore during solidification. Red and blue regions show positively, respectively negatively, curved regions.

volumes of the pore and of the whole sample first decrease, because the pore looses hydrogen by diffusion through the solidifying alloy, and the gas and dense phases (liquid

and solid) shrink. But the "Sample+Pore" curve stays about constant between 564 and 551 °C, whereas the pore volume increases by about 1.07×10^{-2} mm^3. Assuming complete mixing of hydrogen in the solid and in the liquid, the total volume of hydrogen coming from the decrease in solubility of the liquid corresponds to 2.22×10^{-4} mm^3 (taking also into account hydrogen segregation associated with solidification), which is much lower that the observed volume increase. As the temperature is uniform in

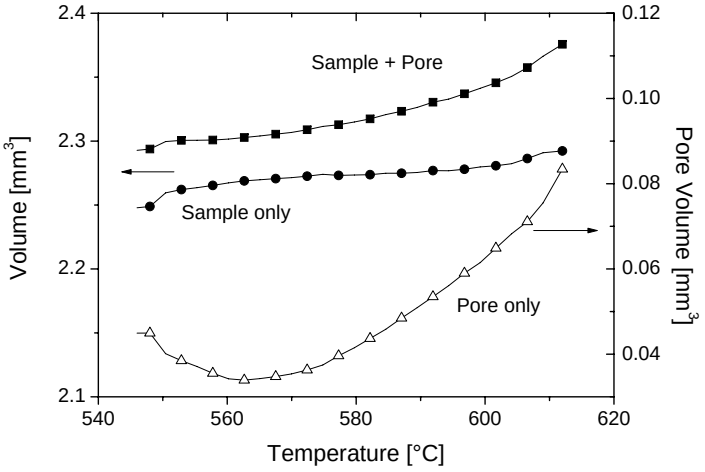

Figure 5.24: Pore and sample volume evolution during solidification.

the whole sample, no eutectic has formed between these 300 s. Therefore, the only possible mechanism for such a pore volume increase is solidification shrinkage. Indeed, at 564 °C (which corresponds to a volume fraction of solid $g_s = 0.8$), the surface of the sample has percolated, and most of the liquid is around the pore. This can be clearly seen on the upper part in Fig. 5.23. Therefore, between 564 and 551 °C, solidification shrinkage can only be compensated by an increase of the pore phase, since the surface of the sample cannot move anymore. Consequently, the pressure in the liquid decreases as solidification proceeds and the pore adapts its volume consequently. To sum up, it seems then that solidification shrinkage plays an important role on the shape of gas porosity and can even be crucial in terms of its volume fraction.

To conclude this section, we would like to show how X-ray tomography offers very interesting possibilities of data gathering. During the present analysis, we have used the density data given by Ganesan and Poirier [21] to convert mass fraction of solid to volume fraction of solid. Considering the voxels of the solid and liquid phases only, the actual volume of the sample can be deduced as a function of temperature, i.e., X-ray tomography becomes a densitometry experiment[3]. It is well known that from the mass conservation equation one has $\frac{V^0}{V(T)} = \frac{\rho(T)}{\rho^0}$, where V^0 ($V(T)$) and ρ^0 ($\rho(T)$) are the initial (temperature dependent) volume and density, respectively. Figure 5.25

[3]This is true under the assumption of lateral deformation only, since the field of view allows observation of the full width of the sample, but not of its full height.

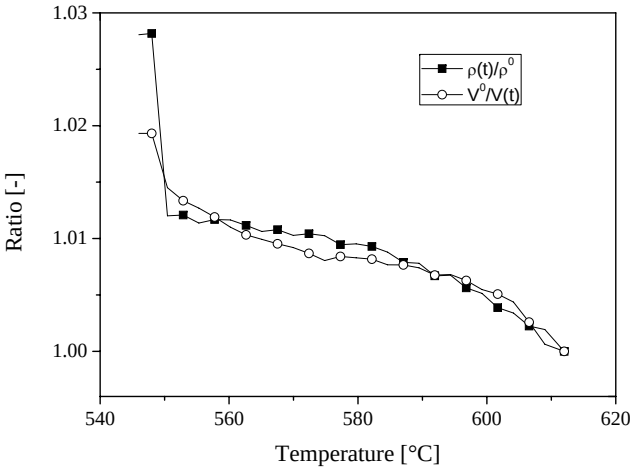

Figure 5.25: Comparison between density data from Ganesan and Poirier [21] (black squares) and experimental data from this work (open circles).

shows the comparison between the density values from [21] (black squares) and the experimental data (open circles) of the sample volume from this work. Although there is some misfit at the eutectic temperature, the agreement is excellent, proving that solidification shrinkage is responsible for the 20vol% increase between 564 and 551 °C, and justifying the use of density values from [21] during this study.

5.4 Influence of curvature and hydrogen diffusion

As described in section 4.3, we will use the effective hydrogen coefficient diffusion developed in this thesis to model pore growth limited by hydrogen diffusion. We define a spherical equivalent pore radius R_p^{sph} so that the relationship $\mathcal{N}_p \frac{4}{3}\pi (R_p^{sph})^3 = g_p$ stands, where $\mathcal{N}_p$ is the density of pores. The domain within which hydrogen diffusion is considered has therefore a typical radius $R_{p0} = \left(\frac{3}{4\pi\mathcal{N}_p}\right)^{1/3}$. We consider the solidification of an Al-7wt%Si alloy, whose solidification path is given by the Scheil approximation (see Eq. 2.2). We then:

1– Use a constant cooling rate of $-2\,^{\circ}\mathrm{C\,s^{-1}}$, and deduce a solidification time $t_f = 18.6\,\mathrm{s}$. Such a solidification time is appropriate, since both characteristic times for the movement of the interface and for hydrogen diffusion are much lower than t_f (see Appendix C for the details). This allow us to use the steady-state solution of the hydrogen diffusion equation. Assume that the temperature within the domain of radius R_{p0} is uniform. This is achieved when $2GR_{p0} \ll \Delta T_0$, where G is the thermal gradient and ΔT_0 the solidification interval. Therefore, the fraction of solid g_s and the effective hydrogen diffusion coefficient are uniform in the sphere of radius R_{p0} at each time t.

2– Deduce the Si composition in the solid and in the liquid at each temperature. This allows us to calculate the hydrogen concentration in both phases as a function

of the Si content (using Table 2.1 and Eqs. 2.30 or 2.37 alternatively,) and thus calculate $\langle X_H \rangle$ using Eq. 4.28.

3– Use the coarsening law ($\lambda_2(t)$) given by Eq. 2.5 to deduce first the secondary dendrite arm spacing at the eutectic temperature $\lambda_2^{eut} = \lambda_2(T = T_{eut})$. Knowing this value, the relationship $R_p(g_s(t), \lambda_2^{eut})$ given by Eq. 5.1 is used to model the pinching of the pore by the solid network and thus for the pressure inside the pore.

Table 5.9 gives the main parameters for the calculations, whereas Fig. 5.26 recalls the model for pore growth as well as the pinching model used in our simulations.

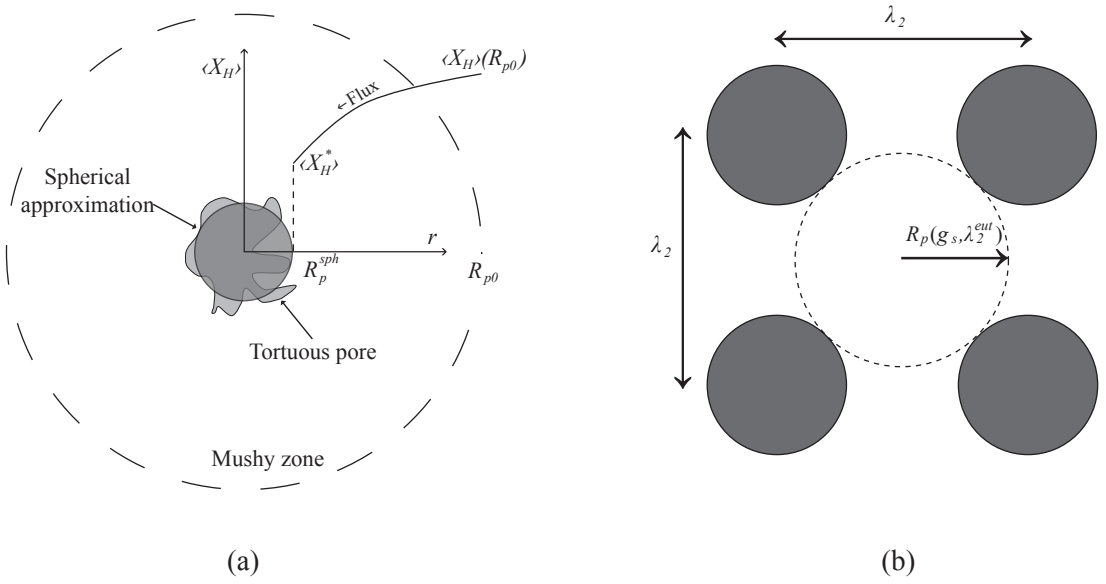

Figure 5.26: (a) Pore growth model and (b) pinching model.

Concerning the curvature restriction of the pore phase by the solid network, we will use the pore curvature results presented in section 5.1. Accordingly, we will apply Eq. 5.1 to calculate the critical radius of the growing pore. At the beginning of the calculation, the pore is assumed to remain spherical. It then grows because of hydrogen diffusion. But once the actual pore radius R_p^{sph} is larger than $R_p(g_s(t), \lambda_2^{eut})$ calculated via Eq. 5.1, the radius of curvature of the pore is maintained constant and does not evolve anymore. However, the pore fraction continues to increase: even if the pore radius is fixed, the pore fraction itself continues to evolves. This approach is similar to that developed by Péquet *et al.* [2]. Note that we use the relationship $R_p(g_s(t), \lambda_2^{eut})$ and not $R_p(g_s(t), \lambda_2(t))$, since it is the final secondary dendrite arm spacing $\lambda_2^{eut} = \lambda_2(T = T_{eut})$ that must be taken into account according to the curvature results of section 5.1.
For the results, in order to investigate the influence of the pinching, $R_p(g_s(t), \lambda_2^{eut})$ will be either set to infinity (no pinching is taken into account) or calculated using Eq. 5.1 (pinching is taken into account).

Table 5.9: Parameters used in the volume-averaged model calculations. Note that the liquid pressure has been taken as a constant (= 1 atm) for the calculations, but a similar law as described by Eq. 2.60 and depicted in Fig. 2.18 could also be assumed.

Parameter	Value
Alloy liquidus	614.2 °C
Alloy eutectic temperature	577 °C
Initial liquid pressure	1×10^5 Pa
Final liquid pressure	1×10^5 Pa
Pore density	$3 \times 10^9\,\mathrm{m}^{-3} \leq \mathcal{N}_p \leq 3 \times 10^{10}\,\mathrm{m}^{-3}$
Pore nuclei radius	1×10^{-5} m
Pore surface energy	$\gamma_{\ell g} = 0$ or $0.8\,\mathrm{J\,m}^{-2}$
Gas nominal concentration	$0.3\,\mathrm{cc_{STP}}/100\mathrm{g}$
Solidification time	18.6 s

For clarification, Fig. 5.27 shows the evolution of R_p^{sph} as well as $R_p(g_s(t), \lambda_2^{eut})$ as a function of the solid fraction (for a final $\lambda_2^{eut} = 36 \times 10^{-6}$ m). As soon as $R_p(g_s(t), \lambda_2^{eut}) < R_p^{sph}$ (dotted line), pinching occurs and if the pinching model is taken into account, the pore radius does not change anymore and stays constant until the end of solidification. We will see that this law is already quite restrictive on the pore radius.

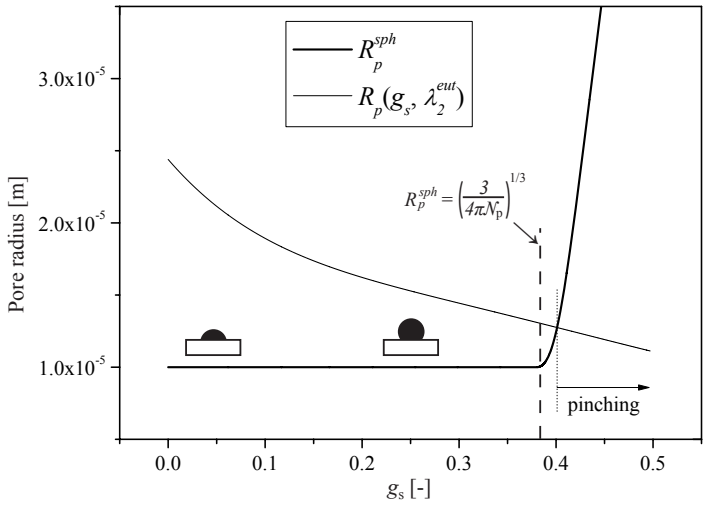

Figure 5.27: Evolution of R_p^{sph} as well as $R_p(g_s(t), \lambda_2^{eut})$ as a function of the solid fraction (for a final $\lambda_2^{eut} = 36 \times 10^{-6}$ m). If pinching is taken into account, the pore radius is kept constant as soon as $R_p(g_s(t), \lambda_2^{eut}) < R_p^{sph}$ (Note that for the purpose of the illustration, this is not the case here).

The results will be presented as follows: the pore radius as well as the pore density will be given as a function of the solid fraction g_s for three cases:

(i) The model assumes a spherical pore during the entire growth (no curvature restriction due to the solid phase), and curvature is neglected, i.e., $\gamma_{\ell g} = 0$. This

allows to assess the influence of hydrogen diffusion only. For that purpose, calculations have been performed with the effective hydrogen diffusion coefficient developed in this work (i.e., limited diffusion) or a value 100× larger ("accelerated diffusion"), i.e., nearly complete mixing of hydrogen in the volume of radius R_{p0},

(ii) The model accounts for limited diffusion and for the influence of curvature, i.e., $\gamma_{\ell g} \neq 0$, but neglects pinching,

(iii) The model takes into account hydrogen limited diffusion, pinching and curvature effects ($R_p(g_s, \lambda_2^{eut})$ is calculated via Eq. 5.1, and $\gamma_{\ell g} \neq 0$).

We remind here that the Fourier number gives the ratio of the solidification time to the time for diffusion at the scale of R_{p0}. For the model to be valid, the Fourier number must be large. Accordingly, we have chosen three different pore densities as given in Table 5.10, that satisfy this condition.

Table 5.10: Relationship between the pore density $\mathcal{N}_p$, the radius of the domain R_{p0}, and the Fourier number for a solidification time of 18.6 s and an effective diffusion coefficient of $\frac{1}{2}\left(D_{\ell H}^{660\,^\circ\mathrm{C}} + D_{sH}^{660\,^\circ\mathrm{C}}\right) = 7.69 \times 10^{-8}\,\mathrm{m^2\,s^{-1}}$, where both liquid and solid diffusion coefficients have been evaluated after [43].

$\mathcal{N}_p$	R_{p0}	Fo
$3 \times 10^9\,\mathrm{m^{-3}}$	$4.30 \times 10^{-4}\,\mathrm{m}$	8
$8 \times 10^9\,\mathrm{m^{-3}}$	$3.10 \times 10^{-4}\,\mathrm{m}$	14
$3 \times 10^{10}\,\mathrm{m^{-3}}$	$2.00 \times 10^{-4}\,\mathrm{m}$	36

As explained earlier, we have first investigated the influence of hydrogen diffusion for a spherical pore without considering the pinching and curvature overpressure, i.e., $\gamma_{\ell g} = 0$. The results are shown in Fig. 5.28. The upper graph of this figure shows the evolution of the pore radius of curvature as a function of the solid fraction g_s for the three considered pore densities. In these calculations, we have either considered a limited diffusion case (thick lines) or an accelerated diffusion case (thin lines). We can see that by the end of the solidification process (i.e., at $g_s = 0.49$: remember that an Al-7wt%Si alloy has a final eutectic volume fraction of about 0.51 assuming a solidification path given by the Scheil approximation), the pore radius of curvature is almost independent of the diffusion coefficient, especially for small R_{p0}, i.e., high $\mathcal{N}_p$. The same conclusion can be drawn from the pore fraction evolution (bottom graph). This shows that, depending on the Fourier number (see Table 5.10) a state of complete mixing of hydrogen is achieved. If this is not the case, the fraction of porosity is lower, as the mushy zone remains slightly supersaturated.

Now that we have seen that limited hydrogen diffusion is an important factor for the growth of pores, we will investigate the curvature and pinching influence on the pore radius and pore fraction. This was first done for a small value of $\mathcal{N}_p = 3 \times 10^9\,\mathrm{m^{-3}}$

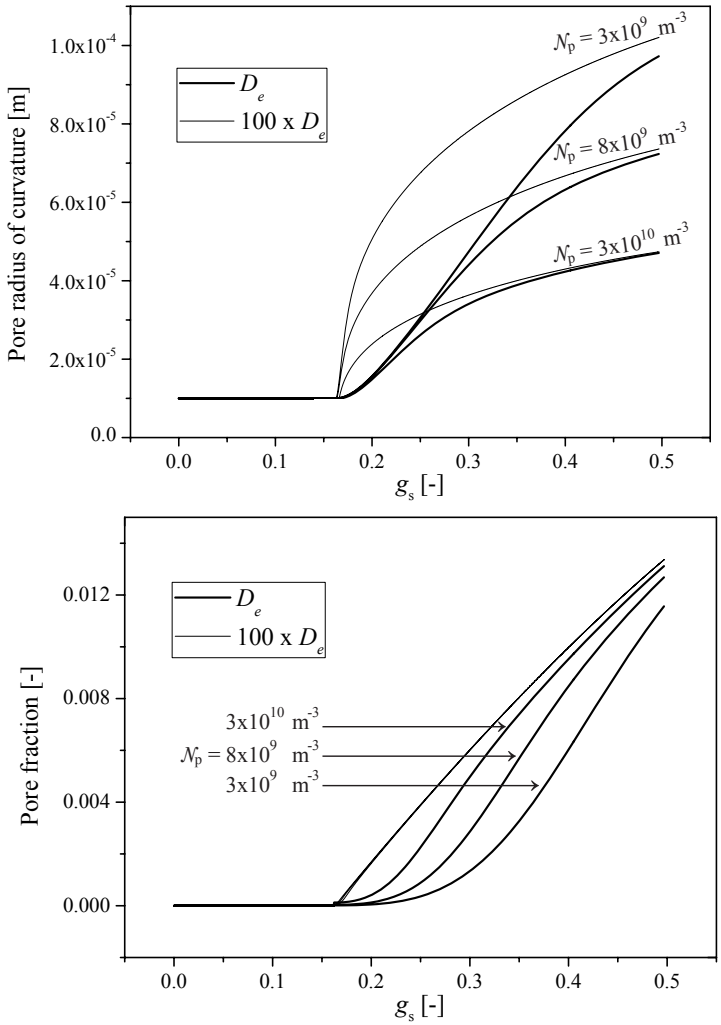

Figure 5.28: Pore radius of curvature (upper graph) and pore fraction (bottom graph) calculated as a function of the solid fraction g_s with the effective hydrogen diffusion coefficient developed in this work (thick lines) and with a value 100 times larger (thin lines). Note that the pore density $\mathcal{N}_p$ is specified in each case and that no pinching effect was taken into account. Note also that the three lines for "accelerated diffusion" are superimposed on the bottom graph, indicating that complete mixing of hydrogen is achieved for all three cases.

(see Fig. 5.29) and then for a larger value of $\mathcal{N}_p = 3 \times 10^{10}\,\mathrm{m}^{-3}$ (see Fig. 5.30). The results are summarized in Table 5.11.

Table 5.11: Final pore fraction and pore radius as a function of the pore density for the three different considered cases.

	No pinching + $\gamma_{\ell g} = 0$		No pinching + $\gamma_{\ell g} \neq 0$		Pinching + $\gamma_{\ell g} \neq 0$	
$\mathcal{N}_p$ [m^{-3}]	g_p [-]	R_p [μm]	g_p [-]	R_p [μm]	g_p [-]	R_p [μm]
3×10^9	9.35×10^{-3}	91	2.62×10^{-3}	59	3.16×10^{-4}	13
8×10^9	1.19×10^{-2}	71	5.19×10^{-3}	53	7.76×10^{-4}	13
3×10^{10}	1.28×10^{-2}	47	7.10×10^{-3}	38	2.01×10^{-3}	13

The influence of the value of $\gamma_{\ell g}$ is obvious: if there is no curvature overpressure due to the Laplace-Young condition, no supersaturation is needed for a pore to nucleate and grow. In that case, the pore nucleates earlier and the pressure inside the pore equals to that of the liquid. This results in a larger final pore radius and pore density.

However, the influence of the pinching effect is much more important than the effect of $\gamma_{\ell g}$. And of course, the lower the pore density, the higher the pinching effect, since a low pore density results in a larger spherical equivalent pore radius. Note also that the final pore radius is independent of the pore density if all the aspects are taken into account, i.e.: (i) hydrogen diffusion, (ii) Laplace-Young effect, and (iii) pinching of the pore phase by the solid network. In that case, it appears that the final radius of curvature is function of $g_\alpha(T_{eut})$ and λ_2^{eut} only.

Finally, we will use the fact that the hydrogen profile is given by $\langle X_H \rangle(r) = A/r + B$ to analyze the evolution of the hydrogen profile in the mush, i.e., in the domain $[R_p^{sph}, R_{p0}]$. Knowing (i) the hydrogen concentration and (ii) the slope of the profile at both $r = R_p$ and $r = R_{p0}$, we can extract for each solid fraction the two dimensionless values

$$\frac{\langle X_H^* \rangle}{\langle X_H \rangle(R_{p0})} = \frac{\langle X_H \rangle_{r=R_p^{sph}}}{\langle X_H \rangle_{r=R_{p0}}} \qquad \text{(see Fig. 5.31)}$$

and

$$\frac{\partial \langle X_H^* \rangle / \partial r}{\partial \langle X_H \rangle(R_{p0})/\partial r} = \frac{\partial \langle X_H \rangle / \partial r_{r=R_p^{sph}}}{\partial \langle X_H \rangle / \partial r_{r=R_{p0}}} \qquad \text{(see Fig. 5.32)}$$

that are representative of the hydrogen profile.

Figure 5.31 shows that a hydrogen composition gradient is necessary in order for the pore to grow. It is clear that, as expected, the higher the pore density, the lower is the composition gradient. It is noteworthy that the shape of the three curves are similar; however, as the Fourier number is very high for $\mathcal{N}_p = 3 \times 10^{10}$, the hydrogen

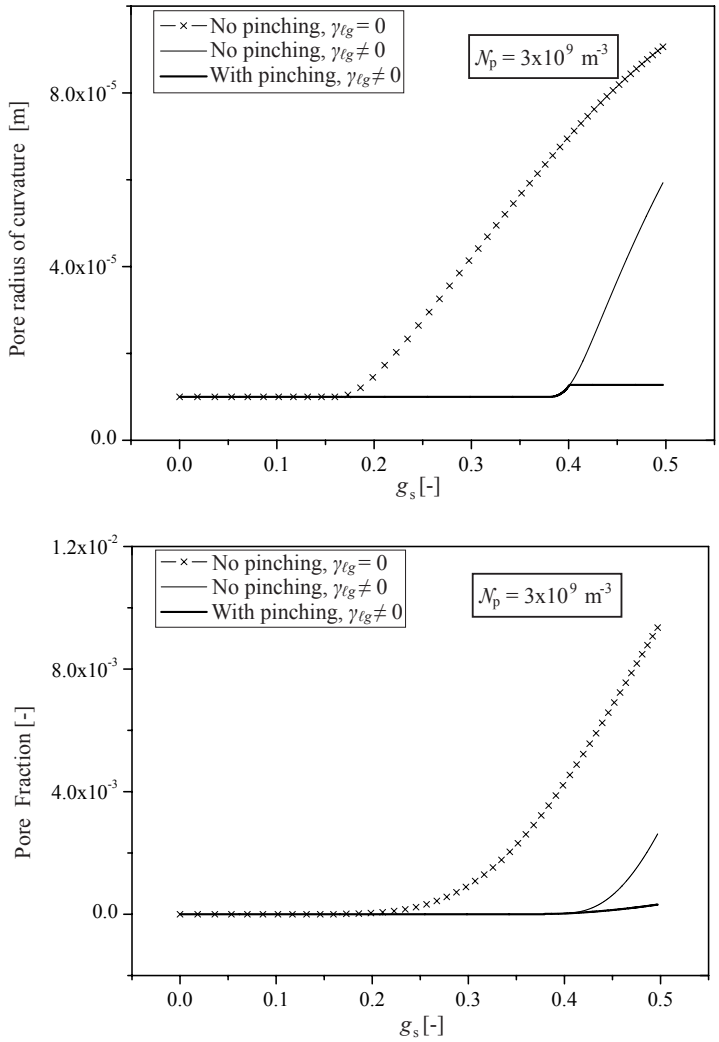

Figure 5.29: Curvature and pinching influence on the pore radius of curvature (upper figure) and on the pore fraction (lower figure) for $\mathcal{N}_p = 3 \times 10^9$ m^{-3}.

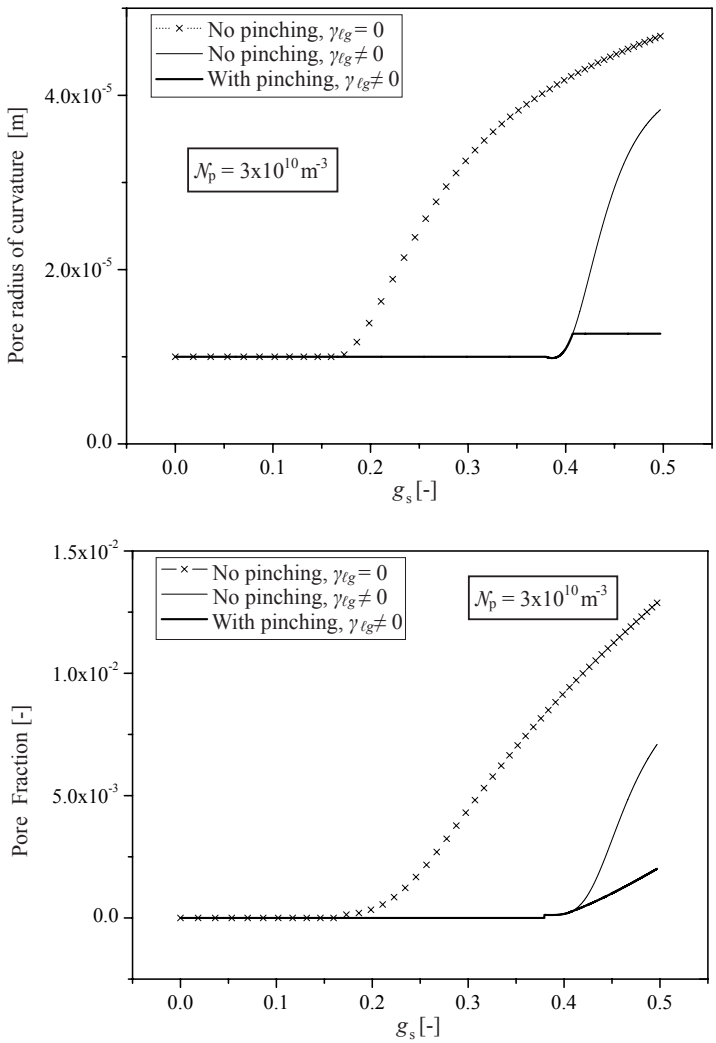

Figure 5.30: Curvature and pinching influence on the pore radius of curvature (upper figure) and on the pore fraction (lower figure) for $\mathcal{N}_p = 3 \times 10^{10}$ m^{-3}.

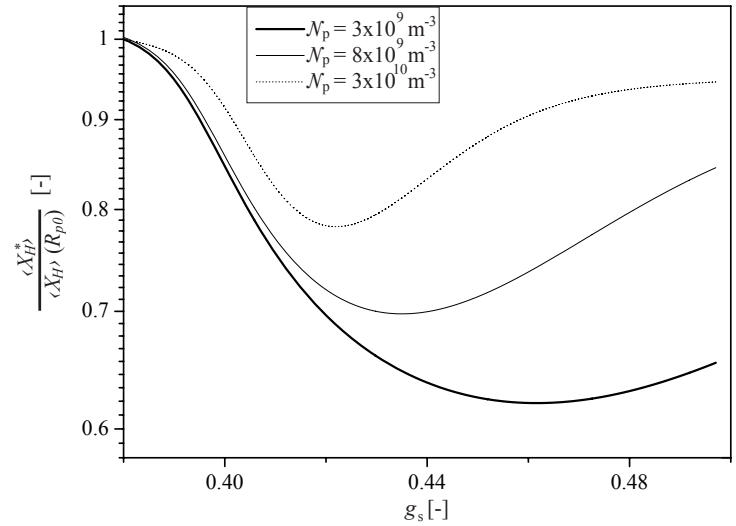

Figure 5.31: Ratio of the hydrogen concentrations in the mushy zone at $r = R_p^{sph}$ and at $r = R_{p0}$ as a function of volume fraction of solid for the three considered pore densities. Note that these calculations were performed with limited hydrogen diffusion without considering pinching and with $\gamma_{\ell g} \neq 0$.

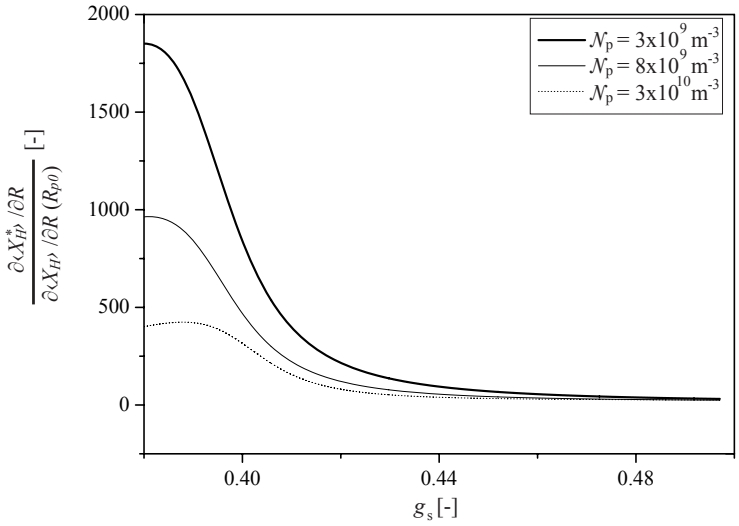

Figure 5.32: Ratio of the slopes of the hydrogen concentration in the mushy zone at the pore surface $r = R_p^{sph}$ and at $r = R_{p0}$ as a function of the volume fraction of solid for the three considered pore densities. Note that these calculations were performed with limited hydrogen diffusion without considering pinching and with $\gamma_{\ell g} \neq 0$.

composition is quickly uniform in the mush, whereas it will take more time as $\mathcal{N}_p$ or the Fourier number decreases.

These findings are corroborated by Fig. 5.32, where one can see that the slope difference is large at the beginning of pore growth. But this ratio tends to 1 by the end of the solidification process, showing that the model gives reliable results for the considered values of the Fourier number.

We saw in section 2.10.3 that in a recent study, Carlson *et al.* [6] developed a volume-averaged model for finite-rate diffusion of hydrogen in an Al-7wt%Si alloy. (see their results given in Fig 2.20). However their approach was different to the present one, since they assumed no hydrogen diffusion through the solid phase. Accordingly, they have estimated a parameter describing the area of the pore in contact with the liquid as a function of g_s (since pore "feeding" in hydrogen happens only at the pore-liquid interface), and this parameter is difficult to estimate. Nevertheless, these authors highlighted the importance of hydrogen diffusion for microporosity prediction by investigating the influence of the cooling rate and by comparing their findings with experimental results reported in [80, 81]: the higher the cooling rate, the lower the porosity fraction, because the time for hydrogen to diffuse is smaller.

Our results corroborate this fact: hydrogen diffusion does play an important role and it has to be taken into account in models of microporosity prediction. But there is a limitation to this effect (i.e., the Fourier number, see below), and we have also shown that one cannot neglect hydrogen diffusion through the solid phase, especially at high volume fractions of solid. Moreover, we have shown that the Fourier number associated with the pore density $\mathcal{N}_p$ (which is related to the characteristic domain defined by the sphere of radius R_{p0}) is useful to predict whether hydrogen diffusion is critical or not. Carlson *et al.* [6] used a value $\mathcal{N}_p = 1 \times 10^{11}\,\mathrm{m}^{-3}$, which leads to a Fourier number of about 80 associated with the radius $R_{p0} = 134$ μm if one uses the effective hydrogen diffusion coefficient developed in this work. 134 μm is a short distance for hydrogen diffusion and a value of 80 for the Fourier number indicates that complete mixing can be assumed in that case. Moreover, these authors have used the simple rule developed by Péquet *et al.* [2] for the pinching of the pore phase by the growing solid network. The analysis of the X-ray tomography data of this thesis have shown that the model of pinching developed by Couturier and Rappaz [4] seems to be more accurate. Using the latter pinching law with an effective hydrogen diffusion coefficient in a model that uses the steady-state solution of the diffusion equation, we have shown that the pinching effect on the final pore radius and pore fraction is much more important than hydrogen diffusion. It is then not only because of hydrogen diffusion but mainly because of the pinching effect that several authors observe a decreasing pore fraction g_p as a function of $\dot{T}$: the higher the cooling rate, the smaller the secondary dendrite arm spacing λ_2^{eut} and the smaller the pore radius and pore fraction.

Note finally that our volume-averaged model of hydrogen diffusion has been developed collectively with developers of ESI-Group, and that this model is ready to be implemented in one of their commercial softwares ProCAST®.

5.5 Phase-field results

In the previous section, we have introduced a model for the prediction of microporosity assuming an equivalent spherical pore shape, but considering pinching by the solid dendrites. The purpose of this section is to present the results of a new phase-field model that has been developed to predict the complex shape of a pore constrained by a solid network. The first part of this section is dedicated to the validation of the model, whereas the influence of the secondary dendrite arm spacing is investigated in the second part of this section. Although limited at present to 2D simple geometries, it constitutes a sound basis for future 3D realistic developments [102].

A first test was carried out in order to test the capability of the model to calculate correctly the pressure and the radius of a spherical pore (in liquid aluminum) for a given set of conditions in terms of (i) hydrogen content $\mathfrak{X}_{H0}$ in the calculation domain, (ii) hydrogen solubility S_ℓ, and (iii) liquid pressure p_ℓ. The calculations were performed in a 2D square domain at the center of which a pore was nucleated with an arbitrary radius. Once steady-state was reached, the pore radius R_p and the pore pressure p_g were compared with the analytical solution obtained from the following set of equations:

$$\mathfrak{X}_{H\ell} = S_\ell \sqrt{\frac{p_g}{p_0}} \tag{5.6}$$

$$p_g = \frac{\mathfrak{X}_{Hg}}{2} \mathcal{R} T \tag{5.7}$$

$$p_g - p_\ell = \frac{\gamma_{\ell g}}{R_p^{eq}} \tag{5.8}$$

$$V_{comp} \mathfrak{X}_{H0} = \pi \left(R_p^{eq}\right)^2 \mathfrak{X}_{Hg} + \left(V_{comp} - \pi \left(R_p^{eq}\right)^2\right) \mathfrak{X}_{H\ell} \tag{5.9}$$

where R_p^{eq} is the equilibrium radius of the circular pore and V_{comp} is the volume of the calculation domain. Table 5.12 summarizes the different parameters used in the calculations. The calculations were started with an initial pore size about 10 times smaller than R_p^{eq}. The initial gas content and pressure in the pore were chosen in order to satisfy the Laplace-Young equation and the perfect gas law. The hydrogen content in the domain was set to $\mathfrak{X}_{H0} = 25\,\mathrm{mol\,m^{-3}}$, which is much larger than the equilibrium concentration given by Sievert's law for the initial pore radius. As the liquid is supersaturated in hydrogen, the pore is expected to grow.

As can be seen in Fig. 5.33, the pore radius calculated with the phase-field model increases rapidly, whereas its pressure decreases, until a steady-state is reached. At a time of about $5 \times 10^{-5}\,\mathrm{s}$, both the steady-state pressure and radius of the pore are very close to the analytical solution. Similar calculations started with different pore radii, either larger or smaller than R_p^{eq}, yielded the same steady-state solution. Thus, the phase-field model is capable of correctly describing a bubble in equilibrium with its surrounding liquid, satisfying simultaneously the mechanical and chemical equilibrium conditions. The transient regime of the calculations corresponds to the time required to homogenize the hydrogen concentration in the liquid. Although hydrogen diffusion

Table 5.12: Parameters used in the phase-field calculations. Note that contact angle is the angle of the liquid-gas interface with the solid boundary.

Parameter	Symbol, unit	Value
Mesh size	d [m]	2.5×10^{-8}
Volume of the calculation domain	V_{comp} [m^2]	1.5625×10^{-10}
Contact angle	θ [-]	$\pi/3$
Interface thickness	δ [m]	4×10^{-8}
Atmospheric pressure	p_0 [Pa]	1×10^5
Liquid pressure	p_ℓ [Pa]	1×10^5
Temperature	T [K]	1000
Interface mobility coefficient	$\mu_{\ell g}$ [m^2 s kg^{-1}]	1×10^{-6}
Hydrogen diffusion diffusion	D_ℓ [m^2 s]	1×10^{-9}
Sievert's constant	S_ℓ [mol m^{-3}]	0.69
Liquid-gas interfacial energy	$\gamma_{\ell g}$ [J m^{-2}]	0.8

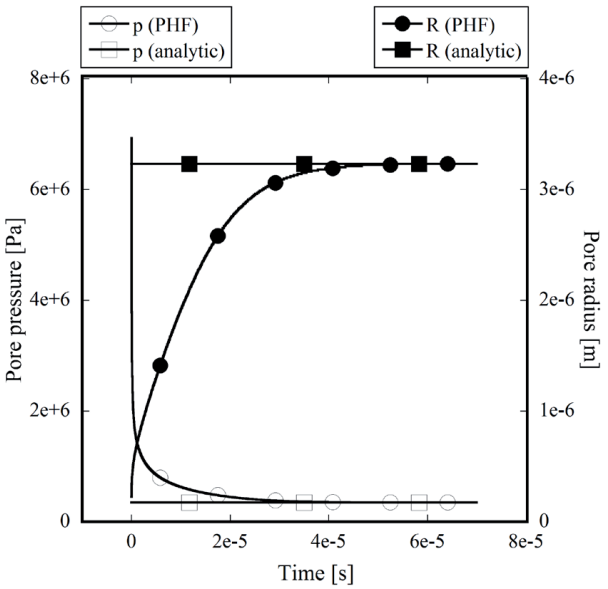

Figure 5.33: Radius and pressure of a circular 2D pore calculated with the phase-field model and with the analytical solution for an overall hydrogen content $\mathfrak{X}_{H0} = 25\,[\mathrm{mol\,m^{-3}}]$ (other parameters given in Table 5.12).

can be the limiting factor for pore growth, the transient regime of the simulation cannot be exploited quantitatively in this preliminary approach. The reason is that the liquid flow induced by the expansion of the bubble, and thereby hydrogen transport by convection, are not considered in the simulations. For this reason, only the steady-state solutions of the simulations will be discussed hereafter.

The model was then used to investigate the morphology and the pressure in a pore growing under the constraint of a surrounding solid. The calculations were performed in a 2D domain composed of a series of rectangular channels connected together by a central canal (see Fig. 5.34). This geometry is aimed at simulating the growth of a pore in between liquid films left between fixed dendrite arms. The contact angle between the liquid-gas interface and the solid boundary was set arbitrarily to $\pi/3$. The overall hydrogen content in the calculation domain $\mathfrak{X}_{H0}$ was set to 25 mol m^{-3}. The calculation were initialized with a pore size 10 times lower than R_p^{eq}, the equilibrium radius of a spherical pore. The other calculation parameters are given in Table 5.12. As the liquid is supersaturated in hydrogen, the pore grows until some steady-state is reached. The final shape of the pore is shown in Fig. 5.34 for three different channel widths ω but identical volumes of calculation. The pressure in the pore, the mean radius of curvature at the liquid-gas interface and the volume of the pore were extracted from the calculations once steady-state was reached. The results are presented in Fig 5.35.

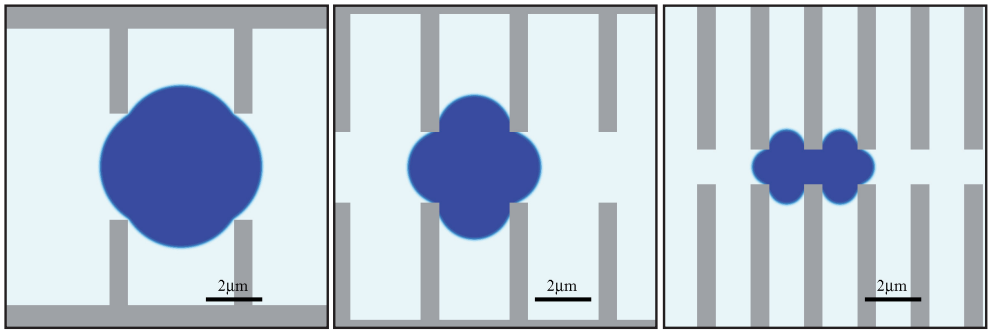

Figure 5.34: Equilibrium pore shape for different liquid channel widths ω. (a) $\omega = 3.725$ μm, (b) $\omega = 2.475$ μm, and (c) $\omega = 1.225$ μm.

As can be seen in Fig. 5.35a, a smaller channel width leads to a higher pressure, a smaller radius of curvature and a lower pore volume as compared with a less constrained pore. This effect is directly related to the fact that the growth of a pore inside a narrow liquid channel requires highly curved liquid-gas interfaces in order to satisfy the contact angles that have been prescribed on the boundary. The pressure in the pore is consequently larger in such pores since the Laplace - Young equation has to be satisfied. The effect of the constraining solid can also be observed in Fig. 5.35b, which shows that the average mean radius of curvature becomes substantially smaller than the unconstrained radius when the channel width is small. In the calculations shown here, the influence of the solid morphology on the volume fraction and the morphology of the pores is substantial. By dividing the channel width by a factor 3, the pressure

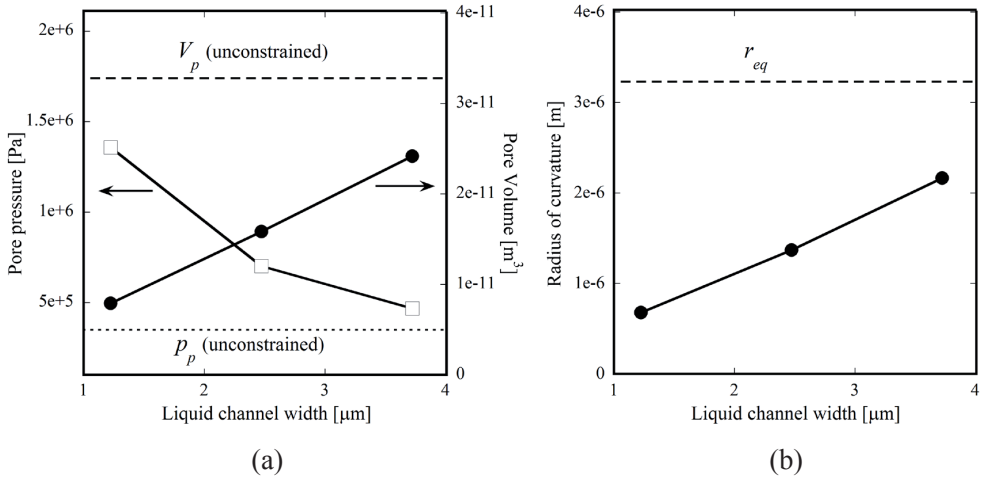

Figure 5.35: (a) Effect of liquid channel width on pore pressure (squares) and pore volume (circles) calculated with the phase-field model. The dashed and dotted lines represent respectively the unconstrained pore volume and unconstrained pore pressure. (b) Effect of liquid channel width on the mean radius of curvature of a pore calculated with the phase-field model (see Eq. 4.53). The dashed line represents the unconstrained equilibrium radius of curvature.

raises and the volume drops also by similar factor. The magnitude of this effect is naturally linked to the fact that the channel widths used in the calculations are rather small. However, such narrow liquid channels are not unrealistic near the end of solidification of the primary phase if the eutectic fraction is small.

To emphasize even more the effect of curvature upon the equilibrium shape of a pore, calculations have been run with a liquid channel having a "T-Bone" like structure (see Fig. 5.36). For these calculations (performed with the same parameters as given in Table 5.12), a small pore is nucleated in the narrow part of the liquid. Very quickly, the pore gets into contact with the solid walls with the prescribed wetting angle. But in the mean time, the pore "sees" that he has more place in the wider channel situated at the right hand side of the figure. The pore then migrates to regions where its curvature overpressure can be relaxed, and adopts finally a spherical shape, which is in that case the equilibrium shape, i.e., the shape that costs the least amount of surface energy to the system.

One of the limitations of this study is the fact that the influence of the solid is taken into account through the geometry of the calculation domain, which contains only liquid and gas phases surrounded by solid. With such a method, only simple solid shapes can be described since the solid-liquid or solid-gas interfaces have to correspond to the boundaries of the orthogonal calculation grid.

An extension of the present work has been developed [103]. It is based on a multiphase-field formulation. The presence of solid, liquid and pores are described through the phase-field variables ψ_s, ψ_ℓ and ψ_g, that can be understood as local volume fractions. This allows for a description of micropores constrained in a solid network

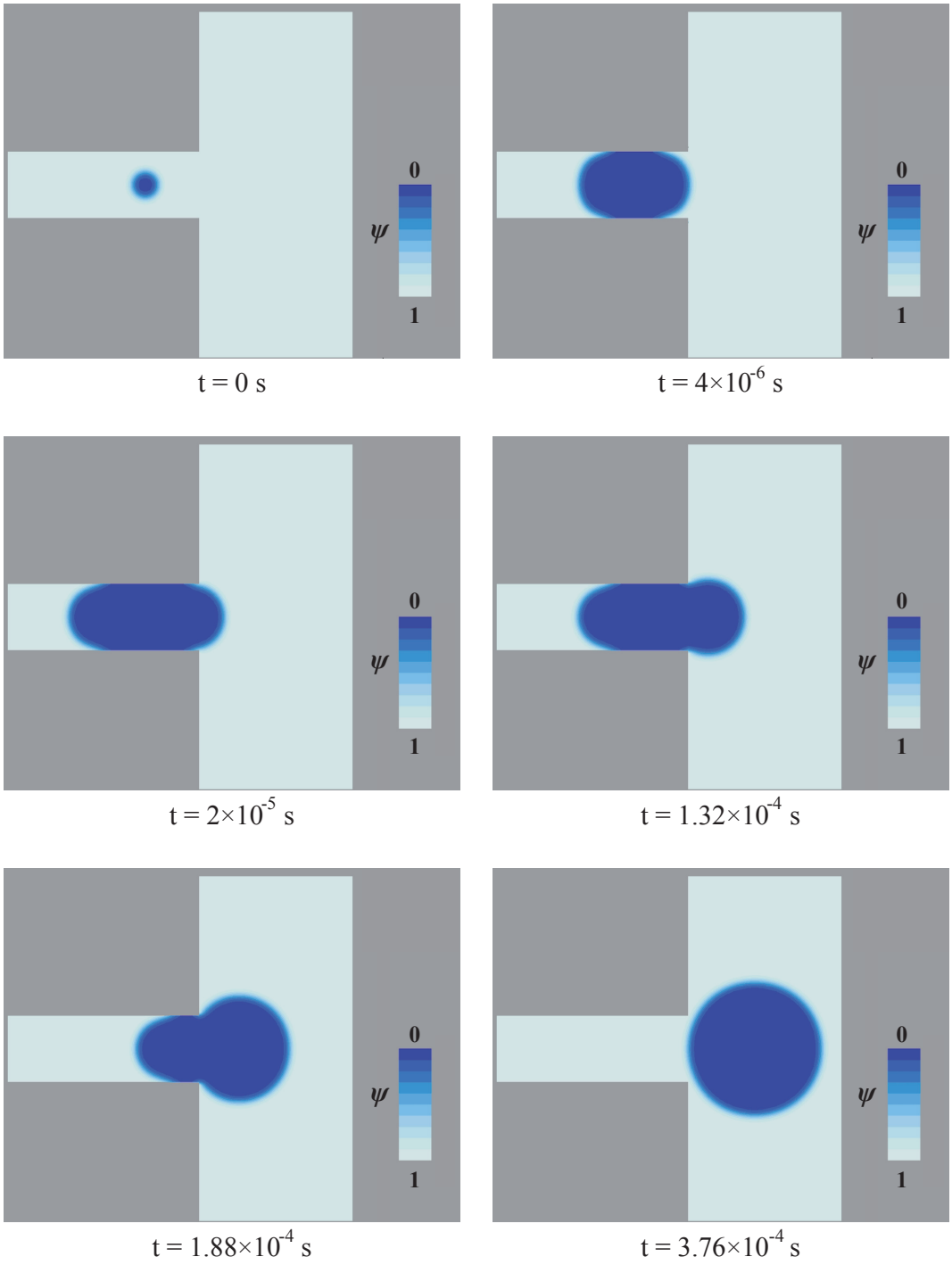

Figure 5.36: Evolution as a function of time of a pore nucleated in a narrow channel connected to a larger one. In order to reduce the energy of the system, the pore migrates to "unconstrained" regions, i.e., regions where the curvature overpressure is as small as possible.

having a more realistic shape. Figure 5.37 shows multiphase-field calculation results of initial (black circle), transient (dotted line) and equilibrium (grey/orange fill) pore shapes for different secondary dendrite arm spacings, but otherwise same parameters. As in this work, the calculations were initialized with a relatively small pore located at the center of the calculation domain and without any contact with the solid. Since the liquid was supersaturated in hydrogen, the pore grew until equilibrium was reached. As can be seen, the pore develops in a non-symmetric way, and may move to a more open space in order to reduce its curvature and thereby its internal pressure. The influence of the λ_2 spacing can be clearly seen here, and similar conclusions as those found in this thesis can be drawn: a lower λ_2 spacing results in a lower pore volume and in a higher pore curvature.

Although this model accounts for hydrogen diffusion in the liquid, which is one of the main aspects governing the growth kinetics of a pore, this approach does not allow at this stage to correctly describe the dynamics of pore formation. To do so, the model should be combined with a description of the liquid flow induced by the pore growth (this effect is similar, although to a much smaller extent, to the vapor expansion of extruded cereals for example [104]). This would permit to properly take into account the effect of hydrogen transport by convection. In order to make a more quantitative investigation of the influence of the solid on the pore morphology, the approach should even be extended to 3D and the evolution of the solid-liquid interface should be considered.

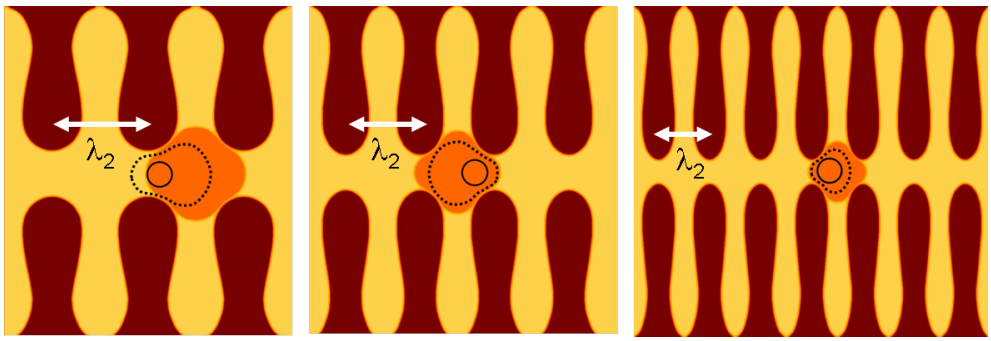

Figure 5.37: Initial (black circle), transient (dotted line) and equilibrium (grey/orange fill) pore shapes for different arm spacings, $\lambda_2 = 5$, 3.75 and 2.5 μm (after [103])

5.6 Pipe shrinkage experiments and simulation results

We saw in section 2.8 that the $g_{s,c}$ parameter, i.e., the critical volume fraction of solid at which the surface of a casting does not move anymore (the point from which mass feeding is stopped), is a parameter that has not been assessed or validated yet for calculations performed with the softwares ProCAST® or CalcoSOFT®.

The validation of pipe shrinkage calculations is a very complex problem, and many attempts have been made during this thesis. Reproducible results of the shape of the

pipe shrinkage are difficult to obtain, since many parameters should be kept constant, while varying the inoculant only. Especially the control of the thermal conditions as well as the width of the oxide skin at the casting surface are difficult to maintain constant. Nevertheless, we could still obtain a fairly good agreement between the shape of pipe shrinkage of (i) simulation results by varying the $g_{s,c}$ parameter and (ii) casting experiments by varying the inoculation of the alloy.

For that purpose, two solidification experiments have been conducted under the same thermal conditions with the D_2S set-up, as described in section 3.2.1. In the first experiment, an inoculated Al-4.5wt%Cu-TiB_2 alloy was cast, whereas an non-inoculated alloy (Al-4.5wt%Cu) was used in the second experiment. Indeed, the critical volume fraction at which mass feeding stops is expected to be higher for an inoculated alloy than for a non-inoculated one, as equiaxed globulitic grains are allowed to move up to about 50 % volume fraction of solid [105]. Simultaneously, 3D simulations of these experiments were performed using the software ProCAST® as described in section 4.5.

Figure 5.38 shows both inoculated and non-inoculated castings, as well as the corresponding simulations performed with two different $g_{s,c}$ parameters. We observe a good correlation of the shape of the pipe shrinkage in both cases, as well as a clear height difference $\Delta H = 5 \times 10^{-3}$ m in the center part of the pipe shrinkage. Consequently, the shape of the pipe shrinkage differs between the two alloys: the slope is more abrupt for the non-inoculated alloy than for the inoculated one (we remind here that the same amount of material was cast in both experiments). For the non-inoculated case indeed, columnar dendrites attached to the mold grow towards the center part of the casting, because of the radial cooling. But liquid must flow in the inverse direction in order to compensate for solidification shrinkage and the growing dendrites are stopped as soon as they reach the surface of the pipe (see Fig. 5.39b). On the other hand in the case of an inoculated alloy, the dendrites can settle down, since some equiaxed dendrites can nucleate in the liquid, and hence not be attached to the mold. This results in a more smooth shape of the pipe shrinkage, as schematized in Fig. 5.39a. Accordingly, the depth of the pipe shrinkage is then influenced by the inoculation of the alloy. In terms of modeling, this influence is taken into account via the $g_{s,c}$ parameter and it seems that a $g_{s,c}$ value of 0.6 and 0.1 in the simulations corresponds fairly well to inoculated and non-inoculated casting conditions, respectively.

Taking a too large $g_{s,c}$ value for an inoculated alloy, or a too low value for a non-inoculated alloy results in a bad approximation of the pipe shrinkage (see Fig. 5.40). The $g_{s,c}$ parameter rules indeed the transition between two boundary conditions. Let us focus on the case of an inoculated alloy: We know from Fig. 2.17 that as long as $g_s < g_{s,c}$, mass feeding occurs and the surface of the casting goes down to compensate for solidification shrinkage. Clearly for $g_{s,c} = 0.8$, mass feeding is too much important and the result does not fit the experimental results. On the other hand for a non-inoculated alloy, taking a $g_{s,c}$ value too low ($g_{s,c} = 0.01$) overestimates the amount of microporosity, because mass feeding is too early hindered. As a consequence, we recommend to use a $g_{s,c}$ value of 0.6 or 0.1 for inoculated and non-inoculated alloys,

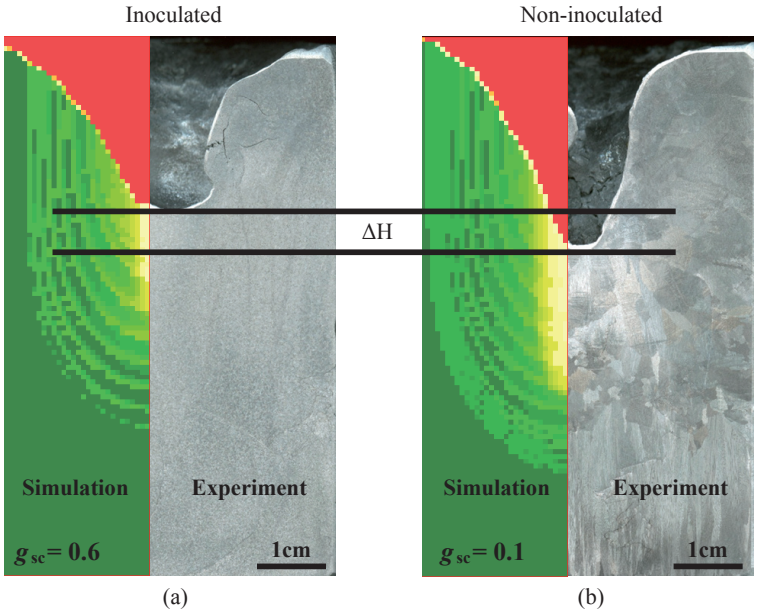

Figure 5.38: Influence of the $g_{s,c}$ parameter and comparison between experimental and simulation results for an inoculated and a non-inoculated Al-4.5wt%Cu alloy solidified with the D_2S set-up. Note that the same cooling conditions (radial + vertical) were used in these castings. For the simulation results, red regions represent regions where pipe shrinkage occurs, green regions represent regions free of microporosity, and yellow regions represent regions with a high volume fraction of microporosity.

respectively.

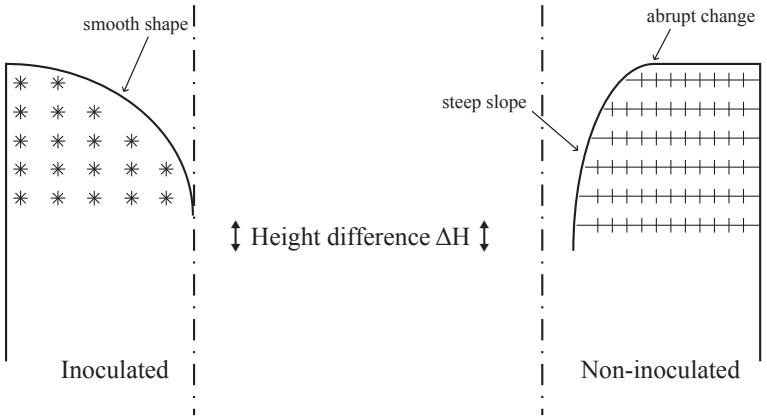

Figure 5.39: (left) Inoculated alloys with equiaxed dendrites that allows a less steep shape of the pipe shrinkage. (right) Non-inoculated alloy with columnar dendrites attached to the mold that grow up to the surface of the pipe, resulting in a more abrupt change of the slope of the pipe shrinkage.

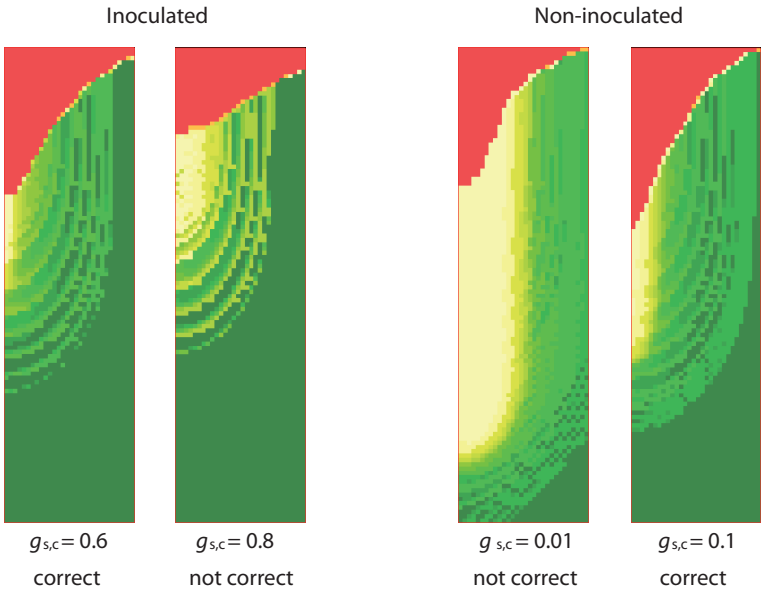

Figure 5.40: (left) Comparison between the estimated and a too large $g_{s,c}$ value to simulate pipe shrinkage of an inoculated alloy. (right) Comparison between the estimated and a too low $g_{s,c}$ value to simulate pipe shrinkage of a non-inoculated alloy. Note that the meaning of the colors are identical to that in Fig. 5.38.

Chapter 6

Conclusion and perspectives

6.1 Summary and conclusion

The problem of porosity formation is very complex, since many physical phenomena come into play and can even interact one with another. A model for the prediction of microporosity, macroporosity and pipe shrinkage during the solidification of alloys has been developed at the Computational Materials Laboratory (LSMX-EPFL) in 2002 and was the subject of a thesis [106]. It was the first model to couple microporosity with macroporosity and pipe-shrinkage predictions in a coherent way, with appropriate boundary conditions. This model has then been improved by taking into account the effect of various alloying elements and gases on porosity formation during a postdoctoral work [3, 4, 5]. The model still needed some improvements, reason why the main focus of this thesis has been made on a better understanding of (i) the curvature of the pore phase and (ii) the influence of hydrogen diffusion on the growth of pores.

Because of the complexity of the pore shape when it is constrained to grow within the solid network, existing porosity models approximate the pore radius to be a function of the solid fraction g_s instead of the pore fraction g_p. In order to investigate the influence of curvature and to provide experimental results that validate an existing pinching model, Al-Cu samples have been cast under controlled conditions to be then analyzed *post-mortem* through high resolution X-ray tomography. The results have shown that the curvature of micropores pinched in either non-inoculated and inoculated Al-4.5wt%Cu alloys can be fairly well approximated to that of a cylinder. The tomography results have also shown that the pinching model to account for pore curvature restriction by the solid phase must be function of (i) the volume fraction of the primary phase g_α and (ii) the secondary dendrite arm spacing λ_2. However, the influence of the initial hydrogen content appears to be negligible. The pinching model developed by Couturier and Rappaz [4] accounts for these observations and their relation fits fairly well the average mean curvature value of our experimental data. We thus recommend to use this model to account for the pinching of pores by the growing solid network, independently of the inoculation of the alloy.

Our results also showed that a pore is elongated along the thermal gradient in the case of a non-inoculated alloy (i.e., columnar dendrites), but adopts rather an equiaxed shape if the alloy is inoculated (i.e., equiaxed dendrites). We also observed that the

high values of the local mean curvature of a pore are in close contact with the eutectic. Since the last liquid to solidify has the eutectic composition, this means that the value $\langle\bar{\kappa}\rangle_{\geq 0}$ (= average mean curvature value taken on positive curvatures only) is characteristic of the pore overpressure near the end of solidification. Values of $\langle\bar{\kappa}\rangle_{\geq 0}$ as high as 0.35 μm^{-1} were observed, leading to a pore overpressure near the end of solidification of about 600 kPa. This is consistent with the results of Couturier *et al.* [3], who found that the liquid near the end of solidification can undertake a negative pressure as low as -200 kPa. Since the pore pressure must be positive, the overpressure due to curvature effects must be then higher than 200 kPa, which is what we found.

In order to investigate the influence of hydrogen diffusion on the growth of pores in aluminum alloys, we have first derived a new model that calculates an effective hydrogen diffusion coefficient $D_e(g_s)$ based on real solidifying microstructures obtained via *in-situ* X-ray tomography. These calculations have then been compared with different effective medium approximations. Among them, the DEM approach is the approximation that fits best the results, because (i) it takes into account the fact that the solid and liquid phases act as inclusions and matrix respectively, and (ii) the phase contrast is larger than 4 (the ability of the solid to transport hydrogen is about 7 times less than that of the liquid), making Maxwell's approximation poor as compared with the DEM one.

Using *in-situ* X-ray tomography, we have then analyzed the behavior of a 300 μm wide pore during an isothermal holding at high temperature as well as during a solidification experiment. For the first time to the author's knowledge, real-time pore coalescence and coarsening could be observed in 3D with a resolution that is high enough to capture the details of the morphology. Then, using the developed $D_e(g_s)$, we have shown that solidification shrinkage plays an important role on the shape of gas porosity and can even be crucial in terms of its volume fraction.

Using the curvature data together with the effective hydrogen diffusion coefficient obtained in this work, we have constructed a new model that accounts for (i) curvature restriction via the (now validated) pinching model of Couturier and Rappaz [4] and (ii) hydrogen diffusion via the developed $D_e(g_s)$. In addition, the conventional physical phenomena (i.e., temperature and solute influence on hydrogen solubility, hydrogen segregation, supersaturation for pore nucleation, etc.) have of course been taken into account. The model has been applied to the solidification of an Al-7wt%Si alloy. We have shown that, although hydrogen diffusion can be a limiting factor for the growth of pores, the curvature restriction of the pore phase due to the growing solid network has a much larger influence. Accordingly, we think that the experimental results of [80, 81] that reported a decreasing porosity fraction with an increasing cooling rate is an effect more due to the pinching of the pore phase than due to limited hydrogen diffusion (λ_2 decreases as the cooling rate increases, leading to a smaller volume for the pore to expand).

A phase-field model has been developed to describe the complex equilibrium shape

of a pore pinched in a solid network. This model accounts also for curvature restriction and hydrogen diffusion, however convection as been ignored. The results of this preliminary model clearly show that the secondary dendrite arm spacing of the microstructure influences the pore shape and pore fraction: the finer the microstructure, the higher the pore curvature at the liquid-gas interface and the larger the pore pressure. Although the model needs many improvements, we have constructed a sound basis for a model that has many possible features as we will see hereafter.

Finally, pipe shrinkage calculations using the software ProCAST® have been compared with experimental observations. We have shown that calculations performed using a $g_{s,c}$ value of 0.6 and 0.1 fit fairly well the shape of the pipe shrinkage obtained in inoculated and non-inoculated casting experiments, respectively. However, a lot of experiments were needed for these validations, and because of the complexity of that problem the results are difficult to reproduce.

6.2 Future work

There is a compromise between the acquisition time and the pixel size in an X-ray tomography experiment: the finer the resolution, the longer the acquisition time. In this work, we have analyzed through *in-situ* X-ray tomography (2.8 μm/pixel) the behavior of a pore pinched by the solid network during a solidification experiment. The large pixel size combined with a low cooling rate were necessary to obtain negligible microstructure change during the rotation time of a scan. Unfortunately, a pixel size of 2.8 μm is not fine enough for a quantitative analysis of the pore curvature evolution as a function of the solid fraction and only a qualitative analysis could be performed.

If the technology evolves to allow for a smaller pixel size, while keeping the acquisition time short, this will open doors to more sophisticated and more realistic theories, such as new pinching models for instance. This is of course difficult to achieve, but when one thinks that a few years ago at ESRF, a complete scan with a pixel size of 0.7 μm took more than one hour, and that such a scan lasts nowadays less than 10 min, such achievements seem not impossible.

The pinching model used in this work gives a single value for the maximum curvature of a spherical pore, whereas we observed experimentally a distribution of curvature values. Another way to develop a refined model would thus be to use and further improve the phase-field model developed in this work. Whereas the third phase (solid) has already been introduced in the model [103], the possible growth of this phase (i.e., solidification) has not been implemented, yet. If such developments can be achieved, direct information of the curvature of the pore phase as a function of the solidification parameters would become accessible, and a relationship between the pore radius and the pore fraction g_p could be developed.

However, we think that the model should be first extended to 3D and combined with a description of the liquid flow induced by the pore growth. This would permit to properly take into account the effect of hydrogen transport by convection. More realistic phase-field calculations could be run then, for example with the same parameters

used to produce the samples of this work. The calculation mesh could be based on the tomography results: as in section 4.2, each solid voxel could be considered as a finite volume cell with a value $\psi_s = 1$ in the phase-field model and each pore or liquid voxel as a finite volume cell with a value $\psi_\ell = 1$. A pore would then be nucleated in the liquid at the beginning of the calculations and the simulation results could directly be compared to our experimental data.

We have shown that the curvature distribution of the eutectic is surprisingly similar to that of the pore phase. Accordingly, "conventional" multiphase-field 3D calculations (i.e., with condensed phases only) could be run with appropriate values of the interfacial energies (and without any anisotropy). The results could be compared with the present X-ray tomography data and if a fair correlation is found, possibilities of new pinching model developments would arise.

The volume-averaged model developed to take into account the influence of both curvature and hydrogen diffusion on the growth of pores assumes a steady-state profile of the hydrogen in the mush. We have seen that this is valid only for high values of the Fourier number, i.e., for pore density values $\mathcal{N}_p \approx 3 \times 10^9\,\mathrm{m}^{-3}$. Although much lower pore density values are rarely encountered, it would be interesting to develop a Zener-like model [38]. There would be no limitation on the Fourier number, and such a model would be quite efficient in terms of CPU time. Moreover, it could be quite easily implemented.

The question whether performing porosity calculations should be performed as a post-processing of the thermal results or should be done simultaneously is still open. The first technique is indeed much more efficient in terms of CPU time [2] and our results showed that only the final λ_2 spacing is important for the pinching model. However, as the thermal results are obtained via an enthalpy method, a node were a pore might exist would have a wrong enthalpy value, which can induce problems in the final results, especially if the fraction of macroporosity is high.

To conclude, we would like to mention that among all the existing models for porosity prediction, the one of Lee *et al.* [77] is one of the fewest that treats porosity nucleation in a stochastic way. We think that this aspect should be integrated in any model for porosity prediction, since pore nucleation can be considered as stochastic as the conventional nucleation of a solid particle in an undercooled melt.

Bibliography

[1] J.E. Hatch. *Aluminum: Properties and Physical Metallurgy.* 1984.

[2] Ch. Pequet, M. Gremaud, and M. Rappaz. Modeling of microporosity, macroporosity, and pipe-shrinkage formation during the solidification of alloys using a mushy-zone refinement method: Applications to aluminum alloys. *Metallurgical Material Transactions A*, 33(7):2095–2106, 2002.

[3] G. Couturier and M. Rappaz. Effect of volatile elements on porosity formation in solidifying alloys. *Modelling and simulation in materials science and engineering*, 14(2):253–271, March 2006.

[4] G. Couturier and M. Rappaz. Modeling of porosity formation in multicomponent alloys in the presence of several dissolved gases and volatile solute elements. In *2006 TMS Annual Meeting*, volume 2006, pages 143–152, San Antonio, TX, 2006.

[5] G. Couturier, J.-L. Desbiolles, and M. Rappaz. A porosity model for multi-gas systems in multi-component alloys. In *Modeling of Casting, Welding and Advanced Solidification Processes - XI*, volume 2, pages 619–626, Opio, 2006.

[6] K.D. Carlson, Z. Lin, and C. Beckermann. Modeling the effect of finite-rate hydrogen diffusion on porosity formation in aluminum alloys. *Metallurgical Material Transactions B*, 38(4):541–555, 2007.

[7] M. Felberbaum and A. Jacot. A phase field method for a geometrical description of micropores constrained by a solid network. In *MCWASP 2009*, Vancouver, BC.

[8] Ch. Thomsen. *Guide to Northern Archaeology.* London, J. Bain, 1848.

[9] R. Drews. *The end of the Bronze Age: Changes in warfare and the catastrophe ca. 1200 B.C.* Princeton University Press, 1993.

[10] http://www2.egeonet.gr/ehw/forms/default.aspx.

[11] A. John. *The Life of Sir Humphry Davy.* 1831.

[12] D.G. Altenpohl. *Aluminum: Technology, Application, and Environment.* 1999.

[13] http://www.steelonthenet.com/prices.html.

[14] C. Beckermann. Modelling of future needs macrosegregation: applications and future needs. *International Materials Reviews*, 47(5):243–261, 2002.

[15] J.-M. Drezet and M. Rappaz. Modeling of ingot distortions during direct chill casting of aluminum alloys. *Metallurgical Material Transactions A*, 27(10):3214–3225, 1996.

[16] M. Rappaz, J.-M. Drezet, and M. Gremaud. A new hot-tearing criterion. *Metallurgical Material Transactions A*, 30(2):449–455, 1999.

[17] J. Campbell. *Castings*. Butterworth Heinemann, 2003.

[18] H.A. Wriedt. The Al-O (aluminum-oxygen) system. *Bulletin of Alloy Phase Diagrams*, 6(6):548–553, 1985.

[19] H.A. Wriedt. The Al-N (aluminum-nitrogen) system. *Bulletin of Alloy Phase Diagrams*, 7(4):329–333, 1986.

[20] Kubo and Pehlke. Matematical modeling of porosity formation in solidification. *Metallurgical Material Transactions B*, pages 359–366, 1985.

[21] S. Ganesan and D.R. Poirier. Densities of aluminum-rich aluminum-copper alloys during solidification. *Metallurgical Material Transactions A*, 18 A(4):721–723, 1987.

[22] P. D. Lee and J. D. Hunt. Hydrogen porosity in directional solidified aluminium-copper alloys: in situ observation. *Acta Materialia*, 45(10):4155–4169, October 1997.

[23] J. Baruchel, J.-Y. Buffière, P. Cloetens, M. Di Michiel, E. Ferrie, W. Ludwig, E. Maire, and L. Salvo. Advances in synchrotron radiation microtomography. *Scripta Materialia*, 55(1 SPEC. ISS.):41–46, 2006.

[24] T. Ohgaki, H. Toda, I. Sinclair, J.-Y. Buffière, W. Ludwig, T. Kobayashi, M. Niinomi, and T. Akahori. Quantitative assessment of liquid Ga penetration into an aluminium alloy by high-resolution X-ray tomography. *Materials Science and Engineering: A*, 427(1-2):1–6, July 2006.

[25] N. Limodin, L. Salvo, E. Boller, M. Suéry, M. Felberbaum, S. Gailliègue, and K. Madi. In situ and real-time 3D microtomography investigation of dendritic solidification in an Al-10 wt. pct Cu alloy. *Acta Materialia*, 57(7):2300 – 2310, 2009.

[26] ASM. *ASM Handbook*. Materials Park, 1992.

[27] H.D. Brody and M.C. Flemings. Solute redistribution in dendritic solidification. *Trans. AIME*, 236:615–624, 1966.

[28] T.W. Clyne and W. Kurz. Solute redistribution during solidification with rapid solid state diffusion. *Metallurgical Material Transactions A*, 12 A(6):965–971, 1981.

[29] R. Heringer, Ch.-A. Gandin, G. Lesoult, and H. Henein. Atomized droplet solidification as an equiaxed growth model. *Acta Materialia*, 54(17):4427–4440, 2006.

[30] W. Kurz and G. W. Fischer. *Fundamentals of solidification*. Trans Tech Publications, 2005.

[31] M. Rappaz and W.J. Boettinger. On dendritic solidification of multicomponent alloys with unequal liquid diffusion coefficients. *Acta Materialia*, 47(11):3205–3219, 1999.

[32] J. Ni and C. Beckermann. A volume-averaged 2-phase model for transport phenomena during solidification. *Metallurgical Material Transactions A*, 22(3):349–361, 1991.

[33] J. A. Dantzig and M. Rappaz. *Solidification*. EPFL Press, 2009.

[34] H. Darcy. Les fontaines publiques de la ville de dijon. *Dalmont*, 1986.

[35] Ø. Nielsen, L. Arnberg, A. Mo, and H. Thevik. Experimental determination of mushy zone permeability in aluminum-copper alloys with equiaxed microstructures. *Metallurgical Material Transactions A*, 30(9):2455–2462, 1999.

[36] P.C. Carman. Fluid flow through granular beds. *Trans. Inst. Chem.*, 15:150, 1937.

[37] C. A. Qiu, G. B. Olson, S. M. Opalka, and D. L. Anton. Thermodynamic evaluation of the Al-H system. *Journal Of Phase Equilibria And Diffusion*, 25:520–527, 2004.

[38] D.A. Porter, K.E. Easterling, and M.Y Sherif. *Phase Transformations in Metals and Alloys*. CRC Press, 2009.

[39] P.A. Javet, P. Lerch, and E. Plattner. *Introduction à la chimie pour ingénieurs*. 1995.

[40] G.K. Sigworth and T.A. Engh. Chemical and kinetic factors related to hydrogen removal from aluminum. *Metallurgical Material Transactions B*, 13(3):447–460, 1982.

[41] P. K. Sung, D. R. Poirier, and S. D. Felicelli. Continuum model for predicting microporosity in steel castings. *Modelling and simulation in materials science and engineering*, 10(5):551–568, 2002.

[42] C. Wagner. *Thermodynamics of Alloys*. Addison-Wesley, 1962.

[43] P.N. Anyalebechi. Critical review of reported values of hydrogen diffusion in solid and liquid aluminum and its alloys. In Crepeau P.N., editor, *Light Metals 2003: Proceedings of the technical sessions presented by the TMS Aluminium Committee at the 132nd TMS Annual Meetings*, pages 857–872, San Diego, CA, 2003.

[44] L.S. Darken and R.W. Gurry. *Physical Chemistry of Metals*. McGraw-Hill, 1953.

[45] J.R. Morris. Complete mapping of the anisotropic free energy of the crystal-melt interface in al. *Physical Review B*, 66:144104–1 to 144104–7, 2002.

[46] H.K.D.H. Bhadeshia and R. Honeycombe. *Steels, Microstructures and Properties*. Elsevier Academic Press Inc, 2006.

[47] D.R. Poirier, K. Yeum, and A.L. Maples. A thermodynamic prediction for microporosity formation in aluminum-rich Al-Cu alloys. *Metallurgical Transactions A*, 18(11):1979–1987, 1987.

[48] A. Prasad, H. Henein, E. Maire, and Ch.-A. Gandin. Understanding the rapid solidification of Al-4.3Cu and Al-17Cu using X-ray tomography. *Metallurgical Materials Transactions A*, 37A:249–257, 2006.

[49] H. D. Zhao, C. Z. Wu, and Y. Y. Li. Porosity formation in columnar region of unidirectional solidified Al-4.5Cu casting. *International journal of cast metals research*, 21(1-4):313–318, 2008.

[50] P. D. Lee and J. D. Hunt. Measuring the nucleation of hydrogen porosity during the solidification of aluminium-copper alloys. *Scripta Materialia*, 36(4):399–404, February 1997.

[51] R. C. Atwood, S. Sridhar, and P. D. Lee. Equations for nucleation of hydrogen gas pores during solidification of aluminium seven weight percent silicon alloy. *Scripta Materialia*, 41(12):1255–1259, November 1999.

[52] K.D. Li and E. Chang. Mechanism of nucleation and growth of hydrogen porosity in solidifying A356 aluminum alloy: an analytical solution. *Acta Materialia*, 52:219–231, 2004.

[53] L Drenchev, J. Sobczak, N. Sobczak, W. Sha, and S. Malinov. A comprehensive model of ordered porosity formation. *Acta Materialia*, 55:6459–6471, 2007.

[54] L. Arnberg and R. H. Mathiesen. The real-time, high-resolution X-ray, video microscopy of solidification in aluminum alloys. *Journal of Metals*, 59(8):20–26, 2007.

[55] A. S. Sabau and S. Viswanathan. Microporosity prediction in aluminum alloy castings. *Metallurgical Material Transactions B*, 33(2):243–255, 2002.

[56] H. Fredriksson and I. Svensson. On the mechanism of pore formation in metals. *Metallurgical Materials Transactions B*, 7B:599–606, 1976.

[57] S.D. Felicelli, L. Wang, C.M. Pita, and E.E. De Obaldia. A model for gas microporosity in aluminum and magnesium alloys. *Metallurgical Material Transactions B*, 40(2):169–181, 2009.

[58] S. Torquato. *Random Heterogeneous Materials*. Springer-Verlag, 2002.

[59] R. Landauer. The electrical resistance of binary metallic mixtures. *J. Appl. Phys.*, 23:779–784, 1952.

[60] J.C. Maxwell. *Treatise on Electricity and Magnetism*. Clarendon Press, 1873.

[61] D. Bruggeman. Berechnung verschiedener physikalischer konstanten von heterogenen substanzen. *Ann. Physik (Leipzig)*, 24:636–679, 1935.

[62] Z. Hashin and S. Shtrikman. A variational approach to the theory of the effective magnetic permeability of multiphase materials. *Journal of Applied Physics*, 33(10):3125–3131, Oct 1962.

[63] R. Tavangar, J.M. Molina, and L. Weber. Assessing predictive schemes for thermal conductivity against diamond-reinforced silver matrix composites at intermediate phase contrast. *Scripta Materialia*, 56(5):357–360, 2007.

[64] R. C. Atwood, S. Sridhar, W. Zhang, and P. D. Lee. Diffusion-controlled growth of hydrogen pores in aluminium-silicon castings: in situ observation and modelling. *Acta Materialia*, 48(2):405–417, January 2000.

[65] A.J. Markworth. The transverse thermal conductivity of a unidirectional fibre composite with fibre-matrix debonding: a calculation based on effective-medium theory. *Journal of material science letters*, 12(19):1487–1489, 1993.

[66] W. J. Boettinger, J. A. Warren, C. Beckermann, and A. Karma. Phase-field simulation of solidification. *Annual review of materials research*, 32:163–194, 2002.

[67] N. Palle and J. A. Dantzig. An adaptive mesh refinement scheme for solidification problems. *Metallurgical Materials Transactions A*, 27(3):707–717, 1996.

[68] T.S. Piwonka and M.C. Flemings. Pore formation in solidification. *Trans. AIME*, 236(8):1157–1165, 1966.

[69] W.S. Pellini. Factors which determine riser adequacy and feeding range. *AFS Transactions*, 61:61–80, 1953.

[70] E. Niyama, T. Uchida, M. Morikawa, and S. Saito. Predicting shrinkage in large steel castings from temperature gradient calculations. *AFS Int Cast Met J*, 6(2):16–22, 1981.

[71] K. D. Carlson and C. Beckermann. Prediction of shrinkage pore volume fraction using a dimensionless niyama criterion. *Metallurgical Material Transactions A*, 40A(1):163–175, 2009.

[72] P. D. Lee, A. Chirazi, and D. See. Modeling microporosity in aluminum-silicon alloys: a review. *Journal of Light Metals*, 1(1):15–30, February 2001.

[73] D.M. Stefanescu. Computer simulation of shrinkage related defects in metal castings - a review. *International journal of cast metal research*, 18(3):129–143, 2005.

[74] P. D. Lee and J. D. Hunt. Hydrogen porosity in directionally solidified aluminium-copper alloys: a mathematical model. *Acta Materialia*, 49(8):1383–1398, May 2001.

[75] Ch.-A. Gandin and M. Rappaz. Coupled finite element-cellular automation model for the prediction of dendritic grain structures in solification processes. *Acta Metallurgica*, 42(7):2233–2246, 1994.

[76] J. S. Wang and P. D. Lee. Simulating tortuous 3D morphology of microporosity formed during solidification of Al-Si-Cu alloys. *International journal of cast metals research*, 20(3):151–158, 2007.

[77] P. D. Lee, A. Chirazi, R. C. Atwood, and W. Wang. Multiscale modelling of solidification microstructures, including microsegregation and microporosity, in an Al-Si-Cu alloy. *Materials Science and Engineering A*, 365(1-2):57–65, January 2004.

[78] W. Kurz, B. Giovanola, and R. Trivedi. Theory of microstructural development during rapid solidification. *Acta Metallurgica*, 34(5):823–830, 1986.

[79] R. C. Atwood and P. D. Lee. Simulation of the three-dimensional morphology of solidification porosity in an aluminium-silicon alloy. *Acta Materialia*, 51(18):5447–5466, October 2003.

[80] D. Emadi and J.E. Gruzelski. Effects of casting and melt variables on porosity in directionally-solidified Al-Si alloys. *AFS Transactions*, pages 307–312, 1994.

[81] Q.T. Fang and D.A. Granger. Porosity formation in modified and unmodified A356 alloy castings. *AFS Transactions*, pages 989–1000, 1989.

[82] P.D. Grasso. *Coalescence and mechanical behaviour of semi-solid aluminium alloys in relation to hot tearing.* PhD thesis, EPFL, 2004.

[83] J.-M. Drezet, M. Rappaz, G.-U. Grun, and M. Gremaud. Determination of thermophysical properties and boundary conditions of direct chill-cast aluminum alloys using inverse methods. *Metallurgical Material Transactions A*, 31(6):1627–1634, 2000.

[84] J.M. Apprill, D.R. Poirier, Maguire, M.C., and T.C. Gutsch. Gasar porous metals process control. In *Material research society symposium proceedings*, volume 521, pages 291–296. Materials research society, 1998.

[85] S. Degallaix and B. Ilschner. *Caractérisation expérimentale des matériaux I.* Traité des matériaux 2, 2007.

[86] http://www.astm.org/standards/e1417.htm.

[87] http://www.techstreet.com/cgi-bin/detail?product_id=1204586.

[88] A.C Kak and M. Slaney. *Principles of computerized tomography imaging.* IEEE Press, 1987.

[89] E. Maire, J.-Y. Buffière, L. Salvo, J.J. Blandin, W. Ludwig, and J.M. Letang. On the application of X-ray microtomography in the field of materials science. *Adv. Eng. Mater.*, 3(8):539–546, 2001.

[90] J. Radon. Mengen konvexer körper, die einen gemeinsamen punkt enthalten. *Mathematische Annalen*, 83:113–115, 1921.

[91] L.A. Feldkamp, L.C. Davis, and J.W. Kress. Practical cone-beam algorithm. *Journal of the Optical Society of America*, 1:612–619, 1984.

[92] D. Favez. *Soudage laser or-acier : métallurgie et procédé*. PhD thesis, EPFL, 2009.

[93] S. Terzi, L. Salvo, M. Suéry, N. Limodin, J. Adrien, E. Maire, Y. Pannier, M. Bornert, D. Bernard, M. Felberbaum, M. Rappaz, and E. Boller. In situ X-ray tomography observation of inhomogeneous deformation in semi-solid aluminium alloys. *Scripta Materialia*, 61(5):449–452, September 2009.

[94] http://rsbweb.nih.gov/ij/index.html.

[95] William E. Lorensen and Harvey E. Cline. Marching cubes: A high resolution 3D surface construction algorithm. *Comput Graphics (ACM)*, 21(4):163–169, 1987.

[96] M. Doube, A. W. Conroy, P. Christiansen, J. R. Hutchinson, and S. Shefelbine. Three-dimensional geometric analysis of felid limb bone allometry. *PLoS ONE*, 4(3):e4742–, March 2009.

[97] Andrew Pressley. *Elementary Differential Geometry*. Springer-Verlag, 2001.

[98] P. G. Batchelor, A. D. C. Smith, D. L. G. Hill, D. J. Hawkes, T. C. S. Cox, and A. F. Dean. Measures of folding applied to the development of the human fetal brain. *Ieee Transactions On Medical Imaging*, 21(8):953–965, 2002.

[99] D. Kammer and P. W. Voorhees. The morphological evolution of dendritic microstructures during coarsening. *Acta Materialia*, 54(6):1549–1558, April 2006.

[100] A. Sémoroz, S. Henry, and M. Rappaz. Application of the phase-field method to the solidification of hot-dipped galvanized coatings. *Metallurgical Material Transactions A*, 31(2):487–495, 2000.

[101] D. Bernard, Ø. Nielsen, L. Salvo, and P. Cloetens. Permeability assessment by 3D interdendritic flow simulations on microtomography mappings of Al-Cu alloys. *Materials Science and Engineering A*, 392(1-2):112–120, February 2005.

[102] Modeling of defect formation in solidification processes using granular dynamics and phase field approaches. Technical report, CCMX-MERU, 2008-2011.

[103] A. Jacot, H. Meidani, and M. Felberbaum. Phase-field simulation of micropores constrained by a solid network. *Transactions of the Indian Institute of Metals*, 62:305–308, 2009.

[104] L. Lach. *Modeling vapor expansion of extruded cereals*. PhD thesis, EPFL, 2006.

[105] A. K. Dahle and L. Arnberg. The effect of grain refinement on the fluidity of aluminium alloys. *Aluminium Alloys: Their Physical and Mechanical Properties, Pts 1-3*, 217:259–264, 1996.

[106] Ch. Péquet. *Modelling of microporosity, macroporosity and pipe shrinkage formation during the solidification of aluminium alloys, using a mushy zone refinement method*. PhD thesis, EPFL, 2002.

Appendix A

Physical properties of an Al-4.5wt%Cu alloy

The liquid Al-4.5wt%Cu alloy is considered to have a viscosity of $1.5 \times 10^{-3}\,\mathrm{kg\,m^{-1}\,s^{-1}}$. The latent heat of solidification of this alloy is equal to $3.88 \times 10^{5}\,\mathrm{J\,kg^{-1}}$, and the liquidus and solidus temperature are equal to 650 and 548 ℃, respectively. The thermal conductivity, density and specific heat as a function of temperature are given in the tables below.

Table 6.1: Thermal conductivity as a function of temperature.

Temperature [°C]	Thermal conductivity [$\mathrm{W\,m^{-1}\,K^{-1}}$]
79.85	188.3
149.85	188.3
199.85	188.3
249.85	188.3
299.85	192.5
501.85	192.5
637.85	82.6
726.85	85.6

Table 6.2: Density as a function of temperature.

Temperature [°C]	Density [$\mathrm{kg\,m^{-3}}$]
208	2780
548	2700
550	2640
578	2630
608	2590
626	2560
646	2430
650	2380
710	2360

Table 6.3: Specific heat as a function of temperature.

Temperature [°C]	Specific heat [$\mathrm{J\,kg^{-1}\,K^{-1}}$]
26.85	882
226.85	969
501.85	1093
637.85	1059

Appendix B

Here we give a script example to calculate the average grey value in sphere for each xyz coordinate given in a file called "AvizoPoints.dat".

```
import ij.*;
import ij.gui.*;
import ij.measure.*;
import ij.plugin.*;
import ij.plugin.filter.*;
import ij.process.*;
import ij3d.image3d.*;
import ij3d.utils.*;
import java.util.*;
import java.awt.*;
import java.awt.event.ItemEvent;
import java.io.BufferedWriter;
import java.io.BufferedReader;
import java.io.FileNotFoundException;
import java.util.StringTokenizer;
import java.io.FileWriter;
import java.io.FileReader;
import java.io.IOException;
import java.io.*;
import java.text.*;
import java.util.Enumeration;
import java.util.Vector;
//Histogram for each pixel in 3D
public class HistoPixel3Drf_ implements PlugInFilter
{
int x,y,z;
ImagePlus imp;
TabUtil tab;
float rad;
float UpperValue;
float LowerValue;
IntImage3D col;
String filename = "D:" + File.separatorChar + "Milan" +
File.separatorChar + "ImageJ" + File.separatorChar +
```

```
"plugins" + File.separatorChar + "AvizoPoints.dat";
private boolean Dialogue()
{
GenericDialog gd = new GenericDialog("3D Histo Pixel");
gd.addNumericField("Radius", rad, 0);
gd.addNumericField("LowerValue", LowerValue, 0);
gd.addNumericField("UpperValue", UpperValue, 0);
gd.showDialog();
rad = (int) gd.getNextNumber();
UpperValue = (int) gd.getNextNumber();
LowerValue = (int) gd.getNextNumber();
return (!gd.wasCanceled());
}
public void run (ImageProcessor ip)
{
rad = 5;
LowerValue = -1;
UpperValue = 256;
col = new IntImage3D (imp.getStack());
if (Dialogue ()) {
try {
read (filename);
}
catch (Exception e) {
System.out.println("error_Milan "+": "+e.getMessage());
}
}
}
private void read (String filename) throws Exception
{
int line = 0;
try {
FileReader file         = new FileReader (filename);
BufferedReader buf      = new BufferedReader    (file);

boolean eof = false;
try {
while (!eof) {
String string = buf.readLine ();
IJ.resetEscape();
if (string == null || IJ.escapePressed()) {
eof = true;
}
else {
this.myread (string);
```

```
tab = col.getNeighborhoodSphere (x, y, z, rad, rad, rad);
float mean = tab.getMean ();
if (mean >= UpperValue && mean <= LowerValue)
IJ.write (/*x + "" + "  " + y + "" + "  " + z + "" +*/"  " + mean);
line++;
}
}
} catch (Exception e) {
System.out.println("error_Milan "+": "+e.getMessage());
}
buf.close ();
}
catch (Exception e) {
System.out.println("error_Milan "+": "+e.getMessage());
}
}
private void myread (String string) throws Exception {
StringTokenizer st    = new StringTokenizer    (string, "\t");
int count      = st.countTokens        ();
int xyz[]      = {0, 0, 0};
//count        = (count > 3) ? 3 : count;
for (int l = 0; l < count; l++) {
String token    = st.nextToken ().trim ();
xyz [l]                = (new Integer (token)).intValue ();
x = xyz [0];
y = xyz [1];
z = xyz [2];
}
}
public int setup (String arg, ImagePlus imp) {
this.imp = imp;
return DOES_8G + DOES_16 + NO_CHANGES;}}
```

Appendix C

The purpose of this section is to validate the model described in section 4.3.1 by a non-dimensional analysis. We will evaluate the characteristic time for diffusion of hydrogen and for the velocity of the interface in order to be sure that the interface moves slowly compared to diffusion. In our case, we have Eq. 4.27 in the mush:

$$\frac{\partial \langle X_H \rangle}{\partial t} = D_e \nabla^2 \langle X_H \rangle \tag{6.1}$$

where ∇ is the gradient in spherical coordinates. Note that we neglect the flux of di-hydrogen (gas) in the pore, since the diffusion of hydrogen in the gas phase is more a mechanical problem. Moreover, one could consider a very high diffusion coefficient (as already done in section 4.4) so that the concentration in the gas is uniform.
We know that the change of number of moles in the pore must be compensated by the diffusive flux of hydrogen at the pore surface. In other terms, we have:

$$\frac{n_{H_2}}{V} 4\pi (R_p^{sph})^2 \frac{R_p^{sph}}{\partial t} = 4\pi (R_p^{sph})^2 \frac{\rho}{\mathcal{M}_{Al}} \left(D_e \frac{\partial \langle X_H \rangle}{\partial r} \right) \tag{6.2}$$

Introducing the perfect gas law, one gets:

$$\frac{2 p_{H_2} \mathcal{M}_{Al}}{\mathcal{R} T \rho} \frac{R_p^{sph}}{\partial t} = D_e \frac{\partial \langle X_H \rangle}{\partial r} \tag{6.3}$$

At the boundary $r = R_p^{sph}$, we have $p_{H_2} = 2\gamma_{\ell g}/R_p^{sph}$, and then:

$$\frac{4\gamma_{\ell g} \mathcal{M}_{Al}}{\mathcal{R} T \rho} \frac{R_p^{sph}}{\partial t} = D_e \frac{\partial \langle X_H \rangle}{\partial r} \qquad \text{at } r = R_p^{sph} \tag{6.4}$$

Finally, at $r = R_{p0}$, there is a no flux condition, i.e., we have a closed system and hence:

$$\frac{\partial \langle X_H \rangle}{\partial r} = 0 \qquad \text{at } r = R_{p0} \tag{6.5}$$

Let us then scale the equations by introducing the dimensionless characteristic time $\tau = t/t_c$ (where t_c is a characteristic time to be determined) as well as the dimensionless radius $r^\dagger = r/R_{p0}$, the dimensionless pore radius $R_p^{sph,\dagger} = R_p^{sph}/R_{p0}$, and finally the normalized composition $\langle X_H \rangle^\dagger = \langle X_H \rangle / X_{H\ell 0}$, where $X_{H\ell 0}$ is the initial alloy hydrogen composition Equation 6.1 becomes then:

$$\frac{R_{p0}^2}{D_e t_D} \frac{\partial \langle X_H \rangle^\dagger}{\partial \tau} = (\nabla^\dagger)^2 \langle X_H \rangle^\dagger \tag{6.6}$$

where $\nabla^\dagger$ is the dimensionless gradient in spherical coordinates, and the well-known Fourier number (Fo $= Dt_c/R_{p0}^2$) appears on the left-hand side of this equation. Concerning the velocity of the interface, Eq. 6.4 becomes:

$$\frac{4\gamma_{\ell g}\mathcal{M}_{Al}}{\mathcal{R}T\rho}\frac{1}{R_p^{sph,\dagger}}\frac{R_{p0}}{t_c}\frac{\partial R_p^{sph,\dagger}}{\partial \tau} = \frac{D_e X_{H\ell 0}}{R_{p0}}\frac{\partial \langle X_H\rangle^\dagger}{\partial r^\dagger} \tag{6.7}$$

Dividing by $D_e X_{H\ell 0}$, one gets:

$$\underbrace{\frac{4\gamma_{\ell g}\mathcal{M}_{Al}}{\mathcal{R}T\rho X_{H\ell 0}R_{p0}}}_{Cte}\frac{1}{t_c}\frac{R_{p0}^2}{D_e}\frac{1}{R_p^{sph,\dagger}}\frac{\partial R_p^{sph,\dagger}}{\partial \tau} = \frac{\partial \langle X_H\rangle^\dagger}{\partial r^\dagger} \tag{6.8}$$

We have isolated here in the constant Cte the terms that do not appear in the diffusion equation (Eq. 6.6) and we have:

$$\begin{aligned} Cte &= \frac{4\gamma_{\ell g}\mathcal{M}_{Al}}{\mathcal{R}T\rho X_{H\ell 0}R_{p0}} \\ Cte &= \frac{4\times 0.8\,\mathrm{N\,m^{-1}}\times 27\times 10^{-2}\,\mathrm{kg\,mol^{-1}}}{8.31\,\mathrm{N\,m\,K^{-1}\,mol^{-1}}\times 900\,\mathrm{K}\times 27\times 10^{2}\,\mathrm{kg\,m^{-3}}\times 6.9\times 10^{-6}\times 5\times 10^{-4}\,\mathrm{m}} \\ Cte &\approx 30 \gg 1 \end{aligned} \tag{6.9}$$

And we can re-write Eq. 6.8 as:

$$Cte\frac{1}{t_c}\frac{R_{p0}^2}{D_e}\frac{1}{R_p^{sph,\dagger}}\frac{\partial R_p^{sph,\dagger}}{\partial \tau} = \frac{\partial \langle X_H\rangle^\dagger}{\partial r^\dagger} \qquad \text{at } r^\dagger = R_p^{sph,\dagger} \tag{6.10}$$

Finally, one gets also from Eq. 6.5

$$\frac{\partial \langle X_H\rangle^\dagger}{\partial r^\dagger} = 0 \qquad \text{at } r^\dagger = 1 \tag{6.11}$$

If we are interested in pore growth, we choose $t_c = Cte \times R_{p0}^2/D_e$ so that Eq. 6.10 becomes:

$$\frac{1}{R_p^{sph,\dagger}}\frac{\partial R_p^{sph,\dagger}}{\partial \tau} = \frac{\partial \langle X_H\rangle^\dagger}{\partial r^\dagger} \tag{6.12}$$

Let us go back now to the partial differential equation:

$$\underbrace{\frac{1}{Cte}}_{\to 0 \text{ for } Cte \gg 1} \times \frac{\partial \langle X_H\rangle^\dagger}{\partial \tau} = (\nabla^\dagger)^2\langle X_H\rangle^\dagger \tag{6.13}$$

This leaves the following set of equation for $X_{H\ell}^\dagger$:

$$(\nabla^\dagger)^2\langle X_H\rangle^\dagger = 0 \tag{6.14}$$

$$\frac{1}{R_p^{sph,\dagger}}\frac{\partial R_p^{sph,\dagger}}{\partial \tau} = \frac{\partial \langle X_H\rangle^\dagger}{\partial r^\dagger} \qquad \text{at } r^\dagger = R_p^{sph,\dagger} \tag{6.15}$$

$$\frac{\langle X_H\rangle^\dagger}{\partial r^\dagger} = 0 \qquad \text{at } r^\dagger = 1 \tag{6.16}$$

A common solution for this set of equations would be to use an equation of the type:

$$\langle X_H \rangle^\dagger = A/r^\dagger + B \tag{6.17}$$

But this equation does not satisfy the boundary condition at $r^\dagger = 1$ (Eq. 6.16). But if we assume that $R_p^{sph,\dagger} \ll 1$ and treat $r^\dagger = 1$ as $r \to \infty$, we can use Eq. 6.17 as an approximate solution. However, we then need to enforce the additional condition:

$$\int_\Omega X_H dV = \frac{4}{3}\pi R_{p0}^3 X_{H\ell 0} \qquad \text{where } \Omega \text{ is the sphere of radius } R_{p0} \tag{6.18}$$

in order for mass to be conserved.

It seems so that the biggest restrictions on validity of the solution given by Eq. 6.17 are:

(i) $R_p^{sph}/R_{p0} \ll 1$, an assumption already done in the first paragraph of section 4.3,

(ii) The solidification time t_f must be chosen so that the Fourier number $\text{Fo} = D_e t_f / R_{p0}^2 \gg 1$ so that the interface of the growing pore moves slowly compared to hydrogen diffusion.

Appendix D

Here we give an Avizo script to extract both principal curvature from a ".tif" binarized stack of images.

```
# This is an Avizo Script (".hx") to extract both
# curvature from a .tif binarized stack
# Milan Felberbaum, December 17, 2009

remove -all
remove MF06_01_0004_0005.tif MF06_01_0004_0005.surf
BothCurvatures SurfaceGen GetCurvature

# Create viewers
viewer setVertical 0

viewer 0 setBackgroundMode 1
viewer 0 setBackgroundColor 0.145098 0.152941 0.176471
viewer 0 setBackgroundColor2 0.435294 0.45098 0.498039
viewer 0 setTransparencyType 5
viewer 0 setAutoRedraw 0
viewer 0 show
mainWindow show

set hideNewModules 0

[ load -tif +mode 2 +box 0 354.2 0 358.4 0 261.8 "C:/Documents
and Settings/mfelberb/Desktop/MF06_01_0004_0005.tif" ]
setLabel MF06_01_0004_0005.tif

MF06_01_0004_0005.tif setIconPosition 20 10
MF06_01_0004_0005.tif sharedColormap setDefaultColor 0.8 0.8 0.8
MF06_01_0004_0005.tif sharedColormap setDefaultAlpha 0.500000
MF06_01_0004_0005.tif fire
MF06_01_0004_0005.tif setViewerMask 65535

set hideNewModules 0
create HxGMC {SurfaceGen}
SurfaceGen setIconPosition 160 40
```

```
SurfaceGen data connect MF06_01_0004_0005.tif
SurfaceGen fire
SurfaceGen smoothing setIndex 0 2
SurfaceGen options setValue 0 0
SurfaceGen options setToggleVisible 0 1
SurfaceGen options setValue 1 0
SurfaceGen options setToggleVisible 1 1
SurfaceGen border setValue 0 1
SurfaceGen border setToggleVisible 0 1
SurfaceGen border setValue 1 0
SurfaceGen border setToggleVisible 1 1
SurfaceGen minEdgeLength setMinMax 0 0 0.800000011920929
SurfaceGen minEdgeLength setValue 0 0
SurfaceGen materialList setIndex 0 0
SurfaceGen fire
SurfaceGen setViewerMask 65535

set hideNewModules 0
[ {SurfaceGen} create {MF06_01_0004_0005.surf}
 ] setLabel {MF06_01_0004_0005.surf}
MF06_01_0004_0005.surf setIconPosition 20 70
MF06_01_0004_0005.surf master connect SurfaceGen
MF06_01_0004_0005.surf fire
MF06_01_0004_0005.surf LevelOfDetail setMinMax -1 -1
MF06_01_0004_0005.surf LevelOfDetail setButtons 1
MF06_01_0004_0005.surf LevelOfDetail setIncrement 1
MF06_01_0004_0005.surf LevelOfDetail setValue -1
MF06_01_0004_0005.surf LevelOfDetail setSubMinMax -1 -1
MF06_01_0004_0005.surf setTransform 1 0 0 0 0 1 0 0 0 0 1 0 0 0 0 1
MF06_01_0004_0005.surf fire
MF06_01_0004_0005.surf setViewerMask 65535

set hideNewModules 0
create HxGetCurvature {GetCurvature}
GetCurvature setIconPosition 160 100
GetCurvature data connect MF06_01_0004_0005.surf
GetCurvature fire
GetCurvature method setValue 0
GetCurvature param setMinMax 0 1 20
GetCurvature param setValue 0 2
GetCurvature param setMinMax 1 0 5
GetCurvature param setValue 1 4
GetCurvature output setIndex 0 6
GetCurvature fire
GetCurvature setViewerMask 65535
```

```
set hideNewModules 0
[ GetCurvature create 6
 ] setLabel {BothCurvatures}
BothCurvatures setIconPosition 20 127
BothCurvatures master connect GetCurvature 6
BothCurvatures surface connect MF06_01_0004_0005.surf
BothCurvatures fire
BothCurvatures setViewerMask 65535
BothCurvatures select

set hideNewModules 0

viewer 0 setCameraOrientation 1 0 0 3.14159
viewer 0 setCameraPosition 0 2.11567e-007 -2.42005
viewer 0 setCameraFocalDistance 2.42005
viewer 0 setCameraNearDistance 1.42005
viewer 0 setCameraFarDistance 3.42005
viewer 0 setCameraType perspective
viewer 0 setCameraHeightAngle 44.9023
viewer 0 setAutoRedraw 1
viewer 0 redraw
```

Appendix E

Here we give a C++ program to extract both principal curvature from a ".raw" binarized stack of images with the software VTK.

```
/*
Milan Felberbaum, December 17th 2009,
This is a vtk filter to deduce both principal
curvatures on a binarized ".raw" binary file
comming from an X-ray tomography scan.
Many thanks to Aurèle Mariaux for his help with vtk.

Compilation command:
g++ -Wno-deprecated -I/sw/include/vtk-5.0 filtre10_tot.cpp -L/sw/lib/vtk
-lvtkIO -lvtkGraphics -lvtkCommon -lvtkFiltering
*/

#include "vtkImageReader.h"
#include "vtkMarchingCubes.h"
#include "vtkWindowedSincPolyDataFilter.h"
#include "vtkCurvatures.h"
#include "vtkXMLPolyDataWriter.h"
#include "vtkPointData.h"
#include <cstdio>
#include <cstring>
#include <cstdlib>

int main(int argc, char* argv[]) {
  char fname[250];
  vtkImageReader* reader;
  vtkMarchingCubes* contours;
  vtkWindowedSincPolyDataFilter* smoother;
  vtkCurvatures* curv;
  vtkXMLPolyDataWriter* writer;
  vtkPolyData* smoothed;
  vtkDataArray* curvVal;
  double spacing;
  int extent[3];
  int numPoints, i, j, test;
```

```
double coords[3];
FILE *file;
if (argc!=6) {
  printf ("Usage: %s prefix spacing X Y Z\n", argv[0]);
  exit (1);
}
spacing = atof (argv[2]);
for (i=0;i<3;i++)
extent[i] = atoi (argv[3+i]);

strcpy (fname, argv[1]);
strcat (fname, ".raw");
reader = vtkImageReader::New();
reader->SetFilePrefix(fname);
reader->SetFilePattern("%s");
reader->SetDataScalarTypeToUnsignedChar();
reader->SetDataByteOrderToLittleEndian();
reader->SetFileDimensionality(3);
reader->SetDataOrigin(0,0,0);
reader->SetDataSpacing(spacing, spacing, spacing);
reader->SetDataExtent(0, extent[0], 0, extent[1], 0, extent[2]);
reader->SetNumberOfScalarComponents(1);

contours = vtkMarchingCubes::New();
contours->SetInputConnection(reader->GetOutputPort());
contours->SetNumberOfContours(1);
contours->SetValue(0, 255);

smoother = vtkWindowedSincPolyDataFilter::New();
smoother->SetInputConnection(contours->GetOutputPort());
smoother->SetNumberOfIterations(10);
smoother->SetPassBand(0.05);

curv = vtkCurvatures::New();
curv->SetCurvatureTypeToMinimum();
curv->SetInputConnection(smoother->GetOutputPort());

strcpy (fname, argv[1]);
strcat (fname, ".vtp");
writer = vtkXMLPolyDataWriter::New();
writer->SetInputConnection(curv->GetOutputPort());
writer->SetByteOrderToLittleEndian();
writer->SetDataModeToBinary();
writer->SetFileName(fname);
writer->Write();
```

```
strcpy (fname, argv[1]);
strcat (fname, "_min.dat");
file = fopen(fname, "wt");
smoothed = curv->GetOutput();
curvVal = smoothed->GetPointData()->GetScalars();
numPoints = smoothed->GetNumberOfPoints();
for (i=0;i<numPoints;i++) {
  test = 1;
  smoothed->GetPoint(i, coords);
  for (j=0;j<3;j++)
    if (coords[j] < 3. || coords[j] > spacing*extent[j] - 3. ) {
  test = 0;
  break;
    }
  if (test)
    fprintf (file, "%lf\n", curvVal->GetTuple1(i));
}
curv = vtkCurvatures::New();
curv->SetCurvatureTypeToMaximum();
curv->SetInputConnection(smoother->GetOutputPort());

strcpy (fname, argv[1]);
strcat (fname, ".vtp");
writer = vtkXMLPolyDataWriter::New();
writer->SetInputConnection(curv->GetOutputPort());
writer->SetByteOrderToLittleEndian();
writer->SetDataModeToBinary();
writer->SetFileName(fname);
writer->Write();

strcpy (fname, argv[1]);
strcat (fname, "_max.dat");
file = fopen(fname, "wt");
smoothed = curv->GetOutput();
curvVal = smoothed->GetPointData()->GetScalars();
numPoints = smoothed->GetNumberOfPoints();
for (i=0;i<numPoints;i++) {
  test = 1;
  smoothed->GetPoint(i, coords);
  for (j=0;j<3;j++)
    if (coords[j] < 3. || coords[j] > spacing*extent[j] - 3. ) {
  test = 0;
  break;
    }
```

```
    if (test)
      fprintf (file, "%lf\n", curvVal->GetTuple1(i));
  }

  fclose(file);
  writer->Delete();
  curv->Delete();
  smoother->Delete();
  contours->Delete();
  reader->Delete();
  return 0;
}
```

Appendix F

Here we give the part of the C++ code developed to calculate both A and B coefficients of the model developed in this thesis (see section 4.3 for the details).

```
/* @(#) $Id: InterpolatorClass.cpp,v 1.5 2009/08/05 10:32:17 gco Exp $ */
//
// DESCRIPTION : class for the calculation of gas porosity
//               fraction and pore radius including H2 diffusion
//
// AUTHOR : Gael Couturier, Milan Felberbaum
// DATE : 2009 sept 15
// COMMENT:
// LAST MODIFICATION : 2010 jan 06
//
#include <cstdio>
#include <cmath>
#include <math.h>
#include <stdio.h>
#include <stdlib.h>
#include <string.h>
#include "DiffGasPoroClass.h"
float stdPres = 100000.;
float pi = 3.1415926;
float perfGasConst = 8.3145;
float KCConv = 273.15;
// Constructor
DiffGasPoroClass::DiffGasPoroClass() {
}
// Destructor
DiffGasPoroClass::~DiffGasPoroClass() {
}
// Initialize members that will not evolve
void DiffGasPoroClass::initFixedMembers(
float poreDensity,
float poreNucleiRadius,
float poreSurfaceEnergy,
float partitionCoef,
float nominalMolarGasConc,
```

```
float alloyDensity,
float alloyMolarMass,
int   diffusionAccelerator)
{
itsPoreDensity = poreDensity;
itsPoreNucleiRadius = poreNucleiRadius;
itsPoreSurfaceEnergy =  poreSurfaceEnergy;
itsPartitionCoef = partitionCoef;
itsNominalMolarGasConc = nominalMolarGasConc;
itsAlloyDensity = alloyDensity;
itsAlloyMolarMass = alloyMolarMass;
itsSphereRadius = pow ( 3. / ( itsPoreDensity * 4. * pi ), 1./3. );
itsGasMoleNbInSphere = itsNominalMolarGasConc * 1. /
itsPoreDensity * itsAlloyDensity / itsAlloyMolarMass;
itsDiffusionAccelerator = diffusionAccelerator;
return;
}
// Initialize evolving variables
void DiffGasPoroClass::initVariableMembers(
float curGasActivity,
float curEquiConst,
float prevPoreFraction,
float prevPoreRadius,
int   constrainedPore,
float prevTemperature,
float curTemperature,
float curSolidFrac,
float prevLiqPres,
float curLiqPres,
float dt)
{
itsCurGasActivity = curGasActivity;
itsCurEquiConst = curEquiConst;
itsPrevPoreFraction = prevPoreFraction;
itsPrevPoreRadius = prevPoreRadius;
itsConstrainedPore = constrainedPore;
itsPrevTemperature = prevTemperature;
itsCurTemperature = curTemperature;
itsCurSolidFrac = curSolidFrac;
itsPrevLiqPres = prevLiqPres;
itsCurLiqPres = curLiqPres;
itsDt = dt;
itsCurPoreFraction = 0.;
itsCurPoreRadius = itsPoreNucleiRadius;
itsNucleation = 0;
```

```
itsCurGasConservation = itsNominalMolarGasConc
* itsAlloyDensity / itsAlloyMolarMass
* ( 4. / 3. * pi * ( pow( itsSphereRadius, 3 ) - pow( itsPoreNucleiRadius, 3 ) ) );
return;
}
// Check if the pore has nucleated
// if it is the case, then itsNucleation = 1, else itsNucleation = 0.
void DiffGasPoroClass::checkIfNucleated( void )
{
float liqPlusLaplacePres;
float gasPartialPres;
float molarGasConc;

if ( itsPrevPoreFraction > 0. )
{
// if the pore has already nucleated at a previous step
itsNucleation = 1;
}
else
{
// the pore nucleates if gas partial pressure exceeds p_l + Laplace overpressure
liqPlusLaplacePres = itsCurLiqPres + 2. *
itsPoreSurfaceEnergy / itsPoreNucleiRadius;
//
// calculation of gas molar concentration dissolved
//in the liquid phase before nucleation
molarGasConc = itsNominalMolarGasConc /
( (1-itsCurSolidFrac) + itsCurSolidFrac * itsPartitionCoef );

gasPartialPres = itsCurEquiConst *
pow( itsCurGasActivity * molarGasConc, 2 ) * stdPres;
//
if ( gasPartialPres >= liqPlusLaplacePres )
{
itsNucleation = 1;
}
}
return;
}
// pore growth model based on gas diffusion:
// calculation of current porosity fraction and current pore curvature radius
void DiffGasPoroClass::poreGrowthModel( float *A, float *B )
{
float curGasPartialPressure;
float curMolarGasConcAtPoreLiq;
```

```
float MeancurMolarGasConcAtPoreLiq;
float prevPoreVol;
float prevGasMolesNbInPore;
float prevGasMolesNbInLiqSol;
float prevGasPartialPressure;
double curDliq, curDsol, curDeff;
float temp1;
float coef1[2][2];
float coef2[3];
float coef3[2];
float gasMolesNbPassingFromLiqToPore;
float prevPoreSize;
float prevPoreSurface;
float poreVolInc;
float curPoreVol;
float curGasMolesNbInPore;
// I.     Determination of the gas concentration profile in the liquid phase
// ( A and B coefficients in relation Xgas = A / r + B ).

// I.1.   Calculation of the gas partial pressure at the current step from
// the pore mechanical equilibrium equation.
// assumption: as pore curvature radius at the current step is still unknown,
// it is assumed equal to the pore curvature radius at the previous step
curGasPartialPressure = itsCurLiqPres +
2. * itsPoreSurfaceEnergy / itsPrevPoreRadius;
//
// I.2.   From I.1. and from the gas solubility products
//deduction of the gas molar concentration in the liquid
// at the interface with the pore at the current step.
curMolarGasConcAtPoreLiq =  pow( curGasPartialPressure /
( stdPres * itsCurEquiConst ), (float) 0.5 ) / itsCurGasActivity;

MeancurMolarGasConcAtPoreLiq = curMolarGasConcAtPoreLiq *
( 1 - itsCurSolidFrac + itsCurSolidFrac * itsPartitionCoef);
//
// I.3.   From the perfect gas law, determination of the
//number of gas moles in the pore at the previous step
if ( itsPrevPoreFraction == 0 )
{
prevPoreVol = 4. / 3. * pi * pow( itsPoreNucleiRadius, 3 );
}
else
{
prevPoreVol = itsPrevPoreFraction * 1. / itsPoreDensity;
}
```

```
prevGasPartialPressure = itsPrevLiqPres +
2. * itsPoreSurfaceEnergy / itsPrevPoreRadius;
prevGasMolesNbInPore = 2 * prevGasPartialPressure * prevPoreVol /
( perfGasConst * ( itsPrevTemperature + KCConv ) );
//
// I.4. From I.3. and from the nominal gas mole number
//in solution in the liquid metal, deduction of the number of
//gas moles in the solid-liquid mixture at the previous step
prevGasMolesNbInLiqSol = itsGasMoleNbInSphere - prevGasMolesNbInPore;
//
// I.5.   To deduce A and B coefficients in relation Xgas = A / r + B,
// a/ spherical integration of the gas concentration profile in
// the solid-liquide mixture at the current step = I.4
// (to conserve gas quantity in sphere and sphere volume,
// integration is done with fixed alloy density),
// b/ + condition: gas concentration in the liquid at
//the interface with the pore (deduced at I.2.),

*A = (-3. * itsAlloyMolarMass * prevGasMolesNbInLiqSol * itsPrevPoreRadius +
4. * 3.1416 * itsPrevPoreRadius * (-pow(itsPrevPoreRadius, 3.) +
pow(pow(3./(4.*pi*itsPoreDensity), 1./3.), 3.)) *
MeancurMolarGasConcAtPoreLiq * itsAlloyDensity)/
(2. * 3.1416 * pow(itsPrevPoreRadius -
pow(3./(4.*pi*itsPoreDensity), 1./3.), 2.) * (itsPrevPoreRadius +
2. * pow(3./(4.*pi*itsPoreDensity), 1./3.)) * itsAlloyDensity);
*B = MeancurMolarGasConcAtPoreLiq - coef1[0][0] * *A;
//
// I.6 Gas conservation check
itsCurGasConservation = prevGasMolesNbInPore +
coef1[1][0] * *A + coef1[1][1] * *B;
//
// II. Determination of the porosity fraction at the current step
// II.1. Calculation of the effective diffusion coefficient at the current step
// a/ Expressions of Dliq and Dsol (Anyalebechi et al.):
// b/ Diffusion of liquid and solid in serial: Deff = ( 1 - gs ) * Dliq + gs * Dsol
// (Close to Deff calculated by Felberbaum et al.):
curDliq = 1.22e-4 * exp( -54455.8 /
( perfGasConst * ( itsCurTemperature + KCConv ) ) );
curDsol = 4.24e-5 * exp( -53163.6 /
( perfGasConst * ( itsCurTemperature + KCConv ) ) );
curDeff = 1*(( 1 - itsCurSolidFrac ) * curDliq + itsCurSolidFrac * curDsol);
if ( itsDiffusionAccelerator == 1 )
{
curDeff *= 100.;
}
```

```
//
// II.2.   determination of the number of gas moles
// passing from the liquid phase to the pore
// Pore is assumed spherical here for the determination
// of prevPoreSurface (pore tortuousity is not considered)
// curDeff = ( 1 - itsCurSolidFrac ) * curDliq + itsCurSolidFrac * curDsol;
prevPoreSurface = 4 * pi * pow ( prevPoreSize, 2 );
gasMolesNbPassingFromLiqToPore = - curDeff * itsAlloyDensity /
itsAlloyMolarMass * *A / pow( prevPoreSize, 2 ) * prevPoreSurface  * itsDt;
//
// II.3.   From II.2. and from the perfect gaz law,
//calculation of the pore volume increment during dt
prevGasPartialPressure = itsPrevLiqPres +
2. * itsPoreSurfaceEnergy/itsPrevPoreRadius;
//
if ( itsConstrainedPore )
{
curGasMolesNbInPore = gasMolesNbPassingFromLiqToPore + prevGasMolesNbInPore;
curPoreVol = 0.5 * perfGasConst * ( itsCurTemperature + KCConv )*
curGasMolesNbInPore/(itsCurLiqPres+2.*itsPoreSurfaceEnergy/itsPrevPoreRadius);
poreVolInc =  curPoreVol - prevPoreVol;
}
else
{
coef2[0] = 0.5*perfGasConst*(itsPrevTemperature + KCConv)/prevGasPartialPressure;
coef2[1] = - 0.5 * perfGasConst * ( itsPrevTemperature + KCConv ) /
pow( prevGasPartialPressure, 2 ) * prevGasMolesNbInPore;
coef2[2] = 0.5 * perfGasConst / prevGasPartialPressure * prevGasMolesNbInPore;
coef3[0] = coef2[0] * gasMolesNbPassingFromLiqToPore + coef2[1] *
(itsCurLiqPres-itsPrevLiqPres)+coef2[2]*(itsCurTemperature-itsPrevTemperature);
coef3[1] = 1.+coef2[1]*itsPoreSurfaceEnergy/(2.*pi*pow(itsPrevPoreRadius,4));
poreVolInc = coef3[0] / coef3[1];
}
//
// II.4.   From II.3. calculation of the pore fraction at the current step
itsCurPoreFraction = ( prevPoreVol + poreVolInc ) * itsPoreDensity;
//
// II.5.   Calculation of the pore curvature radius  at the current step
if ( itsConstrainedPore )
{itsCurPoreRadius = itsPrevPoreRadius;}
else
{itsCurPoreRadius = pow ( 3. / ( 4. * pi ) *
( prevPoreVol + poreVolInc ), 1./3. );}
return;
}
```

Milan Felberbaum

Av. de Milan 28
1007 Lausanne

+41 21 944 19 35
+41 78 798 22 44

milan.felberbaum@gmail.com

27 ans
Single
Swiss

EDUCATION

2005-2010	***PhD*** at the Computational Materials Lab, EPFL.
2000-2005	Master degree in ***Materials science and engineering***, EPFL.
2004	Exchange ***Erasmus*** in Zürich, ETHZ.
1997-2000	Baccalaureate (Latin – Maths) in Lausanne.

PROFESSIONAL ACHIEVEMENTS

2005 (6 months)	***Rolls-Royce*** Fuel Cells Ltd in Derby (UK); improvement and implementation in the production scale of the fuel cell electrolyte fabrication process.
2004-2005	***Research assistant*** at the non-metallic materials lab at ETH-Zürich; Solid Oxide Fuel Cells characterization

EXTRA-PROFESSIONAL EXPERIENCE

1999-2003	Swiss ice hockey referee (national level).

TECHNICAL AND COMPUTATIONAL SKILLS

Metal casting (lab level), metallography, optical and electronic microcopy (***SEM***) coupled with electron back-scattered diffraction (***EBSD***), Energy-dispersive X-ray spectroscopy (***EDX***), X-ray diffraction analysis (***XRD***), Pulsed laser deposition (***PLD***), X-ray tomography (***X-ray µCT***), fuel cells characterization.
Windows, Linux, Mac OS.
MS Office, Mathematica, C/C++, Java, Adobe softwares, Image analysis (ImageJ, VTK/Paraview, Amira).

LANGUAGES

French (mother), ***English*** (fluent, C2 level of the European standard), ***German*** (good, C1 level), ***Italian*** (bases, A2 level), understand ***Swiss-German***.

HOBBIES & INTERESTS

Sports (Ice hockey), travel.

LIST OF PUBLICATIONS

Phase-fleld simulation of micropores constrained by a solid network,
Jacot, A. and Meidani, H. and Felberbaum, M., **Transactions of The Indian Institute of Metals** 62 (2009), To be published.

In situ and real-time 3-D microtomography investigation of dendritic solidification in an Al–10 wt.% Cu alloy,
Limodin, N. and Felberbaum, M. and Suéry, M. et al., **Acta Materialia** 57 (2009) 2300–2310.

In situ X-ray tomography observation of inhomogeneous deformation in semi-solid aluminium alloys,
Terzi, S. and Felberbaum, M. and Suéry, M. et al., **Scripta Materialia** 61 (2009) 449–452.

A phase field model for a geometrical description of micropores constrained by a solid network,
Felberbaum, M. and Jacot, A., TMS Annual Meeting, **MCWASP XII**, Vancouver (BC) 2009.

Microporosity in aluminium cast alloys observed by X-ray tomography,
Felberbaum, M. and Rappaz, M., **Metall. Mat. Trans.**, To be submitted.

An effective hydrogen diffusion coefficient for solidifying aluminum alloys,
Felberbaum, M. and Rappaz, M. et al., **Acta Materialia**, To be submitted.

Shrinkage influence upon gas porosity observed in-situ by X-ray tomography,
Felberbaum, M. and Salvo, L. and Rappaz, M. et al., **Acta Materialia**, To be submitted.

Influence of anode thickness on the electrochemical performance of SC-SOFC,
Buergler, B.E. and Felberbaum, M. and Gauckler, L.J. et al., **CESP** 2006 27 (4), pp. 37-45.